UNIVERSITY OF SOUTHAMPTON

FACULTY OF SCIENCE

DEPARTMENT OF PHYSICS

INVESTIGATIONS INTO YTTERBIUM, YTTERBIUM-ERBIUM AND THULIUM-DOPED SILICA-BASED FIBRE LASERS

by

Ian Richard Perry

A thesis submitted for the degree of Doctor of Philosophy

January 1991

CONTENTS

UNIVERSITY OF SOUTHAMPTON

ABSTRACT

FACULTY OF SCIENCE

PHYSICS

Doctor of Philosophy

INVESTIGATIONS INTO YTTERBIUM, YTTERBIUM-ERBIUM AND THULIUM-DOPED SILICA-BASED FIBRE LASERS

by Ian Richard Perry

Continuous-wave monomode laser oscillation has been demonstrated in ytterbium-doped fibre at 974nm and around 1040nm for pump wavelengths in the 0.8μm region. High slope efficiencies (up to 78%) and low threshold powers (10mW absorbed) were measured for this device. Tunable operation from 1000nm to 1162nm, the generation of Q-switched pulses, and efficient amplified spontaneous emission have also been demonstrated, and some of these features have been modelled.

A fibre doped with erbium and sensitised with ytterbium has been investigated to study the effect of energy transfer from the ytterbium co-dopant to the erbium ions after excitation at wavelengths in the 0.8μm region. The effects of pump excited state absorption on the threshold and slope efficiency have been characterised. Continuous-wave monomode laser oscillation was observed at 1.564μm with a 5mW absorbed threshold power. The laser wavelength was tunable from 1.521μm to 1.562μm.

Continuous-wave monomode laser action in a thulium-doped fibre, also pumped in the 0.8μm region, was observed at around 2μm with an absorbed threshold power of about 30mW. The laser wavelength was tunable from 1810nm to 2014nm. A change of pump source to a high power Nd:YAG laser operating at 1.064μm yielded fibre laser output powers of up to 1.35W with a threshold power of 600mW. Pump excited state absorption at 1.064μm and the resulting upconverted visible fluorescence has been investigated and modelled.

ACKNOWLEDGEMENTS

I wish to express my gratitude to all those who have contributed their time, effort and expertise to the research described in this thesis. Particular thanks are due to my supervisor Professor David Hanna, and to Dr. Anne Tropper, for their guidance and encouragement. I would also like to thank my co-workers whose contributions have made this work possible, most notably Richard Smart and Paul Suni (whose help with the computer modelling was invaluable), and also Matthew McCarthy, John Lincoln and Mike Percival. A special debt of gratitude is owed to Janet Townsend for fabricating the fibres used during this research.

CHAPTER 1

INTRODUCTION

This thesis describes research into rare-earth-doped silica based optical fibres, with an emphasis on the laser performance of these devices when placed into a resonant structure such as a Fabry-Perot cavity. Three different fibre laser systems were investigated, involving fibres doped with ytterbium (Yb^{3+}), thulium (Tm^{3+}), and doubly-doped with both ytterbium and erbium (Er^{3+}). All of the fibres used in the experiments described in the following chapters were fabricated by Janet Townsend of the Optical Fibre Group in the Department of Electronics and Computer Science at the University of Southampton.

An introduction to the principles of optical propagation in fibres and a discussion of the features that make the doping of such fibres attractive for laser operation is given in Chapter 2, which also details the experimental techniques for constructing fibre laser resonators and goes on to describe the basic theory of operation.

Chapter 3 provides a brief summary of the important features of rare-earth ions as impurities in a glass host, including the salient points of the Judd-Ofelt theory leading to the Fuchtbauer-Ladenburg relation for calculating radiative lifetimes from measurements on the absorption spectrum of a particular rare-earth transition.

Chapters 4 to 7 form the main part of this thesis: the experimental results of the investigations into three different fibre laser systems. The experimental techniques necessary for this research are introduced at appropriate points in the text and for this reason some of the methods described in Chapter 4 for measuring, *e.g.*, the spectrum of fluorescence emitted radially from the fibre, or the lifetime of a particular excited state, are applicable in later chapters. Chapter 4 describes the spectroscopy and laser operation of Yb^{3+}-doped fibre when pumped in the 0.8μm region with a Styryl 9M dye laser. The dye laser was employed to assess the fibre laser performance when pumped at wavelengths achieveable from commercially available GaAlAs diode lasers, since in most practical applications of fibre lasers a compact, cheap and reliable pump source would be a necessity. The fluorescence spectrum for emission in the infrared, around 1μm, is investigated, and evidence for a cooperative luminescence process giving emission in the visible region around 500nm is also described. Continuous-wave single mode laser action in the 1μm region on the $^2F_{5/2} \rightarrow {}^2F_{7/2}$ transition is shown to occur via a three-level transition to the ground state and a quasi-four-level transition to a Stark level in the ground state multiplet. The particular transition that exhibits laser action can be selected by appropriate choice of fibre length and pump wavelength. The laser gain for both transitions is modelled as a function of fibre length and pump power, for the purpose of predicting the minimum possible threshold power and the length of fibre required to achieve this, if cavity losses can be specified. Preliminary results of continuously tunable operation on the four-level transition are developed to the point where a fibre loop polarisation controller is incorporated into the resonator to eliminate output power fluctuations due to wavelength dependent cavity losses. Laser operation in the form of Q-switched pulses is demonstrated using an acousto-optic deflector to modulate the cavity loss, and the output power and pulse duration are modelled. In addition to providing an efficient fibre laser source in the 1μm region, the Yb^{3+}-doped fibre also exhibits amplified spontaneous emission (ASE) due to the high single pass gain available from this system, and the output characteristics for the three- and four-level transitions are presented, together with supporting calculations to describe the phenomenon.

Chapter 5 describes the characteristics of a fibre containing both Er^{3+} as a laser-active dopant and Yb^{3+} as a sensitiser to absorb GaAlAs diode laser-compatible wavelengths where a singly-doped Er^{3+} fibre exhibits excited state absorption. The effect of pump wavelength (provided by a Styryl 9M dye laser) on the slope efficiency and threshold power for continuous-wave single-mode laser action on the $^4I_{13/2} \rightarrow {}^4I_{15/2}$ transition in Er^{3+} at 1.5μm is investigated, and optimum pump wavelengths in the 0.8μm region are identified. Some preliminary results for tunable operation are also described.

In Chapter 6, details of investigations into a Tm^{3+}-doped fibre pumped with a Styryl 9M dye laser at around 0.8μm are presented. Continuous-wave single mode oscillation on the $^3H_4 \rightarrow {}^3H_6$ transition at 2μm and tunable operation in this wavelength region are described, and fluorescence spectra are included for pumping at 0.8μm and also at 476nm, where an argon ion laser was used to excite the higher lying levels.

Tm^{3+}-doped fibre was also found to possess a weak absorption at the Nd:YAG wavelength of 1.064μm, and the ready availability and high power output of this type of source led to investigation of its use as a pump for a high power fibre laser at 2μm. These experiments are described in Chapter 7, where modifications of the fibre design are shown to permit continuous-wave single mode 2μm fibre laser output at power levels in excess of 1 Watt. The realisation of a high power fibre laser source at this wavelength is one of the most significant results of the work described in this thesis, and may find applications in a variety of situations. In addition to 2μm emission, the fibre also fluoresces at visible wavelengths around 470nm due to a multiphoton sequential absorption scheme when pumped at 1.064μm. This upconversion fluorescence is described and a model is developed to predict the laser gain at 2μm in the presence of the upconversion process as a function of fibre length and input power. As with the Yb^{3+} model, the minimum possible threshold can be predicted if the cavity losses are known. Finally, some comparisons of the spectroscopy and laser performance are made between three different types of Tm^{3+}-doped fibre, where the differences are due to changes in the silica-based host composition and the dopant concentration.

Chapter 8 concludes this thesis with a summary of the main features of these investigations into fibre lasers, and makes some suggestions for continuation and development of the work.

It should be noted that, since the experimental programme detailed in this thesis was in general a collaborative effort of a team of researchers, some parts of the results presented herein have appeared elsewhere [1.1], specifically the laser and ASE performance of the Yb^{3+}-doped fibre and the Yb^{3+}-Er^{3+} co-doped fibre characteristics. However, with respect to the Yb^{3+} results: the modelling of the laser transitions and the ASE, the Q-switched operation, and the characterisation of visible emission, are unique to this thesis.

Reference

[1.1] R.G. Smart, Ph.D. Thesis, University of Southampton (1990)

CHAPTER 2

FIBRE LASERS

2.1 Introduction

The present intense research into fibre lasers and amplifiers, due in no small part to developments in the telecommunications industry and improvements in optical fibre design and fabrication techniques, follows a relatively recent resurgence of interest in a technology that dates back almost as far as the laser itself. The glass fibre laser was invented by Elias Snitzer in 1961 [2.1], with subsequent reports in 1963-64 [2.2, 2.3], again by Snitzer, involving a flashlamp pumped multicomponent neodymium-doped fibre with a 10μm core diameter. The possibilty of semiconductor diode pumping, a common feature of present-day fibre lasers, was first suggested by Koester in 1966 [2.4], and in 1973 Stone and Burrus [2.5] reported longitudinal pumping by a coherent source of a 40μm core diameter fused silica neodymium-doped fibre, with thresholds as low as 1-2mW absorbed. Thus by the mid-1970s, all the major features of the typical fibre laser were in place, albeit involving multimode rather than single mode fibres.

Interest in the subject went into decline over the next ten years until the development by the Southampton University Optical Fibre Group of a method of fabricating single mode silica fibre doped with laser-active rare-earth impurities [2.6] while still retaining the ultra low loss characteristics of telecommunications grade fibre (typically 0.5dB/km at 1.3μm or 0.25dB/km at 1.55μm). Initial work concentrated on the $^4F_{3/2} \rightarrow {}^4F_{11/2}$ transition in Nd^{3+} around 1.06μm. Diode-pumped single mode laser operation was reported [2.7, 2.8], followed by reports of Q-switched operation [2.9, 2.10], mode-locked operation [2.11, 2.12], superfluorescent operation [2.13] and tunable operation [2.14, 2.15]. Laser action was also demonstrated on the $^4F_{3/2} \rightarrow {}^4I_{9/2}$ transition at ≈ 0.9μm [2.16-2.18] and on the $^4F_{3/2} \rightarrow {}^4I_{13/2}$ transition at 1.39μm [2.19]. The 1.536μm $^4I_{13/2} \rightarrow {}^4I_{15/2}$ transition in Er^{3+} also stimulated a great deal of interest, since this wavelength falls within the so-called third telecommunications window at 1.55μm. As with Nd^{3+}, a range of Er^{3+}-doped active fibre devices was developed (further details of erbium-doped fibre lasers may be found in Chapter 5) for use as sources, signal repeaters, amplifiers and detector preamplifiers [2.20-2.32].

However, doped optical fibre has many and varied uses in fields other than telecommunications, such as medical applications, sensor technology and spectroscopy. In view of this, the optical properties of several rare-earth dopants in fibre hosts have been studied over the last few years to investigate the range of emission wavelengths and performance characteristics attainable with devices of this nature, most notably in the form of fibre lasers. To date, seven of the fifteen rare-earth elements have exhibited laser action in silica fibre, with wavelengths ranging from 651nm in samarium to beyond 2μm in thulium and holmium. A summary of these laser transitions is given in Table 2.1.

Studies involving silica fibres containing ytterbium, erbium and thulium are presented in Chapters 4, 5, 6 and 7 of this thesis. The remainder of this chapter considers some of the basic principles of fibre lasers and the advantages for laser action afforded by the fibre geometry.

2.2 Basic Features of Fibre Lasers

Fibre lasers are in essence extremely simple devices. Rare-earth dopant ions may be incorporated into the core region of cylindrical glass optical fibres to form a medium which exhibits optical gain under appropriate excitation conditions of these ions. This excitation is achieved usually through longitudinal pumping by focusing light into the core of the fibre at one end. The light then propagates along the fibre core, confined by a layer of glass possessing a lower refractive index to that of the core. Pump light of an appropriate wavelength undergoes absorption by the dopant ions as it propagates, whereby the energy of the pump photons promotes electrons in the ground state of these ions to higher lying energy levels. Relaxation of these excited levels transfers the absorbed pump energy back to the ground state either by the production of phonons (the quanta of vibrations of the silica host material) or by a radiative process involving the creation of a photon. If sufficient pump energy is absorbed to create a population inversion, laser action may then be induced by placing the fibre within a resonant structure such as a Fabry-Perot cavity, providing that the gain due to the stimulated photons exceeds the total losses of the resonant cavity.

Dopant	Transition	Wavelength (μm)	References
Pr^{3+}	${}^1D_2 \rightarrow {}^3F_{3,4}$	1.08	[2.33, 2.34]
	$D_2^1 \rightarrow F_2^3, H_6^3$	0.888	[2.34]
Nd^{3+}	${}^4F_{3/2} \rightarrow {}^4I_{13/2}$	1.39	[2.19]
	${}^4F_{3/2} \rightarrow {}^4F_{11/2}$	1.055 - 1.14	[2.7-2.15]
	${}^4F_{3/2} \rightarrow {}^4I_{9/2}$	0.9 - 0.95	[2.16-2.18]
Sm^{3+}	${}^4G_{5/2} \rightarrow {}^6H_{9/2}$	0.651	[2.35]
Ho^{3+}	${}^5I_7 \rightarrow {}^5I_8$	2.04	[2.36]
Er^{3+}	${}^4I_{13/2} \rightarrow {}^4I_{15/2}$	1.51 - 1.60	[2.20-2.32]
Tm^{3+}	${}^3H_4 \rightarrow {}^3H_6$	1.780 - 2.056	[2.37-2.39]
Yb^{3+}	${}^2F_{5/2} \rightarrow {}^2F_{7/2}$	0.974	[2.40-2.43]
	${}^2F_{5/2} \rightarrow {}^2F_{7/2}$	1.000 - 1.162	

Table 2.1

Rare-earth doped fibre lasers clearly have many similarities, from a spectroscopic aspect, to laser systems involving rare-earth doped bulk glasses or crystals. The imposition of a fibre geometry onto a rare-earth doped glass laser system does however offer several important advantages over conventional bulk devices.

Perhaps the most striking feature of fibre lasers is the small cross sectional dimension of the active region, with core diameters for monomode fibres typically less than 5μm. This fact, combined with the waveguiding properties of the fibre and the good power handling properties of the silica host, means that a high pump intensity can be maintained within the doped core for relatively low input powers, and in many cases readily available semiconductor diode lasers of modest output power can be used as pump sources. The small pumped volume offers a significant reduction in threshold requirements over bulk systems. In general, longitudinal pumping of a bulk laser medium is preferable to transverse excitation since the pumped volume can be minimised by focusing the pump beam to a spot size w_0 such that the length L of the active medium is equal to the confocal parameter $2\pi w_0^2/\lambda$, where λ is the pump wavelength. The pumped area is then of the order of $L\lambda$. For monomode fibres, the core radius of only a few micrometers means the pumped area is typically two to three orders of magnitude lower than in the bulk longitudinally pumped arrangement. The reduction in threshold by this same factor thus brings the typical threshold requirement for fibre lasers down to the milliwatt level.

A further advantage over bulk systems due to the fibre geometry is the high surface area to volume ratio. This allows rapid heat dissipation to take place, unlike the situation in bulk lasers where the lower dissipation rate can often prevent continuous-wave oscillation and preclude three-level operation when the high pump rate required cannot be met by the rate of heat removal, leading to fracture or optical damage. The rapid heat dissipation from pumped fibres also circumvents the problems of thermal distortion common in bulk glass lasers.

If the fibre is made to be single transverse mode at both the pump and laser wavelengths, then the good spatial overlap of the two propagating fields makes the most efficient use of the pump energy, although it is common for fibres to be slightly multimode at the pump wavelength so that the core radius can be as large as possible (without compromising single mode operation at the laser wavelength) to facilitate the launching of pump power into the fibre and maximise the launch efficiency. In other circumstances, as small a core size as possible is desirable for high pump intensity and maximum gain in, for example, telecommunications amplifiers, so clearly the exact fibre design depends on the potential application under consideration. A single mode waveguide automatically provides a reliable fundamental mode Gaussian intensity-profile output which may be easily matched to an undoped fibre for delivery of the fibre laser radiation to a remote location. Developments in optical fibre technology have produced a range of fibre devices such as polarizers, wavelength selective beamsplitters, modulators and integral gratings with which fibre lasers are fully compatible. Directional couplers are especially important since they can be formed into loops which act as reflectors, thus replacing bulk mirrors and eliminating the associated diffraction losses.

The broad inhomogeneous bandwidth of the optical transitions of rare-earth ions in an amorphous glass host such as silica (arising mainly from site to site variations in the host electric fields) in conjunction with the high optical damage threshold of silica, make it possible to obtain short duration, high peak power pulses from fibre lasers when operated in Q-switched or mode locked conditions. The broad fluorescence also allows tunable laser operation over significant ranges, and broadband amplification is possible when the fibre is removed from a resonant cavity environment. The long interaction length of the waveguiding structure allows weak absorption to be fully exploited, so that pumping far into the wings of an absorption band can still provide sufficient gain for laser action if a long enough fibre is used.

Fibre lasers thus have many unique and interesting features that make them an important addition to the range of solid state laser devices currently available. The presence of pump bands accessible by GaAlAs diode lasers is of particular relevance in the realisation of cheap, practical, compact and reliable fibre laser devices. However, even in situations where large pump sources such as argon ion, neodymium:YAG or dye lasers are required, doped fibres have a role as simple and efficient wavelength converters, requiring little more than a set of suitable mirrors and a means of launching pump light into the fibre.

2.3 Fibre Laser Fabry-Perot Resonators

The simplest cavity for a fibre laser is a Fabry-Perot design, formed by placing the ends of the fibre directly against flat mirrors formed from dielectric coated substrates, a process known as "butting". The mirror at the pumped end of the fibre (the input mirror) is usually highly transmitting at the pump wavelength and highly reflecting at the laser wavelength. The mirror at the other end (the output coupler) has a transmission of typically a few percent at the laser wavelength to couple out a fraction of the circulating power. The fibre is longitudinally pumped by focusing light from an external laser source on to the end of the fibre through the input mirror. If the pump wavelength coincides with one of the dopant ion absorption bands then laser action may occur within the resonant structure formed by the two mirrors. Under high gain conditions, the ≈ 4 percent Fresnel reflections from the ends of the fibre may themselves define the resonant structure without the need for additional bulk mirrors. Alternatively, dielectric coatings may be applied directly onto the fibre ends to form mirrors and so eliminate the butting procedure, where the fibre ends are often damaged on contact with a bulk mirror. Conventional mirrors may be dispensed with altogether by using fibre loop reflectors, where the fibre is formed into a loop and fused onto itself so that light entering the loop is either transmitted through the output end or "reflected" back through the input end.

A simple modification to the bulk optic version of the Fabry-Perot cavity allows the incorporation of intracavity elements, such as wavelength selective devices for tuning and modulators for Q-switching or mode locking, to be inserted usually between the fibre output end and the output coupler. The output light from the fibre must then be collimated with an intracavity lens with a numerical aperture close to that of the fibre so that the insertion losses are minimised. Q-switching [2.10] and mode locking [2.11] have been demonstrated with arrangements of this type. Tuning of the fibre laser wavelength can also be achieved with the introduction of an intracavity wavelength selective element such as a set of birefringent Lyot filters [2.39], or simply a prism [2.42], so that only a limited region of the lasing bandwidth resonates in the cavity. An alternative means of tuning is to replace the output coupler with a reflection diffraction grating [2.32]. This arrangement still requires an intracavity lens to collimate the fibre output onto the grating, and to provide a gap into which a beamsplitter may be placed to extract the useful output.

Tuning of fibre laser resonators is also possible without recourse to bulk optical components, an attractive feature due to the reduction in insertion losses which otherwise increase the threshold power for laser action. The fibre loop reflectors described above have a reflectivity that is dependent on the coupling ratio, which is itself dependent on the wavelength. Tuning can be achieved [2.44] by changing the temperature of the fused region, which alters the coupling ratio and hence the wavelength at which the loop is reflective. Another tuning technique that avoids a bulk wavelength selective element is the formation of a grating directly onto the fibre by polishing away a few millimetres longitudinally to expose the core region into which grooves are etched [2.45]. A resonator is formed by a high reflector at the fibre input end and the grating at the other end acting as a distributed feedback reflector.

For the work described in this thesis, resonators were formed using bulk mirrors and bulk intracavity components. This was far more convenient than coated fibre ends, or fibre reflectors, etc., since the bulk set-up allowed rapid and easy changes of, *e.g.*, output coupling or fibre length. The following section describes some of the practical points to be considered when constructing resonators of this type.

2.4 Constructing Fibre Laser Resonators

If the ends of a fibre are to be butted up against dielectric mirrors, or dielectric layers are to be deposited directly onto the ends, then it is important that the ends are of a high quality so that irregularities or imperfections do not degrade the laser performance by introducing additional losses. The fibre ends should ideally be flat and perpendicular to the fibre axis. The mirror surface, in the case of bulk optics, should also be perpendicular to this axis, so that when the fibre is butted there is no gap between the fibre and the mirror. Angular misalignment can have a marked adverse effect on the cavity loss. Hanna *et al.* [2.46] observed an increase in the single pass loss of $\approx 10\%$ when the output coupler mirror angle of a neodymium-doped fibre laser was changed by as little as 1°. This loss arises because the fraction of emergent power from the fibre that is coupled back in after reflection is reduced by the angular offset. An angled fibre end face is similarly detrimental, as light refracted at the fibre/air interface is not recaptured by the core if the angle is too great. The deliberate formation of angled ends may in fact be used to suppress end face reflections in applications where resonance is undesirable.

There are two principal methods of preparing the fibre ends prior to butting against mirrors. The fibre may be fixed with epoxy resin into a short piece (a few cm) of glass capillary tube and polished on a grinding wheel using successively finer grades of polishing paper to produce a high quality flat surface. Perpendicularity of the fibre end face with its axis does of course depend on the fibre and capillary tube axes being parallel and the tube being held perpendicular to the polishing surface. This method is rather unsatisfactory since it is time consuming and prone to damage at the weak point where the fibre leaves the capillary tube. A more serious drawback is the difference in hardness between the capillary glass and the silica fibre, with the relative softness of the latter resulting in the formation of a depression in the polished surface in the region of the fibre. This means that a gap exists between the fibre and mirror even if the capillary tube is in contact with the mirror.

The polishing method has since been virtually abandoned in favour of a far simpler and more reliable technique, that of cleaving the fibre via the propagation of a crack initiated at its edge. This is most effectively performed using a commercially available cleaving tool such as the *FK 11* device designed by York Technology Limited for cleaving telecommunications fibres in the field. The end few centimetres of the fibre are firstly stripped of the protective plastic coating and cleaned thoroughly in a suitable solvent such as acetone or methanol, and the fibre is then placed under longitudinal tension between a pair of clamps. Cleaving is achieved by introducing a diamond blade (vibrating at 60kHz) perpendicular to the fibre axis. When contact is made between the blade and the fibre, the crack propagation cleaves the fibre. The fibre end is then inspected interferometrically using the offcut piece, where the number of interference fringes indicates the angle made between the fibre end face and a reference optical flat. The tension may then be altered if necessary until the number of fringes is satisfactory. With this device, end face angles of 0.5° or better can be achieved.

When both ends of the fibre have been prepared in this way, the cavity may be constructed. The fibre ends are located in V-grooves (about $100\mu m$ deep and 4cm long) cut into metal blocks and secured in place by small magnets. A few millimetres (1-2mm) of fibre protrude from the end of the block where the mirror will make contact. These assemblies are then mounted onto micropositioning equipment so that each end can be moved along three independent, orthogonal axes, *i.e.*, along the fibre (z) axis and in the plane perpendicular to this (x-y plane). The particular micropositioners used for the fibre laser experiments described in chapters 4, 5, 6 and 7 were manufactured by Martock Design Limited and allowed sub-micron positioning accuracy of the fibre ends. Pump light is launched into the fibre (and collimated at its output) with, in most cases, a microscope objective mounted on a micropositioner. Graded index (GRIN) lenses were also used and found to perform adequately, but the ready availability of microscope objectives of various powers meant that these were the preferred means of launching into the fibre. The objectives are arranged so that the distance between the end of the objective and the fibre end face is approximately equal to the working distance. The mirror is situated between the objective and the fibre end, mounted in a holder possessing a rudimentary form of position control so that the mirror angle (with respect to the fibre end face) can be adjusted. The mirror holder is mounted onto a fixed platform so that the fibre end is manoeuvred with respect to the mirror during the butting process.

Launching of the pump light is maximised by observing the transmitted signal on a photo-diode located at the fibre output. When the input objective micropositioner has been adjusted for maximum fluorescence signal, the fibre end is gradually moved towards the mirror, with the objective position correspondingly moved away to maintain a maximised signal. When the fibre end is within a few microns of the mirror, the fluorescence signal increases markedly as light emerging from the fibre is reflected back in by the mirror. Modulations in this signal are observed as the fibre is moved, due to the etalon formed by the air gap between the fibre end and the mirror. When contact is made the modulations cease and the fluorescence signal becomes stable, a characteristic sign that the fibre and mirror are butted. This procedure is then repeated for the other end of the fibre in the case of a cavity with butted mirrors at both ends. Again, the modulations are observed, terminated upon butting when a dramatic increase in the signal indicates that laser oscillation is occurring (assuming the pump power is above the threshold power). Laser action can be confirmed by the presence of relaxation oscillations in the output signal, induced by an optical chopper in the pump beam.

2.5 Fibre Fabrication

The significant results of fibre laser research to date would not have been possible without the development of reliable methods of incorporating rare-earth dopants into fibres without compromising the low-loss characteristics at wavelengths away from the rare-earth absorption bands. There are four principal methods for doped fibre fabrication, namely: modified chemical vapour deposition (MCVD); rod-in-tube; vapour axial deposition (VAD); and casting. The silica-based fibres used for the experiments described in this thesis were fabricated by Janet Townsend (of the Optical Fibre Group in the Southampton University Department of Electronics and Computer Science) using a development of the MCVD process [2.47] known as solution-doping [2.48].

The fabrication process begins with the manufacture of a preform from which the fibre will be drawn. A silica tube with typically a 25mm diameter and 1.5mm walls is rotated slowly above a burner. A stream of gases comprising, for instance, $SiCl_4$, $POCl_3$ and CCl_2F_2 in an oxygen carrier, is passed through the tube, reacting in the high temperature (about $1500^\circ C$) to form a glassy layer on the inside of the tube. The initial layers deposited in this way form the cladding. The core material, at this stage containing no rare-earth dopant ions, is deposited in a similar manner but at a reduced temperature of about $1000^\circ C$ so that the layer is unsintered rather than glassy. Incorporation of the dopant ions is achieved by soaking the tube in a solution of rare-earth chloride which permeates into the porous unsintered layer. The tube is then dried out, and the deposited material oxidised, in a stream of $Cl_2/He/O_2$ before being sintered and pulled down into fibre form.

The rare-earth dopants are typically incorporated at the level of a few hundred parts per million silicon ions, and therefore have a negligible effect on the refractive index of the core. The index is raised by the addition of Ge or Al to the gas stream depositing the core region, so that after the heat reaction the core is either $GeO_2 - SiO_2$ or $Al_2O_3 - SiO_2$, commonly referred to as germano-silica and almina-silica, respectively.

2.6 Propagation in Optical Waveguides

The invariant field distributions which can propagate in dielectric optical waveguides are solutions of Maxwell's wave equation under the particular waveguide geometry. Each different solution is termed a mode and propagates with a different phase and group velocity, leading to dispersion if several modes are present. In a cylindrical waveguide there exist modes where both the electric field vector E and the magnetic field vector H have in general longitudinal, radial and azimuthal components. The modes can, however, be separated into two classes, termed EH if the axial electric field is dominant or HE if the axial magnetic field is dominant. Analytical simplification is made by assuming the "weak guidance" condition, *i.e.*, $n_{co} - n_{cl} \ll n_{cl}$, where n_{co} and n_{cl} are the core and cladding refractive indices, respectively. This is the situation that generally applies in optical fibres, and leads to simplified solutions to the wave equation in the form of linearly polarised, or LP_{lm}, modes where the non-negative integer subscripts l,m denote the order of the mode. These modes are almost transversely polarised and each is dominated by one transverse electric field component and one transverse magnetic field component. For each of these approximate solutions to Maxwell's equation, there exists another independent mode with electric and magnetic fields orthogonal to those of the first solution. The results derived from this simplification are sufficiently accurate for most applications. A full treatment of the analysis may be found in references [2.49] and [2.50] and is not duplicated here. The main features of the weak guidance approximation may be summarised by noting that, for a circularly symmetric step-index waveguide, the characteristic equation for the LP_{lm} modes is given by Gloge [2.49] as

$$U\,[J_{l-1}(U)/J_l(U)] = -\,W\,[K_{l-1}(W)/K_l(W)] \qquad (2.1)$$

where $J(U)$ is a Bessel function and $K(W)$ is a modified Hankel function. The parameters U and W are defined as

$$U = \rho\left(k^2 n_{co}^2 - \beta^2\right)^{1/2} \qquad (2.2)$$

$$W = \rho\left(\beta^2 - k^2 n_{cl}^2\right)^{1/2} \tag{2.3}$$

where β is the propagation constant of the mode, $k = 2\pi/\lambda$ is the free space wave number and ρ is the core radius (the cladding is assumed to extend to infinity in this analysis). The parameters U and W are related by a third parameter V given by

$$V^2 = U^2 + W^2 \tag{2.4}$$

This parameter is referred to as the V number of the fibre, and is in essence a normalised frequency since by substituting for U and W in Eq.2.4, V may be expressed as

$$V = \frac{2\pi\rho}{\lambda}\left(n_{co}^2 - n_{cl}^2\right)^{1/2} \tag{2.5}$$

The cut off condition is given by $W = 0$, *i.e.*, when the mode fields extend well into the cladding layer rather than being confined to the core so that the mode propagation constant equals kn_{cl}. Confinement thus takes place for values of W between 0 and ∞. For $W = 0$, Eq.2.1 gives $J_{l-1}(U) = 0$. In the limit $W \rightarrow \infty$, Eq.2.1 gives $J_l(U) = 0$. Therefore the solutions for confined modes are given by solutions for U which lie between the zeros of $J_{l-1}(U)$ and $J_l(U)$. For each value of l, the set of modes associated with each solution for U comprises four modes labelled by the additional subscript m. The lowest order mode, characterised by LP_{01}, has a cut off given by the lowest root of the equation $J_{-1}(U) = -J_1(U) = 0$, *i.e.*, at $V = 0$. Thus there will always be at least one propagating mode irrespective of the fibre V number. As V is increased from zero, the number of propagating modes also increases. The first additional mode to the LP_{01} mode is the LP_{11} mode which propagates for $V \geq 2.405$. Therefore, if single mode operation is required at a particular wavelength, the fibre must have a diameter no larger than ρ_{max} which, from Eq.2.5, is given by

$$\rho_{max} = 2.405 \frac{\lambda}{2\pi\left(n_{co}^{2} - n_{cl}^{2}\right)^{1/2}} \tag{2.6}$$

For single mode propagation at, for instance, 1μm, the core radius must then be no larger than about 2μm (using values for refractive indices found in typical fibres).

2.7 Fibre Laser Theory

A comprehensive treatment of the theory of fibre lasers and amplifiers by, for instance, Digonnet and Gaeta [2.51], or Armitage [2.52], appears in the literature. Useful expressions can be derived for the threshold power and the slope efficiency, and a brief description of the theory applicable to four-level systems in general follows below.

Digonnet and Gaeta give the following rate equations for a longitudinally pumped, homogeneously broadened four-level laser medium of length l in steady state, based on the work of Kubodera and Otsuka [2.53]:

$$\frac{dn(x,y,z)}{dt} = r(x,y,z) - \frac{n(x,y,z)}{\tau_f} - \frac{\sigma c n(x,y,z)}{n_{co}} \sum_{j=1}^{N} s_j(x,y,z) = 0 \tag{2.7}$$

$$\frac{dS_i}{dt} = \frac{c\sigma}{n_{co}} \iiint_{cavity} n(x,y,z) s_i(x,y,z)\, dv - \frac{c\delta_i}{2 l n_{co}} S_i = 0 \tag{2.8}$$

where c is the speed of light, σ is the emission cross section, δ_i is the round trip loss for the ith mode, τ_f is the upper level fluorescence lifetime, n_{co} is the core refractive index, $r(x,y,z)$ is the pump rate per unit volume, $n(x,y,z)$ is the upper level population density, s_i is the signal photon density of the ith mode and S_i is the total number of signal photons in the ith mode. The normalised distribution functions $r_0(x,y,z)$ and $s_{0,i}(x,y,z)$ are given by

$$r(x,y,z) = R r_0(x,y,z) \tag{2.9}$$

$$s_i(x,y,z) = S_i s_{0,i}(x,y,z) \tag{2.10}$$

and normalised such that the integral of both r_0 and s_0 over the cavity volume is unity. The summation in Eq.2.7 is carried out over the N transverse modes in the cavity. In the case of single mode operation, the only term in the summation is S_1 and the analysis is greatly simplified. With this assumption, Eq.2.7 is solved for $n(x,y,z)$ and substituted into Eq.2.8. Substitution of Eqs.2.9 and 2.10 then gives the following relation:

$$\iiint_{\text{cavity}} \frac{s_{0,1}(x,y,z)\ r_0(x,y,z)}{1 + \frac{\sigma c \tau_f}{n_{co}} S_1 s_{0,1}(x,y,z)}\, dv = \delta_1/(2\tau_f \sigma R l) \tag{2.11}$$

The pump rate R_{th} required for the oscillator to reach threshold is found by setting $S_1 = 0$ in Eq.2.11. This threshold pump rate is equivalent to $\eta_q P_{th,abs}/h\nu_p$, where $P_{th,abs}$ is the absorbed power at threshold, $h\nu_p$ is the pump photon energy and η_q is the pump quantum efficiency, *i.e.*, the fraction of absorbed photons that are pumped to the upper level. Thus the threshold power is given by

$$P_{th,abs} = \frac{h\nu_p \delta_1}{2\, l \sigma \tau_f \eta_q} \left\{ \iiint_{\text{cavity}} r_0(x,y,z) s_{0,1}(x,y,z)\ dv \right\}^{-1} \tag{2.12}$$

If the mode structure of the pump and signal is neglected, then a plane wave analysis equating the pump rate to the fluorescence decay rate at threshold (*i.e.*, no stimulated emission) gives:

$$\frac{P_{th,abs}}{h\nu_p} = \frac{n_{th} A l}{\tau_f \eta_q} \tag{2.13}$$

where n_{th} is the threshold population density in the upper laser level and A is the area of the fibre core, assuming that both pump and signal occupy the same volume, *i.e.*, the core region. From Eq.2.8, the right hand side of Eq.2.13 then becomes equivalent to $\delta_1/(2l\sigma\tau_f)$ such that

$$P_{th,abs} = \frac{h\nu_p \delta_1}{2\sigma\tau_f \eta_q} A \qquad (2.14)$$

Thus it is apparent that the effect of considering the mode structure is equivalent to defining an effective pump area A_{eff} given by

$$A_{eff}^{-1} = l \iiint_{cavity} r_0(x,y,z) s_{0,1}(x,y,z) \; dv \qquad (2.15)$$

and the threshold pump power given by Eq.2.12 becomes

$$P_{th,abs} = \frac{h\nu_p \delta_1}{2\sigma\tau_f \eta_q} A_{eff} \qquad (2.16)$$

when mode structure is under consideration. Digonnet and Gaeta [2.51] give general expressions for the pump power density and signal photon density for LP_{lm} modes which can be used to calculate the mode structure and effective area. However, the expression for effective area may be simplified by assuming Gaussian mode profiles [2.54] for both the pump distribution r_0 and the signal distribution $s_{0,1}$ as follows:

$$\begin{aligned} r_0 &= \frac{2}{\pi l w_p^2 \eta_p} \, exp\left(-2r^2/w_p^2\right) & r \leq \rho \\ &= 0 & r \geq \rho \end{aligned} \qquad (2.17)$$

$$s_{0,1} = \frac{2}{\pi \, l w_s^2} \, exp\left(-2r^2/w_s^2\right) \qquad (2.18)$$

where r is the radial distance from the fibre axis, w_p and w_s are the pump and signal spot sizes, respectively, and η_p is the fraction of the pump power propagating in the core given by

$$\eta_p = \iiint\limits_{\substack{\text{active}\\ \text{region}}} r_0(x,y,z)\,dv = 1 - exp\,(-2\rho^2/w_p^2) \tag{2.19}$$

Any z variation in r_0 and $s_{0,1}$ has been neglected. Substitution of Eqs.2.17 and 2.18 into Eq.2.15 then gives the following expression for the effective area:

$$A_{eff} = \frac{\pi\left(w_p^2 + w_s^2\right)\eta_p}{2\left\{1 - exp\left[-2\rho^2\left(1/w_p^2 + 1/w_s^2\right)\right]\right\}} \tag{2.20}$$

For a step index fibre, the Gaussian mode spot size may be approximated [2.55] by

$$w = \frac{\rho}{(\ln\ V)^{1/2}} \tag{2.21}$$

where V is the fibre V number. In most practical situations, the value of A_{eff} is very close to that of the actual core area $A_{core} = \pi\rho^2$. As an example, consider the ytterbium-doped fibre described in Chapter 4. The pump wavelength of 850nm and the signal wavelength of 1050nm give spot sizes of $w_p = 1.99\mu$m and $w_s = 2.31\mu$m for the pump and signal, respectively, for a core radius of 1.8μm. The LP_{11} mode cut off wavelength is 805nm, so both the pump and signal are single mode and assumed to be Gaussian. Eq.2.20 thus gives an effective area of $A_{eff} = 1.23 \times 10^{-11}$ m^2, compared to a core area of $A_{core} = 1.02 \times 10^{-11}$ m^2. Given the assumptions made in determining A_{eff} (no z variation of the distributions, step index fibre, pure four-level system) the actual core area is generally acceptable for threshold calculations if both pump and signal are propagating single mode.

The parameter η_p also has a role in the effective attenuation coefficient of the doped core experienced by the pump light as it propagates along the fibre. If the plane wave attenuation coefficient is α_p, then the effective coefficient α is given by $\alpha = \eta_p \alpha_p$ and can be measured directly by cutting back the fibre (see Chapter 4). The attenuation coefficient is useful in determining the absorption cross section σ_a, given by $\alpha_p = \sigma_a N$, where N is the dopant ion concentration. In practice however, α and α_p are taken to be equivalent, since the error introduced into the calculation of absorption cross sections by this assumption is almost certainly exceeded by the error in the quoted dopant concentration.

The slope efficiency η_s is defined as

$$\eta_s = \frac{dP_{out}}{dP_{abs}} \tag{2.22}$$

where P_{abs} is the total pump power absorbed by the active medium and P_{out} is the output power at the fibre laser wavelength. The absorbed power is related to the total pumping rate R by

$$P_{abs} = \frac{h\nu_p}{\eta_q} R \tag{2.23}$$

and the output power is related to the total photon number S_1 by

$$P_{out} = T \frac{c}{2ln_{co}} h\nu_s S_1 \tag{2.24}$$

where $h\nu_s$ is the signal photon energy and T is the output coupler transmission (the input mirror is assumed to have zero transmission at the signal wavelength). Clarkson and Hanna, following the method of Kubodera and Otsuka, show that by substituting Eqs.2.23 and 2.24 into Eq.2.11, the slope efficiency may then be expressed as

$$\eta_s = \frac{h\nu_s}{h\nu_p}\,\eta_q \eta_c\,\frac{T}{\delta_1} \tag{2.25}$$

where η_c is given by

$$\eta_c = \frac{\left[\displaystyle\iiint_{\text{cavity}} \frac{r_0(x,y,z)\,s_{0,1}(x,y,z)}{1 + \frac{\sigma c \tau_f}{n_{co}} S_1 s_{0,1}(x,y,z)}\,dv\right]^2}{\displaystyle\iiint_{\text{cavity}} \frac{r_0(x,y,z)\,s_{0,1}^2(x,y,z)}{\left\{1 + \frac{\sigma c \tau_f}{n_{co}} S_1 s_{0,1}(x.\,y,z)\right\}^2}\,dv} \tag{2.26}$$

which is the factor by which the plane wave expression for η_s is modified by the distributions of the pump and signal modes, and characterises the extent to which these modes overlap in the fibre. Eq.2.26 is therefore commonly termed the "overlap integral" for the pump and signal radiation. For low power operation, defined by $\sigma c \tau_f S_1 s_{0,1}/n_{cp} \ll 1$, Eq.2.26 is expressible in a much simplified form:

$$\eta_c = \frac{\left[\displaystyle\iiint_{\text{cavity}} r_0(x,y,z)\,s_0(x,y,z)\;dv\right]^2}{\displaystyle\iiint_{\text{cavity}} r_0(x,y,z)\,s_0^2(x,y,z)\;dv} \tag{2.27}$$

and by assuming Gaussian distributions for the pump and signal modes, as in Eqs.2.17 and 2.18, the overlap integral then becomes

$$\eta_c = \frac{w_p^2\left[2\,w_p^2 + w_s^2\right]\left(1 - exp\left[-2\rho^2\left(1/w_s^2 + 1/w_p^2\right)\right]\right)^2}{\eta_p\left[w_p^2 + w_s^2\right]^2\left(1 - exp\left[-2\rho^2\left(2/w_s^2 + 1/w_p^2\right)\right]\right)} \tag{2.28}$$

where w_p and w_s are the lowest order pump and signal spot size, respectively. As an example, consider the ytterbium-doped fibre described above where, for a pump wavelength of 850nm and a signal wavelength of 1050nm, the pump and signal spot sizes were 1.99μm and 2.31μm, respectively. The core radius of ρ = 1.8μm thus gives (from Eq.2.28) an overlap of $\eta_c = 0.74$. This increases to $\eta_c = 0.80$ for a pump wavelength of 900nm, tending to unity as the two wavelengths become equal. This demonstrates how the overlap can have a significant effect on the slope efficiency of a fibre laser. The fundamental limit on the slope efficiency is simply $(h\nu_s/h\nu_p)\eta_q$, since for a low loss cavity the ratio T/δ_1 approaches unity, and for good overlap $\eta_c \approx 1$.

2.8 Concluding Remarks

This chapter has described the basic features of fibre lasers and some of the important developments in the field, in addition to discussing some of the practical aspects of constructing fibre laser resonators. Theoretical expressions for two important parameters of laser action, the threshold power and slope efficiency, have been presented. The physical properties of dopant rare-earth ions in a glass host are described in the following chapter, and the remainder of this thesis considers several specific fibre laser systems in detail.

References

[2.1] E. Snitzer, 'Optical maser action of Nd^{+3} in a barium crown glass', *Phys. Rev. Lett.*, 7, 444 (1961)

[2.2] E. Snitzer, 'Neodymium glass laser', 999, *Proc. Third International Conference on Solid State Lasers*, Paris, France (1963)

[2.3] C.J. Koester and E. Snitzer, 'Amplification in a fiber laser', *Appl. Opt.*, 3, 1182 (1964)

[2.4] C.J. Koester, 'Laser action by enhanced total internal reflection', *IEEE J. Quantum Electron.*, QE-2, 580 (1966)

[2.5] J. Stone and C.A. Burrus, 'Neodymium-doped silica lasers in end-pumped fiber geometry', *Appl. Phys. Lett.*, 23, 388 (1973)

[2.6] S.B. Poole, D.N. Payne and M.E. Fermann, 'Fabrication of low-loss optical fibres containing rare-earth ions', *Electron. Lett.*, 21, 737 (1985)

[2.7] R.J. Mears, L.Reekie, S.B. Poole and D.N. Payne, 'Neodymium-doped silica single-mode fibre lasers', *Electron. Lett.*, 17, 738 (1985)

[2.8] M.W. Phillips, H. Gong, A.I. Ferguson and D.C. Hanna, 'Optical chaos and hysterisis in a laser-diode pumped Nd doped fibre laser', *Opt. Comm.*, 61, 215 (1987)

[2.9] I.M. Jauncey, J.T. Lin, L. Reekie and R.J. Mears, 'Efficient diode-pumped Cw and Q-switched single-mode fibre laser', *Electron. Lett.*, 22, 198 (1986)

[2.10] I.P. Alcock, A.C. Tropper, A.I. Ferguson and D.C. Hanna, 'Q-switched operation of a neodymium-doped monomode fibre laser', *Electron. Lett.*, 22, 84 (1986)

[2.11] I.P. Alcock, A.I. Ferguson, D.C. Hanna and A.C. Tropper, 'Mode-locking of a neodymium-doped monomode fibre laser', *Electron. Lett.*, 22, 268 (1986)

[2.12] G. Geister and R. Ulrich, 'Neodymium-fibre laser with integrated-optic mode locker', *Opt. Comm.*, 68, 187 (1988)

[2.13] K. Liu, M. Digonnet, H.J. Shaw, B.J. Ainslie and S.P. Craig, '10mW superfluorescent single-mode fibre source at 1060nm', *Electron. Lett.*, 23, 1320 (1987)

[2.14] I.P. Alcock, A.I. Ferguson, D.C. Hanna and A.C. Tropper, 'Tunable, continuous-wave neodymium doped monomode fibre laser', *Opt. Lett.*, 11, 709 (1986)

[2.15] L. Reekie, R.J. Mears S.B. Poole and D.N. Payne, 'Tunable single-mode fibre lasers', *J. Lightwave Technol.*, LT-4, 956 (1986)

[2.16] I.P. Alcock, A.I. Ferguson, D.C. Hanna and A.C. Tropper, 'Continuous-wave oscillation of a monomode neodymium-doped fibre laser at 0.9μm on the $^4F_{3/2} \rightarrow {}^4I_{9/2}$ transition', *Opt. Comm.*, 58, 405 (1986)

[2.17] I.P. Alcock, A.C. Tropper, A.I. Ferguson and D.C. Hanna, 'Q-switching, mode-locking and tunable operation around 0.9μm of a neodymium-doped monomode fibre laser', *IEE Proc. J*, 134, 183 (1987)

[2.18] L. Reekie, I.M. Jauncey, S.B. Poole and D.N. Payne, 'Diode-laser-pumped Nd^{3+}-doped fibre laser operating at 938nm', *Electron. Lett.*, 23, 884 (1987)

[2.19] H. Po, F. Hakimi, R.J. Mansfield, B.C. McCollum, R.P. Tumminelli and E. Snitzer, 'Neodymium fiber laser at 0.905, 1.06 and 1.4μm', in *Proc. OSA Meeting*, Seattle, WA, USA (1986)

[2.20] R.J. Mears, L. Reekie, S.B. Poole and D.N. Payne, 'Low threshold tunable CW and Q-switched fibre laser operating at 1.55μm', *Electron. Lett.*, 22, 159 (1986)

[2.21] M. Yamada, M. Shimizu, T. Takeshita, M. Okayasu, M. Horiguchi, S. Uehara and E. Sugita, 'Er^{3+}-doped fiber amplifier pumped by 0.98μm laser diodes', *IEEE Photon. Technol. Lett.*, 1, 422-424 (1989)

[2.22] R.J. Mears, L. Reekie, S.B. Poole and D.N. Payne, 'Low threshold tunable CW and Q-switched fibre laser operating at 1.55μm', *Electron. Lett.*, 22, 159 (1986)

[2.23] P.L. Scrivener, E.J. tarbox and P.D. Maton, 'Narrow linewidth tunable operation of Er^{3+}-doped single-mode fibre laser', *Electron. Lett.*, 25, 549 (1989)

[2.24] C.G. Atkins, J.F. Massicott, J.R. Armitage, R. Wyatt, B.J. Ainslie and S.P. Craig-Ryan, 'High-gain, broad spectral bandwidth erbium-doped fibre amplifier pumped near 1.5μm', *Electron. Lett.*, 25, 910 (1989)

[2.25] T.J. Whitley, 'Laser diode pumped operation of Er^{3+}-doped fibre amplifier', *Electron. Lett.*, 24, 1537 (1988)

[2.26] M.S O'Sullivan, J. Chrostowski, E. Desurvire and J.R. Simpson, 'High-power narrow-linewidth Er^{3+}-doped fiber laser', *Opt. Lett.*, 14. 438 (1989)

[2.27] W.L. Barnes, P.R. Morkel, L. Reekie and D.N. Payne, 'High-quantum-efficiency Er^{3+} fiber lasers pumped at 980nm', *Opt. Lett.*, 14, 1002 (1989)

[2.28] R. Wyatt, B.J. Ainslie and S.P. Craig, 'Efficient operation of an array pumped Er^{3+}-doped silica fibre laser at 1.5μm', *Electron. Lett.*, 24, 1362 (1988)

[2.29] C.A. Millar, I.D. Miller, B.J. Ainslie, S.P. Craig and J.R. Armitage, 'Low-threshold CW operation of an erbium-doped fibre laser pumped at 807nm wavelength', *Electron. Lett.*, 23, 865 (1987)

[2.30] Y. Kimura and M. Nakazawa, 'Lasing characteristics of Er^{3+}-doped silica fibres from 1553 up to 1603nm', *J. Appl. Phys.*, 64, 516 (1988)

[2.31] L. Reekie, I.M. Jauncey, S.B. Poole and D.N. Payne, 'Diode-laser-pumped operation of an Er^{3+}-doped single-mode fibre laser', *Electron. Lett.*, 23. 1076 (1987)

[2.32] R. Wyatt, 'High power broadly tunable erbium-doped silica fibre laser', *Electron. Lett.*, 25, 1498 (1989)

[2.33] L. Reekie, R.J. Mears, S.B. Poole and D.N. Payne, 'A Pr^{3+}-doped single-mode fibre laser', *IEE Symposium*, May 1986

[2.34] R.M. Percival, M.W. Phillips, D.C. Hanna and A.C. Tropper, 'Characterization of spontaneous and stimulated emission from praseodymium (Pr^{3+}) ions doped into a silica-based monomode optical fibre', *IEEE J. Quantum Electron.*, 25, 2119 (1989)

[2.35] M.C. Farries, P.R. Morkel and J.E. Townsend, 'Samarium^{3+}-doped glass laser operating at 651nm', *Electron. Lett.*, 24, 709 (1988)

[2.36] D.C Hanna, R.M. Percival, R.G. Smart, J.E. Townsend and A.C. Tropper. 'Continuous-wave oscillation of holmium-doped silica fibre laser', *Electron. Lett.*, 25, 593 (1989)

[2.37] D.C. Hanna, I.M. Jauncey, R.M. Percival, I.R. Perry, R.G. Smart, P.J. Suni. J.E. Townsend and A.C. Tropper, 'Continuous-wave oscillation of a monomode thulium-doped fibre laser', *Electron. Lett.*, 24, 1222 (1988)

[2.38] D.C. Hanna, R.M. Percival, I.R. Perry, R.G. Smart, P.J. Suni and A.C. Tropper, 'Continuous-wave oscillation of a monomode thulium-doped silica fiber laser', in *Tunable Solid State Lasers*, M.L. Shand and H.P. Jenssen, eds., OSA Proc. Series, 5, 350 (1989)

[2.39] D.C. Hanna, R.M. Percival, R.G. Smart and A.C. Tropper, 'Efficient and tunable operation of a Tm-doped fibre laser', *Opt. Comm.*, 75, 283 (1990)

[2.40] D.C. Hanna, R.M. Percival, I.R. Perry, R.G. Smart, P.J. Suni, J.E. Townsend and A.C. Tropper, 'Continuous-wave oscillation of a monomode ytterbium-doped fibre laser', *Electron. Lett.*, 24, 1111-1113 (1988)

[2.41] D.C. Hanna, R.M. Percival, I.R. Perry, R.G. Smart, P.J. Suni and A.C. Tropper, 'Continuous-wave tunable and superfluorescent operation of a monomode ytterbium-doped fiber laser', in *Tunable Solid State Lasers*, M.L. Shand and H.P. Jenssen, eds., OSA Proc. Series, 5, 340 (1989)

[2.42] D.C. Hanna, R.M. Percival, I.R. Perry, R.G. Smart, P.J. Suni and A.C. Tropper, 'An ytterbium-doped monomode fibre laser: broadly tunable operation from 1.010μm to 1.162μm and three-level operation at 974nm', *J. Modern Opt.*, 37, 517-525 (1990)

[2.43] D.C. Hanna, I.R. Perry, R.G. Smart, P.J. Suni. J.E. Townsend and A.C. Tropper, 'Efficient superfluorescent emission at 974nm and 1040nm from an Yb-doped fiber', *Opt. Comm.*, 72, 230-234 (1989)

[2.44] C.A. Millar, I.D. Miller, D.B. Mortimore, B.J. Ainslie and P. Urquhart, 'Fibre laser with adjustable fibre reflector for wavelength tuning and variable output coupling', *IEE Proc. J*, 135, 303 (1988)

[2.45] I. Bennion, D.C. Reid, C.J. Rowe and W.J. Stewart, 'High-reflectivity monomode fibre grating filters', *Electron. Lett.*, 22, 341 (1986)

[2.46] D.C. Hanna, R.G. Smart, P.J. Suni, A.I. Ferguson and M.W. Phillips, 'Measurements of fibre laser losses via relaxation oscillations', *Opt. Comm.*, 68, 128 (1988)

[2.47] S.R. Nagel, MacChesney and K.L. Walker, 'An overview of the modified chemical vapour deposition (MCVD) process and performance', *IEEE J. Quantum Electron.*, QE-18, 459 (1982)

[2.48] J.E. Townsend, S.B. Poole and D.N. Payne, 'Solution-doping technique for fabrication of rare-earth-doped optical fibres', *Electron. Lett*, 23, 329 (1987)

[2.49] D. Gloge, 'Weakly guiding fibres', *Appl. Opt.*, 10, 2252 (1971)

[2.50] A. Yariv, 'Optical Electronics', 3rd Edn, Holt-Saunders (1985)

[2.51] M.J.F. Digonnet and C.J. Gaeta, 'Theoretical analysis of optical fiber laser amplifiers and oscillators', *Appl. Opt.*, 24, 333 (1985)

[2.52] J.R. Armitage, 'Three-level fiber laser amplifier: a theoretical model', *Appl. Opt.*, 27, 4831-4836 (1988)

[2.53] K. Kubodera and K. Otsuka, 'Single-transverse-mode $LiNdP_4O_{12}$ slab waveguide laser', *J. Appl. Phys.*, 50, 653 (1979)

[2.54] W.A. Clarkson and D.C. Hanna, 'Effects of transverse-mode profile on slope efficiency and relaxation oscillations in a longitudinally-pumped laser', *J. Modern Opt.*, 36, 483 (1989)

[2.55] A.W. Snyder and J.D. Love, 'Optical Waveguide Theory', Chapman and Hall (1983)

CHAPTER 3

RARE-EARTHS IN GLASS

3.1 Introduction

This chapter considers some of the factors influencing the electronic energy levels of rare-earth dopant ions in a glass host. Detailed theoretical descriptions of optical transitions and the spectroscopy of ions in solids may be found elsewhere [3.1, 3.2, 3.3] and only a very basic outline will be given here. A description of the electronic configuration of the rare-earth is followed by a brief explanation of the theory developed by Judd and Ofelt to predict the line strengths of electric and magnetic dipole transitions, and subsequently the radiative lifetime of a given energy level from measurements on the absorption spectrum of a rare-earth-doped medium.

3.2 The Rare-Earths

The trivalent lanthanide, or rare-earth, elements are probably the most widely used and studied activators in both glasses and crystals. The 15 elements, ranging from lanthanum with atomic number 57 through to lutetium with atomic number 71, have a wide range of fluorescing levels amongst them and can be readily excited with widely available pump sources from the infrared to the ultraviolet region. Optical transitions occur between $4f$ electron states, and the three outer configurations of all rare-earth atoms, *i.e.*, $5s$, $5p$ and $6s$, are filled. However, rare-earth ions are usually incorporated into glass hosts in a triply ionised (trivalent) state, whereby two $6s$ electrons and one $4f$ electron are removed. The remaining $5s$ and $5p$ shells remain filled and consequently partially shield the 4*f* electrons from external fields which would otherwise strongly influence the position of the energy levels and the excited state decay rates. This shielding allows the local fields to be treated as small perturbations to the free-ion energy levels, and the radiative decay rates can be calculated using the theory due to Judd and Ofelt, as described below.

Rare-earth ions are incorporated into a glass host as either network modifier cations or as substitutes for network former cations, depending on the ion size and valence state. Since glass is a disordered, amorphous network, the random distribution of ions around an individual ion site causes a site to site variation in the environment of each ion. This difference in bonding to nearest neighbour ions and the consequent variation in local fields produces a site to site variation in the energy levels and the radiative and nonradiative transition probabilities. Following broadband excitation, emission from excited levels thus comprises contributions from individual ions in a range of local environments, and the spectrum is inhomogeneously broadened with widths of typically a few cm^{-1} to a few tens of cm^{-1}. This inhomogeneity is also manifested in a spread of emission lifetimes, such that the decay is not single exponential in character. However, with laser excitation only a subset of ions with absorption energies resonant with the pump photon energy (to within the homogeneous linewidth) will be excited, and the subsequent decays are more singly exponential, with a lifetime characteristic of the particular subset of excited ions. For example, the decay lifetime of Yb^{3+} in a silicate host has been observed to vary from 1.1ms to 2.6ms depending on the excitation energy [3.6], although it should be noted that no such variation of lifetimes in an Yb^{3+}-doped silica fibre was detected (see Chapter 4). An additional source of broadening (homogeneous) is due to the coupling of electronic states to phonon states of the host. Since the mean phonon energy and distribution of phonon states are temperature dependent, a corresponding distribution in the photon energy follows from energy conservation.

The broad spectral width is an attractive feature of rare-earth ions in glass, since it allows pumping of a particular transition over a considerable wavelength range, and efficient excitation at wavelengths significantly detuned from the peaks in the absorption spectrum is a common feature of rare-earth-doped laser systems.

3.3 Transition Probabilities of Rare-Earth Ions

The shielding afforded by the outer 5*s* and 5*p* electrons of the rare-earth ions renders the potential at the ion site due to its environment a weak effect, and as such this potential may be considered as a perturbation to the free-ion energy. The free-ion Hamiltonian, to which this perturbation is applied, may be written as

$$\mathcal{H}_{\mathrm{free\text{-}ion}} = \mathcal{H}_{0} + \mathcal{H}_{\mathrm{C}} + \mathcal{H}_{\mathrm{SO}} \tag{3.1}$$

where the subscripts 0, C and SO represent the Hamiltonian due to the interaction of each optically active electron with the ion core, the Coulomb interaction of electrons with each other, and the spin-orbit interaction, respectively. $\mathcal{H}_0$ gives rise to the $4f^N$ atomic electron orbitals forming the electron configuration. This configuration state is split by $\mathcal{H}_C$ into *LS* terms, *i.e.*, a number of states of different energy characterised by values of total orbital angular momentum *L* and total spin angular momentum *S*. The effect of $\mathcal{H}_{SO}$ is to further split each *LS* term into a number of *J* multiplets, *i.e.*, states characterised by the total angular momentum *J*, and $(2J + 1)$-fold degenerate. These degenerate levels are then characterised by M_J values. In the Russell-Saunders approximation, mixing of different *LS* terms is neglected, but in fact the different *LS* terms are not sufficiently separated for this approximation to be valid, and the spin-orbit interaction mixes states of the same *J* and M_J from different *LS* terms in the so-called intermediate-coupling approximation. The free-ion energies are perturbed by the local field at the ion site and the degeneracy of the *J* multiplets is removed, giving Stark splittings of $\approx 100\mathrm{cm}^{-1}$. Differences in the local field environment of the host (coordination number, ligand distance and degree of covalent bonding) impose a site to site variation of the Stark splitting and consequently optical transitions are inhomogeneously broadened, with spectral widths up to several tens of cm^{-1}.

Since the free-ion levels are formed from the $4f^N$ configuration and thus have the same parity, electric dipole transitions are strictly forbidden. Only magnetic dipole and electric quadrupole transitions are allowed, subject to the relevant selection rules.

However, optical transitions in rare-earth ions are predominantly forced electric dipole processes and for this to be possible states of opposite parity must be mixed into the wavefunctions associated with at least one of the two levels involved. This mixing may be brought about by a local field of the host which lacks inversion symmetry (as in many crystals), although the transitions may still be electric dipole even at sites appearing to possess inversion symmetry, suggesting that distortion of the environment by the rare-earth ion may remove the inversion symmetry. The admixing of J states is due to odd terms in the local field potential, whereby the opposite parity $4f^{N-1}5d$ configuration is mixed into the $4f^N$ configuration so that $4f \rightarrow 4f$ transitions are parity-allowed.

The probability of the electric dipole transitions was derived independently by Judd [3.4] and Ofelt [3.5], who showed that the probability of radiative transitions can be expressed as the sum of a number of phenomenological parameters determined by the best fit of observed oscillator strengths. It is assumed that all the Stark components of the ground multiplet are equally populated, and although this is certainly not true in practice, the theory is known to work well for low symmetry sites such as glass or yttrium aluminium garnet (YAG). The Judd-Ofelt theory is briefly summarised in the following discussion.

The rare-earth ion eigenstates in the intermediate coupling regime, $|f^N\{\gamma SL\}J\rangle$, are written in terms of the Russell-Saunders states, $|f^N\gamma SLJ\rangle$, as

$$|f^N\{\gamma' S' L'\}J\rangle = \sum_{\gamma SL} C(\gamma SL)\ |f^N\gamma SLJ\rangle \tag{3.2}$$

where the C coefficients are the coupling coefficients transforming the Russell-Saunders states to intermediate-coupled states. The symbol γ represents all other quantum numbers specifying the states excluding J, which is a good quantum number in the intermediate-coupling regime, and S and L, which are not. The line strength for electric dipole and magnetic dipole transitions between an upper J multiplet specified by bJ' to a lower multiplet aJ is then given by

$$S_{ed}(aJ,bJ') = e^2 \sum_{t=2,4,6} \Omega_t \left(\langle f^N[\gamma SL]J \| U^{(t)} \| f^N[\gamma' S' L']J' \rangle \right)^2 \tag{3.3}$$

$$S_{md}(aJ,bJ') = \frac{e^2\hbar^2}{4m^2c^2} \left(\langle f^N[\gamma SL]J \| \vec{L} + \vec{S} \| f^N[\gamma' S' L']J' \rangle \right)^2 \tag{3.4}$$

where e and m are the electron charge and mass, respectively, Ω_t are phenomenological intensity parameters, and $U^{(t)}$ are doubly reduced matrix elements of tensor operators of rank t, with t = 2, 4, 6, and are generally host independent. These elements can be calculated, and the sources for tabulated values are given by Riseberg and Weber [3.7]. The dimensionless oscillator strength f of a transition of frequency ν from level J to level J' is given by

$$f(aJ,bJ') = \frac{8\pi^2 m\nu}{3h(2J+1)e^2} \left[\chi_{ed} S_{ed}(aJ,bJ') + \chi_{md} S_{md}(aJ,bJ') \right] \tag{3.5}$$

where χ_{ed} and χ_{md} are the local field correction factors for the electric dipole and magnetic dipole transitions, respectively, where $\chi_{ed} = n(n^2+2)^2/9$ and $\chi_{md} = n^3$, and n is the refractive index of the medium. Electric quadrupole transitions, although allowed, are much smaller in strength than either of the dipole transitions and have therefore been neglected in Eq.3.5. The Ω_t parameters are determined by a least squares fit of measured oscillator strengths of the absorption transitions to the value predicted by Eq.3.5. The measured oscillator strength f_{meas} is found from

$$f_{meas} = \frac{mc}{\pi e^2 N} \int \sigma(\nu)\, d\nu \tag{3.6}$$

where $\sigma(\nu)$ is the absorption cross section at frequency ν and N is the dopant ion concentration. Thus by measuring the integrated absorption for a number of transitions from the ground state, the Judd-Ofelt Ω_t parameters can be found and used to calculate the line strengths S_{ed} and S_{md} from Eqs.3.3 and 3.4. The spontaneous emission probabilities between any two J multiplets can then be calculated using these values.

The Einstein spontaneous emission probability A between levels a and b is given by

$$A(aJ,bJ') = \frac{64\pi^4\nu^3}{3h(2J+1)c^3}\left[\chi_{ed}S_{ed}(aJ,bJ') + \chi_{md}S_{md}(aJ,bJ')\right] \qquad (3.7)$$

If only the electric dipole contribution is considered, then Eqs.3.5, 3.6 and 3.7 may be used to give the Fuchtbauer-Ladenburg relation between the emission probability and the integrated absorption spectrum between lower level J and upper level J' as follows

$$\int\sigma(\nu)\,d\nu = \frac{c^2}{8\pi n^2\nu^2}\,\frac{2J'+1}{2J+1}\,A(aJ,bJ') \qquad (3.8)$$

Thus measurement of the integrated absorption cross-section for a given transition is a convenient and simple way of finding the spontaneous emission probability $A(aJ,bJ')$.

The radiative lifetime τ_R of an excited state i is given by the sum of emission probabilities to all terminal states j by

$$1/\tau_R = \sum_j A_{i,j} \qquad (3.9)$$

where the sum includes both electric and magnetic dipole transitions. However, electronic states of rare-earths in crystals and glasses can also relax via nonradiative routes, and the lifetime of the excited state is therefore reduced from its calculated radiative value. The fluorescence lifetime τ_F (*i.e.*, the observed lifetime) of the upper level in the absence of energy transfer is then given by

$$1/\tau_F = 1/\tau_R + W_{NR} \tag{3.10}$$

where W_{NR} is the probability of nonradiative decay. The rate of nonradiative relaxation depends on the number of phonons required for energy conservation during the transition, and also on the energy gap between the excited state and the next lower level. Dopant ions interact with local vibrations of the host through electron-phonon coupling, and rapid nonradiative transitions occur between levels separated by less than the maximum phonon energy permitted by the coupling. For energy gaps greater than the phonon energy, nonradiative relaxation may occur by multiphonon emission, although the probability is reduced the larger the energy separation, and thus radiative emission is more likely (the probability of radiative emission increases as ΔE^3, where ΔE is the energy gap).

Several methods have been proposed for calculating W_{NR}, such as the Huang-Rhys model [3.8] which calculates the temperature dependence of nonradiative emission using a single-configuration-coordinate model incorporating nonradiative transitions at a single phonon energy. Riseberg and Moos [3.9] developed a phenomenological model from time-dependent perturbation theory, again assuming single frequency phonons in the nonradiative transition, and derived the following expression for the nonradiative probability at temperature T :

$$W_{NR}(T) = W_{NR}(0) \left[\frac{exp(\hbar\omega/kT)}{exp(\hbar\omega/kT) - 1}\right]^p \tag{3.11}$$

where $\hbar\omega$ is the phonon energy, $W_{NR}(0)$ is the low temperature multiphonon emission rate and $p = \Delta E/\hbar\omega$ is the number of phonons emitted, where ΔE is the energy gap of the transition, and the temperature independent term is expressed by Reisfeld *et al.* [3.10] as $W_{NR}(0) = B\ exp(-\xi\Delta E)$, where B and ξ are host-dependent constants.

The research described in this thesis was performed using silica based fibres exclusively. However, the nature of the host glass has significant effects on the position, line strength, linewidth and lifetime of the rare-earth dopants. The recently developed fluorozirconate fibres, consisting of ZrF_4-BaF_4-LaF_3-AlF_3-NaF-PbF_2 and referred to as ZBLANP, have lower phonon energies than their silica counterparts (about $600cm^{-1}$ compared to $1000cm^{-1}$ in silica). Thus more phonons are required for energy conservation in a particular transition than would be needed in silica, and hence the nonradiative decay rate is lower, resulting in generally longer fluorescence lifetimes. For instance, the fluorescence lifetime of the $^3H_4$ level in Tm^{3+} is 6ms in fluorozirconate fibre [3.11], whereas in silica it does not exceed 500μs (see Chapter 7). Laser action in fluorozirconate fibres was first demonstrated by Brierley *et al.*[3.12] and there have been many subesequent reports in this field (see Reference 3.13 for a review). Fluorozirconate fibres are particularly attractive for operation in the 2-3μm region where silica begins to absorb strongly whereas fluorozirconates remain highly transparent, providing a complimentary technology to existing silica based fibre lasers.

References

[3.1] M.J. Weber, 'Laser excited fluorescence spectroscopy in glass', in Laser Spectroscopy of Solids, 2nd Edn., W.M. Yen and P.M. Selzer, eds., Springer-Verlag (1986)

[3.2] G.F. Imbusch and R. Kopelman, 'Optical spectroscopy of electronic centers in solids', in Laser Spectroscopy of Solids, 2nd Edn., W.M. Yen and P.M. Selzer, eds., Springer-Verlag (1986)

[3.3] B.G. Wybourne, *Spectroscopic Properties of Rare Earths*, Wiley-Interscience (1965)

[3.4] B.R. Judd, 'Optical absorption intensities of rare-earth ions', *Phys. Rev.*, 127, 750 (1962)

[3.5] G.S. Ofelt, 'Intensities of crystal spectra of rare-earth ions', *J. Chem. Phys.*, 37, 511 (1962)

[3.6] M.J. Weber, J.A. Paisner, S.S. Sussman, W.M. Yen, L.A. Riseberg, C. Brecher, 'Spectroscopic studies of rare-earth ions in glass using fluorescence line narrowing techniques', *J. Luminescence*, 12/13, 729 (1976)

[3.7] L.A. Riseberg and M.J. Weber, 'Relaxation phenomena in rare-earth luminescence', *Prog. Opt.*, 14, 91 (1976)

[3.8] K. Huang and A. Rhys, 'Theory of light absorption and non-radiative transitions in F-centres', *Proc. R. Soc. London*, Ser. A, 204, 406 (1950)

[3.9] L.A. Riseberg and H.W. Moos, 'Multiphonon orbit-lattice relaxation of excited states of rare-earth ions in crystals', *Phys. Rev.* 174, 429 (1968)

[3.10] R. Reisfeld, L. Boehm and N. Spector, 'Multiphonon relaxation rates and fluorescence lifetimes for Tm^{3+} in four oxide glasses', *Chem. Phys. Lett.*, 49, 251 (1977)

[3.11] J.Y. Allain, M. Monerie and H. Poignant, 'Blue upconversion fluorozirconate fibre laser', *Electron. Lett.*, 26, 166 (1990)

[3.12] M.C. Brierley and P.W. France, 'Neodymium-doped fluorozirconate fibre laser', *Electron. Lett.*, 23, 815 (1987)

[3.13] R.G. Smart, Ph.D. Thesis, University of Southampton (1990)

CHAPTER 4

YTTERBIUM-DOPED FIBRE

4.1 Introduction

The basic spectroscopic features of ytterbium in a silica host fibre are described in this chapter. Laser action is demonstrated using a variety of resonator configurations, operating on both three- and four-level transitions at 974nm and around 1040nm, respectively. The basic fibre laser configuration is developed to allow tunable emission from 1.010μm to 1.162μm on the four-level transition and Q-switched operation on both transitions. By preventing optical feedback, both transitions may be operated in a superfluorescent mode to give broadband emission in the 1μm region, and investigations into the relevant spectroscopy and superfluorescent device performance are also presented. Some of these features have been modelled, and a reasonable agreement between experiment and theory is obtained.

The first report of laser action from the Yb^{3+} ion came in 1962 [4.1], when Etzel *et al.* used a xenon-filled flashtube to pump an Yb-doped LiMgAlSi glass rod. Oscillation at 1.015μm was observed when the glass was cooled to liquid nitrogen temperature. Three absorption bands were located in the near infrared from 914-976nm, together with two bands in the ultraviolet, although the infrared bands were found to be those primarily responsible for laser action. Laser action has also been observed in systems where Nd^{3+} is used as a co-dopant acting as a sensitiser in Yb^{3+}-doped glass. In this arrangement, nonradiative energy transfer from Nd^{3+} to Yb^{3+} can occur due to the overlap in Nd^{3+} fluorescence and Yb^{3+} absorption, significantly improving the efficiency for flashlamp pumping. This led to room temperature operation at 1.015μm in a CaLiB glass [4.2], and subsequently in a silicate glass [4.3], also at room temperature, but in this case lasing at both 1.015μm and 1.06μm, with the longer emission wavelength being due to contributions from the Nd^{3+} ions as well as the Yb^{3+}. Apart from the incorporation of Yb^{3+} as a sensitiser in, for instance, Er^{3+} laser systems [4.4, 4.5], the early interest in Yb^{3+} as a laser ion evaporated, due in no small part to the development of Nd^{3+}-doped glass lasers which operated with much greater efficiency and higher output power in a similar wavelength region. However, as will be demonstrated below, Yb^{3+}-doped glass is a system with several interesting features, including a broad fluorescence band, a lack of excited state absorption and the possibility of pumping at wavelengths within reach of GaAlAs diode lasers. The doping of Yb^{3+} into silica fibre has brought about a reassessment of its performance as a laser ion and has in addition shown it to be efficient as both a laser and superfluorescent source.

4.2 Spectroscopy

4.2.1 Introduction

The ground configuration of Yb^{3+} is $4f^{13}$, giving rise to the two manifolds $^2F_{7/2}$ and $^2F_{5/2}$ with the J = 5/2 level lying about 10000-10500cm^{-1} above the J = 7/2 ground state manifold. Both of these J manifolds are split through interaction with the local fields to give, in principle, four Stark levels in the ground state manifold and three in the excited state manifold. There are no other excited levels for this configuration: the ultraviolet absorption bands observed by Etzel *et al.* [4.11] correspond to f-d transitions and are not relevant for the excitation energies used in the present work. Extensive investigations into the spectroscopy of Yb^{3+} exist in the literature, most notably the work of Fournier in collaboration with Robinson [4.6, 4.7] and Bartram [4.8], who studied the spectroscopy and co-ordination of Yb^{3+} in several multicomponent glasses including silicates. At low temperature (20K) the Stark levels of both manifolds were clearly resolved, with each J-level exhibiting the maximum number of Kramers doublets.

4.2.2 Absorption Measurements

The Yb^{3+}-doped fibre used in the work described in this chapter was fabricated by the solution-doping technique [4.9]. Two samples were obtained, one containing a dopant concentration of 580ppm (nominal) and another containing 2500ppm (nominal). The host glass composition was GeO_2- SiO_2 in the core, with the index raised by 0.0095 above that of the SiO_2 cladding to give a numerical aperture of 0.17 for both fibres. The cladding diameter was 125μm, and the LP_{11} mode cut off wavelength had been determined as 805nm implying, under the weak guidance approximation and assuming a step refractive index profile, a core diameter of 3.6μm.

Fig.4.1 shows the absorption spectrum supplied with the low doped (580ppm) fibre, taken with a white light source and recorded using a 30cm length of fibre with data points taken at 5nm intervals. The spectrum has not been normalised for the wavelength response of the silicon photo-diode used to make the measurements. Only two absorption peaks, located at 910nm and 974nm, are resolved for this GeO_2 - SiO_2 host at room temperature, although there is a suggestion of a third unresolved absorption in the 965-970nm region. It is interesting to compare the position of these peaks to those observed by Fournier and Robinson in silicate glass [4.7], where the principal absorption peaks were at 910.0nm, 960.0nm and 972.3nm. It was noted by these authors that the peak positions were similar in silicate, phosphate and germanate glasses, suggesting that Yb^{3+} is incorporated in similar sites in these glasses, and the similarities in the absorption spectrum for the silica fibre appear to support this argument.

If equal population of the Stark components in each multiplet is assumed, then the absorption spectrum may be used to calculate the radiative lifetime for the ${}^2F_{5/2}$ - ${}^2F_{7/2}$ transition by applying the Fuchtbauer-Ladenburg relation [4.10, see also Eq.3.8] given by

$$\int \alpha(\lambda)\ d\lambda = \frac{N(\bar{\lambda})^4(2J' + 1)}{8\pi c n^2(2J + 1)} A \tag{4.1}$$

where J is the total angular momentum of the initial level, J' the total angular momentum of the final level, N the dopant ion

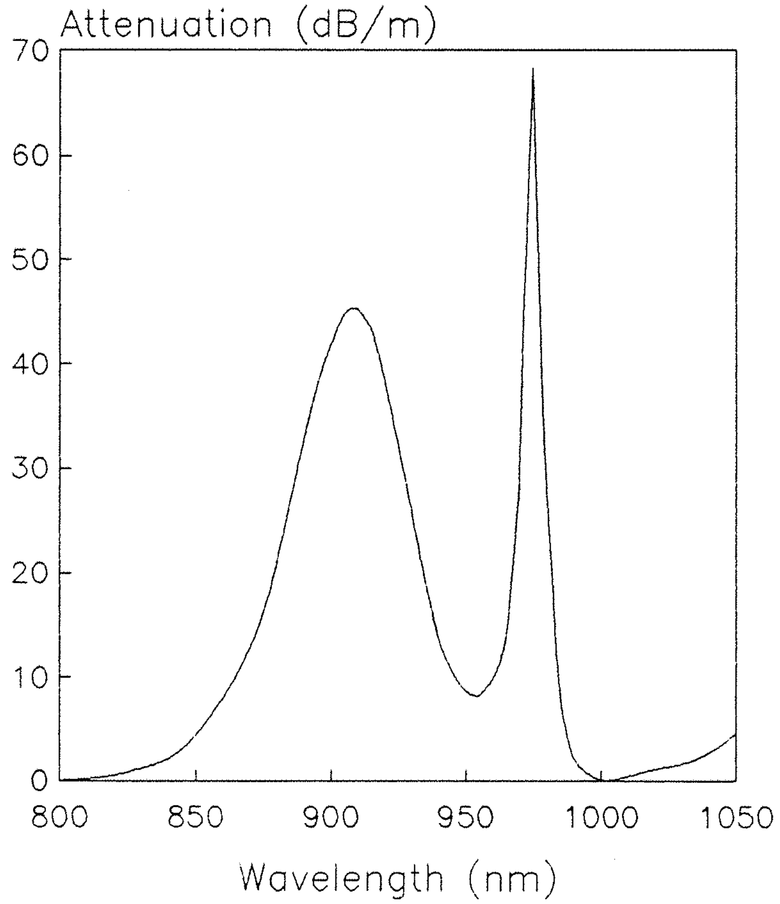

Fig.4.1 Absorption spectrum for fibre containing 580ppm Yb^{3+}

concentration, n the bulk refractive index of the host medium, $\bar{\lambda}$ the mean wavelength of the absorption band and A the spontaneous emission probability. For Yb^{3+}, $J = 7/2$, $J' = 5/2$, $N \approx 1.3 \times 10^{19}$ ions/cm^3, $n = 1.4585$ and $\bar{\lambda} = 910$nm. The integrated absorption coefficient $\int \alpha(\lambda)\ d\lambda$, found by measuring the area under the curve in Fig.4.1 between 800nm and 1000nm, is 7.526×10^{-7}. These values yield $A = 1805s^{-1}$, the inverse of the radiative lifetime, *i.e.*, $\tau_{rad} = A^{-1} = 554\mu s$. The considerable uncertainty in the value of the dopant ion concentration does however render this an approximate value only.

For the remainder of the investigations into the Yb^{3+}-doped fibre, the pump source was a tunable Styryl 9M dye laser, chosen because its range of emission wavelengths in the 0.8μm region (where Yb^{3+} has a significant absorption) coincide with the operating wavelengths of commercially available GaAlAs diode lasers, which would be the ideal pump source in a practical application due to their small size, reliability and low cost.

The value of the absorption coefficient for wavelengths in the 0.8μm region could be measured independently of the white light absorption data supplied with the fibre by a cut back technique to monitor the amount of transmitted (unabsorbed) pump power as the length was progressively decreased. Cut backs were performed on the 580ppm fibre for pump wavelengths of 820nm, 840nm, 850nm, 880nm, 900nm and 910nm. For the shorter wavelengths (820nm, 840nm and 850nm) where the absorption was known to be relatively weak, a thermopile power meter was used to measure the unabsorbed pump power at the fibre output. An incident pump power of 50mW was used at 820 and 840nm, and 10mW at 850nm. For the longer wavelengths where the absorption is higher, a lower pump power had to be used to avoid saturation of the pump transition. A value of 1mW was chosen, too low to yield pump output powers measurable on the thermopile but measurable instead with a calibrated silicon photo-diode.

If the natural log of the output pump power $P(l)$ is plotted against fibre length l then, according to the Beer law

$$P(l) = P(0)\ exp\ (-\alpha l) \tag{4.2}$$

where $P(0)$ is the launched pump power, the effective absorption coefficient α is given by the gradient. The results obtained in this way for Styryl 9M pumping are summarised in Table 4.1, where the attenuation in dB/m is also given. In a similar cut back at a pump wavelength of 840nm, the more heavily doped fibre was found to have an absorption coefficient approximately 4.6 times that of the low doped fibre, *i.e.*, $1.52\mathrm{m}^{-1}$, in reasonable agreement with the ratio of nominal dopant concentrations for the two fibres.

λ (nm)	α (m^{-1})	(dB/m)
820	0.17	0.74
840	0.33	1.43
850	0.83	3.60
880	4.69	20.37
900	9.57	41.56
910	10.55	45.82

Table 4.1

In addition to the standard cut back technique for the 2500ppm fibre, a second method was tried. This involved winding a length of fibre around a plastic cylinder cut with a spiral groove, such that the fibre loops were regularly spaced along the length of the cylinder. The plastic coating on the fibre was stripped away to allow scattered (unguided) pump light to escape unhindered in a radial direction. A silicon photo-diode was then traversed along the fibre loops on a line parallel to the cylinder axis using a stepping motor drive, with the signal recorded on an X-T chart recorder. The photo-diode had a narrow slit aperture to prevent contributions to the signal from adjacent loops of fibre. The output consisted of a series of regularly spaced peaks in side light emission, corresponding to the points at which the photo-diode passed over the loops, with the intensity varying in an exponential manner with length in accordance with Eq.4.2 as with the normal cut back method. For a pump wavelength of 840nm, the absorption coefficient was $0.37\mathrm{m}^{-1}$, consistent with the value of $0.33\mathrm{m}^{-1}$ obtained in the conventional manner. The advantage of the "travelling detector" method is that, in principle, it is nondestructive. In practice, however, it is all too easy to break the fibre when stripping off long lengths of plastic coating. An alternative method, that of stripping off only small regions of the fibre *in situ* at the points over which the photo-diode passed, was equally prone to mishap, and it was concluded therefore to continue with the cut back procedure in future. This method has the added advantage of determining the launch efficiency in addition to the absorption coefficient, since Eq.4.2 can be used to find $P(0)$ and hence the overall launch efficiency is found simply by dividing this launched power by the measured pump power incident on the launch optics.

4.2.3 Infrared Emission

The emission spectra of doped fibres may be recorded by monitoring either guided fluorescence emitted from the end of the fibre, or unguided fluorescence escaping in a radial direction. This latter approach is preferable since, due to the small radial dimensions involved, the optical attenuation is typically $< 10^{-5}$ dB [4.11] and so the effects of ground state reabsorption of fluorescence, which would otherwise distort the spectrum, are insignificant. In addition, gain or amplified spontaneous emission, which essentially rely on the long interaction length afforded by optical guidance in a fibre, are also insignificant in side light, and distortion due to these mechanisms should not be a problem. To record spectra in side light requires some means of collecting the radial fluorescence before passing it through a monochromator. There are several ways in which this can be done, such as by fixing part of the fibre between the entrance slits of the monochromator, or by running the fibre through an integrating sphere with the monochromator at its exit port. For the investigations described here however, a commercially available fibre bundle in a slit-to-slit configuration was used. One end was held over a region of fibre (with the protective coating stripped off) near the input end where the fluorescence signal is strongest, while the other end was placed into the entrance of the monochromator. The fibre bundle itself was assumed to have a wavelength dependent loss insignificant compared to its total losses over the range 0.9–1.2μm. The full experimental arrangement for side light fluorescence spectroscopy is shown in Fig.4.2. Pump light was launched into the fibre with an 18X microscope objective and the emission wavelength was scanned with a stepping-motor-driven 0.25m grating monochromator and detected on a germanium photo-diode. The signal was then processed by a phase sensitive detector to improve the signal-to-noise ratio before a final output was obtained on a Y-T chart recorder. The monochromator contained a grating blazed for 1μm, and the slits were set at 1.0mm.

A typical side light fluorescence spectrum is shown in Fig.4.3.

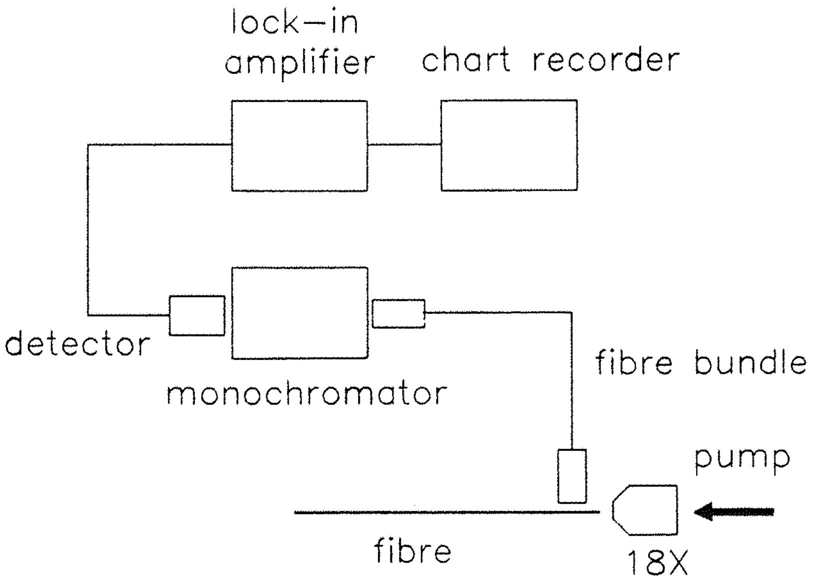

Fig.4.2 Apparatus for observation of side light fluorescence

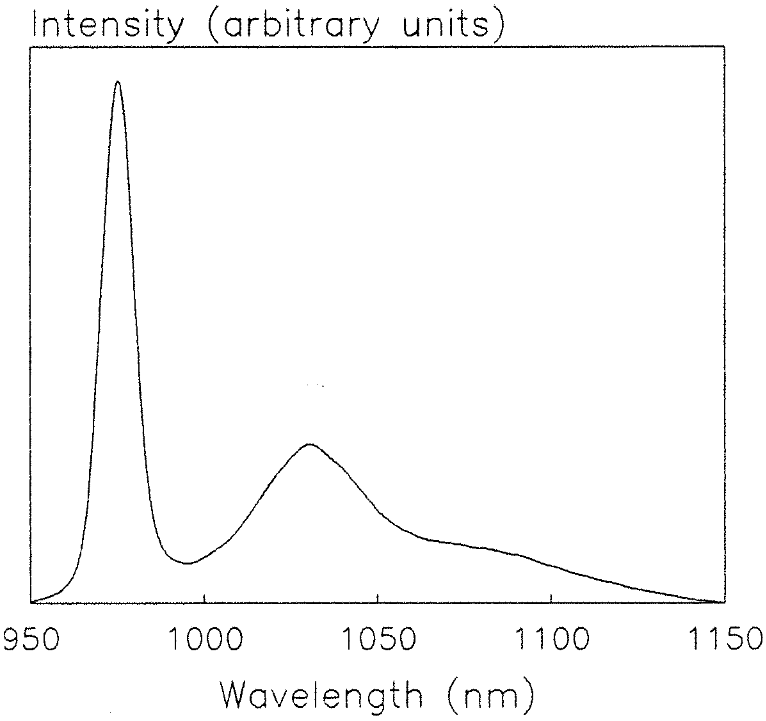

Fig.4.3 Side light fluorescence spectrum for 580ppm fibre pumped at 900nm

For this spectrum the low doped fibre was used. The pump wavelength was 900nm with 45mW incident on the launch objective. Two peaks are clearly resolved at 974nm and 1034nm, and a third feature is just discernible in the long wavelength tail. By fitting Gaussian distributions (*i.e*, inhomogeneous broadening [4.12] is assumed to be the dominant broadening mechanism) to the two resolved peaks and subtracting from the full spectrum locates this third peak at approximately 1082nm (neglecting any wavelength scaling for the fluorescence intensity). The side light spectrum was investigated under a variety of pump conditions, with the low doped fibre pumped at 850nm, 880nm and 900nm to test the response to pumping increasingly closer to the resonance at 910nm. No dependence of spectral characteristics with pump wavelength was observed. For all three pump wavelengths the emission peaks were at 974.0 ± 0.5nm and 1034.0 ± 0.5nm. Incident powers were varied from 5-100mW with no shift in the peak positions. The full width at half maximum of the peak at 974nm is about 10nm and that of the 1034nm peak is 40nm where, in this latter case, the full width is found by doubling the half width measured on the short wavelength side to eliminate the contribution of the fluorescence tail on the long wavelength side.

The heavily doped fibre (2500ppm) was pumped from 790nm to 880nm at 10nm intervals, with similar results to those of the low doped sample. For both fibres, the broad nature of the peak centred at 1034nm indicates the potential for wide tunability of laser emission on this transition. To find the long wavelength limit of this fluorescence, the detection system gain was maximised and a spectrum taken in the extreme regions of the tail. For an incident pump power of 50mW at wavelengths of 840-870nm in 10nm steps, the fluorescence tail extended to a maximum of 1250nm.

The information gathered from the absorption and emission spectra allows the energy level diagram for Yb^{3+} in the particular silica-based host glass used in these experiments to be constructed. The absorption peaks at 910nm, 965-970nm and 974nm indicate upper manifold Stark levels at $10989cm^{-1}$, $10350cm^{-1}$ and $10267cm^{-1}$, respectively. Emission (assumed to take place from the lowest-lying upper manifold Stark level) at 974nm, 1034nm and 1082nm indicates Stark levels in the ground state multiplet at $0cm^{-1}$, $596cm^{-1}$ and $1000cm^{-1}$, respectively. These levels are shown in Fig.4.4, labelled *a* to *g* for later reference. Level *b*, at about $360cm^{-1}$ above ground was

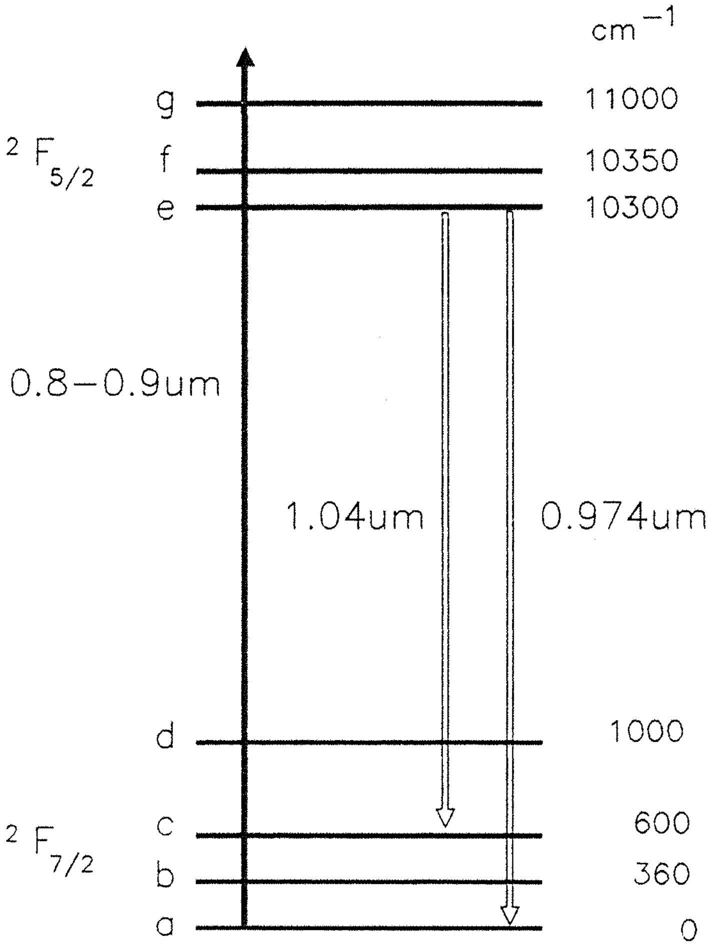

Fig.4.4 Energy levels for Yb^{3+}-doped fibre

located through comparison with the data of Fournier and Robinson [4.7].

The fluorescence lifetime of Yb^{3+} was measured using the arrangement shown in Fig.4.5. A mechanical chopper interrupted the pump beam and the subsequent decay of the fluorescence signal was observed on an oscilloscope. The addition of a digital storage adapter allowed the signal to be averaged over many cycles to improve the signal-to-noise ratio. Single exponential decay is given by

$$I(t) = I(0)\ exp\ (-t/\tau) \tag{4.3}$$

where $I(t)$ is the signal intensity at time t, $I(0)$ is the intensity at time $t = 0$, and τ is the fluorescence lifetime. Taking natural logs of both sides of Eq.4.3 gives a straight line of gradient $-1/\tau$ if the decay is single exponential. The decay was found to be single exponential with a lifetime of 710μs.

In the presence of nonradiative decay from an upper level, the measured lifetime will be less than the lifetime calculated from integrated absorption measurements on the particular transition. The fact that the 710μs lifetime measured for Yb^{3+} is greater than the 554μs calculated lifetime reflects the level of uncertainty in the dopant ion concentration.

The detection system response time was measured by observing the decay of the pump signal after interruption by the chopper and averaging over many cycles as before. This decay is not exponential, so the time for the signal to fall from 90% of its initial (uninterrupted) level to 10% of this is taken as a measure of the system response. For the germanium photo-diode used in the fluorescence lifetime measurements this response time was 55μs.

4.2.4 Visible Emission

In addition to the infra red fluorescence, emission was also observed in the visible part of the spectrum in the form of a weak green glow along the length of the fibre when pumped in the 800-900nm region. The effect was observable with the lower doped fibre but was most apparent for the heavily doped sample, and for this reason the 2500ppm fibre was used for investigation to provide the largest possible fluorescence signal. A pump wavelength of 837nm was chosen since the pump power was roughly maximised at this wavelength. The side light spectrum shown in Fig.4.6 was taken in a similar way to the infrared spectra described above, with the exception that part of the fibre was mounted in and along the entrance slit of the monochromator because the fibre bundle was not available at this time. The monochromator contained a grating blazed at 500nm and the output signal was detected with a photomultiplier tube, which was unresponsive to the infrared emission wavelengths. The visible spectrum is similar in overall shape to the infrared spectrum, in that it has a sharp peak on the short wavelength side with a broader peak at longer wavelengths. The sharp peak is located at 489nm ± 2nm, where the error has been estimated from the uncertainty in the linecentre position derived from several spectra. The full width at half maximum, found by doubling the half width on the short wavelength side, is about 5nm. The peak of the broader emission is at 505nm ± 2nm, with a full width at half maximum of about 20nm, again found from the half width on the short wavelength side. By reconstructing the long wavelength half of this peak (assuming it to be identical to the short wavelength side) and subtracting from the observed spectrum roughly locates a third peak at about 522nm. Note that these features at 489nm and 522nm are located, to within 1%, at positions corresponding to half the wavelength of the infrared emission peaks at 974nm and 1036nm, respectively.

The source of the green emission was originally suspected to be impurities other than Yb^{3+} in the core, but the striking correlation of the fluorescence peaks with those of the infra red emission strongly indicates that Yb^{3+} is the source. In fact, since the photon energy of the green emission is almost exactly twice that of the infra red emission, it strongly suggests that the visible emission arises from a simultaneous radiative relaxation of two excited Yb^{3+} ions emitting a single photon in cooperation. This effect was first observed in $YbPO_4$ by Nakazawa and Shionoya [4.13], who termed it "cooperative luminescence" by analogy with the then already well known process of cooperative absorption.

The peak at 505nm could be the result of the de-excitation of two Yb^{3+} ions whereby one emits to the lowest-lying ground state Stark level (level *a* in Fig.4.4) and the other to a higher Stark level (level *c*), since the 505nm wavelength is mid-way between that given by de-excitation of both ions to either level *a* (489nm) or level *c*

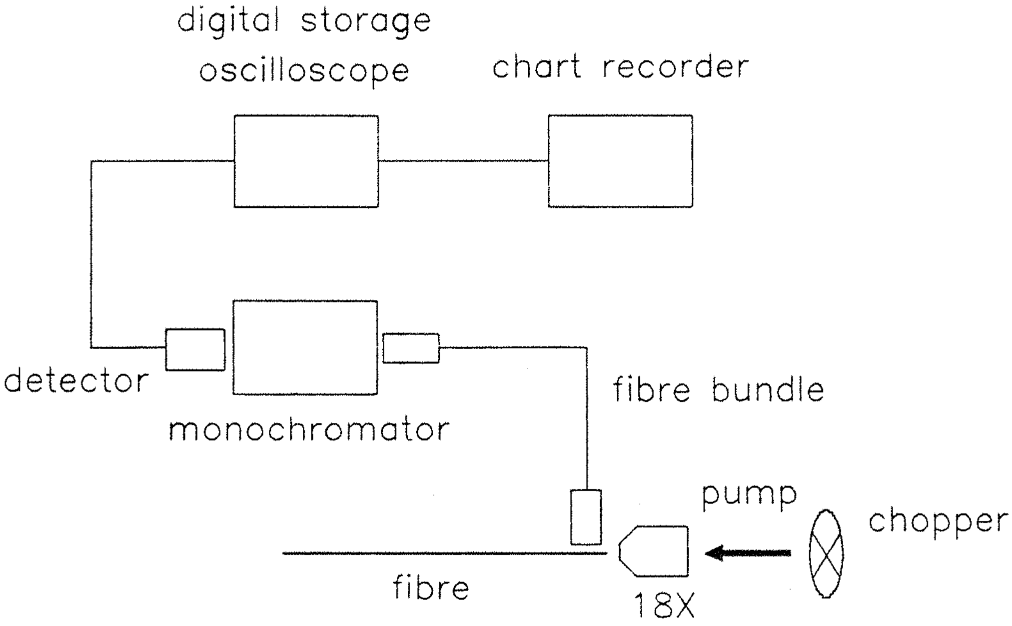

Fig.4.5 Apparatus for lifetime measurements

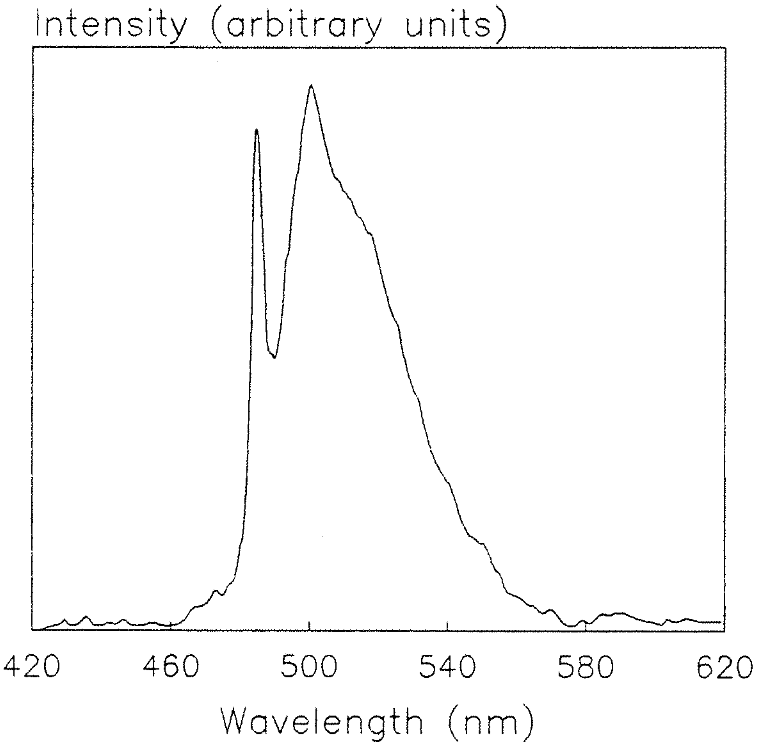

Fig.4.6 Side light fluorescence in the visible region for 837nm pump wavelength

(522nm). It may also arise simply from the de-excitation of both ions in the pair to an intermediate Stark level (level *b*). This latter argument suggests that, since the emission at 489nm and 522nm correlates so well with the infrared emission at 974nm and 1036nm, the peak at 505nm may also have an infra red counterpart at about 1010nm. This would give a ground state Stark level at about 360cm^{-1}, as shown by level *b* in the energy level diagram of Fig.4.4, and correlates with the spectra of Fournier and Robinson [4.7].

If the green emission is indeed due to a two ion process, then its intensity should vary quadratically with the intensity of the pump light, since two photons must be absorbed before an ion pair can relax. The arrangement for side light detection was used to monitor the signal at 489nm while the pump power at 837nm was increased from 40mW to 80mW in increments of 10mW. If the intensity of the green fluorescence, I_g, is due to the absorption of m infra red pump photons then I_g will vary as a function of pump power P according to

$$I_g \propto P^m \tag{4.4}$$

The number of photons m is found by plotting log I_g against log P, where the gradient is equal to m. This is shown in Fig.4.7, where the gradient yields m = 1.94, indicating a two photon process as expected.

The cooperative luminescence process also has implications for the fluorescence lifetime of the green emission. The fluorescence decays of the infra red and visible emission may be written as

$$I_{ir}(t) \propto n_{ir}(t) = n_{ir}(0)\ exp\ (-t/\tau_{ir}) \tag{4.5}$$

$$I_g\ (t) \propto n_g(t) = n_g(0)\ exp\ (-t/\tau_g) \tag{4.6}$$

where I is the fluorescence intensity, n is the number of excited ions (or pair of ions) and τ is the lifetime, and the subscripts *ir* and *g* refer to the infra red and green emission, respectively. At the start of the decay (when the pump is blocked), the ion pair population $n_g(0)$ is proportional to P^2 and $n_{ir}(0)$ is proportional to P (since the infra

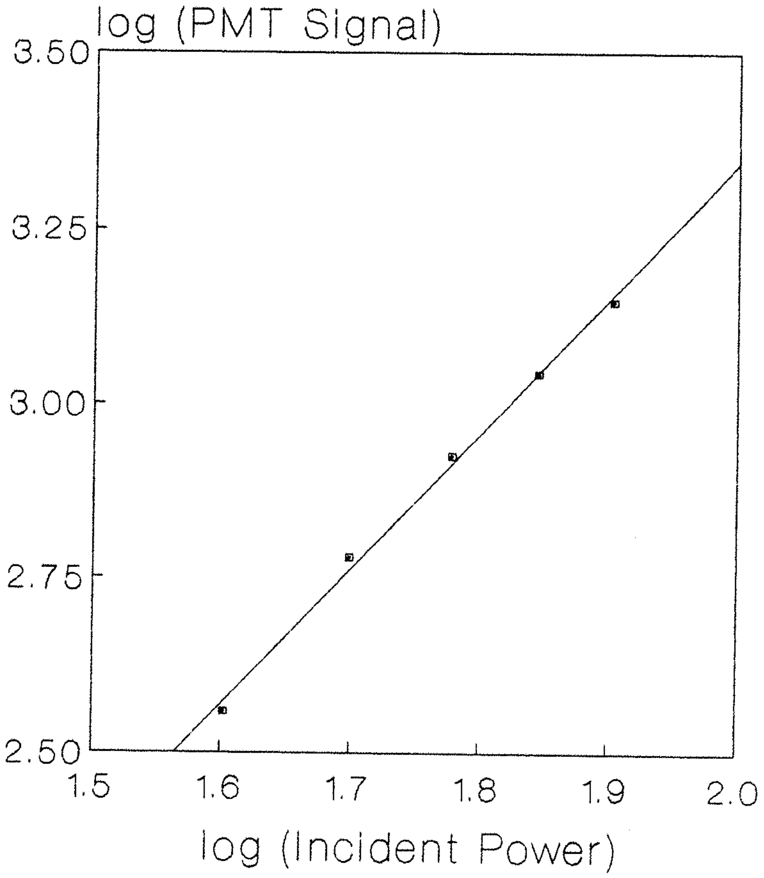

Fig.4.7 Log plot for emission at 489nm versus pump power for 837nm pump wavelength

red emission follows the absorption of a single photon).

Nakazawa and Shionoya [4.13] point out that these proportionalities imply that $\tau_g = \tau_{ir}/2$. The lifetime of the green emission was measured in a similar way to the infrared emission, and was found to be 394μs, where the detection system response was 20μs. This is not quite the expected factor of two reduction on the infra red lifetime of 710μs. However, the ratio of the lifetimes is 0.555 which is close to the ratio of 0.563 observed by Nakazawa and Shionoya [4.13].

An excitation spectrum for this green emission taken in side light is shown in Fig.4.8. The pump wavelength was varied between 800nm and 880nm with a stepping motor drive operating the birefringent tuning mechanism on the dye laser. The excitation spectrum, normalised for the dye laser power spectrum, shows a peak at 847nm. This appears to indicate some degree of site selectivity (where some rare earth ions appear to be located in sites which render them more susceptible to ion pair formation) since the 847nm wavelength is neither the wavelength of highest dye laser power nor a wavelength corresponding to an absorption peak. Further characterisation of this visible emission is required before any definite conclusions are drawn.

4.3 Laser Operation

4.3.1 Determination of the Laser Transition

Operation of the Yb^{3+}-doped fibre as a laser medium is the subject of this section. The laser experiments described below were performed using the low doped (580ppm) fibre in a Fabry-Perot resonator configuration, and energy level notation refers to the diagram in Fig.4.4.

The side light fluorescence spectrum described in Section 4.2.3 indicates that emission occurs on both three-level (*e* to *a*) and four-level (*e* to *b*, *c* and *d*) transitions. The term "four-level" is perhaps not strictly accurate in the conventional sense since the lower laser level is not empty, as in an ideal four-level system, but is a Stark component of the ground state multiplet and therefore has a thermal population determined by the Boltzmann distribution. However, since the pump and fluorescence cycle does involve four distinct levels, the transition is referred to as "four-level". A qualitative assessment of the expected laser transition under specified pump and fibre conditions may be made as follows.

A comparison of the linecentre fluorescence intensities, and hence emission cross sections, at 974nm and 1034nm shows a ratio of about 4:1 in favour of three-level emission at 974nm. However, this transition will suffer a significant reabsorption loss by ground state population in level *a*, and unless this loss is kept small the gain on the three-level transition will be reduced below that of the gain on the four-level transition as light propagates along the fibre. Reabsorption losses are kept small by ensuring that a substantial length of the fibre is inverted with respect to the three-level transition, *i.e.*, at least half of the population is excited to the upper level throughout most of the fibre. Under these conditions, since the three-level gain is higher than that on the four-level transition, laser oscillation will take place around 974nm. For three-level inversion, the pump intensity in the fibre must be equal to or greater than the pump saturation intensity I_{sat}, given by $I_{sat} = h\nu_p/\sigma_a\tau$, where h is Planck's constant, ν_p is the pump frequency, σ_a is the absorption cross section and τ is the upper level lifetime (710μs for Yb^{3+} in a silica host). The pump saturation power P_{sat} is given by $P_{sat} = I_{sat} \times A_{eff}$, where A_{eff} is the effective core area derived from consideration of the mode overlap of the pump and signal fields (see Section 4.6.4), although the actual core area is a good approximation. Thus for a given input pump power level, the saturation requirement imposes a limit on the length of fibre that may be used for three-level operation. The optimum length will be that for which the pump power emerging from the fibre end is just equal to P_{sat}. For a fibre shorter than the optimum length, there is "excess" power emerging from the end which could otherwise be used to pump more fibre, and so the gain is not maximised. In a longer fibre, there will be a region at the end where the pump power has fallen below P_{sat} and, since the three-level transition is no longer inverted here, the consequent reabsorption in this region causes a reduction in the gain. If this loss is large enough, the gain on the four-level transition will now dominate, provided that inversion is maintained with respect to the thermal population of levels *b* and *c*. In a pure four-level system this gain increases with length until all the pump power is absorbed, but since the lower levels of the Yb^{3+} ion are thermally populated, the small reabsorption loss prevents the fibre being made arbitrarily long if maximum power is required. It should be noted that these comments for oscillation wavelength selection with fibre length apply only in a situation where a laser is formed using broad-band reflectors, *i.e.*, neither transition is discriminated against by the reflectivity of the cavity mirrors.

The effect of fibre length on laser wavelength for the four-level transition was demonstrated with a Fabry-Perot cavity where the fibre ends were butted against dielectric mirrors. The input mirror was >99.5% reflective in the range 980-1120nm and the output coupler was 1% transmissive in the range 1040-1160nm. The fibre was pumped with about 50mW launched at 840nm. The variation of lasing wavelength with fibre length is shown in Fig.4.9. For long lengths the reabsorption losses of levels *b* and *c* force oscillation on the *e* to *d* transition at about 1100nm, despite the lower emission cross section when compared to the three-level transition. Reducing the fibre length brings about oscillation on the *e* to *c* transition around 1050nm since the higher emission cross section now outweighs the higher reabsorption loss of level *c* compared to level *d*. The single pass internal losses were also measured for each length using the relaxation oscillation method [4.14]. For the longer lengths (8-10m), the loss was about 10%, whereas for the shorter lengths (2-5m) the loss was higher at about 25%, a result of the increased reabsorption loss as the transition switches from $e \rightarrow d$ to $e \rightarrow c$. The incident threshold power reflects this increased loss, varying from 5mW for a 10m length to 13mW for a length of 3.25m.

The shortest fibre used above in demonstrating the effect of length on oscillation wavelength (1.2m) was too long to permit three-level operation due to insufficient pump power at 840nm for inversion on this transition, *i.e.*, there existed a region of fibre at the end where the pump power was below the saturation level, and the subsequent reabsorption in this region prevented three-level operation. The expression for the absorption cross section $\sigma_a = \alpha/N$, where the dopant concentration $N = 1.3 \times 10^{25}$ ions/m^3, is used in conjunction with the values for α given in Table 4.1 to obtain $\sigma_a(\lambda)$, where λ is the pump wavelength, and the pump saturation power found using $\sigma_a(\lambda)$ is shown in Table 4.2 below.

With a maximum output from the dye laser of about 150mW at 840nm three-level operation is not possible, since not even the power coupled into the fibre at its input end (≈ 75mW) will reach the

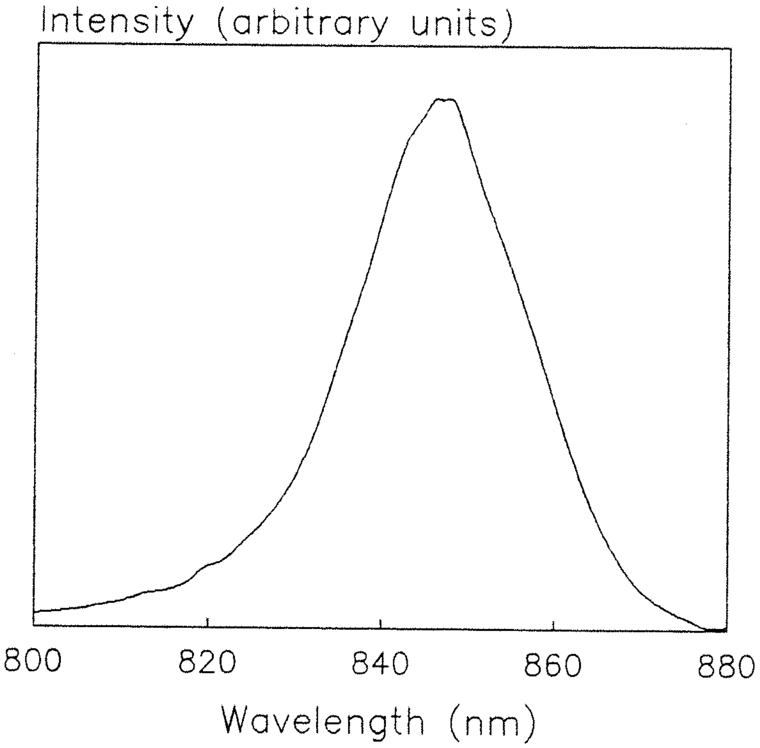

Fig.4.8 Excitation spectrum for emission at 489nm

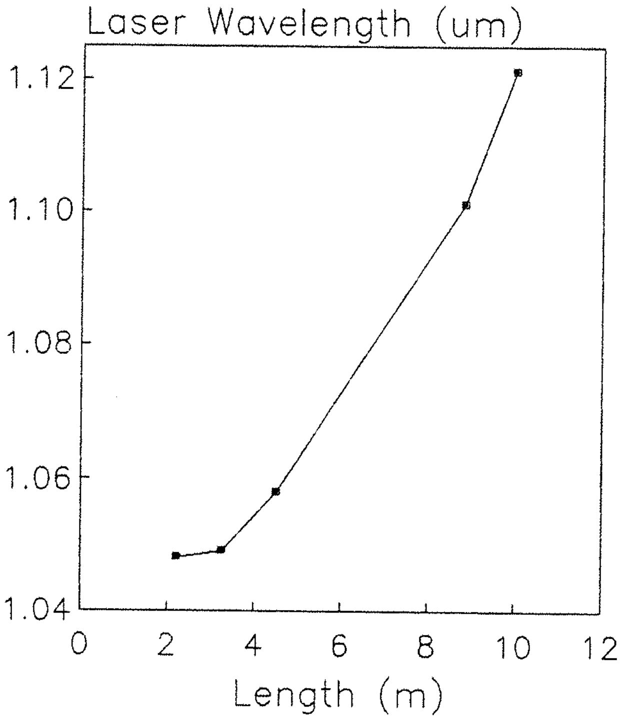

Fig.4.9 Laser wavelength versus fibre length for 840nm pump wavelength

saturation power. However, at 900nm the saturation power of 4mW is easily obtainable from the pump source, with up to 65mW available at this wavelength.

λ (nm)	P_{sat} (mW)
820	262
840	132
850	52
880	9
900	4
910	4

Table 4.2

There are two reasons for not pumping at even longer wavelengths closer to the absorption peak at 910nm. The first is that very little power is available from the dye laser due to the limitations in the Styryl 9M tuning curve, and secondly, as pointed out by Armitage [4.15], for wavelengths longer than about 900nm the emission cross sections are no longer zero, so that at high pumping rates the ratio of the upper level to lower level population tends towards the ratio of the absorption to emission cross sections and complete inversion cannot be achieved.

4.3.2 Laser Oscillation on the Three-Level Transition

To observe laser action on the three-level transition, a resonator was set up with a mirror butted at the input end with reflectivity >99.5% in the range 930-1200nm. A fibre length of 20cm was pumped at 900nm. While setting up the pump launch, laser oscillation was observed from the fibre without a mirror butted at the output end. It was therefore decided to allow the 3.5% Fresnel reflection from the fibre end face to form the output mirror. A suitable filter to separate the pump and signal wavelengths at the fibre output was not available, so output powers were measured by passing the beam through a monochromator after collimation by a microscope objective. The total power before entry to the monochromator was divided in the ratio of the powers at each of the two wavelengths measured at its exit. The slits were opened to about 2-3mm, ensuring that the entire bandwidth of each signal was passed while also maintaining adequate discrimination between the two wavelengths. Under these conditions the laser characteristic shown in Fig.4.10 was obtained, where the output power at 974nm is plotted against the absorbed pump power.

Absorbed pump powers were calculated by subtracting the measured output pump power (corrected for transmission of the microscope objective used to collimate the output) from the launched pump power. This latter figure was determined from the overall launch efficiency, which was itself found using the cut back data, extrapolated to zero fibre length to calculate the power at the input end of the fibre for a known pump power incident on the launch objective. The launch efficiency derived in this way was 0.5. Note that the input mirror used for laser operation was in place during the cut backs, so the launch efficiency value is directly applicable for laser operation.

The laser characteristic of Fig.4.10 has a slope efficiency of 46% with respect to absorbed power. The threshold was 12mW launched (4mW absorbed) and the maximum observed output power was 4.3mW for 17.4mW absorbed (65mW incident on the launch objective). However, pump output powers were greater than the calculated saturation power throughout the range of incident powers used (20-65mW), with about 15mW exiting for 65mW incident. To maximise the available gain of this system, the fibre length was increased to 50cm, a length at which pump output powers were comparable to P_{sat}, such that for 65mW incident the pump output was 5.2mW, falling to 2.7mW at threshold. The laser characteristic for this optimised length is shown in Fig.4.11. The slope efficiency is 63% with respect to absorbed power, with a maximum observed output power of 9.3mW for 27.3mW absorbed (65mW incident). The threshold was 15mW launched (12mW absorbed).

Inversion on the three-level transition was also achievable with a pump wavelength of 850nm (the prohibitively high value of P_{sat} at shorter pump wavelengths prevented oscillation occurring for pumping below 850nm). From Table 4.2, at 850nm the saturation power is about 50mW and, with a maximum dye laser power of 145mW here, it was possible to invert the three-level transition over a short length of fibre. To demonstrate this a 20cm fibre was pumped at 850nm, with an identical mirror to that used previously butted at the input. To reduce the cavity losses, a similar high reflector was butted at the output. With this arrangement the maximum output power at 974nm was only of the order of 1mW for 70mW launched. However, this does at

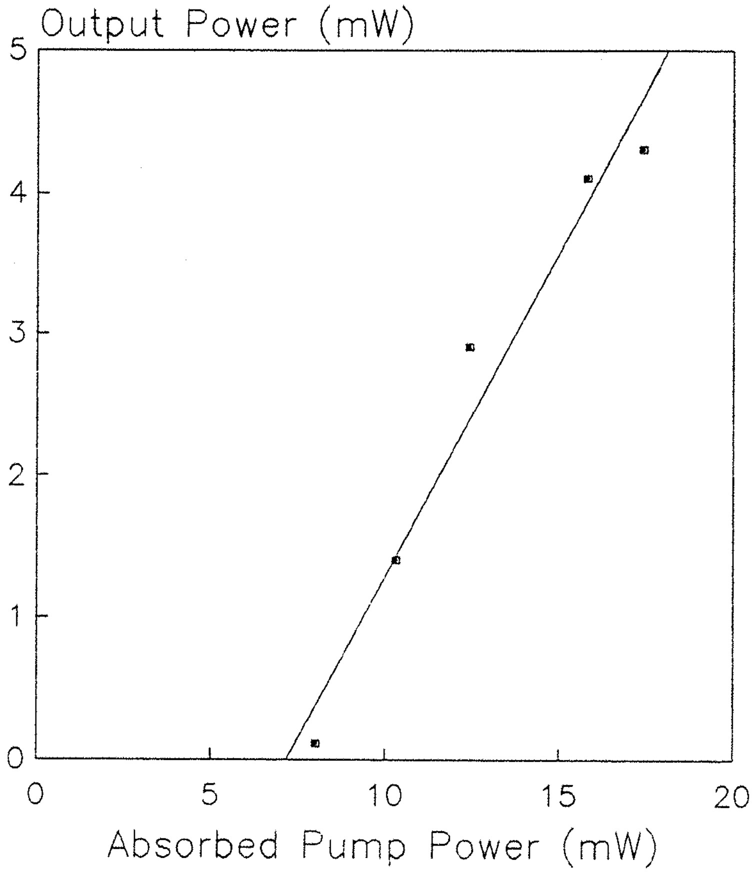

Fig.4.10 Laser characteristic at 974nm for 20cm fibre pumped at 900nm

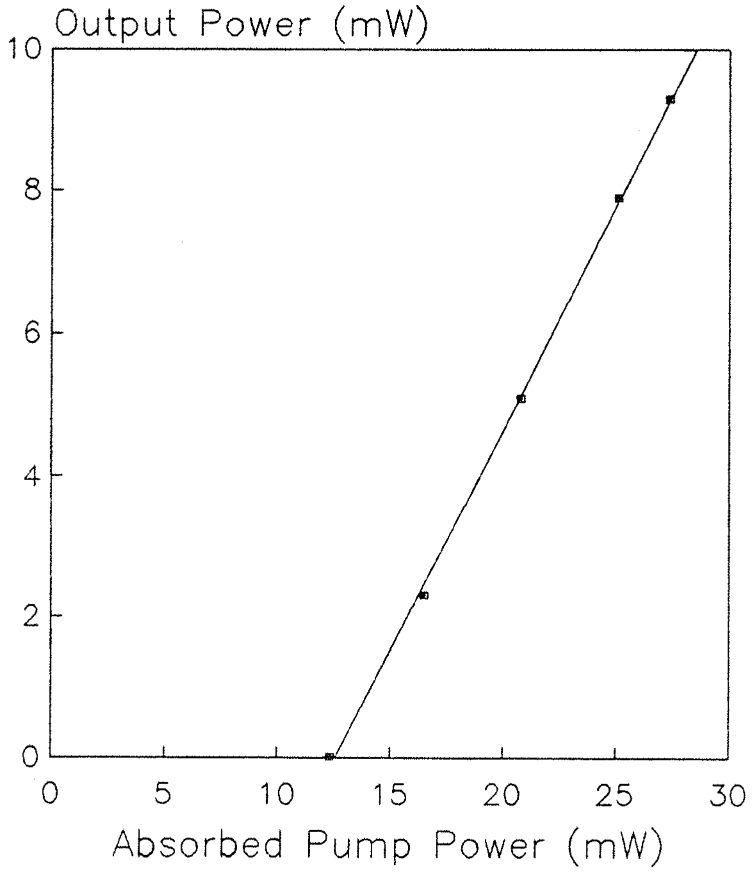

Fig.4.11 Laser characteristic at 974nm for 50cm fibre pumped at 900nm

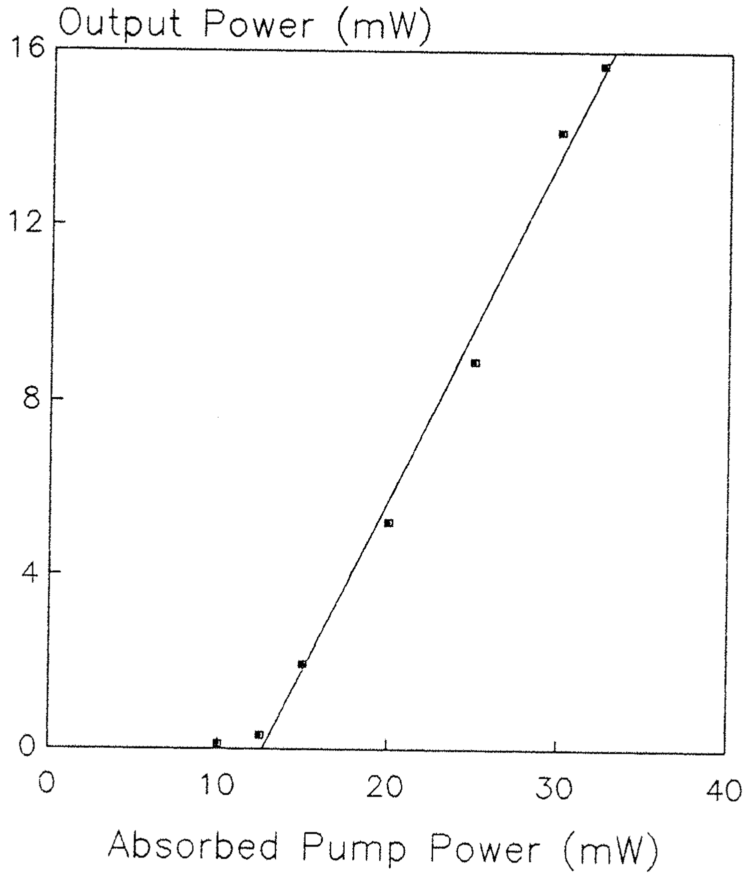

Fig.4.12 Laser characteristic at 1036nm for 1.1m fibre pumped at 900nm

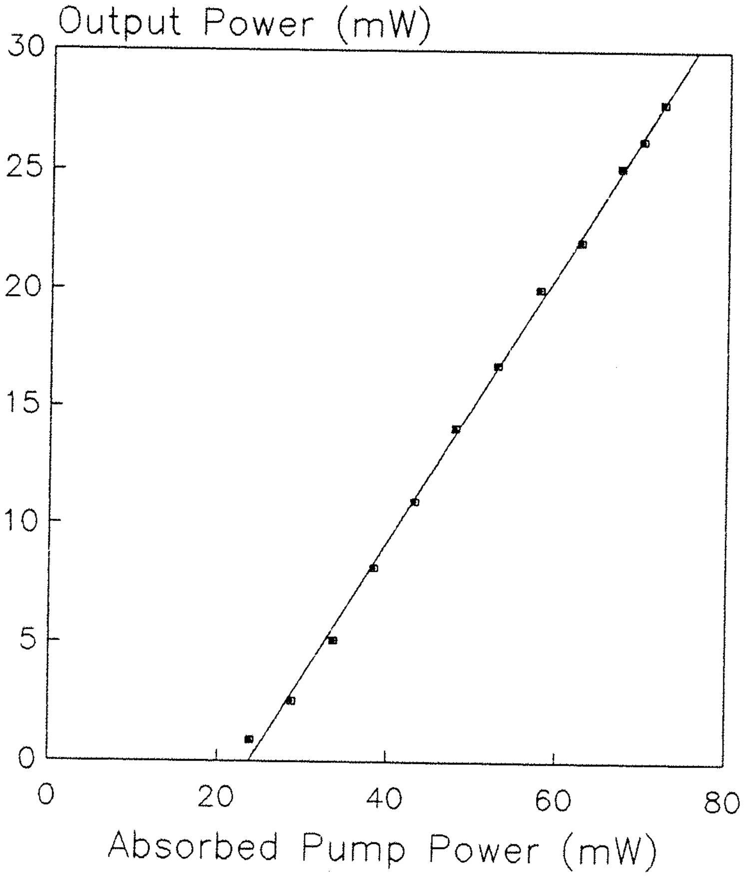

Fig.4.13 Laser characteristic at 1050nm for 4m fibre pumped at 850nm

least demonstrate that three-level laser action is achievable for pump wavelengths within the reach of GaAlAs diode lasers.

4.3.3 Laser Oscillation on the Four-Level Transition

To induce oscillation on the four-level transition, the fibre length is simply increased to the point where the three-level reabsorption losses become too great to sustain laser action. The variation of four-level oscillation wavelength with fibre length was described briefly in Section 4.3.1, where lengths up to 10m were used. However, the output power was extremely low (of the order of a milliwatt) as a result of the low pump power at 840nm (due to problems with an ageing dye solution) and reabsorption losses in the longer lengths. A 1.1m length pumped with up to 65mW at 900nm (using a new dye solution) in the single butted mirror configuration had a greatly improved performance, with all of the available pump power absorbed in this length. The fibre laser wavelength was 1036nm. The laser characteristic is shown in Fig.4.12: the slope efficiency with respect to absorbed power was 78%; threshold was 10mW absorbed, and the maximum observed output power was 16mW for 33mW absorbed.

For diode laser wavelength emulation, the pump wavelength was again changed to 850nm. Since the absorption is lower at this wavelength, the fibre length must be increased if all the pump is to be absorbed in an attempt to maximise the output power. Virtually all the power was absorbed in a 4m length for up to 150mW incident (the maximum available) at 850nm. Using this length in the single butted mirror configuration, the laser characteristic shown in Fig.4.13 was obtained, with a slope efficiency with respect to absorbed power of 57% and a threshold of 25mW absorbed. The maximum observed output power was 28mW for 72mW absorbed. The laser wavelength in this case was 1050nm, shifted slightly due to reabsorption of the short wavelength components.

4.4 Modelling of the Three- and Four-Level Transitions

It is possible to model performance on the two transitions in Yb^{3+} using a rate equation analysis with a few simplifications. The fibre is modelled as a uniformly-doped medium which saturates homogeneously, and no account is taken of the spatial profile of the pump and signal modes since, for the wavelengths and V numbers involved, the extent of the overlap between the two modes approaches unity. The quantum efficiency of the upper laser level is taken as unity (implied by the measured lifetime of 710μs compared with the calculated radiative lifetime of 554μs). The model is applicable at or below the threshold of laser operation, and predicts the variation of single pass gain with fibre length in the presence of an absorbing lower laser level: either the thermally populated level in the case of four-level operation, or the ground state in the three-level case. Consideration of the losses due to the cavity mirrors and the lower level reabsorption allow an "above threshold" operating region to be predicted.

4.4.1 The Four-Level Model

The four-level scheme is illustrated in Fig.4.14, where the populations of the four levels 1, 2, 3 and 4 at position z along the fibre are $n_1(z)$, $n_2(z)$, $n_3(z)$ and $n_4(z)$, respectively. Referring to the Yb^{3+} energy levels shown in Fig.4.4, levels 1 and 2 represent the ground state manifold sublevels *a* and *c*, respectively, and levels 3 and 4 represent the excited manifold sublevels *e* and *g*, respectively. For the purposes of the model, level *b* is incorporated into level *a*. The decay from the pump band (level 4) to the upper laser level (level 3) is assumed to be very fast so that $n_4 \approx 0$. Rapid nonradiative decay from level 2 to level 1 is also assumed, so that levels 1 and 2 are in thermal equilibrium. The total population n_0 is thus given by

$$n_0 = n_1(z) + n_2(z) + n_3(z) \qquad (4.7)$$

The thermal population of level 2 may be written as

$$n_2(z) = \beta n_1(z) \qquad (4.8)$$

where $\beta = exp\,[-(E_2 - E_1)/k_B T]$ is the Boltzmann factor, where E_1 and E_2 are the energies of levels 1 and 2, respectively, k_B is Boltzmann's

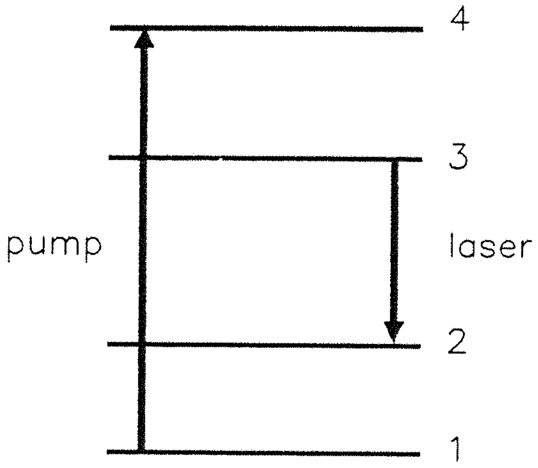

Fig.4.14 Four-level laser scheme

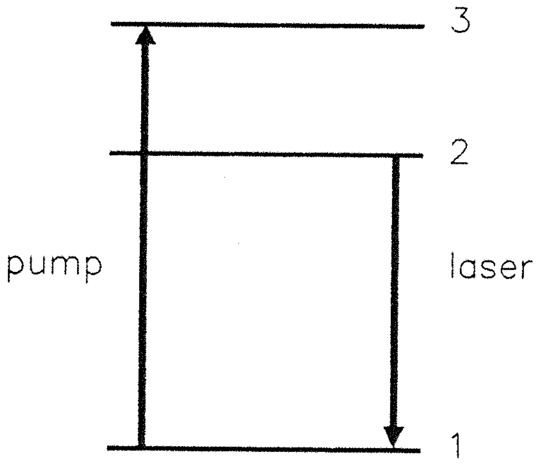

Fig.4.18 Three-level laser scheme

constant and T is the absolute temperature. The rate equation for level 3 is given by

$$\frac{dn_3(z)}{dt} = W_p(z)n_1(z) - W_{32}n_3(z) + W_{23}n_2(z) - \frac{n_3(z)}{\tau} \tag{4.9}$$

where $W_p(z)$ accounts for the pump rate at position z along the fibre length, W_{32} is the stimulated emission rate from level 3 to level 2, W_{23} is the stimulated emission rate from level 2 to level 3, and τ is the upper level lifetime. The stimulated emission rates from levels 2 to 3 and 3 to 2 are assumed to be equal, *i.e.*, $W_{32} = W_{23} = W$. In the steady state, $dn_3(z)/dt = 0$ and using Eqs.4.7 and 4.8 to eliminate $n_3(z)$ gives

$$n_1(z) = n_0 \frac{1 + W\tau}{(1 + \beta) + (1 + 2\beta)W\tau + W_p(z)\tau} \tag{4.10}$$

At this point the further assumption that $W\tau \ll 1$ is made, and the pump rate is written as $W_p(z) = \sigma_a I_p(z)/(h\nu_p)$, where σ_a is the absorption cross section, $I_p(z)$ is the pump intensity at position z and $h\nu_p$ is the pump photon energy. This, in conjunction with the pump saturation intensity $I_{sat} = h\nu_p/(\sigma_a\tau)$, gives

$$n_1(z) = n_0 \frac{1}{(1 + \beta) + I_p(z)/I_{sat}} \tag{4.11}$$

The pump absorption $dI_p(z)/dz = -\sigma_a n_1(z) I_p(z)$ can then be expressed as

$$\frac{dI_p(z)}{dz} = - \frac{\sigma_a n_0 I_p(z)}{(1 + \beta) + I_p(z)/I_{sat}} \tag{4.12}$$

Integrating over the fibre length from $z = 0$ to $z = l$ yields

$$\ln\left[\frac{I_p(l)}{I_p(0)}\right] + \frac{1}{I'_{sat}}\left[I_p(l) - I_p(0)\right] = \frac{\sigma_a n_0 l}{(1 + \beta)} \qquad (4.13)$$

where $I'_{sat} = (1 + \beta)\, I_{sat}$. The unabsorbed pump power $I_p(l)$ can now be calculated as a function of l by computer solution methods.

The total single pass gain G may be written in terms of the exponential gain coefficient g as $G = exp\ (g)$, where g is given by

$$g = \sigma_e \int_0^l \Big(n_3(z) - n_2(z)\Big)\ dz \qquad (4.14)$$

and σ_e is the emission cross section. Using Eqs.4.7 and 4.8 yields

$$g = \sigma_e n_0 l - (1 + 2\beta)\sigma_e \int_0^l n_1(z)\ dz \qquad (4.15)$$

which, using Eqs.4.11 and 4.12, may be further expressed as

$$g = (1 + 2\beta)\,\frac{\sigma_e}{\sigma_a}\left[\frac{\sigma_a n_0 l}{(1 + 2\beta)} + \ln\Big(I_p(l)/I_p(0)\Big)\right] \qquad (4.16)$$

Eqs.4.13 and 4.16 can now be used to calculate the remaining pump power at position l along the fibre and subsequently the corresponding single pass gain over this length. To simplify the expressions the following parameters are adopted:

$$f'' = \frac{\sigma_a n_0 l}{(1 + 2\beta)} \qquad x = \frac{I_p(l)}{I_p(0)} \qquad k' = \frac{I_p(0)}{I'_{sat}} \qquad g' = \frac{g}{(\sigma_e/\sigma_a)}$$

Eq.4.13 can then be written as

$$\ln x + (x - 1)k' = -\ f'' \qquad (4.17)$$

where $f'' = (1 + 2\beta)f'/(1 + \beta)$, and Eq.4.16 becomes

$$g' = (1 + 2\beta)\left(\frac{1 + \beta}{1 + 2\beta} f'' + \ln x\right) \qquad (4.18)$$

If k' and β are fixed, Eq.4.17 can be solved for x with computer iteration methods for a range of values of l (through the length parameter f''), and then these values of x can be used to solve Eq.4.18 for g' versus l. By changing k', *i.e.*, the input pump power, the process can be repeated to obtain a family of curves showing the variation of gain parameter g' with length parameter f'' for a range of input powers in the presence of a non-zero lower laser level population.

4.4.2 Interpretation of the Model

A typical plot of gain versus fibre length (strictly, g' versus f'') is shown in Fig.4.15. The operating region for laser action is bounded by the curve given by $k' = \infty$, *i.e.*, $x = 1$. In this case g' becomes equal to $(1 + \beta)f''$, a straight line which represents the maximum gain available versus length if all the ions are inverted. If the total losses are greater than this at a particular length then the laser cannot operate. In the operating region below this line there must be sufficient gain at a particular length l to overcome the ground state reabsorption loss at the laser wavelength λ_L, scattering losses (which will be length dependent) and the fixed cavity losses due to output coupling at the mirrors. The scattering losses are not treated in this model, and the reabsorption loss has been incorporated in the gain calculation. The fixed losses γ due to the mirror transmission are written as $\gamma = \ln (R_1R_2)^{-1/2}$, where R_1 and R_2 are the reflectivities of the input and output mirrors, respectively. This fixed loss defines a second straight line intercepting the g' axis at $\Delta = \gamma/(\sigma_e/\sigma_a(\lambda_p)$, where Δ is the value of the loss scaled by the cross section ratio. These two straight lines defining the upper and lower bounds for laser operation are shown in Fig.4.15. There will exist some value of k' for which the g' versus f'' curve just touches the line of the lower bound. This gives the minimum possible value of k', *i.e.*, the minimum possible input power, for laser action to occur, and also specifies

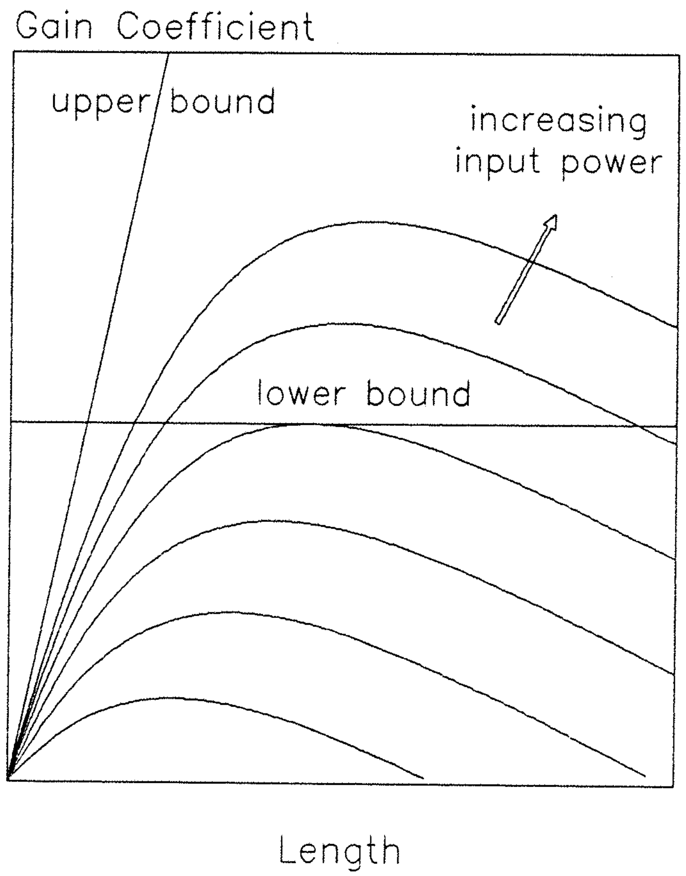

Fig.4.15 Generic plot of four-level gain versus fibre length for increasing input power

the corresponding length of fibre needed for this minimum threshold (the length at which the curve touches the line). For this particular value of k', longer or shorter fibre lengths have insufficient gain to overcome the combined losses.

4.4.3 Applications of the Four-Level Model: Case 1

As an example of how the model may be applied to existing data, consider the fibre pumped at 850nm with laser emission at 1050nm described in Section 4.3.3. Output coupling was provided by the 3.5% Fresnel reflection of the fibre end face, and a ≈ 100% reflector was butted at the input end. Hence the fixed losses are $\gamma = 1.68$ (additional butting losses are negligible compared to the high transmission of the fibre end face). The absorption cross section at 850nm is given by the ratio of the absorption coefficient α (Table 4.1) and the dopant concentration, *i.e.*, $\sigma_a \approx 0.065 \times 10^{-24}\ \text{m}^2$, and the emission cross section at 1050nm is $\sigma_e \approx 0.37 \times 10^{-24}\ \text{m}^2$ [4.15], hence $\Delta = 0.3$. The separation of the lower laser level (level c in Fig.4.4) and the ground state is about 600cm^{-1}, so the Boltzmann factor β is 0.056 at room temperature (300K).

A plot of g' versus f'' incorporating these values is shown in Fig.4.16 for k' values of 0.3, 0.4, 0.45, 0.5 and 0.6. The upper bound for $k' = \infty$ is also shown, together with the loss line given by $\Delta = 0.3$. The graph shows that the minimum possible value of k' for which laser action can occur is $k' = 0.45$ at $f'' = 2.58$. Given that $P_{sat} =$ 52mW at 850nm (Table 4.2) and $\beta = 0.056$, the threshold launched pump power $P_p(0) = k' P_{sat}(1 + \beta)$ is therefore 24.7mW, and the value of l corresponding to $f'' = 2.58$ is $l = 3.28$m.

Thus the model predicts a minimum launched threshold power of about 25mW for a 3.3m fibre. The existing experimental data for a 1050nm laser pumped at 850nm indicates a 25mW launched threshold power (where $k' = 0.46$) for a 4m length (where $f'' = 3.14$). Therefore, the laser was operated very close to its minimum possible threshold power. This provides a useful guide to the minimum power required from, for example, a GaAlAs laser diode pump source. Given the ≈ 50% overall launch efficiency for pump light, the modelling indicates that diode power in excess of 100mW is necessary at 850nm. The model is also useful in predicting the range of fibre length over which laser action is possible for a given input pump power. For instance, consider an

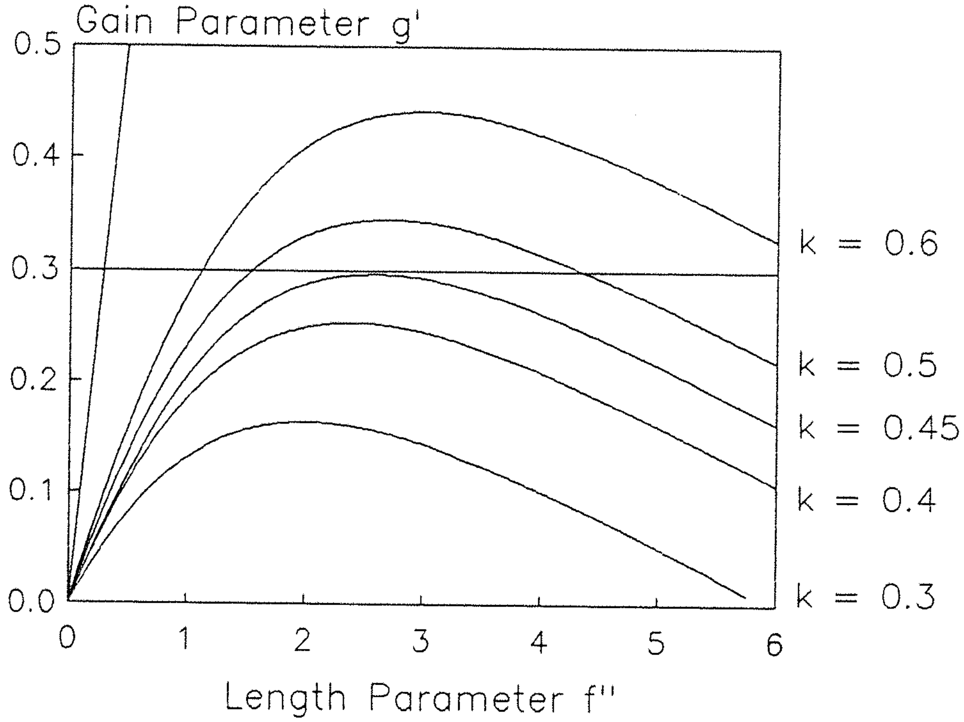

Fig.4.16 Four-level gain versus length. Loss line Δ = 0.3 for 850nm pump wavelength and 1050nm laser wavelength

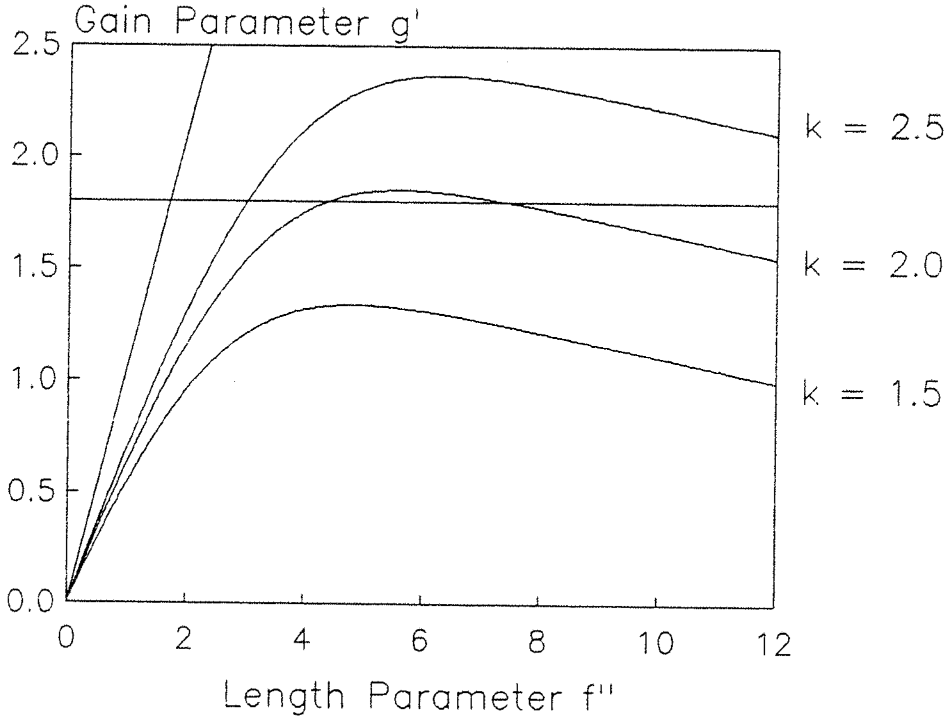

Fig.4.17 Four-level gain versus length. Loss line Δ = 1.8 for 900nm pump wavelength and 1036nm laser wavelength

input of 27mW at 850nm, corresponding to $k' = 0.5$ in Fig.4.16. The g' versus f'' curve is then above the loss line for fibre lengths between 1.5m and 4.3m.

4.4.4 Applications of the Four-Level Model: Case 2

A second example is based on the a fibre pumped at 900nm with laser action at 1036nm (see Section 4.3.3). Here $\sigma_a \approx 0.75 \times 10^{-24}$ m^2 (based on the value of α in Table 4.1) and $\sigma_e \approx 0.7 \times 10^{-24}$ m^2 [4.15]. The resonator mirrors were identical to those of Case 1, *i.e*, $\gamma = 1.68$, but $\Delta = 1.8$ here due to the different cross section ratio. Fig.4.17 shows g' versus f' for k' values of 1.5, 2.0 and 2.5, with the $k' = \infty$ line and $\Delta = 1.8$ loss line also shown. The figure shows that the minimum launched power is given by $k' \cong 1.95$ at $f' = 5.5$. Taking $P_{sat} = 4$mW at 900nm (Table 4.2), the threshold launched pump power is $P_p(0) = 8.2$mW at $l = 0.6$m.

The threshold obtained experimentally was 10mW launched for a length of 1.1m. This corresponds to $k' = 2.4$ and $f' = 9.9$, a point which lies inside the predicted operating region (*i.e.*, above the loss line), but suggests that a slightly lower threshold would have been attainable with a shorter fibre length where reabsorption losses are reduced.

4.4.5 The Three-Level Model

The rate equation analysis may also be applied to the three-level transition illustrated in Fig.4.18, where level 1 represents the ground state manifold sublevel *a* of Fig.4.4 and levels 2 and 3 represent the excited sublevels *e* and *g*. The populations of levels 1, 2 and 3 are n_1, n_2 and n_3, respectively. The decay from level 3 to level 2 is assumed to be fast so that $n_3 \approx 0$. The total population n_0 is then

$$n_0 = n_1 + n_2 \tag{4.19}$$

and the rate equation for level 2 is

$$\frac{dn_2(z)}{dt} = W_p(z)n_1 - Wn_2 + Wn_1 - \frac{n_2}{\tau} \qquad (4.20)$$

Proceeding in a similar manner to the four-level analysis, and again assuming $W\tau \ll 1$, gives

$$n_1(z) = \frac{n_0}{1 + I_p(z)/I_{sat}} \qquad (4.21)$$

This is identical to Eq.4.11 with β set to zero, and comparison with Eqs.4.13 and 4.17 gives, for the three-level transition:

$$\ln (x) + (x - 1)k = - f \qquad (4.22)$$

where $f = \sigma_a n_0 l$ and $k = I_p(z)/I_{sat}$. The exponential gain coefficient g is given by

$$g = \sigma_e \int_0^l \left(n_2(z) - n_1(z)\right) dz \qquad (4.23)$$

Using Eqs.4.19 and 4.12 with $\beta = 0$ gives

$$g = \frac{\sigma_e}{\sigma_a} \int_0^l \left(1/I_p(z) - 1/I_{sat}\right) dI_p(z) \qquad (4.24)$$

which, upon integration, becomes

$$g = \frac{\sigma_e}{\sigma_a} \left[\ln \left(I_p(l)/I_p(0)\right) - \left(I_p(l) - I_p(0)\right)/I_{sat}\right] \qquad (4.25)$$

By introducing $g' = g/(\sigma_e/\sigma_a)$ and substituting for x and k, Eq.4.25 may be expressed in the simplified form of

$$g' = \ln x - (x - 1)k \tag{4.26}$$

which, using Eq.4.22 may also be written as

$$g' = 2\ln x + f \tag{4.27}$$

As with the four-level case, two equations (Eqs.4.22 and 4.27) can be solved for x and g' versus l for a range of k values, and hence the variation of single pass gain versus length can be found as the input pump power is varied.

4.4.6 Applications of the Three-Level Model

In Section 4.4.2, the performance of the three-level laser was described, with lengths of 20cm and 50cm pumped at 900nm, both giving emission at 974nm. Fig.4.19 shows g' versus f for the case of λ_p = 900nm and λ_L = 974nm, with k values of 2.20, 2.75, 3.25 and 3.75. Also shown is the line given by $k = \infty$ which, since $x = 1$ here, is given by Eq.4.27 as $g' = f$. The mirror losses are identical to those of the four-level case, *i.e.*, $\gamma = 1.68$, and the fixed loss Δ is again given by $\Delta = \gamma/(\sigma_e/\sigma_a(\lambda_p)$. Taking $\sigma_a(\lambda_p) \approx 0.75 \times 10^{-24}$ m^2 (based on α in Table 4.1) and $\sigma_e \approx 3.1 \times 10^{-24}$ m^2 [4.15] gives $\Delta = 0.41$.

The model predicts that the minimum threshold, where the gain curve of Fig.4.19 just touches the fixed loss line, is given by the curve where $k = 2.2$ and occurs at $f = 2$. The pump saturation power of 4mW at 900nm (Table 4.1) then implies a launched threshold power of ≈ 9mW, and $f = 2$ implies that the required fibre length is $l = 0.21$m. The 20cm fibre investigated experimentally was found to have a launched power threshold of 12mW, in reasonably good agreement with the predicted value of 9mW for the same fibre length.

For the 50cm fibre, where $f = 4.8$, the measured launched threshold power was 15mW, corresponding to $k = 3.75$. The gain at $f = 4.8$ on the $k = 3.75$ curve is, as shown in Fig.4.19, well above the loss line and tends to suggest that a lower threshold should have been attainable. In fact the figure suggests that the $k = 3$ curve (not shown) would cut the loss line at $f = 4.8$, giving a predicted threshold of 12mW.

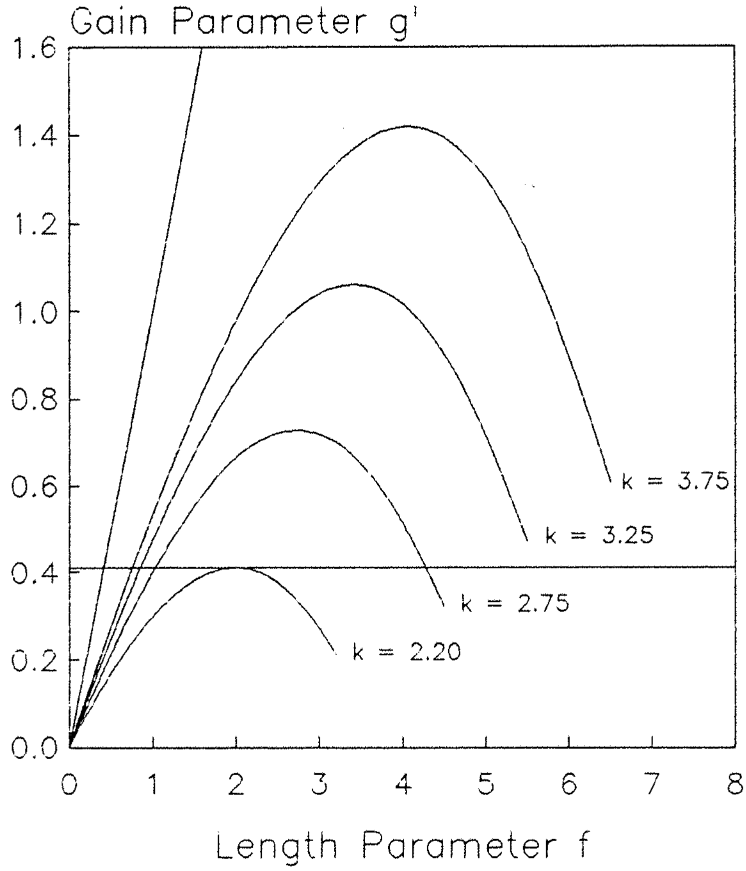

Fig.4.19 Three-level gain versus length. Loss line Δ = 0.41 for 900nm pump wavelength and 974nm laser wavelength

4.4.7 Summary of the Model

A model has been developed to predict the minimum launched threshold power and the corresponding fibre length for both the three- and four-level transitions. For 850nm pumping, the four-level transition had a predicted minimum threshold power of 25mW for a 3.3m fibre. This compares favourably with the 25mW threshold measured with a 4m fibre. At a pump wavelength of 900nm, the predicted four-level minimum threshold was 8mW for a 60cm fibre. The experimental data, taken before the modelling was performed, involved a 1.1m fibre where the threshold was 10mW, suggesting that a slightly lower threshold could have been obtained with a shorter fibre.

The three-level transition minimum threshold power for 900nm pumping is predicted to be 9mW for a 20cm fibre, compared with the 12mW measured threshold with a fibre of similar length. The three-level transition was not modelled for a pump wavelength of 850nm, since the high powers needed for pump saturation render it a rather impractical candidate for diode laser pumping.

Given the simplicity of the rate equation model, the agreement between experiment and theory is sufficiently good that, given a specified pump wavelength and an estimate of the cavity loss, gain curves could be generated to predict the minimum possible threshold power and the required fibre length. This would be particularly useful in ascertaining whether the specifications (*i.e.*, operating wavelength and output power) of a given pump source such as a diode laser could achieve threshold in an Yb^{3+}-doped fibre.

4.5 Tunable Operation

4.5.1 Preliminary Investigations

As mentioned above in Section 4.2.3, the broad nature of the fluorescence peak at around 1034nm indicates the possibility of a wide tuning range for laser operation. In order to tune the wavelength, it is necessary to insert into the cavity an element with a wavelength-dependent loss. This may be, for instance, a set of birefringent tuning plates [4.16], a diffraction grating [4.17, 4.18], a fibre coupler [4.19, 4.20, 4.21], or simply a prism.

In the preliminary stages of tuning the four-level emission in

Yb^{3+}, tuning was achieved with a grating in the resonator configuration shown in Fig.4.20. Pump light at 840nm was launched into the fibre with a graded index lens after passing through a mirror (highly reflecting at the laser wavelength), angled to reflect counter-propagating laser emission onto a grating. The grating, blazed for 1μm, was a standard Applied Photophysics monochromator grating in the Littrow configuration acting as a high reflector to retro-reflect into the fibre. Output coupling was provided by a butted mirror transmitting about 20% at the laser wavelength, and the output was passed through a monochromator before reaching a germanium photo-diode. The grating was mounted in a rotatable holder so that tuning could be achieved by making small changes of angle to alter the feedback wavelength. The tuning curve for a 3.5m length of the 2500ppm fibre (pumped with 150mW incident on the launch objective) is shown in Fig.4.21. The tuning range is continuous and broad (1034nm to 1142nm), but the output signal appears heavily modulated with an average peak separation of about 10nm. A similar modulated curve was obtained when a set of three birefringent tuning plates (taken from a Coherent dye laser) was inserted intra-cavity between the output coupler and the fibre end, with the grating simply replaced by a second high reflector at the laser wavelength.

Although successful in achieving tuning, the two arrangements detailed above involve removing the wavelength selective elements from other equipment. A more practical approach, that of using a prism, was investigated with the cavity arrangement shown in Fig.4.22. From this point onwards, all tuning experiments were performed with the 580ppm fibre. The input end of the fibre was butted against a highly reflecting mirror (> 99.5%) in the range 930-1200nm. Output from the other end of the fibre was collimated with an intra-cavity objective before passing through a prism onto a feedback mirror, which was a high reflector of similar specification to that at the input. In view of the extremely low output coupling, the laser output was detected via the reflection from the prism (see Fig.4.22). This has the added advantage of a fixed angle of reflection, invariant with respect to the laser wavelength, whereas if the detector had been placed behind the output coupler its position would need to be optimised for each wavelength due to the differing refraction angle in the prism. The light was analysed with the monochromator/detector combination as in the preliminary tuning experiments. Tuning was achieved by making a

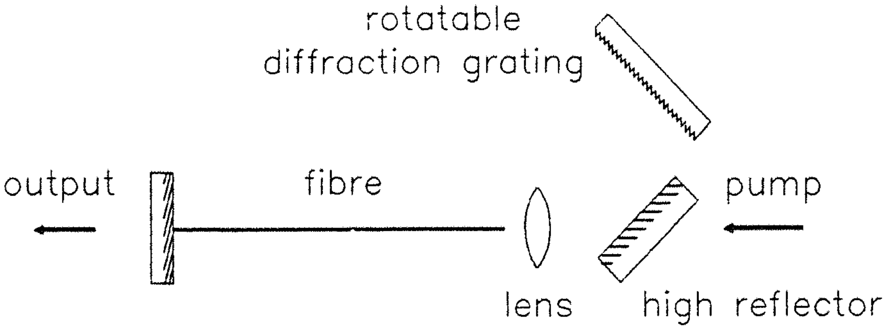

Fig.4.20 Resonator for tuning using a rotatable diffraction grating as a wavelength selective high reflector

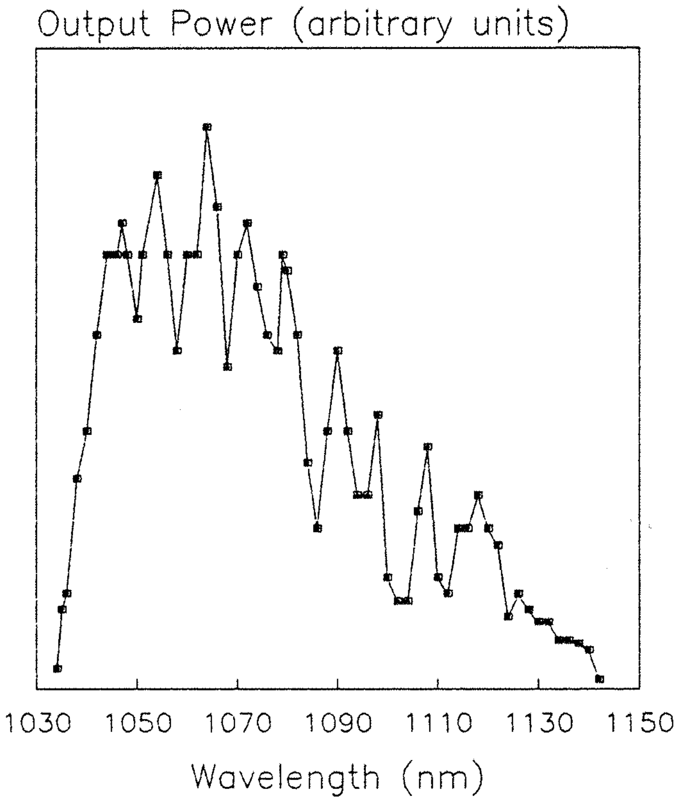

Fig.4.21 Tuning curve obtained with the resonator shown in Fig.4.20 for 3.5m of the 2500ppm fibre pumped at 840nm

small rotation of the feedback mirror to select a particular wavelength for reflection back into the cavity. The fibre output end was fixed into a glass capillary tube and inserted in a cell containing index matching fluid, a necessary precaution since without some means of preventing feedback from the end face, laser action at 1044nm occurred off the Fresnel reflection of the fibre/air interface and tuning was prevented.

A 3m fibre was pumped at 840nm with 280mW incident on the launch objective. About 100mW was coupled into the fibre core with 75% of this absorbed. The lasing wavelength was tuned in 2nm steps by setting the monochromator pass wavelength and rotating the feedback mirror to select this wavelength, with the cavity optimised at each stage for maximum output signal. A typical tuning curve under these conditions is shown in Fig.4.23, extending from 1020nm to 1150nm. Again, as with the grating and the birefringent tuner, the output signal is modulated. The modulation is not due to an etalon in the cavity, since the free spectral range *FSR* of about 7nm (indicated by the separation of the peaks in the tuning curve) would give, according to $FSR = \lambda^2/(2nd)$, an etalon spacing d of about 90μm in air or 60μm in glass, where n is the relevant refractive index of 1.0 or 1.5, respectively, and λ is the lasing wavelength, taken here as 1.1μm (roughly the mid-point of the tuning range). No spacings of these dimensions existed in the cavity, and systematic adjustment of all the cavity components failed to remove the modulation. The prism was eventually identified as the element producing the modulation, since the reflection losses at its surface depend on the polarisation state of light incident upon it which, in turn, as will be described below, depends on the wavelength. To minimise cavity loss, the prism was aligned close to Brewster's angle so that the horizontally polarised component of the laser signal was subjected to a much lower loss than the vertical component. The prism was not aligned exactly at Brewster's angle so that there was a small horizontal component in reflection which could then be detected as a measure of the laser power. Since the state of polarisation depends on wavelength, the amount of power in the vertical component, and hence the power lost from the cavity, was also wavelength-dependent, leading to the observed modulation. Similar considerations apply for tuning with the grating and birefringent tuner. Fortunately the polarisation state of light in the cavity could be controlled in a way that eliminated the

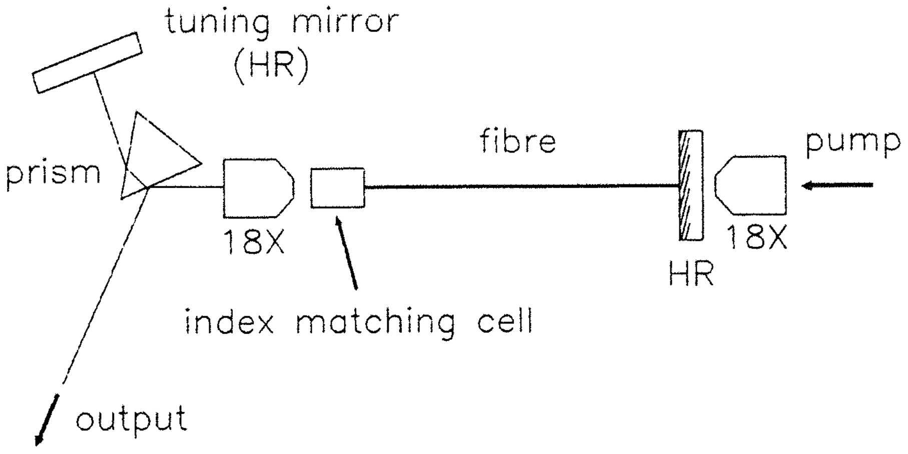

Fig.4.22 Resonator for tuning using a prism for dispersion and a rotatable high reflector for wavelength selection

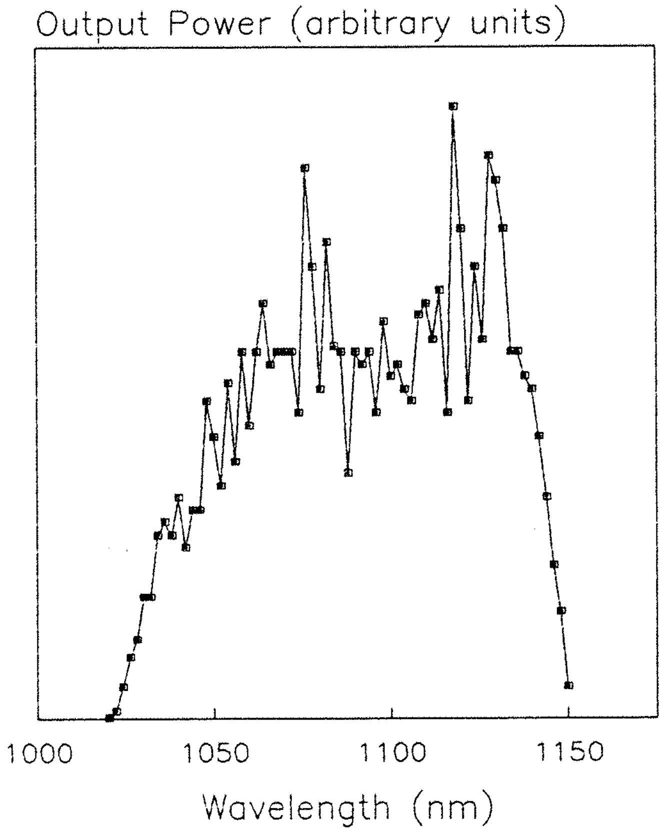

Fig.4.23 Tuning curve obtained with the resonator shown in Fig.4.22 for 3m of the 580ppm fibre pumped at 840nm

modulation by ensuring that the light incident on the prism was predominantly horizontally polarised. This was first noticed when, at a minimum in the output signal, slight bending of the fibre was found to increase the signal up to the level of the adjacent peaks, indicative of a stress-induced effect such as birefringence. This is described in more detail in the following section.

4.5.2 The Effects of Fibre Birefringence

Birefringence occurs in optical fibres [4.22, 4.23, 4.24, 4.25] through several processes which may be grouped into two main classes, "internal" and "external". The internal birefringence arises from the lack of circular symmetry in the core cross section, and if both polarisation modes are excited (the HE_{11} mode can be decomposed into two orthogonal linearly polarised modes), the state of polarisation evolves cyclically as the different propagation constant of each mode causes periodic beating to occur. Externally induced birefringence, large compared to the internal birefringence, arises from mechanical stresses that yield an elasto-optical anisotropy and allows coupling of power between the modes. These stresses are due to twisting or bending of the fibre, the application of transverse pressure, or to temperature changes (where differential thermal expansion applies transverse forces).

The effects of this birefringence cause a wavelength dependence in the polarisation state of the fibre output, arising from the wavelength dependence of the beat period between the two modes. This leads to the observed modulations in output power because of the varying reflection loss at the prism as the emergent state of polarisation changes with wavelength. To prevent the output power variations in the tuning curve, some means must be found of ensuring that the polarisation state is always predominantly horizontal at the prism, *i.e*, after it has been fed back into the fibre and undergone a round-trip it emerges with the polarisation state horizontal, even though it will have evolved during its passage through the fibre. Note that even launching horizontally polarised light into the fibre at the prism end is not sufficient, since it can be resolved into two orthogonal components with respect to the axes of birefringence and so in general will have developed a vertical component when it emerges after a round trip. One method of obviating this problem would be to use a correctly aligned polarisation-maintaining fibre, where a highly elliptical core cross section or increased stress-induced anisotropy maintains a high intrinsic birefringence. The intermodal coupling is therefore very weak, and propagation occurs essentially in one polarisation eigenmode only, providing power is launched into only one of these modes. In the absence of such a fibre, however, the simple method proposed by Lefevre [4.26] was employed. This provides a means of inducing linear birefringence in a controllable manner by coiling the fibre into a series of loops, making a device analogous to a set of fractional wave plates to form an effective polarisation controller (see also [4.27]).

Lefevre's analysis considers a pair of principal axes, one along the fibre diameter in the plane of the bend (fast axis), and another orthogonal to this, again along the fibre diameter but perpendicular to the plane of the bend (slow axis). By consideration of the difference δn in the extraordinary and ordinary stress-induced refractive indices, it is possible to derive the relation

$$\delta\beta = \frac{\pi EC}{\lambda}\left(\frac{r}{R}\right)^2 \text{ radians/m} \tag{4.28}$$

where the birefringence $\delta\beta$ is the difference in the propagation constants of the two polarisation modes, E is Young's modulus, C is the stress-optical coefficient, r is the fibre radius (including the cladding) and R is the fibre bend radius. If the fibre is coiled into a loop of N turns, a total phase delay between the two polarisation modes of $2\pi NR\delta\beta$ is produced, where $2\pi NR$ is simply the total length of fibre in the loop. Hence a required phase delay of π, $\pi/2$ or $\pi/4$ (corresponding to $\lambda/2$, $\lambda/4$ or $\lambda/8$ devices) implies the relation

$$|\delta\beta|\ 2\pi NR = 2\pi/m \tag{4.29}$$

where m = 2,4 or 8. Thus the bend radius required to give a phase delay specified by m is simply

$$R = \frac{\pi EC}{\lambda}\ Nmr^2 \tag{4.30}$$

For silica, $E = 7.75 \times 10^9$ kg/m^2, and $C \approx -3.5 \times 10^{-11}$ m^2/kg at a wavelength of 633nm. Although C varies slightly with wavelength, the quoted value is taken as valid in the 1μm region where the Yb^{3+} fibre laser operates. For the Yb^{3+} doped fibre used here, r = 62.5μm. For a single loop (N = 1) "quarter wave plate" where m = 4 and the wavelength is taken as 1.1μm (the approximate mid-point of the tuning range), the bend radius is R = 1.2cm. For a "half wave plate" device where m = 2, a single loop of half this radius (*i.e*, 0.6cm) is required, or alternatively two turns (N = 2) of radius 1.2cm. The two turn approach is preferable for simplicity of construction, and also to avoid the risk of the fibre either breaking, or having too great a radiation loss, due to the smaller radius of curvature.

Thus it is easily possible to construct an in-line device comprising two $\lambda/4$ loops to control the ellipticity and one $\lambda/2$ loop to control the orientation of the output polarisation. Control is achieved by rotating the plane of the loops, which twists the fibre and rotates the orientation of the axes of the induced birefringence. In practice the device consists of three plastic discs of appropriate radius with grooves cut into the edges to accommodate the fibre. Two of the discs have one fibre loop, the other has two, and all three discs are fixed to mounts which allow independent rotation of the plane of each of the discs about a mutual tangential axis. Such a device, termed a "fibre loop polarisation controller", was used to significantly improve the tunable performance of the Yb^{3+} fibre laser. These results are described in the following section.

4.5.3 Improved Tuning Performance

The new resonator configuration is shown in Fig.4.24, where the fibre loop polarisation controller has been incorporated. A further improvement is the addition of a second prism, since a tendency to oscillate on more than one wavelength simultaneously (regardless of the inclusion of the polarisation controller) had been observed during the course of the tuning experiments. This second prism provided increased dispersion and prevented feedback of unwanted wavelengths, which otherwise depopulate the upper laser level and cause a reduction in the available gain at the desired wavelength. The output from the fibre was again taken in the form of a reflection from the first prism, slightly offset from Brewster's angle to allow a small reflection of the horizontal component. This was then passed through a Glan-Taylor polariser to ensure that only this horizontal component was selected before being analysed by a monochromator and germanium photo-diode. As with the initial prism-tuned performance, the fibre length was 3m, pumped with about 280mW incident on the launch objective at 840nm. The tuning curve, recorded in 2nm steps, is shown in Fig.4.25. Laser action was observed continuously from 1010nm to 1162nm, with a threshold of 30mW absorbed. The angle of each loop in the polarisation controller was adjusted at each step to maximise the output signal, with the result that the modulation effect has virtually disappeared.

The short wavelength limit of the tuning range may be reduced by cooling the fibre to 77K by immersing as much of it as possible (about 2.5m) in a Dewar containing liquid nitrogen. The low temperature significantly reduces the thermal population of the Stark levels in the ground state multiplet, reducing the reabsorption loss otherwise suffered by the shorter emission wavelengths. The tuning curve for a LN_2-cooled 3m length of fibre pumped at 840nm is shown in Fig.4.26. The short wavelength limit is indeed reduced, from 1010nm (at room temperature) to 1000nm. However, it is uncertain why the long wavelength limit is also reduced (from 1162nm to 1150nm) as the cooling should have little effect on transitions to the higher-lying Stark levels in the ground manifold. This long wavelength limit might, in fact, be expected to extend further in the case of both room temperature and liquid nitrogen cooled operation, since the fluorescence continues out to 1250nm and the cavity mirrors remained highly reflecting to 1200nm. However, the maximum observed tuning range of 152nm at room temperature compares favourably with dye laser tuning ranges and represents an energy tuning range of almost $1300cm^{-1}$. Finally, since the resonator used two high reflectors, the output power emerging from either mirror is extremely small, *e.g.*, the output from the rotatable feedback mirror was about $3\mu W$ in the plateau region of the tuning curve. Further developments of the tunable Yb^{3+}-doped fibre laser will require optimisation of the output coupling to increase the power, although this would almost certainly impose the penalty of some reduction in the tuning range.

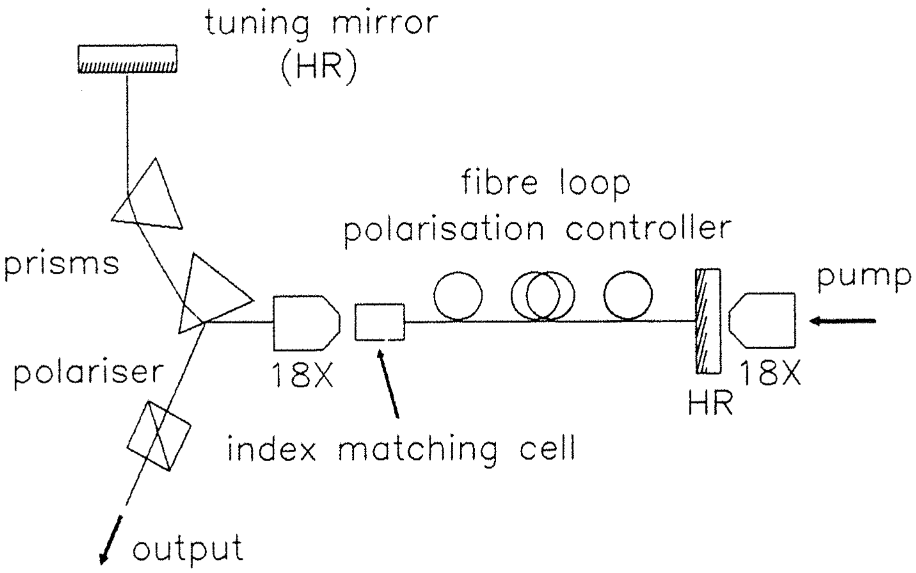

Fig.4.24 Resonator for tuning incorporating a fibre loop polarisation controller to reduce output power modulation

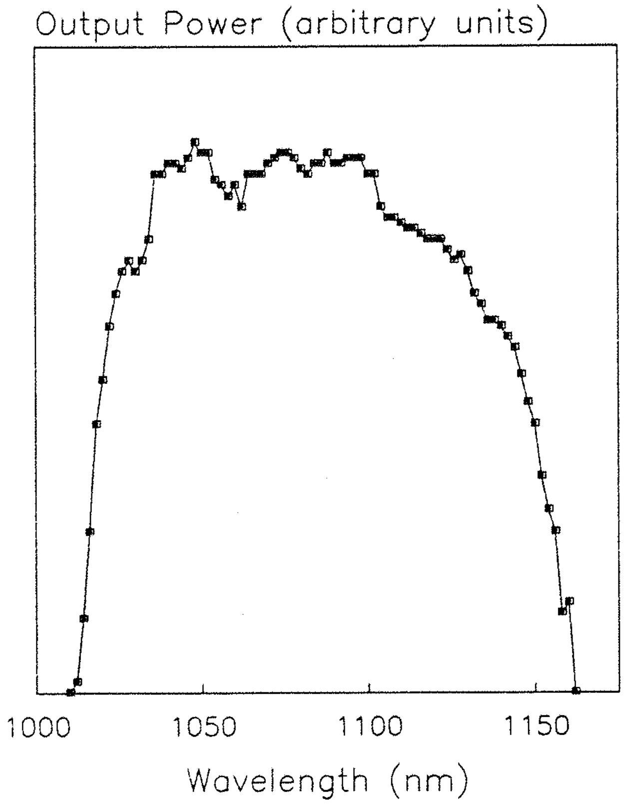

Fig.4.25 Tuning curve obtained with the resonator shown in Fig.4.24 for 3m of the 580ppm fibre pumped at 840nm

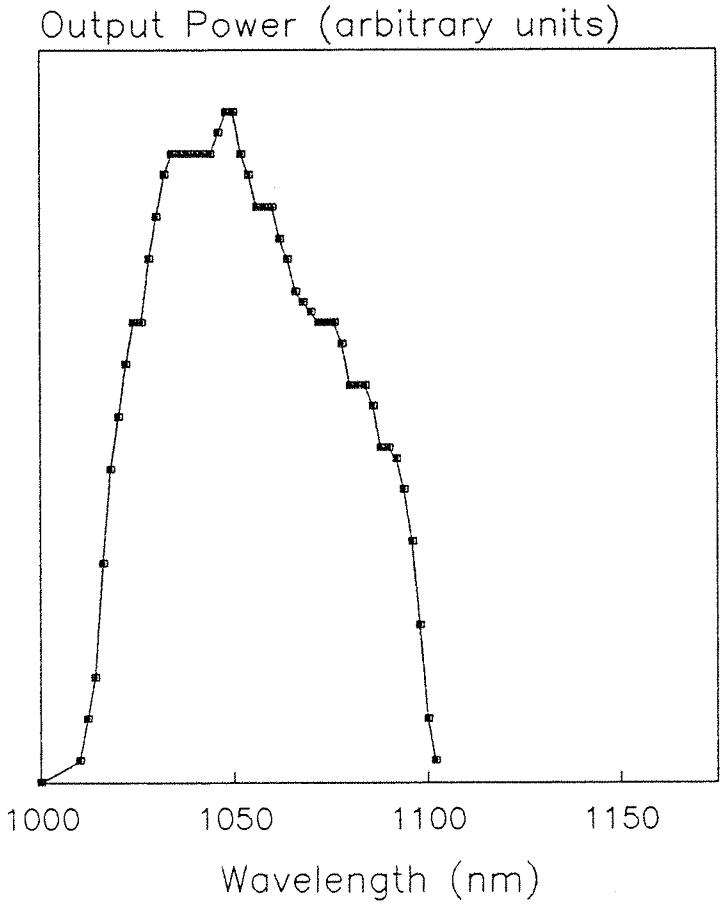

Fig.4.26 Tuning curve obtained with the resonator shown in Fig.4.24 for 3m of the 580ppm fibre pumped at 840nm and cooled to 77K

4.6 Superfluorescent Operation

4.6.1 Introduction

The tuning experiments described in Section 4.5 above led to the discovery that under appropriate conditions the Yb^{3+} fibre could produce significant amounts of amplified spontaneous emission (ASE), a phenomenon commonly termed "superfluorescence". Attempts to tune the three-level transition using a short (20cm) 580ppm fibre pumped at 900nm were unsuccessful. No tunability was observed on this transition (the tuning range would in any case be limited by the narrow linewidth of the transition), but the fibre was observed to emit several milliwatts at 974nm for very modest incident powers (typically 40-50mW). Since the output end was terminated in an index matching cell to suppress lasing off the uncoated fibre end (which otherwise prevented tunable operation), this implied a strong fluorescence output rather than laser emission, confirmed by the absence of relaxation oscillations induced by the optical chopper. It was concluded that the emission must be due to superfluorescence, a phenomenon that occurs in high-gain laser media due to single- or double-pass amplification of spontaneous emission without the benefit of optical feedback. The process is shown in Fig.4.27. Spontaneously emitted photons in an active medium travel in all directions, but in the case of a fibre some will be emitted into the numerical aperture and guided along the core. These photons stimulate excited ions to emit, and the photons produced by this process are of course also emitted into the numerical aperture and guided by the fibre. Further emission is stimulated by these photons, and the signal is therefore amplified as it propagates, rapidly becoming predominantly stimulated emission.

Digonnet has suggested that doped fibres could be used as superfluorescent sources [4.28] as an alternative to the superluminescent diodes [4.29] used as sources in ring laser gyroscopes. Such diodes have several disadvantages, including short operational lifetime, low output power, poor wavelength stability and low coupling efficiency to a monomode fibre system. The highest reported output power from a superluminescent diode is about 30mW [4.30], but only about 20% of this could be launched into a monomode fibre. The output from a superfluorescent fibre, however, can be easily coupled into a fibre system due to the good matching of spatial modes, and in addition it has been observed that the SiO_2 host environment can stabilise the emission wavelength [4.31] with respect to temperature to a greater extent than a semiconductor host, where the emission wavelength varies by typically 0.05nm/degree C. Superfluorescent sources find applications where broadband, nonresonant emission is required, such as the fibre gyroscope where short coherence lengths (tens of microns or better) are needed to reduce Rayleigh backscattering noise. Evidence of superfluorescent emission from a fibre was first reported by Po *et al.* [4.32], but the first practical device was a Nd^{3+}-doped fibre producing about 10mW at 1.06μm with a full width at half maximum of 17nm reported by Liu *et al.* [4.33]. Significant improvements have followed, and recently Duling *et al.* [4.34] reported 80mW of superfluorescent emission from a diode-pumped Nd^{3+}-doped offset core fibre.

4.6.2 Superfluorescence Measurements

For investigations into the superfluorescent performance of the Yb^{3+}-doped fibre, pump light was launched in through a butted mirror, highly reflecting (>99.5%) in the range 930-1200nm. The purpose of this mirror was to reflect the backwards-travelling signal and add it to the output signal through the other end of the fibre (*i.e.*, a double-pass configuration), thus reducing by a factor of two the pump power needed for the same gain with a single-pass configuration. The output end was terminated in an index-matching cell to prevent feedback from the fibre/air interface which would otherwise cause laser oscillation and give a longitudinal mode structure to the emission spectrum. Note that the addition of the index matching cell is the only difference between the configuration for superfluorescent output and that used for three- and four-level laser emission. Output powers were measured in the same manner as that described in Sections 4.3.2 and 4.3.3, where a monochromator was used to separate pump and signal wavelengths and the total power measured at the fibre output was divided in the ratio of the germanium photo-diode signal measured at each wavelength after the monochromator.

Superfluorescence was observed on both the three- and four-level transitions, the dominant transition being determined by fibre length as described qualitatively for the laser emission in Section 4.3.1.

This qualitative behaviour was confirmed experimentally by cutting back a length of fibre from 2.20m to about 0.25m while monitoring the pump and signal powers. The fibre was pumped with 60mW incident on the launch objective at a wavelength of 900nm, where the relatively high power available from the dye laser gave the highest superfluorescent power, despite the slight detuning from the absorption peak at 910nm, since the dye laser tuning range was falling off at this longer wavelength.

Fig.4.28 shows the results of the cut back. For lengths greater than about 1m, the four-level emission dominates at about 1040nm (the exact emission wavelength depends on fibre length as described in Section 4.3.1). For the three-level transition, the considerations of the pump saturation power P_{sat} discussed in Section 4.4.1 apply. Although the fibre is inverted with respect to both transitions at the input end where the pump power in the core is greater than P_{sat}, the three-level emission is reabsorbed in the region where the pump power falls below this value and the four-level emission dominates. The four-level emission shows the expected behaviour, increasing with increasing length until the output power peaks when all the pump power is absorbed in about 1.5-2.0m. The output power then shows a roll-off with increasing length after a peak at about 1.75m. This could be interpreted as the effect of reabsorption by thermal population in the lower levels (*b* and *c* in Fig.4.4) preventing the fibre being made arbitrarily long if maximum power is a criterion, as with the laser performance. However, the effect is somewhat more marked than expected and in fact a repeat cut back taken only for 1040nm emission for fibre lengths from 2 to 5m showed that the power tended asymptotically towards about 12mW with no evidence of four-level reabsorption for this range of fibre lengths. These measurements are not shown in the figure since the pump power was different and the launch not fully optimised.

The output power at 974nm on the three-level transition begins to increase as the fibre length is progressively cut back from about 1m, *i.e.*, the length of the absorbing region at the end of the fibre is being reduced. The power peaks at a length of about 50cm and then decreases with decreasing length, with the peak defining the optimum length where the pump power leaving the fibre is equal to P_{sat}. The cut back shows that the residual pump at this point is about 4mW. This is in excellent agreement with the value given in Table 4.2 where P_{sat}

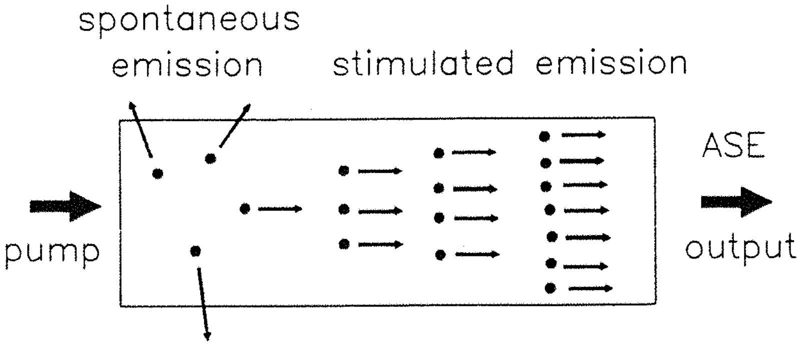

Fig.4.27 Generation of amplified spontaneous emission in a single pass configuration

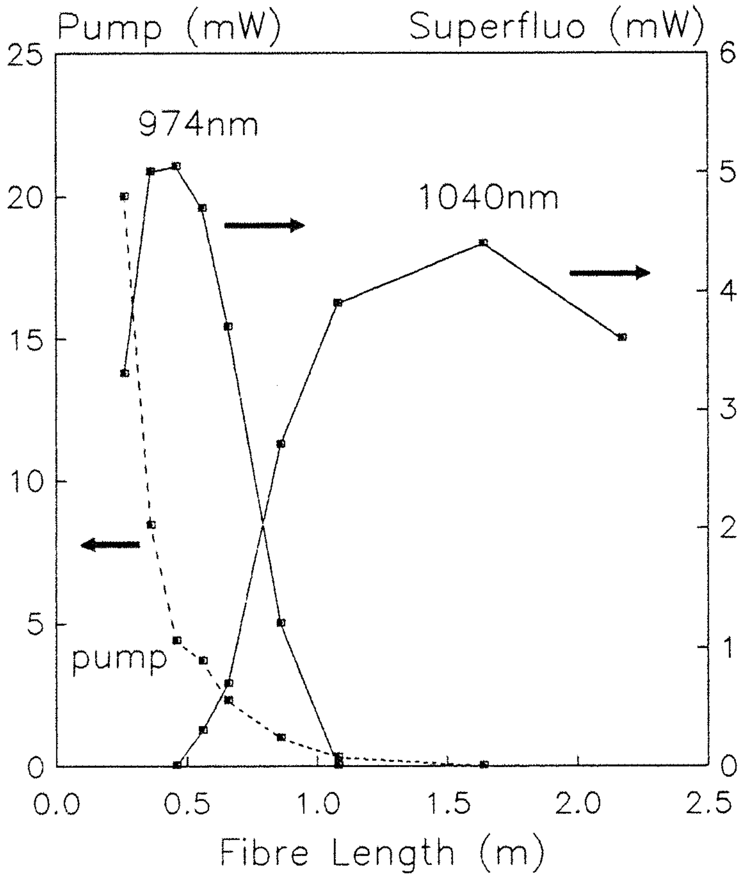

Fig.4.28 ASE output power and residual pump power versus fibre length

is 4mW for a pump wavelength of 900nm. It should be noted that the description of power versus length given above, and particularly the determination of the optimum length for three-level emission, apply for specific values of pump power (which determines the length of the fibre that is inverted) and pump wavelength (which determines the saturation power).

The output characteristic curve for three-level emission at 974nm versus pump power is shown in Fig.4.29. A length of 50cm and a pump wavelength of 900nm were used, optimum for an incident power of 60mW or, assuming a 50% launch efficiency, a launched power of 30mW. This value of 60mW was the maximum available from the dye laser at the time that this and the superfluorescence cut back measurements were carried out. However, during preliminary investigations into the superfluorescent performance, the dye was considerably fresher, and a fibre of comparable length was pumped with 80mW incident. The resulting 12mW fibre output is also shown in Fig.4.29. The absorbed power for this maximum power point was 32mW, and the slope efficiency was approximately 47% for output powers up to 5mW. The threshold power is arbitrarily defined by Digonnet [4.28] as the absorbed pump power P_{abs} for which the output power is 1% of P_{abs}. Using this definition the threshold was less than the lowest pump power (12.5mW absorbed) used in the measurements.

To investigate the four-level transition at 1040nm, the pump wavelength was changed to 850nm since more pump power was available here (up to 160mW). At this wavelength, P_{sat} is about 50mW so that, in conjunction with a longer fibre, emission at 974nm is discriminated against. A length of 5m was chosen, with at least 90% of the pump power absorbed in this length. The output characteristic curve is shown in Fig.4.30. The maximum output power was 27mW for 67mW absorbed, and the slope efficiency was approximately 62%. The threshold was again less than the lowest pump power (18mW absorbed) used.

For a double-pass configuration in the high gain limit where saturation has set in, the theoretical limit on the slope efficiency η_s is given by [4.31] as

$$\eta_s = h\nu_s / h\nu_p \qquad (4.31)$$

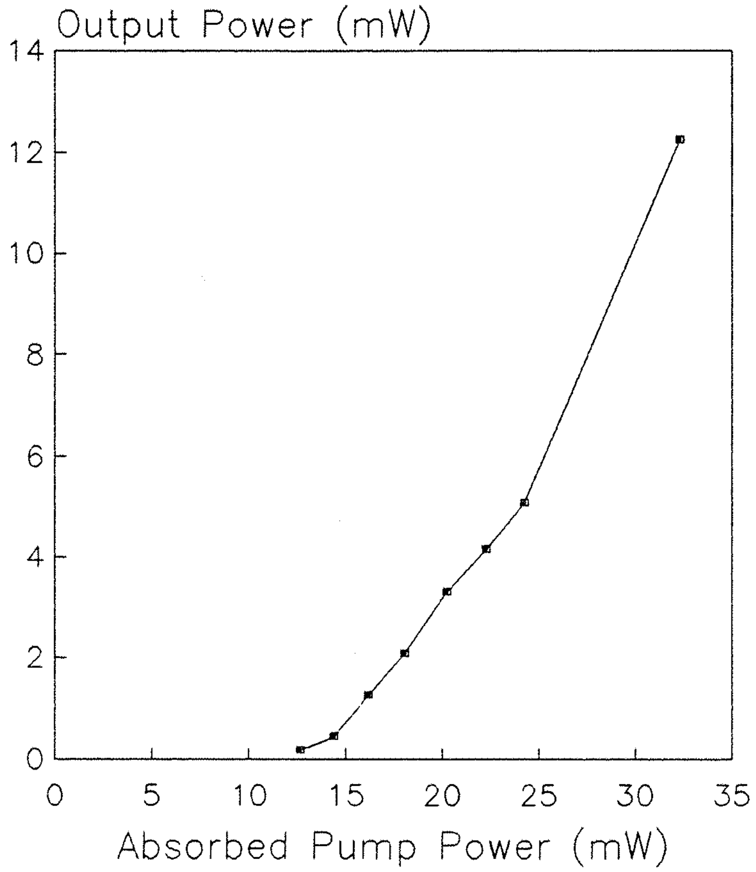

Fig.4.29 Characteristic for ASE at 974nm for 50cm fibre pumped at 900nm

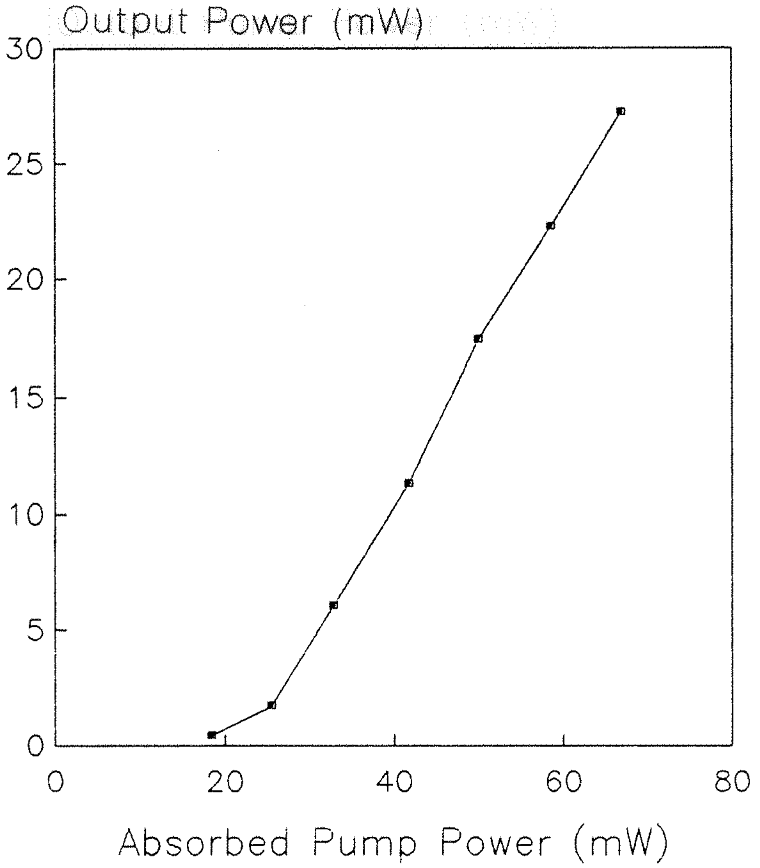

Fig.4.30 Characteristic for ASE at 1040nm for 5m fibre pumped at 850nm

where $h\nu_s$ and $h\nu_p$ are the signal and pump photon energies, respectively. In the case of a fibre geometry, the overlap of the pump and signal modes must also be taken into account. Assuming these modes to be Gaussian, the expression given by [4.35] for the overlap integral η_o may be used, so that the slope efficiency becomes

$$\eta_s = \eta_o \frac{h\nu_s}{h\nu_p} \tag{4.32}$$

where unity quantum efficiency and no loss due to the input butt are assumed. For the case of the fibre pumped at 900nm with emission at 974nm, the overlap is $\eta_o = 0.90$, whereas for the fibre pumped at 850nm with emission at 1040nm, $\eta_o = 0.92$. These values yield maximum slope efficiencies of 83% and 75% for the three- and four-level transitions, respectively. The experimentally measured values of 47% and 62% are somewhat lower, and reflect the loss of cavity photons at the butted end and by reabsorption in the lower level.

4.6.3 Lineshape Measurements

The spectrum of the superfluorescent output was measured for the three- and four-level transitions by passing the end light through a monochromator. The output was detected on a germanium photo-diode and plotted on a Y-T chart recorder. Fig.4.31 shows a typical spectrum for a 50cm fibre pumped with 60mW at 900nm. The peak emission wavelength is 974nm and the full width at half maximum is 2.9nm (monochromator resolution 0.5nm). The spectrum is free from any evidence of resonant mode structure, *i.e.*, the index matching cell is effective in preventing optical feedback.

The linewidth is expected to narrow as the pump power is increased [4.28, 4.31], since frequency components near the centre of the gain curve are subject to a higher gain than components lying away from linecentre. To give as wide a range of pump power as possible, the pump wavelength was changed to 850nm (up to 150mW available) and the fibre length increased to 4m so that the four-level transition was under investigation. A typical spectrum for emission at about 1040nm (incident pump power 120mW) is shown in Fig.4.32. Spectra were

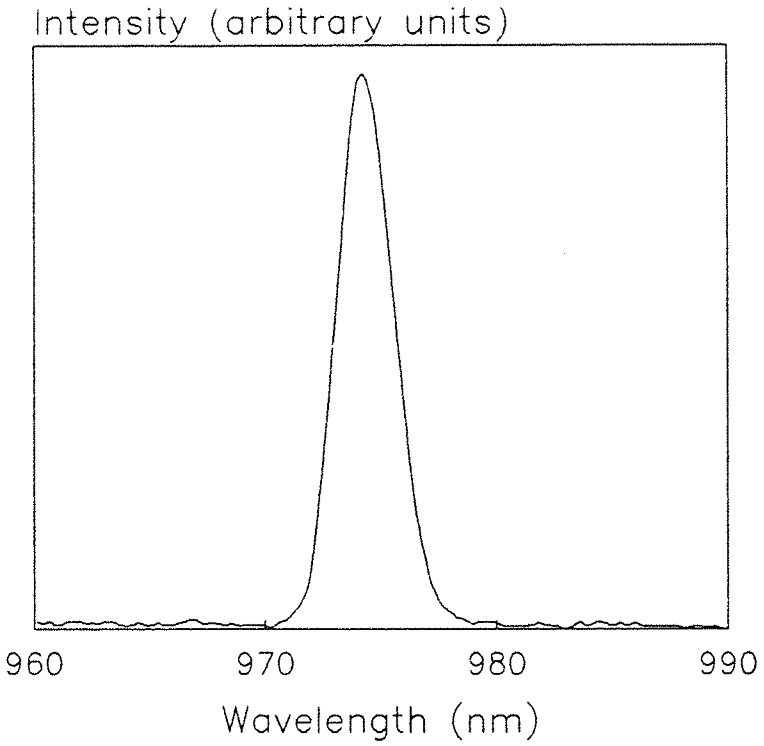

Fig.4.31 End light ASE spectrum for 50cm fibre pumped at 900nm

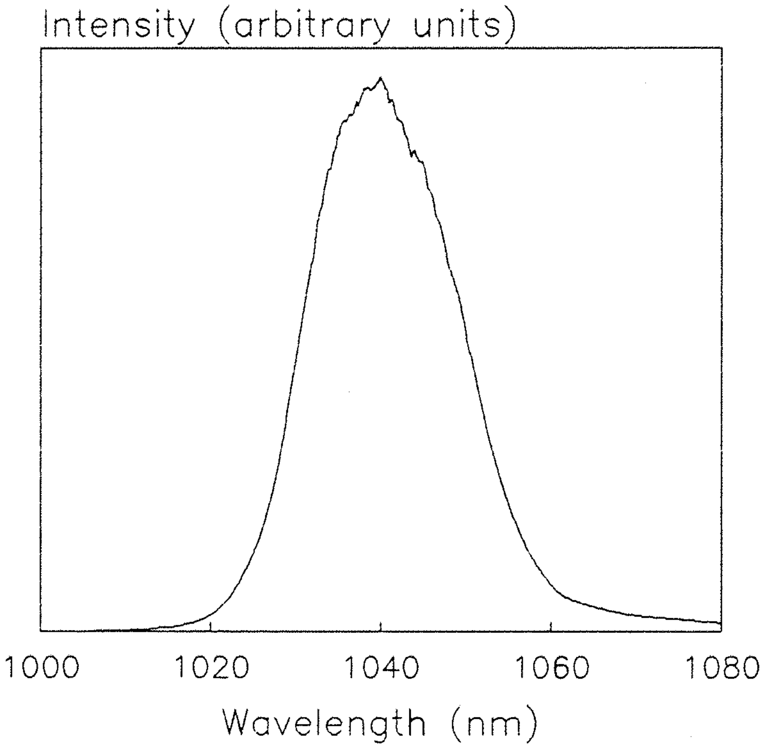

Fig.4.32 End light ASE spectrum for 5m fibre pumped at 850nm

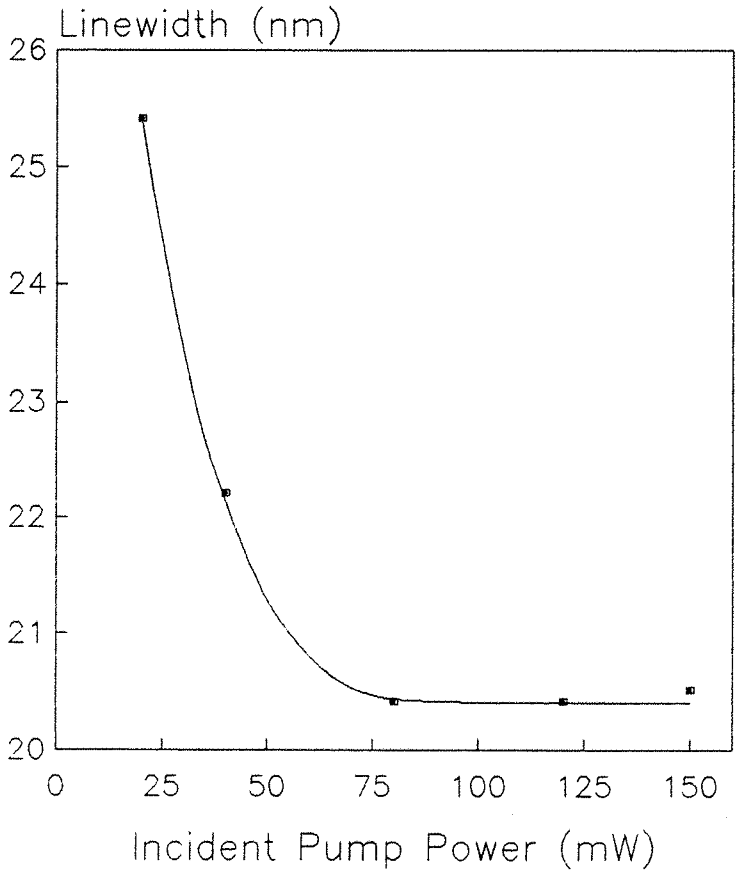

Fig.4.33 Four-level ASE linewidth versus pump power for 5m fibre pumped at 850nm

recorded for a range of incident pump power between 20mW and 150mW, and some evidence of line narrowing was obtained: the full width at half maximum varied from 25.4nm for 20mW incident to 20.5nm for 150mW incident. The variation of linewidth with pump power is shown in Fig.4.33. The general behaviour is as predicted [4.28], *i.e.*, the linewidth narrows rapidly before tending to a quasi-asymptotic value for high powers.

4.6.4 Output Modelling

The model developed by Digonnet [4.28, 4.31] is applied in this section to predict the superfluorescence power in a double-pass device in the absence of gain saturation. The output curves in Figs.4.29 and 4.30 are essentially linear over much of the range of pump powers used and lack detail in the region before this linearity sets in. In order to model the unsaturated region of the characteristic, another set of data was taken for the four-level transition by pumping a 3m length of fibre at 900nm with incident pump powers between 25mW and 50mW. The peak of the superfluorescence output was located at 1035nm in this instance.

For modelling purposes, a lossless fibre with a step refractive index profile and a uniformly doped core region is assumed. Let $f(\nu)$ be the gain lineshape with a full width at half maximum of $\Delta\nu_0$, normalised to unity at linecentre ν_s. The single-pass gain coefficient $g(\nu)$ may then be written as

$$g(\nu) = g(\nu_s)\ f(\nu) \tag{4.33}$$

The total superfluorescence power emitted, P, is found by integrating the number of photons $n(\nu)$ per unit bandwidth over the emission lineshape, where

$$n(\nu) = exp\ [g(\nu)] - 1 \tag{4.34}$$

The integration yields the following expression for emitted power:

$$P = P_0 \{exp\ [2g(\nu_s)] - 1\}\ \xi \qquad (4.35)$$

where ξ is a normalised dimensionless integral that depends on $g(\nu_s)$ and $f(\nu)$. The value of ξ is extracted from the data in [4.31]. The factor of two in the exponent arises from the collection of backwards travelling fluorescence by the high reflector, doubling the available gain. The coefficient P_0 is the power emission of one photon per mode, given by

$$P_0 = m\beta\Delta\nu_0 h\nu_s \qquad (4.36)$$

where m is the number of polarisation modes, $h\nu_s$ is the superfluorescence photon energy and β is a normalisation factor given by

$$\beta = \int_{-\infty}^{+\infty} f(\nu)\ d\nu \qquad (4.37)$$

β is taken to be 1.064 by assuming a Gaussian lineshape. The signal photon energy is 1.92×10^{-19} J and the linewidth is taken as about 20nm from the spectra discussed in Section 4.5.3. It is further assumed that both of the orthogonal polarisation modes are excited so that $m = 2$. Taking these values gives $P_0 \approx 2\mu W$.

The small signal, undepleted ground state gain coefficient at linecentre $g(\nu_s)$ is given by [4.31] as

$$g(\nu_s) = (\sigma_s \tau_f / h\nu_p)\ (F/\eta_p)\ P_{abs}/A_{core} \qquad (4.38)$$

where σ_s is the stimulated emission cross section at ν_s, τ_f is the upper level lifetime, $h\nu_p$ is the pump photon energy, η_p is the fraction of the pump energy carried in the core, A is the core area and F is a dimensionless coefficient describing the amount of overlap between the pump and signal modes and can be given in terms of the effective core area A_{eff} by [4.28] as

$$F = A_{core}/A_{eff} \tag{4.39}$$

A_{core} is the active core area given by $\pi\rho^2$, but cancels out of Eq.4.38 when substituting for *F*. If the pump and signal modes are assumed to have a Gaussian form (*i.e.*, monomode propagation) along the fibre length, then the effective area [4.35, see also Eq.2.20] is

$$A_{eff} = \frac{\pi\left(w_s^2 + w_p^2\right)\left(1 - exp\left(-2\rho^2/w_p^2\right)\right)}{2\left(1 - exp\left(-2\rho^2\left(1/w_p^2 + 1/w_s^2\right)\right)\right)} \tag{4.40}$$

where w_p and w_s are the spot sizes for the pump and signal modes, respectively. The pump and signal spot sizes are given by the approximation [4.36] $w = \rho\ (\ln\ V)^{-1/2}$ where *V* is the fibre *V* number at the pump or signal wavelength.

For the Yb^{3+} fibre used here, the *V* number is 2.136 at the pump wavelength of 900nm and 1.858 at the signal wavelength of 1035nm. Taking the core radius as $\rho = 1.8\mu m$ yields an effective core area of $1.13 \times 10^{-11}\ m^2$. The *V* number at 900nm is used to calculate (Eq.2.19) the fractional power in the core as $\eta_p = 0.77$. The gain coefficient may now be written as $g(\nu_s) = 3.7 \times 10^{23}\ \sigma_s P_{abs}(mW)$. Eq.4.35 is then used to calculate the theoretical output power versus absorbed power curve for comparison with the experimental data, with σ_s as a fitting parameter. The best fit was found for $\sigma_s = 0.5 \times 10^{-24}\ m^2$, hence $g(\nu_s)$ may be expressed as

$$g(\nu_s) = 0.19\ P_{abs}(mW) \tag{4.41}$$

The curve calculated from this relationship is shown in Fig.4.34, together with the experimental data. The fit is good until the absorbed power reaches about 20mW. At this point it may be inferred

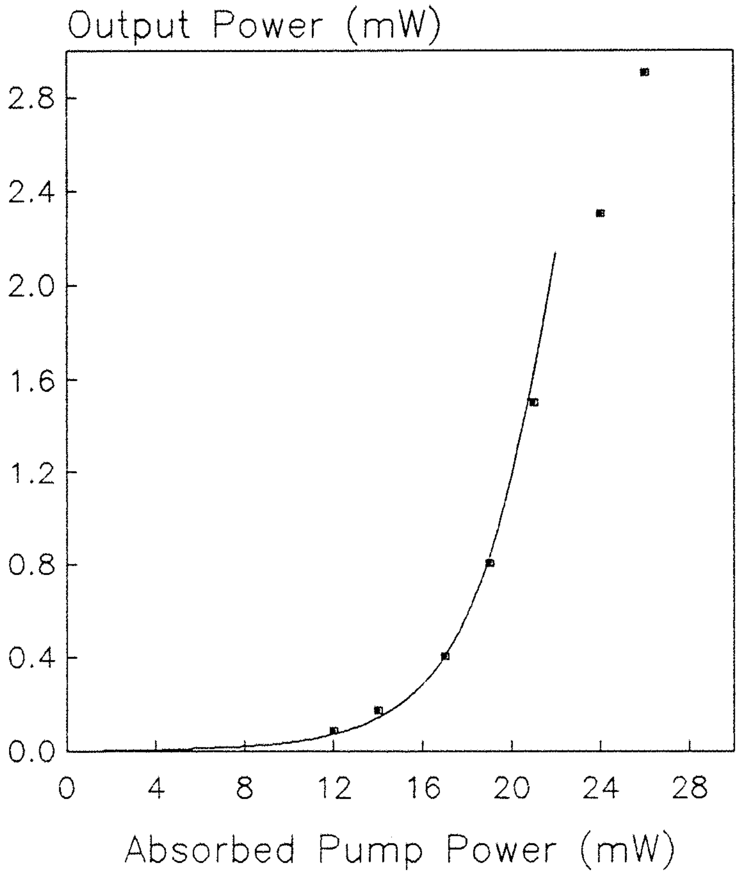

Fig.4.34 Four-level ASE output versus pump power for 3m fibre pumped at 900nm with calculated curve added

that gain saturation begins to set in here, and the curve will be linear for higher absorbed powers. The threshold for superfluorescence, as defined in Section 4.5.2, is about 12mW absorbed. Eq.4.41 then implies that the round trip gain $2g$ at threshold is about 20dB, consistent with the predictions of Digonnet [4.28] for the gain required for superfluorescence in doped fibres.

The high gains available from Yb^{3+}-doped fibre have revealed it to be a surprisingly interesting and notable fibre system, with laser operation using a highly transmitting (≈ 96%) end face as an output coupler, and superfluorescent operation when the output coupling is increased to 100%. In the following section, the resonator design is modified again to demonstrate some preliminary results of Q-switching on both the three- and four-level transitions.

4.7 Q-Switched Operation

4.7.1 Introduction

Q-switched operation has been previously demonstrated with fibre lasers [4.38, 4.39, 4.40]. For instance, a Nd^{3+}-doped fibre laser has yielded 70ns pulses at 0.9μm, and 200ns pulses at 1.08μm with a peak power of about 9W [4.39]. Q-switched Er^{+}-doped fibre lasers have also been demonstrated, with 60ns pulses at 1.55μm and 2W peak power [4.40].

The high gain demonstrated in the Yb^{3+}-doped fibre system makes it a prime candidate for high peak power operation under Q-switching conditions. In order to accommodate a Q-switching mechanism, the basic fibre laser cavity was modified as shown in Fig.4.35. An intracavity microscope objective collimated the fibre output before passing it through the Q-switch on to the output coupler. The other end of the fibre was butted against a mirror highly reflecting in the range 930-1200nm. The Q-switch used here was a Crystal Technology Model 3080 acousto-optic modulator with specifications given in Table 4.3 below. The Q-switch power supply was driven with a 5V TTL input signal from a pulse generator capable of providing variable driving pulse widths and repetition rates. Output pulses were detected with a fast photo-diode (response time 1-10ns) and displayed on an oscilloscope with 100MHz bandwidth.

Initial measurements of the Q-switched performance were made

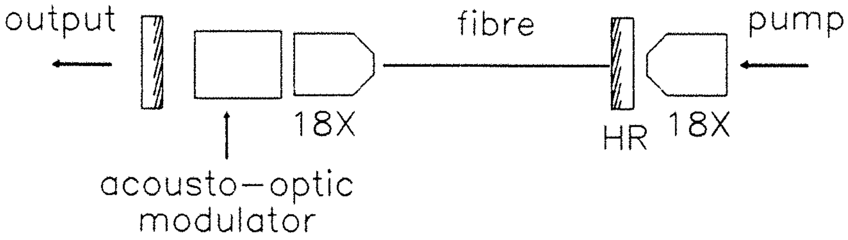

Fig.4.35 Resonator for Q-switching

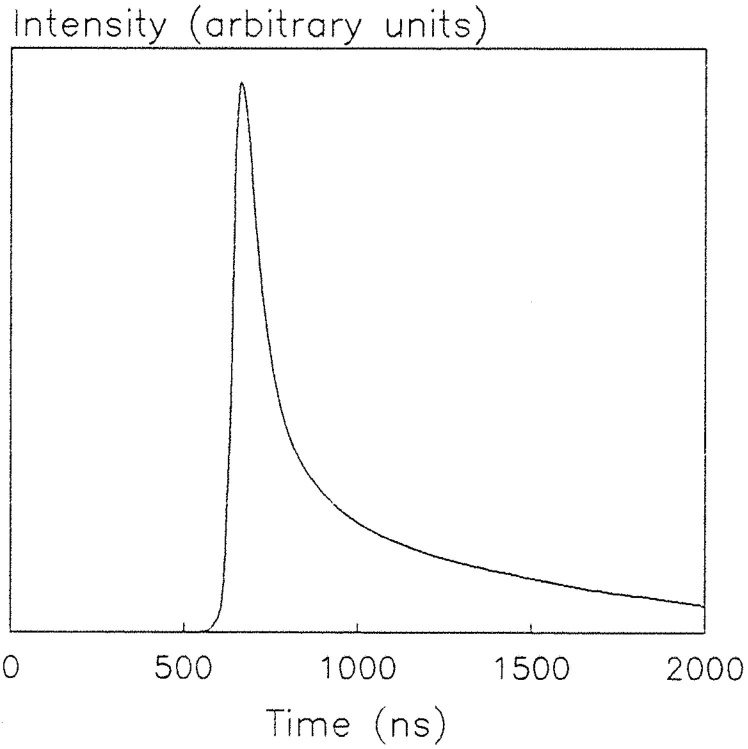

Fig.4.36 Output pulse at 1036nm for 1.1m fibre pumped at 850nm

using a 1m length of fibre pumped at 850nm. The output coupler had a transmission of about 20% at the laser wavelength of 1041nm. Output pulses were observed, but the modulator did not provide sufficient hold-off in its low-Q state to prevent continuous-wave lasing. This was suspected to be a result of the polarisation-sensitive nature of the modulator, so the diffraction efficiency of the first order diffracted beam was measured for the vertical and horizontal components. The measurement was made by removing the output coupler and inserting a Glan-taylor polariser between the intracavity objective and the modulator. The diffraction efficiency for the vertical component was 40%, but only 20% for the horizontal component. Neither of these efficiencies is particularly high, but it did prove possible to hold off laser oscillation in the low-Q state with the incorporation of a fibre loop polarisation controller, as described in Section 4.5.2. This could be adjusted to ensure that, after a round trip through the fibre, the polarisation state at the modulator was predominantly vertical and therefore subject to a higher diffraction loss. In selecting the Q-switch repetition rate the upper laser level lifetime of 710μs was taken into account. Pumping for one or two lifetimes is sufficient to ensure appreciable population inversion, since at any given instant ions excited one or two lifetimes previously will have largely decayed and are no longer available for stimulated emission. Consequently, repetition rates between 1.0kHz and 1.2kHz were used.

Q-Switch Specifications:

spectral range..........0.44-1.20μm
A-O medium..............tellurium dioxide (TeO_2)
acoustic velocity.......4.26mm/μs
aperture................1.0mm
centre frequency........80MHz

Table 4.3

4.7.2 Q-Switched Operation on the Four-Level Transition

The improved resonator was set up as described above and pumped with, initially, up to 70mW incident on the launch objective at 850nm. With a fibre length of 1.1m, the laser wavelength was 1036nm, and the threshold for Q-switched laser action was 30mW incident on the input objective. The output coupler transmission was 20% at the laser wavelength. The average output power for the pump and signal wavelengths was measured on a thermopile detector at the exit slit of a monochromator (located at the fibre laser output), and corrected for the monochromator transmission by measuring the total power at the entrance slit. For an incident pump power of 70mW, the average laser power was 0.6mW. The 1.2kHz repetition rate therefore implies that the pulse energy was 500nJ. The output pulse shape is shown in Fig.4.36. The long (about 1.5μs) tail is unexpected but could be caused by the detector response, since some photo-detectors display a long decay when responding to an intense input signal. An expanded region of the pulse is shown in Fig.4.37. The pulse width at the half intensity points is 100ns. If the entire 500nJ was delivered in a pulse of this duration, then the peak power would be about 5W.

4.7.3 Output Modelling of the Four-Level Transition

To model this Q-switched performance, a pure four-level system (Fig.4.14) is assumed and a simple rate equation analysis is used to predict the peak output power, output energy and pulse width. The comprehensive analysis by Siegman [4.41], or the more simplified version of Svelto [4.12], provide further details to the basic description given below. The four-level rate equations may be written as follows:

$$\frac{dn_3}{dt} = W_p n_1 - Bqn_3 - n_3/\tau \qquad (4.42)$$

$$\frac{dq}{dt} = V_a Bqn_3 - q/\tau_c \qquad (4.43)$$

where n_1 and n_3 are the populations of the ground state and upper laser level, respectively, W_p is the pump rate per ion, B is the stimulated transition rate per atom and per mode, V_a is the mode volume within the active medium, q is the number of photons in the cavity, τ is the upper level fluorescence lifetime and τ_c is the photon cavity lifetime. The lower level population n_2 and the pump level population n_4 are assumed to decay rapidly so that $n_2 \approx n_4 \approx 0$, and so $n_1 + n_3 = n_T$, where n_T is the total population of active ions. The population inversion n is then given by $n = n_3 - n_2$. This allows Eqs.4.42 and 4.43 to be simplified to:

$$\frac{dn}{dt} = W_p(n_T - n) - Bqn - n/\tau \tag{4.44}$$

$$\frac{dq}{dt} = (V_a Bn - 1/\tau_c)\, q \tag{4.45}$$

Under Q-switching conditions, the time evolution of n and q is short compared to the pump rate and upper level decay rate, and an additional simplification can be made by neglecting the $W_p(n_T - n)$ and n/τ terms in Eqs.4.44 and 4.45. This then yields

$$\frac{dn}{dt} = -Bqn \tag{4.46}$$

$$\frac{dq}{dt} = (V_a Bn - 1/\tau_c)\, q \tag{4.47}$$

At the peak of the Q-switched pulse, $dq/dt = 0$ and Eq.4.47 gives

$$n_p = 1/(V_a B\tau_c) \tag{4.48}$$

where n_p is the inversion at the peak. This may also be written [4.12]

$$n_p = \gamma/(\sigma_e l) \tag{4.49}$$

where γ is the total logarithmic loss per pass, σ_e is the emission cross section and l is the length of the active medium. This expression is identical to that for the critical (*i.e.*, threshold) inversion n_c for laser action. The threshold pump rate $W_{p,th}$ is found by putting $dn/dt = 0$, $n = n_c$ and $q = 0$ in Eq.4.44, which yields

$$W_{p,th} = \frac{n_c}{(n_T - n_c)\tau} \tag{4.50}$$

If $n_c \ll n_T$ then $W_{p,th} \approx n_c/(n_T\tau)$. If the pump rate is now set at x times the threshold rate, *i.e.*, $W_p = xW_{p,th}$ (and assuming no pump saturation), the following relation may be derived

$$W_p n_T \tau = x n_c = x n_p \tag{4.51}$$

since n_c and n_p are identical. In a continuously pumped repetitively Q-switched laser, in the time τ_p between consecutive pulses the pump rate must restore the initial inversion n_i (the inversion at the time that the switch "opens") starting from the final inversion n_f (the inversion after the pulse is over). Putting $W_p(n_T - n) \approx W_p n_T$ and $q = 0$ in Eq.4.44 gives

$$\frac{dn}{dt} = W_p n_T - n/\tau \tag{4.52}$$

Integrating this equation from n_i to n then yields

$$n_i = (W_p n_T \tau) - (W_p n_T \tau - n_f)\ exp\ (-\tau_p/\tau) \tag{4.53}$$

which can be rewritten, using Eq.4.51, in the form

$$x\ (n_p/n_i)\ [1 - exp\ (-\tau_p/\tau)] = 1 - (n_f/n_i)\ exp\ (-\tau_p/\tau) \tag{4.54}$$

Since x is known (from the ratio of pump power to threshold power), either n_p/n_i or n_f/n_i can be found if one of these ratios is known. To proceed, the ratio of Eqs.4.46 and 4.47 is taken and Eq.4.48 applied to obtain:

$$\frac{dq}{dt} = - V_a(1 - n_p/n) \tag{4.55}$$

Integrating from q_i to q (*i.e.*, n_i to n) and neglecting the small initial number of photons q_i yields the following relation:

$$q = V_a[n_i - n - n_p \ln (n_i/n)] \tag{4.56}$$

The final inversion n_f is found by setting $q = 0$, which gives

$$(n_i - n_f)/n_i = (n_p/n_i) \ln (n_i/n_f) \tag{4.57}$$

Eqs.4.54 and 4.57 can now be solved for n_i/n_p. This value is then used to calculate the peak output power, output energy and pulse width, as described below.

The output power P through one of the cavity mirrors having reflectivity R is given by [4.12] as

$$P = \left(\frac{\gamma' c}{2L} \right) h\nu q \tag{4.58}$$

where $\gamma' = - \ln R$ is the logarithmic loss per pass through the mirror, L is the optical path length, ν is the frequency of emission and q is the number of cavity photons. At the peak of the pulse, the power is given by P_p and the number of photons by q_p (found by putting $n = n_p$ in Eq.4.56). Using Eq.4.49 for n_p and noting that the cavity lifetime is given by $\tau_p = - L/(c\gamma)$ gives

$$P_p = \frac{\gamma' A\ h\nu}{2\sigma_e \tau_c}\left(n_i/n_p - \ln\,(n_i/n_p) - 1\right) \qquad (4.59)$$

where V_a has been approximated as Al, where A is the area of the active medium and l the length.

The output energy E is found from the following:

$$E = \int_0^\infty P(t)\ dt = \left(\frac{\gamma' c}{2L}\right) h\nu \int_0^\infty q(t)\ dt \qquad (4.60)$$

where Eq.4.58 has been used for P. The integral of q is found by integrating Eqs.4.46 and 4.47, and by noting that $q(0) = q(\infty) = 0$ to obtain

$$E = \left(\frac{\gamma'}{2\gamma}\right)(n_i - n_f)\ (V_a h\nu) \qquad (4.61)$$

To rewrite this in terms of the ratio n_i/n_p, Eq.4.57 is used in a different form by noting that the left hand side can be defined as the inversion utilisation factor $\eta_E = (n_i - n_f)/n_i$, so that Eq.4.57 can be recast as

$$(n_i/n_p)\eta_E = -\ln\,(1 - \eta_E) \qquad (4.62)$$

Again approximating V_a as Al and using Eq.4.49 for n_p, Eq.4.61 takes the following form:

$$E = (\gamma'/2)\ (n_i/n_p)\ \eta_E\ (A/\sigma_e)\ h\nu \qquad (4.63)$$

This equation may now be used in conjunction with Eq.4.59 to obtain an approximate value for the pulse width $\Delta\tau$ by defining this width as $\Delta\tau = E/P_p$. Hence, from Eqs.4.59 and 4.63

$$\Delta\tau = \frac{\tau_c \eta_E (N_i/N_p)}{\left((n_i/n_p) - \ln (n_i/n_p) - 1\right)} \tag{4.64}$$

It may now be determined whether these equations accurately describe the Q-switched operation of an Yb^{3+}-doped fibre laser in practice. From the results given in Section 4.7.2, x = 2.333 (from the ratio of the 70mW pump power to the 30mW threshold). The repetition rate of 1.2kHz means that τ_p = 833μs which, together with the fluorescence lifetime τ of 710μs, gives τ_p/τ = 1.17. Substituting for x and τ_p/τ in Eq.4.56, and using Eq.4.57, yields the solution n_i/n_p = 1.76, and from Eq.4.62, η_E = 0.717. These values can then be used in Eqs.4.59, 4.63 and 4.64 to find P_p, E and $\Delta\tau$.

In order to calculate the peak output power the photon cavity lifetime τ_c is required. This is given by [4.12] as

$$\tau_c = \frac{-\ 2L}{c \ln \left(R_1 R_2\ (1 - T_i)^2\right)} \tag{4.65}$$

where R_1 and R_2 are the reflectivities of the two cavity mirrors, L is the optical path length of the cavity and T_i is the fractional internal loss per pass. The intracavity objective has a transmission loss of about 10%, and in addition the efficiency of relaunching light into the fibre with this objective must be taken into account. If it is assumed that all the light emitted from the fibre end is collected by the objective, but only 50% is relaunched after reflection by the output coupler, then the single pass launch loss will be $1 - (0.5)^{1/2} \approx 0.3$. The total internal fractional loss per pass is therefore $T_i = 1 - [(1 - 0.1) \times (1 - 0.3)] = 0.37$. The optical path length in this instance was 1.83m and so, with R_1 = 1.00 and R_2 = 0.80, the cavity lifetime is τ_c = 10.6ns. In addition, the logarithmic loss due to the output coupler is $\gamma' = -\ln R_2 = 0.22$.

Substituting into Eq.4.59 for τ_c and n_i/n_p, together with $A = \pi\rho^2$ (where the core radius ρ is 1.8μm), and taking $\sigma_e \approx 0.7 \times 10^{-24}$ m^2 [4.15] at 1036nm yields a peak output power of P_p = 5.64W. The output energy is found from Eq.4.63, solving first for η_E = 0.717 for n_i/n_p = 1.76 in Eq.4.62. With the values of A, σ_e and γ' given above, E =

390nJ. Using these calculated values of E and P_p, the width of the output pulse is given approximately by $E/P_p = 70$ns. These calculated pulse parameters are given in Table 4.4, together with the measured values for comparison.

	calculated	measured
P	5.6W	5.0W
E	390nJ	500nJ
$\Delta\tau$	70ns	100ns

Table 4.4

The agreement between the calculated and measured parameters is generally reasonable suggesting, even if somewhat tentatively, that the observed long pulse tail is probably due to the detector response and not some phenomenon of the laser emission.

4.7.4 Q-Switched Operation on the Three-Level Transition

The fibre length was reduced to 25cm for operation on the three-level transition at 974nm, and the pump wavelength was changed to 884nm for increased absorption. The short length meant it was not possible to incorporate the fibre loop polarisation controller, as this device alone took up in excess of 50cm of fibre, and a strong tendency for prelasing was a persistent problem. With 20% output coupling at 974nm, the incident threshold power was 25mW and the maximum available pump power was 40mW, yielding an average Q-switched output power of 0.2mW. The 1kHz repetition rate then implies an output energy of 200nJ. The output pulse is shown in Fig.4.38, where the pulse width at the half intensity points is 25ns. As with the four-level transition, the pulse has a long decay of about 1.5μs, although this is not shown in the figure. If all the output energy appeared in the pulse, the peak power would be 8W, but with perhaps 90% of the energy in the long ($\approx$ 0.75ms) prelase signal, the actual peak power may be only about 1W. Due to these uncertainties and experimental difficulties in preventing prelasing, Q-switched operation on the three-level transition was pursued no further. However, the possibility of Q-switching the Yb^{3+}-doped fibre laser has been demonstrated, and there remains

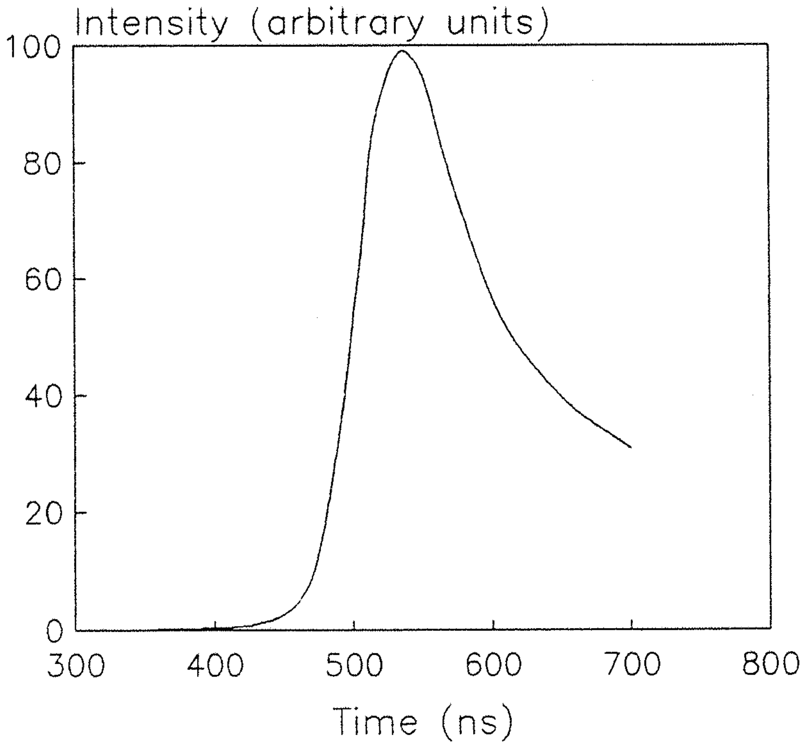

Fig.4.37 As Fig.4.36, with expanded time scale

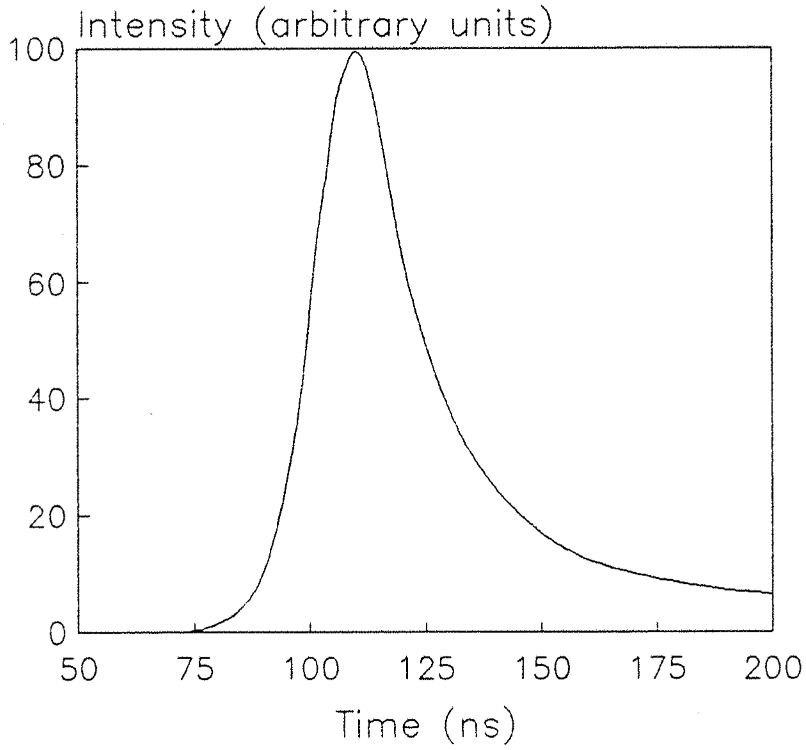

Fig.4.38 Output pulse at 974nm for 25cm fibre pumped at 884nm

considerable scope for further development and improvement with a more effective Q-switch and optimised fibre length and output coupling.

4.8 Concluding Remarks

Continuous-wave laser action in the 1μm wavelength region has been demonstrated in Yb^{3+}-doped silica based fibres [4.42, 4.43] pumped at wavelengths achieveable from GaAlAs diode lasers in the 0.8μm region. The considerable detuning ($\approx$ 900cm^{-1}) from the peak Yb^{3+} absorption around 0.9μm demonstrates the attractive features of the large inhomogeneous broadening of rare-earths in a glass host.

Emission on the three- and four-level transitions at 974nm and $\approx$ 1040nm, respectively, was observed with a pump wavelength of 850nm provided by a Styryl 9M dye laser. A 20cm fibre with high reflectors butted at both ends yielded 1.4mW at 974nm for 70mW launched. Increasing the fibre length to 4m yielded laser action at 1050nm in a resonator with a butted high reflector at the input but using the 3.5% reflectivity fibre/air interface at the output end for feedback. A slope efficiency of 57% with respect to absorbed power was measured, and the threshold power was 25mW absorbed. The maximum observed output power at 1050nm was 28mW for 72mW absorbed. Hence both three- and four-level operation is expected to be possible with diode laser pumps at 850nm, particularly if laser diode arrays are considered. However, the need for two high reflectors for 974nm emission and the high pump saturation power required to invert the absorption (about 50mW) indicates that longer wavelength diodes operating closer to the Yb^{3+} peak absorption would be a necessity if diode pumped operation of this transition is to be practical.

For longer pump wavelengths closer to the $^2F_{7/2} \rightarrow {}^2F_{5/2}$ absorption peak, the three-level performance is greatly improved. A 50cm fibre pumped at 900nm, again with the end face providing feedback, yielded up to 9mW at 974nm for 27mW absorbed, with a threshold power of 12mW absorbed. The slope efficiency with respect to absorbed power was 63%. Laser action on the four-level transition was investigated for this pump wavelength by increasing the fibre length to 1.1m. The laser wavelength was then 1036nm. A 78% slope efficiency with respect to absorbed power was observed with this fibre, with a threshold power of 10mW absorbed. The maximum output power was 16mW for 33mW absorbed. The high slope efficiencies attainable on both transitions is attributed to the lack of excited state absorption in the Yb^{3+} system, and offers the prospect of scaling to higher powers if the Styryl 9M pump laser was replaced with, for instance, a Ti:sapphire source.

A model has been developed to predict the minimum possible threshold power and the required fibre length for the three- and four-level transitions. The model predicts (for the particular resonators used) minimum launched threshold/length combinations of 9mW/0.2m for the three-level transition, and 8mW/0.6m for the four-level transition, for 900nm pumping in both cases. For a pump wavelength of 850nm, the four-level threshold is predicted as 25mW for a 3.3m fibre length. These values are in reasonable agreement with the measured characteristics.

The broad fluorescence on the four-level transition around 1040nm allowed continuously tunable laser operation [4.43] over a wide range of wavelengths using a prism as the dispersive element. The tuning range extended from 1010nm to 1162nm at room temperature, with the lower limit reduced to 1000nm at 77K. Output power modulations with the operating wavelength were found to be caused by the birefringent nature of the fibre, and were alleviated by the incorporation of fibre loop polarisation controllers.

The high gains available from the Yb^{3+}-doped fibre (modelling calculations show the round trip gain at threshold to be about 20dB) allowed the demonstration of superfluorescence, or amplified spontaneous emission (ASE), on the three- and four-level transitions [4.44]. A 50cm fibre pumped at 900nm yielded 12mW at 974nm for 32mW absorbed, with a 47% slope efficiency with respect to absorbed power. With the fibre length increased to 5m and a pump wavelength of 850nm, up to 27mW was observed at 1040nm with a slope efficiency of 62% with respect to absorbed power. This superfluorescence may find important applications in ring laser gyroscopes, where broadband nonresonant sources are required

Q-switched operation, using an acousto-optic deflector to modulate the cavity loss, gave measured peak output powers of 5W at 1036nm and several (but indeterminate) watts at 974nm. Improvements in performance may be expected with a modulator having a higher diffraction efficiency than the one used in the experiments, since prelasing due to insufficient cavity loss was found to be a persistent problem.

Ytterbium-doped fibre lasers thus have many interesting features and may find applications as efficient wavelength converters of GaAlAs diode laser wavelengths to the 1μm region, and also as tunable spectroscopic sources over a significant wavelength range.

References

[4.1] H.W. Etzel, H.W. Gandy and R.J. Ginther, 'Stimulated emission of infrared radiation from ytterbium activated silicate glass', *Appl. Opt.*, 1, 534 (1962)

[4.2] G.E. Peterson and P.M. Bridenbaugh, 'Application of resonance cooperation of rare-earth ions Nd^{3+} and Yb^{3+}', *Appl. Phys. Lett.*, 4, 201 (1964)

[4.3] E. Snitzer, 'Laser emission at 1.06μ from Nd^{3+}-Yb^{3+} glass', *IEEE J. Quantum Electron.* QE-2, 562 (1966)

[4.4] E. Snitzer and R. Woodcock, 'Yb^{3+}-Er^{3+} glass laser', *Appl. Phys. Lett.*, 6, 45 (1965)

[4.5] E.I. Galant, V.N. Kalinin, S.G. Lunter, A.A. Mak, A.K. Przhevuskii, D.S. Prilezhaev, M.N. Tolstoi and V.A. Fromzelă, 'Stimulated emission from laser-pumped ytterbium- and erbium-activated glasses', *Sov. J. Quantum Electron.*, 6, 1190 (1976)

[4.6] C.C. Robinson and J.T. Fournier, 'Coordination of Yb^{3+} in some inorganic glasses from optical absorption and emission studies', *Chem. Phys. Lett.*, 3, 517 (1969)

[4.7] C.C. Robinson and J.T. Fournier, 'Co-ordination of Yb^{3+} in phosphate, silicate, and germanate glasses', *J. Phys. Chem. Solids*, 31, 895 (1970)

[4.8] J.T. Fournier and R.H. Bartram, 'Inhomogeneous broadening of the optical spectra of Yb^{3+} in phosphate glass', *J. Phys. Chem. Solids*, 31, 2615 (1970)

[4.9] J.E. Townsend, S.B. Poole and D.N. Payne, 'Solution-doping technique for fabrication of rare-earth-doped optical fibres', *Electron. Lett.*, 23, 329 (1987)

[4.10] W.F. Krupke, 'Induced-emission cross section in neodymium laser glasses', *IEEE J. Quantum Electron.*, QE-10, 450 (1974)

[4.11] R.M. Percival, M.W. Phillips, D.C. Hanna and A.C. Tropper, 'Characterization of spontaneous and stimulated emission from praseodymium (Pr^{3+}) ions doped into a silica-based monomode optical fiber', *IEEE J. Quantum Electron.*, 25, 2119 (1989)

[4.12] O. Svelto, 'Principles of Lasers', 3rd Edition, Plenum Press (1989)

[4.13] E. Nakazawa and S. Shinoya, 'Cooperative luminescence in $YbPO_4$', *Phys. Rev. Lett.*, 25, 1710 (1970)

[4.14] D.C. Hanna, R.G. Smart, P.J. Suni, A.I. Ferguson and M.W. Phillips, 'Measurement of fibre laser losses via relaxation oscillations', *Opt. Comm.*, 68, 128 (1988)

[4.15] J.R. Armitage, R. Wyatt, B.J. Ainslie and S.P. Craig-Ryan, 'Efficient 980nm operation of an Yb^{3+} doped silica fibre laser', *Electron. Lett.*, 25, 298 (1989)

[4.16] I.P. Alcock, A.I. Ferguson, D.C. Hanna and A.C. Tropper, 'Tunable, continuous-wave neodymium-doped monomode-fiber laser operating at 0.900-0.945 and 1.070-1.135μm', *Opt. Lett.*, 709 (1986)

[4.17] W.V. Sorin and S.A. Newton, 'Tunable single-mode output of a multimode laser in a tunable fibre grating external cavity', *Electron. Lett.*, 390 (1987)

[4.18] R. Wyatt, 'High-power broadly tunable erbium-doped silica fibre laser', *Electron. Lett.*, 25, 1498 (1989)

[4.19] M.J.F. Digonnet and H.J. Shaw, 'Analysis of a tunable single mode optical fiber coupler', *IEEE J. Quantum Electron.*, QE-18, 746 (1982)

[4.20] C.A. Millar, I.D. Miller, D.B. Mortimore, B.J. Ainslie and P. Urquhart, 'Fibre laser with adjustable fibre reflector for wavelength tuning and variable output coupling', *IEE Proc.J.* 135, 303 (1988)

[4.21] Y. Chaoyu, P. Jiangde and Z. Bingkun, 'Tunable Nd^{3+}-doped fibre ring laser', *Electron. Lett.*, 101 (1989)

[4.22] D.N. Payne, A.J. Barlow and J.J. Ramskov Hansen, 'Development of low- and high-birefringence optical fibers', *IEEE J. Quantum Electron.*, QE-18, 477 (1982)

[4.23] F.P. Kapron, N.F. Borrelli and D.B. Beck, 'Birefringence in dielectric optical waveguides', *IEEE J. Quantum Electron.*, QE-8, 222 (1972)

[4.24] R. Ulrich, S.C. Rashleigh and W Eickhoff, 'Bending-induced birefringence in single-mode fibers', *Opt. Lett.*, 5, 273 (1980)

[4.25] R. Ulrich and A. Simon, 'Polarization optics of twisted single-mode fibers', *Appl. Opt.*, 18, 2241 (1979)

[4.26] H.C. Lefevre, 'Single-mode fibre fractional wave devices and polarisation controllers', *Electron. Lett.*, 16, 778 (1980)

[4.27] B.G. Koehler and J.E. Bowers, 'In-line single-mode fiber polarization controllers at 1.55, 1.30, and 0.63μm', *Appl. Opt.*, 24, 349 (1985)

[4.28] M.J.F. Digonnet, 'Theory of superfluorescent fiber lasers', *J. Lightwave Technol.*, LT-4, 1631 (1986)

[4.29] C.S. Wang, W.H. Cheng, C.J. Hwang, W.K. Burns and R.P Moeller, 'High-Power low-divergence superradiance diode', *Appl. Phys. Lett.*, 41, 587 (1982)

[4.30] G.A. Alphonse, D.B. Gilbert, M. Harvey, E. Depiano and M. Ettenberg, 'High power superluminescent diodes', *OFC/IOOC '87*, Reno, Nevada, USA (1987)

[4.31] M.J.F. Digonnet and K. Liu, 'Analysis of a 1060-nm Nd:SiO_2 superfluorescent fiber laser', *J. Lightwave Technol.*, 7, 1009 (1989)

[4.32] H. Po, F. Hakimi, R.J. Mansfield, B.C. McCollum, R.P. Tumminelli and E. Snitzer, 'Neodymium fiber laser at 0.905, 1.06 and 1.4μm', in *Proc. OSA Meeting*, Seattle, WA, USA (1986)

[4.33] K. Liu, M. Digonnet, H.J. Shaw, B.J. Ainslie and S.P. Craig, '10mW superfluorescent single-mode fibre source at 1060nm', *Electron. Lett.*, 23, 1320 (1987)

[4.34] I.N. Duling III, W.K. Burns and L. Goldberg, 'High-power superfluorescent fiber source', *Opt. Lett.*, 15, 33 (1990)

[4.35] K. Kubodera and K. Otsuka, 'Single-transverse-mode $LiNdP_4O_{12}$ slab waveguide laser', *J. Appl. Phys.*, 50, 653 (1979)

[4.36] A.W. Snyder and J.D. Love, 'Optical Waveguide Theory', Chapman and Hall (1983)

[4.37] D. Gloge, 'Weakly guiding fibres', *Appl. Opt.*, 10, 2252 (1971)

[4.38] I.P. Alcock, A.I. Ferguson D.C. Hanna and A.C. Tropper, 'Q-switched operation of a neodymium-doped monomode fibre laser', *Electron. Lett.*, 22, 84 (1986)

[4.39] I.P. Alcock, A.C. Tropper, A.I. Ferguson and D.C. Hanna, 'Q-switching, mode-locking and tunable operation around 0.9μm of a neodymium-doped monomode fibre laser', *IEE Proc. J*, 134, 183 (1987)

[4.40] R.J. Mears, L. Reekie, S.B. Poole and D.N. Payne, 'Low threshold tunable CW and Q-switched fibre laser operating at 1.55μm', *Electron. Lett.*, 22, 159 (1986)

[4.41] A.E. Siegman, 'Lasers', Oxford University Press (1986)

[4.42] D.C. Hanna, R.M. Percival, I.R. Perry, R.G. Smart, P.J. Suni, J.E. Townsend and A.C. Tropper, 'Continuous-wave oscillation of a monomode ytterbium-doped fibre laser', *Electron. Lett.*, 24, 1111 (1988)

[4.43] D.C. Hanna, R.M. Percival, I.R. Perry, R.G. Smart, P.J. Suni and A.C. Tropper, 'An ytterbium-doped monomode fibre laser: broadly tunable operation from 1.010μm to 1.162μm and three-level operation at 974nm', *J. Modern Opt.*, 37, 517 (1990)

[4.44] D.C. Hanna, I.R. Perry, R.G. Smart, P.J. Suni, J.E. Townsend and A.C. Tropper, 'Efficient superfluorescent emission at 974nm and 1040nm from an Yb-doped fiber', *Opt. Comm.*, 72, 230 (1989)

CHAPTER 5

YTTERBIUM-SENSITISED ERBIUM-DOPED FIBRE

5.1 Introduction

The recent revolution in optical communications technology has stimulated immense interest in the development of the sources and amplifiers required for this type of data transmission. Of particular interest are erbium-doped glass lasers, since the operating wavelength of ≈ 1.55μm lies within the third transmission window of silica-based fibres, where typical losses are only ≈ 0.25dB/km. This compares very favourably with the 0.5dB/km loss at 1.3μm, where most fibre-optic communications systems currently operate to exploit the presence of a zero dispersion point at this wavelength. However, so-called dispersion-shifted fibres can also be made with zero dispersion at 1.55μm, where the lower transmission losses make this longer wavelength more suitable for long distance and submarine cables.

Erbium-doped fibres, rather than bulk glass devices, are obviously well suited as the sources and amplifiers for a communications system operating at 1.55μm due to their low threshold operation (or high gain for a given input pump power). The presence of absorption bands at wavelengths attainable by laser diodes is a further attraction, and indeed Er^{3+}-doped fibre lasers and amplifiers have been extensively reported in the literature [5.1-5.19]. It is possible to achieve inversion using several pump wavelengths [5.9] since there are four main absorption bands, centred at 528nm, 807nm, 980nm and 1480nm. From a practical device point of view, diode pumping is to be preferred, which rules out the 528nm band, although high gain (1.36dB/mW launched) amplifiers have been demonstrated using a pump wavelength of 532nm [5.9] and high power (≈ 100mW) tunable output [5.10] has been reported for a pump wavelength of 514.5nm. Laser action and amplification (2.2dB/mW launched) has also been demonstrated using the 980nm pump band [5.9, 5.11, 5.12, 5.13]. This longer pump wavelength has the advantage of ensuring good overlap between the pump and signal modes since the fibre can be made single mode at both wavelengths, and in addition it is free from the pump excited state absorption [5.20] encountered at ≈ 0.8μm, making it possibly the optimum pump wavelength for the erbium-doped system. Laser diodes operating at 980nm are now available, *e.g.*, GaAsSb-AlGaAsSb [5.21] and strained quantum well structure InGaAs semiconductors [5.22], and are viable pump sources but nonetheless still an emerging and relatively untried technology. InGaAsP laser diodes at ≈ 1.5μm, with their well established technology, are also under intensive investigation [5.14], although there are drawbacks in that this is a pump wavelength known to suffer from amplifier noise in the Er^{3+} system and also involves a relatively high power requirement. Er^{3+}-doped fibre lasers and amplifiers pumped through the ≈ 0.8μm pump band are attractive since this band is accessible by GaAlAs laser diodes with their advantages of being widely available, cheap and reliable. Slope efficiencies of 13.5% and output powers of 8mW have been reported when pumped with a diode array at 806nm [5.15], and thresholds as low as 1mW absorbed have been observed [5.16]. The peak absorption wavelength at 807nm is, however, prone to excited state absorption from the upper laser level, and although longer or shorter pump wavelengths may reduce this problem, the fall-off in absorption prevents this course of action if efficiency is a prime concern.

One means of circumventing the restriction on the choice of pump wavelength in the GaAlAs diode laser wavelength region is to co-dope, or sensitise, the Er^{3+}-doped silica host with a second rare-earth possessing absorbing transitions at more suitable and, hopefully, less restrictive wavelengths. The excitation of the co-dopant is then transferred to the laser active ions either resonantly or, if the energy mismatch between the relevant levels is large, by a phonon-assisted process. Energy transfer occurs through a dipole-dipole interaction which is too small to significantly affect the energy level structure but does allow energy to be transferred nonradiatively to another unexcited ion which may then radiate the energy. The dipole-dipole interaction transfer rate varies as r^{-6}, where *r* is the mean ion separation between the "donor" and "acceptor" ion species, and this dependence on separation suggests that clustering of dopant ions can be beneficial, since the localised mean ion separation will be decreased from the global mean. The transfer of energy from donor to acceptor in solid state materials was first treated by Förster [5.23] and Dexter [5.24], and more recently a comprehensive study was made by Wright [5.25].

One well known suitable co-dopant for an energy transfer scheme involving Er^{3+} is Yb^{3+}, since its $^2F_{5/2}$ excited state lies at an energy very close to that of the $^4I_{11/2}$ excited state of Er^{3+}. The first demonstration of laser action of an Yb^{3+}-sensitised Er^{3+}-doped glass laser was by Snitzer and Woodcock [5.26] in 1965, where laser action at 1.5426μm was observed from a xenon flashlamp-pumped silicate glass rod at room temperature. This was also the first demonstration of the three-level laser transition in Er^{3+}, which had previously operated at 1.612μm on its four-level transition at 77K. Subsequent developments led to reports of laser-pumped operation [5.27, 5.28, 5.29], and then in 1988 Snitzer *et al.* reported an Yb^{3+}-Er^{3+} fibre laser [5.30], closely followed by other reports of laser action in Yb^{3+}-Er^{3+} fibres pumped with Nd:YAG lasers at 1.06μm [5.31, 5.32] and also in the 0.8μm region [5.33, 5.34].

The broad absorption band of the $^2F_{7/2} \rightarrow {}^2F_{5/2}$ transition in Yb^{3+} allows pumping over a wide range of wavelengths, from around 0.8μm to 1.2μm. The energy levels for Yb^{3+} and Er^{3+} are shown in Fig.5.1. Excitation of the $^2F_{5/2}$ level in Yb^{3+} allows resonant energy transfer to take place to the $^4I_{11/2}$ level in Er^{3+}, followed by rapid nonradiative decay to the metastable $^4I_{13/2}$ level. Direct absorption by the Er^{3+} ions at 0.98μm can also take place into $^4I_{11/2}$ and at around 0.8μm into $^4I_{9/2}$, again followed in both instances by rapid nonradiative decay to $^4I_{13/2}$. Laser action may then take place from $^4I_{13/2}$ to the $^4I_{15/2}$ ground state. The transition is three-level in nature, so that at least half of the ground state population must be excited to achieve inversion between the excited state and the lowest ground state Stark level and, as with any three-level transition, the gain from the bleached section of fibre must exceed the reabsorption loss in any unbleached region in addition to the fixed resonator losses, imposing an optimum fibre length for a given input pump power.

The presence of excited state absorption from the upper laser level is a particular problem since the three-level nature of the

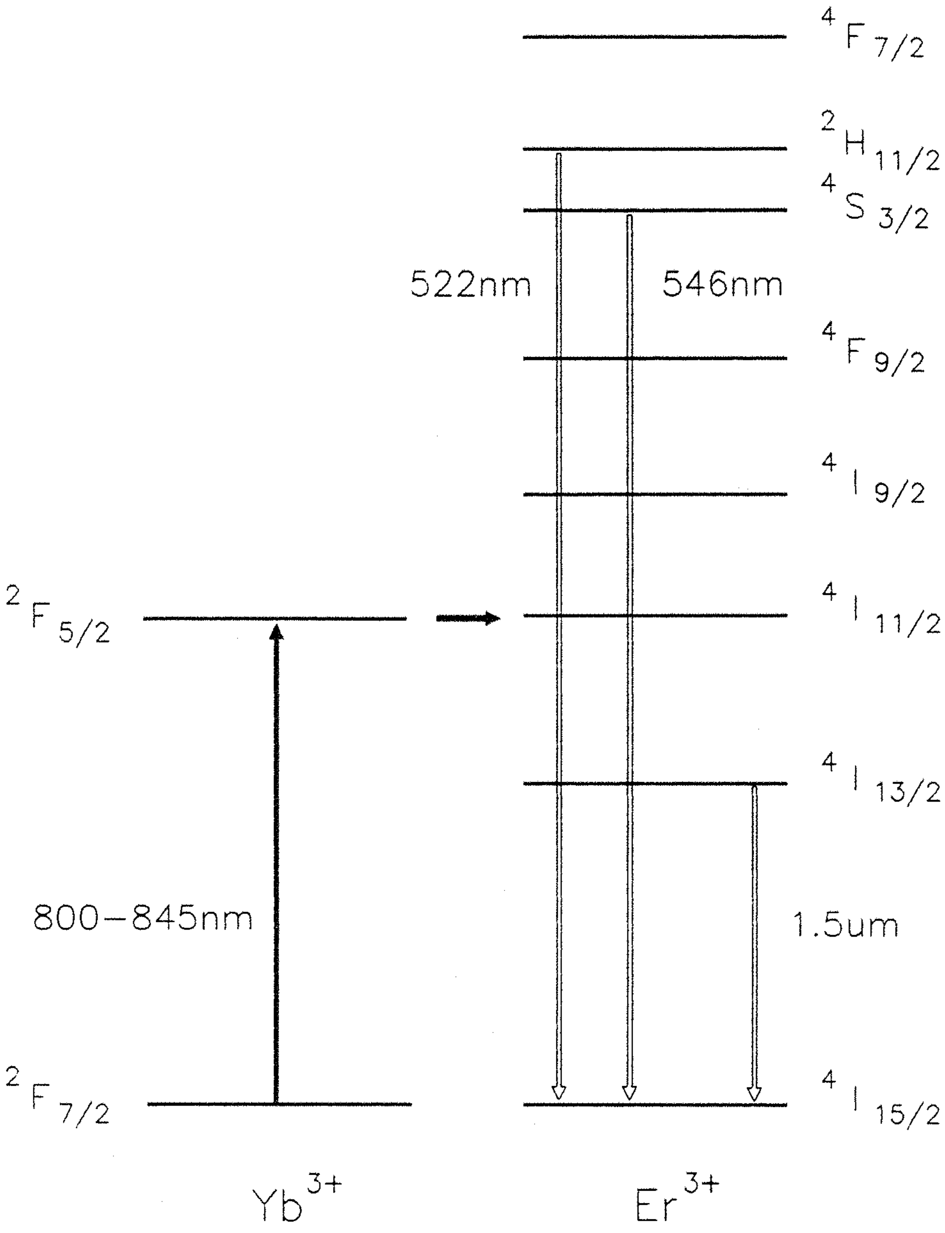

Fig.5.1 Energy levels for Yb-Er-doped fibre

amplifying transition requires a large population in this level, and the subsequent depletion of this population by ESA makes inefficient use of the available pump energy. For pump wavelengths in the GaAlAs diode laser region this is particularly relevant at around 0.8μm since this wavelength corresponds to direct absorption from the $^4I_{13/2}$ metastable level into $^2H_{11/2}$ and $^4S_{3/2}$. In addition, $^2H_{11/2}$ is also populated thermally from the lower lying $^4S_{3/2}$ level. Radiative decay to the ground state from $^2H_{11/2}$ and $^4S_{3/2}$ yields fluorescence at 522nm and 546nm, respectively. The green-emitting levels may also be populated by a two step resonant energy transfer process [5.35], whereby an excited Yb^{3+} ion transfers energy resonantly to the $^4I_{11/2}$ level in Er^{3+}, followed by a second resonant transfer exciting the Er^{3+} ion from $^4I_{11/2}$ to $^4F_{3/2}$, from where rapid nonradiative decay takes place to $^4S_{3/2}$.

The potential for extending the range of possible diode-compatible pump wavelengths of Er^{3+}-doped fibre lasers by the incorporation of Yb^{3+} as a co-dopant has been investigated and is described in this chapter. The effect of excited state absorption on the threshold and slope efficiency is also described, and an optimum wavelength for GaAlAs diode laser pumping is identified, using a Styryl 9M dye laser as a pump source to emulate diode laser wavelengths.

5.2 Spectroscopy

A silica-based fibre was fabricated by the solution doping technique [5.36], with the the core index raised by 5 mole % Al_2O_3 and 5 mole % P_2O_5. This inclusion of aluminium and phosphorus also serves to improve the rare-earth ion solubility and prevent devitrification [5.37].The Yb^{3+} and Er^{3+} dopants were incorporated in the ratio of 20:1 by weight, such that the fibre core contained 1.70 wt% Yb (6000ppm) and 0.08 wt% Er (300ppm). To ensure single transverse mode operation at the expected laser wavelength of ≈ 1.55μm and good launch efficiency for the ≈ 800nm pump light, the fibre was designed to have an LP_{11} cut off wavelength of 1.5μm. The core radius was 2.3μm and the numerical aperture was 0.25.

The fibre was end pumped with a Coherent 599 Styryl 9M dye laser at wavelengths in the range 795nm to 880nm. The previously reported excited state absorption [5.20] was evidenced by a green fluorescence from the side of the fibre over much of this pumping range, and was most noticeable for pump wavelengths of 800nm and ≈ 840nm. This ESA will be considered in more detail below.

In the absence of a reliable absorption spectrum the absorption coefficient was measured at several discrete wavelengths by cutting back the fibre from ≈ Im to ≈ 0.4m while monitoring the unabsorbed pump power. This also allowed the overall launch efficiency (ratio of launched power to power incident on the launch objective) to be found. During these measurements the input end of the fibre was butted against a high reflector (at 1.55μm) to simulate the launch conditions encountered under laser operating conditions. Table 5.1 shows the attenuation coefficient α versus the pump wavelength. The pump power was maintained below the saturation level for each wavelength investigated by ensuring that the unabsorbed pump power was directly proportional to the input power.

Pump Wavelength (nm)	α (m^{-1})
800	1.42
810	1.19
820	1.34
825	1.39
830	1.53
835	1.92
840	3.08
845	3.76

Table 5.1

The effect of the Yb^{3+} co-dopant is immediately obvious when compared to an absorption spectrum for a fibre doped only with Er^{3+} [5.34], where the absorption centred at ≈ 0.8μm is spectrally narrow (about 20nm). The presence of Yb^{3+} greatly extends the effective absorption band to longer wavelengths within reach of commercially available GaAlAs laser diodes. The overall launch efficiency at 825nm was 0.43 which, taking into account the high reflector and microscope objective transmissions at 825nm of 0.75 and 0.90 respectively, gives a coupling efficiency (ratio of launched power to power incident on the fibre end face) of about 65%.

Fluorescence was observed in the 1.5μm region for the range of pump wavelengths used, but the side light signal was too weak to be adequately discernible above noise. Instead, the guided end light fluorescence was used to record the spectrum, although it should be noted that the three-level nature of the $^4I_{13/2} \rightarrow {}^4I_{15/2}$ transition means that some distortion by reabsorption in the ground state multiplet can be expected. A 0.7m length of the fibre was pumped with 150mW at 820nm. The end light fluorescence was focused onto the input slit of a 0.25m monochromator containing a grating blazed for 1μm. The signal from the output slit was detected with a germanium photo-diode as the fluorescence wavelength was scanned by a stepping motor drive fixed to the monochromator. The resulting spectrum is shown in Fig.5.2, where the peak of the fluorescence appears at 1.534μm with a full width at half maximum of 40nm.

An excitation spectrum was recorded by setting the monochromator to 1.55μm and monitoring the photo-diode signal as the pump wavelength was varied between 785nm and 880nm with a second stepping motor drive fixed to the dye laser wavelength control. The end light excitation spectrum is shown in Fig.5.3. This has not been corrected for the dye laser output power spectrum, which has a peak at 825nm using the standard set of optics, since the uncorrected spectrum is more applicable in the selection of pump wavelength when power fall off with wavelength is a factor. The excitation spectrum shows a maximum 1.55μm fluorescence yield for a pump wavelength of 820nm.

The upconverted fluorescence arising from pump ESA was strong enough to be observed in side light. An arrangement similar to that used for side light measurements in ytterbium was employed, with a fibre bundle located near to the input end of the fibre (where the signal is strongest) transferring the fluorescence to the monochromator. The monochromator was fitted with a grating blazed for 500nm and a photomultiplier tube was used to detect the visible fluorescence. The pump wavelength was 840nm with about 200mW incident on the launch optics. The side light spectrum is shown in Fig.5.4, which shows fluorescence peaks located at 522nm and 546nm, corresponding to emission to the $^4I_{15/2}$ ground state from $^2H_{11/2}$ and $^4S_{3/2}$, respectively. An excitation spectrum for this visible emission is shown in Fig.5.5, and identifies 800nm and ≈ 840nm as the most significant wavelengths for pump ESA in the 0.8μm region, consistent with ESA from $^4I_{13/2}$ into $^2H_{11/2}$ at about 800nm and $^4S_{3/2}$ at about

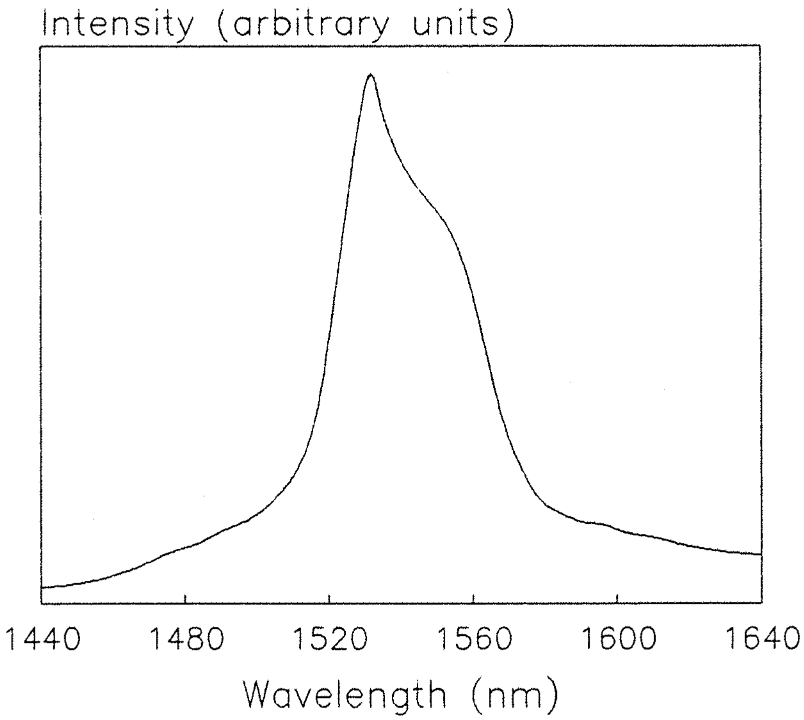

Fig.5.2 End light fluorescence spectrum for 70cm fibre pumped at 820nm

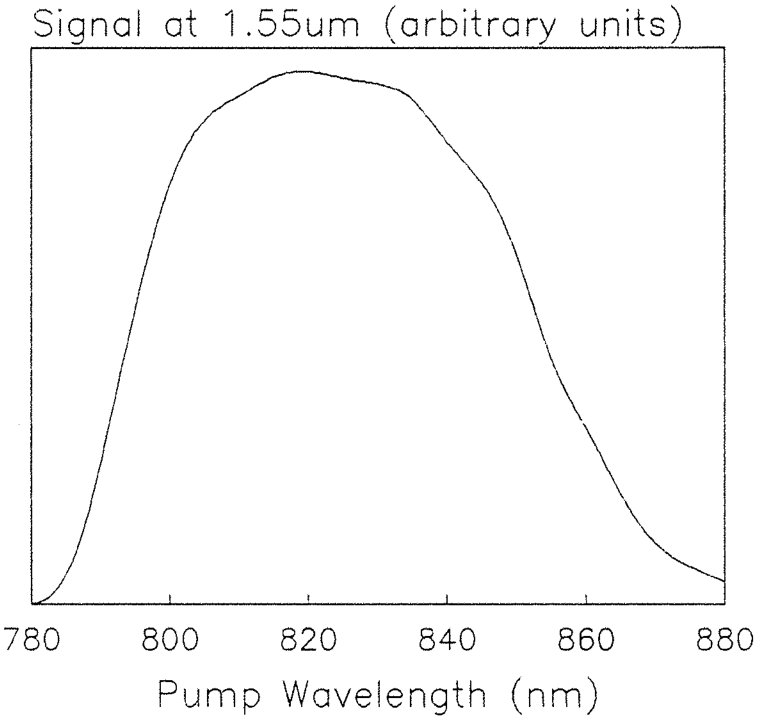

Fig.5.3 Excitation spectrum for emission at 1.55μm

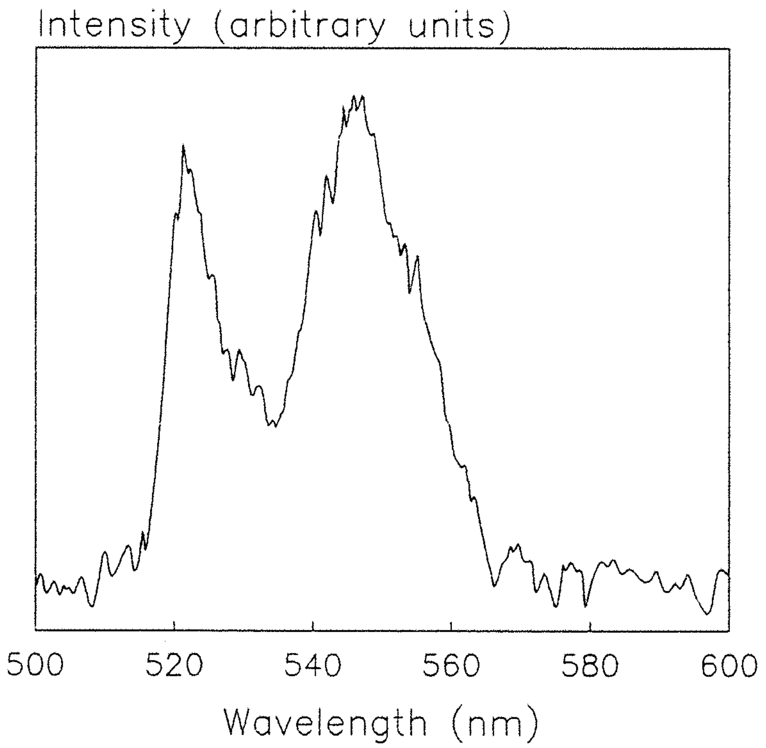

Fig.5.4 Side light fluorescence spectrum in the visible region for 840nm pump wavelength

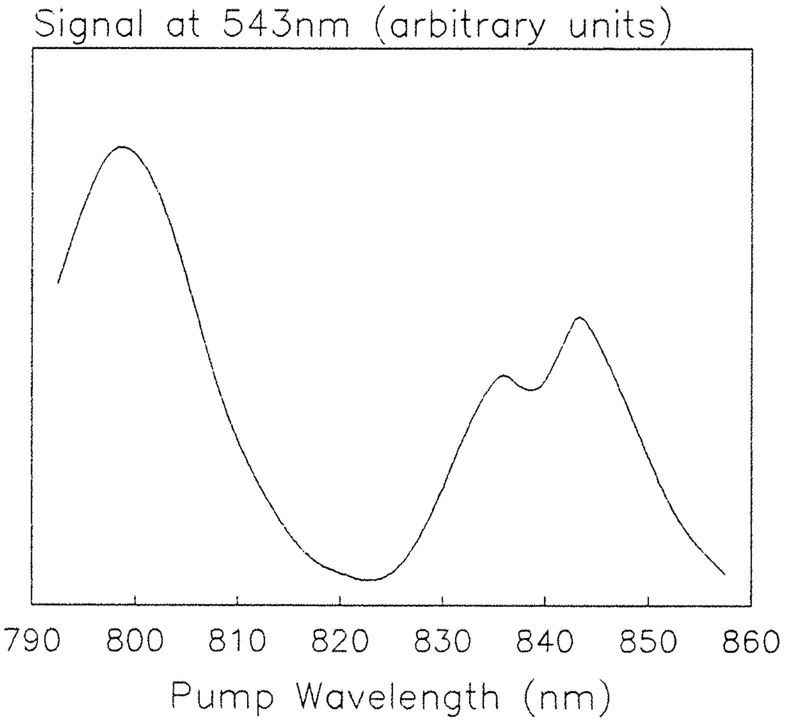

Fig.5.5 Excitation spectrum for emission at 543nm

840nm.

Fluorescence lifetimes were measured by interrupting the pump beam with a mechanical chopper and observing the decay of the fluorescence signal on the appropriate detector in combination with a digital storage oscilloscope. The visible emission at 546nm was measured with a photomultiplier tube in end light from a 0.3m fibre, since the side light signal was too small for this measurement. The non-exponential decay took ≈ 40μs to fall from 90% to 10% of its uninterrupted level. However, the detection system response time, found by observation of the signal decay of chopped output pump light, was also ≈ 40μs, and the visible emission lifetime measurement is therefore detector limited. The build-up time for the 546nm emission to reach steady state under uninterrupted pumping was about 25-30ms. The fluorescence decay of the $^4I_{13/2} \rightarrow {}^4I_{15/2}$ erbium transition giving fluorescence at 1.528μm (the fluorescence peak in the 0.3m fibre) measured in end light was single exponential with a e^{-1} lifetime of 9.6ms. The detector used here was a germanium photo-diode, and the system response had a 90%-10% decay time of 175μs. Using this same detection system, fluorescence at 974nm from the $^2F_{5/2} \rightarrow {}^2F_{7/2}$ transition in the ytterbium co-dopant could be detected in side light using the fibre bundle. The decay was single exponential with a e^{-1} lifetime of 575μs. These lifetimes are summarised in Table 5.2.

Dopant	Transition	Emission Wavelength (μm)	Lifetime
Er^{3+}	$^4I_{13/2} \rightarrow {}^4I_{15/2}$	1.528	9.6ms
Er^{3+}	$^4S_{3/2} \rightarrow {}^4I_{15/2}$	0.546	≤ 40μs
Yb^{3+}	$^2F_{5/2} \rightarrow {}^2F_{7/2}$	0.974	575μs

Table 5.2

An estimate of the transfer efficiency from Yb^{3+} to Er^{3+} may be made by comparison of the fluorescence lifetime of Yb^{3+} in the doubly-doped fibre with that in a fibre doped only with Yb^{3+}. The transfer efficiency η_T is given by

$$\eta_T = (\tau_s)^{-1} (\tau_s - \tau_d) \tag{5.1}$$

where τ_s is the lifetime in the singly-doped fibre and τ_d is the lifetime in the doubly-doped fibre. From Chapter 4, τ_s = 710μs and from Table 5.2, τ_d = 575μs, giving η_T = 0.2. Clearly, a substantial fraction of ions excited to the $^2F_{5/2}$ level in Yb^{3+} decay back to its $^2F_{7/2}$ ground state without cross-relaxing to Er^{3+}. The efficiency could probably be improved by using higher doping levels to increase the transfer rate by reducing the average ion separation.

5.3 Laser Action at 1.5μm

Initial investigations into the laser performance of the Yb^{3+}-Er^{3+}-doped fibre were made with a 0.7m sample (approximately one absorption length at a pump wavelength of 800nm) butted against dielectric mirrors in a Fabry-Perot cavity. The input mirror was ≥99% reflective at 1.55μm but varied in reflectivity over the range of pump wavelengths, from 87% at 800nm to 60% at 845nm. The output coupler had a transmission of 28% at 1.55μm and was 22% reflective over the pump range. This choice of output coupler was dictated simply by the availability of mirrors with transmission at 1.55μm, the only other suitable mirror being another high reflector. The fibre laser wavelength was 1.564μm for this 0.7m fibre.

With a tunable pump source, it was possible to pump the fibre at a range of wavelengths and observe the variation in both fibre laser slope efficiency and threshold power. The lower wavelength limit was set at 800nm, since the Yb^{3+} absorption is negligible for shorter wavelengths. An upper limit of 845nm reflected the maximum wavelength then achieveable from commercially available GaAlAs diode lasers (simulated by the Styryl 9M dye laser).

Fibre laser output powers were measured on a thermopile power meter with a filter to block the unabsorbed pump light. The pump power was varied from zero to a maximum of 150mW. Thresholds were measured by reducing the pump power until laser action (indicated by the presence of relaxation oscillations) ceased. These relaxation oscillations were induced by interrupting the pump beam with a mechanical chopper and observed with a germanium photo-diode in place of the power meter. Absorbed pump powers were calculated by subtracting the unabsorbed pump power from the launched power (determined using the launch efficiencies found from cut back measurements made at several wavelengths). The threshold measurements were repeated for a fibre length of 0.4m. Slope efficiency measurements were not possible with this shorter fibre due to the low fibre laser power imposed by the reduced pump absorption in this shorter length.

The variation of absorbed threshold power with pump wavelength is shown in Fig.5.6 for the two lengths. In both cases there is a region between about 820nm and 830nm for which the threshold is minimised, the lowest measured value being 5mW absorbed in the 70cm length for a pump wavelength of 825nm. The thresholds increase gradually as the wavelength is decreased from this point, but the effect is much more marked for longer wavelengths, where the thresholds for both fibres rise rapidly to a peak at a pump wavelength of ≈ 840nm and then appear to fall off as the wavelength is increased further. This behaviour is reflected in the variation of slope efficiency (with respect to absorbed power) with pump wavelength, shown in Fig.5.7 for the 0.7m fibre. The slope efficiency shows a peak of 8.5% for a pump wavelength of 830nm, falling off rapidly for shorter and longer wavelengths, and the peak in threshold at 840nm is manifested as a local dip in the slope efficiency at the same wavelength. The degraded performance, particularly at a pump wavelength of 840nm but also in the region of 800nm, is consistent with the excitation spectrum for upconverted emission (Fig.5.5), indicating clearly that pump induced ESA at these two wavelengths is responsible for increased thresholds and decreased slope efficiencies compared to the performance when pumped at ≈ 825nm, where ESA is not as effective at removing population from the upper laser level. This wavelength dependence is illustrated further in Fig.5.8, which shows the laser characteristics for pump wavelengths of 800nm, 825nm and 840nm for the 0.7m fibre. The slope efficiencies (with respect to absorbed power) at 800nm, 825nm and 840nm are 6.3%, 8.3% and 4.5%, respectively.

It was also possible to achieve laser action on the $^2F_{5/2} \rightarrow {}^2F_{7/2}$ ytterbium transition by replacing the input mirror with a high reflector (>99%) in the range 980-1120nm and 90% transmitting at the 835-840nm pump wavelength. The output coupler had a transmission of 10% at the Yb^{3+} laser wavelength, and the fibre length remained at

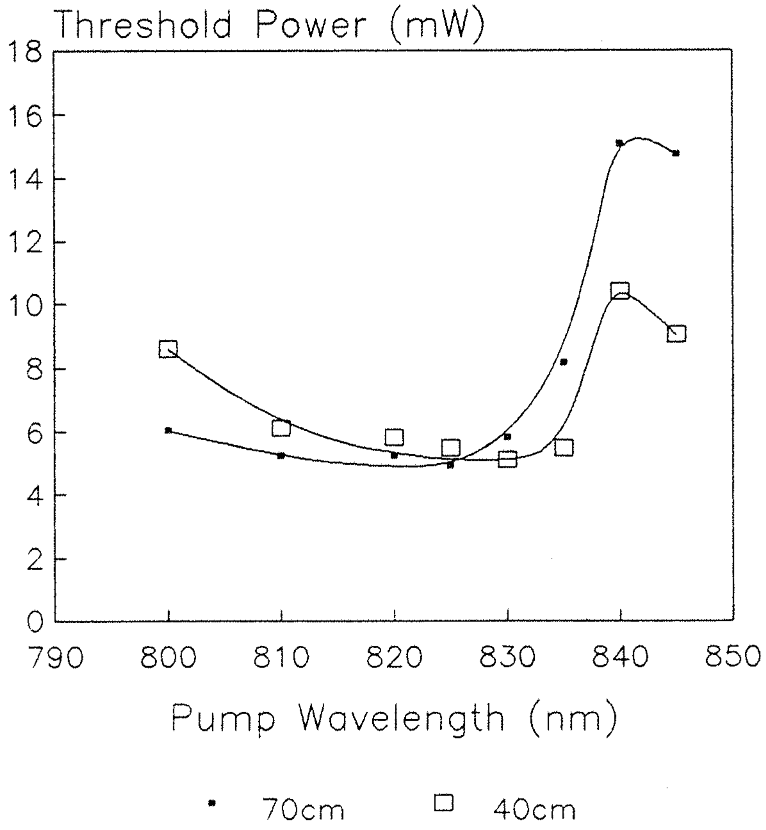

Fig.5.6 Absorbed threshold power versus pump wavelength for fibre lengths of 40cm and 70cm

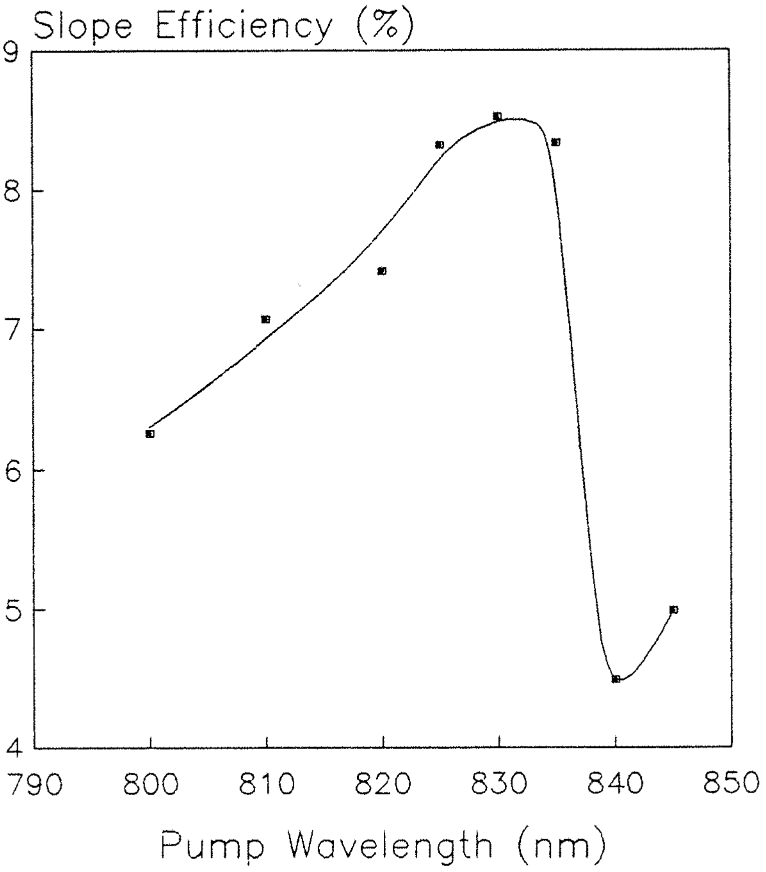

Fig.5.7 Slope efficiency (with respect to absorbed power) versus pump wavelength for a fibre length of 70cm

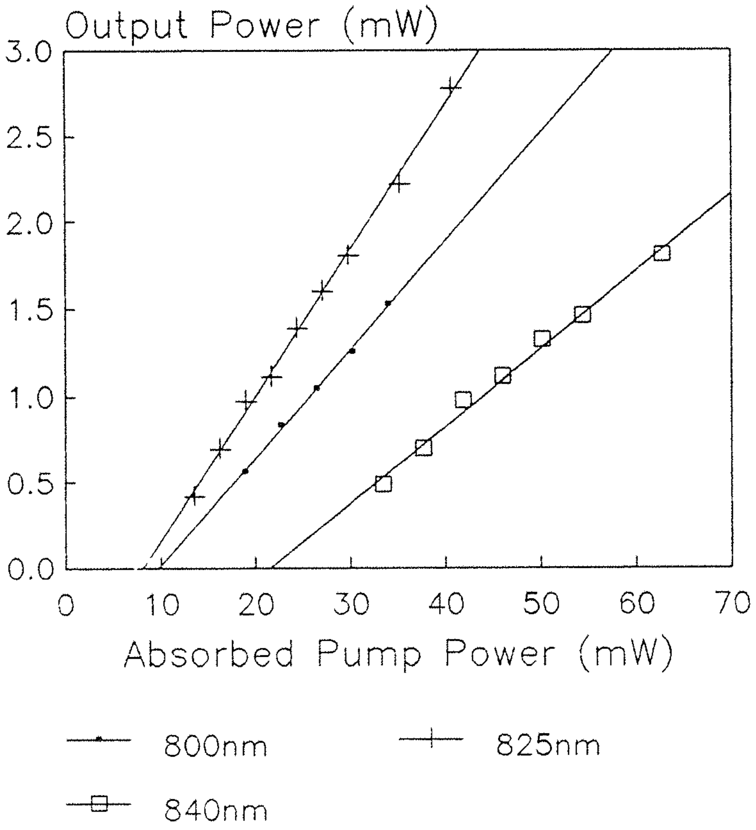

Fig.5.8 Laser characteristic for pump wavelengths of 800nm, 825nm and 840nm

0.7m. The high ytterbium concentration results in high reabsorption losses on the transitions yielding oscillation at 0.974μm and 1.040μm described in Chapter 4. Laser action therefore took place to a higher lying Stark level in the ground state multiplet where the thermal population was low enough to allow oscillation at 1.088μm. Even so, there remained a considerable total cavity loss: relaxation oscillation measurements [5.38] indicated losses of ≈ 50% per pass, and the threshold power incident on the launch objective varied from 30mW for a pump wavelength of 860nm to 100mW for 810nm.

5.4 Tunable Laser Performance

The end light fluorescence spectrum of Fig.5.2 indicates that the erbium transition may be tunable in the region of 1.5-1.6μm. A prism-tuned resonator design similar to that used for the tuning of the ytterbium fibre was set up, the only modifications necessary for the Yb:Er fibre being the removal of the (unnecessary) index-matching cell and a change of mirrors. Two high reflectors (≥99% in the range 1.425μm to 1.640μm) were used to compensate for the losses imposed by the inclusion of an intracavity objective. A 0.7m length of Yb^{3+}-Er^{3+} fibre was pumped at 820nm, where the ESA losses are minimised. A pump power of 180mW (the maximum then available from the dye laser at 820nm) incident on the launch objective was used, with the output fibre laser signal, in the form of a reflection from the prism, analysed by a monochromator (1μm grating) and germanium photo-diode. The tuning curve, shown in Fig.5.9, extends from 1.521μm to 1.562μm, a range of 41nm (173cm^{-1}).

Although laser action was continuous over this range, the spectrum consisted of two prominent emission peaks located at 1.527μm and 1.552μm, as observed by Mears *et al.* [5.1] in singly-doped Er^{3+}-doped fibre and corresponding to peaks in the fluorescence spectrum. Another possible explanation for this preferential oscillation on two wavelengths may be the inclusion of phosphorus pentoxide (P_2O_5) as one of the core constituents. It has been reported [5.11, 5.34] that silica fibres containing Al_2O_3 and P_2O_5 operate on a set of discrete wavelengths corresponding to transitions between a limited number of the Stark components in the ground and excited state. Barnes *et al.* [5.11] suggest only two Stark levels in each of the ground and excited states are involved, giving emission

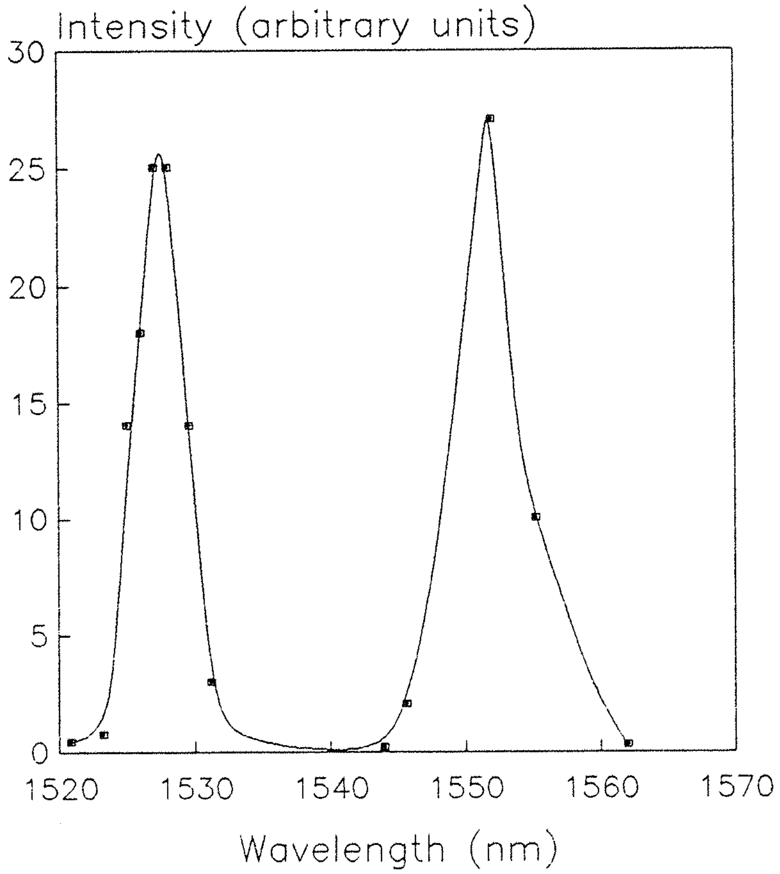

Fig.5.9 Tuning curve for 70cm fibre pumped at 820nm

wavelengths of 1.53μm, 1.57μm and 1.60μm. In comparison, GeO_2-SiO_2 fibres have a more gradual transition of operating wavelength [5.17, 5.18] involving a greater number of Stark levels (changes of operating wavelength are revealed principally by changes in the fibre length so that reabsorption by ground state Stark levels is a factor in determining which transition will dominate). However, it should be noted that continuous tuning has been observed over the range 1.51-1.58μm [5.19] with a fibre containing phosphorus pentoxide, and the reason for the pronounced double peak in the tuning curve described above is likely to be insufficient dispersion by the prism preventing the low gain wavelengths being separated from the high gain wavelengths at the fluorescence peaks which subsequently dominate the emission.

5.5 Concluding Remarks

Laser action in an Er^{3+}-doped silica fibre using Yb^{3+} as a sensitising co-dopant has been described. The incorporation of the Yb^{3+} co-dopant enabled the $^4I_{13/2}$ upper laser level in Er^{3+} to be populated at pump wavelengths which are inefficient or incapable of achieving inversion in a fibre doped only with Er^{3+}. Pump wavelengths in the range 800-845nm have been investigated using a tunable dye laser to provide the wavelengths currently available from GaAlAs diode lasers, since these are an established technology and are the cheapest and most reliable of the many possible pump sources for erbium fibre lasers and amplifiers. Laser action at 1.564μm has been demonstrated with thresholds easily attainable by diode lasers (5-15mW absorbed). A minimum in the threshold (5mW) was identified for pump wavelengths in the range 820-830nm for fibre lengths of 40cm and 70cm, and is attributed to a significant reduction in the pump induced excited state absorption. This ESA is apparent at pump wavelengths of 800nm and 840-850nm where it is responsible for an increase in the threshold power, and results in visible emission at 522nm and 546nm. The slope efficiency for the laser performance also revealed the effects of ESA, with a measured maximum of 8.5% for pumping a 70cm fibre at 830nm and a minimum of 4.5% at 845nm. It should be noted that the fibre laser was not optimised with respect to fibre length or output coupling, and so it is difficult to compare the results with those for fibres doped only with Er^{3+} where the performance has been optimised to some extent. However, later studies [5.34] comparing Er^{3+} and Yb^{3+}-Er^{3+} fibre lasers revealed no significant difference in performance for pumping at 810nm. The benefit of the co-dopant is nonetheless readily apparent since the range of possible diode-compatible pump wavelengths is greatly increased, and ESA may be significantly reduced by choice of the appropriate wavelength.

When the experiments described in this chapter were performed, diode lasers at 980nm were not a practical contender for the selection of a pump source. The identification of 980nm as perhaps the optimum pump wavelength for Er^{3+}-doped fibres, and recent developments in diode laser technology, mean that GaAlAs diode laser pumping in the 0.8μm region will probably give way to sources at 980nm. If 980nm diodes continue to be unreliable or suffer from short operational lifetimes, then perhaps Yb^{3+} will prove useful once more, since its three-level laser transition at 974nm would be suitable as a pump source for Er^{3+}-doped fibre lasers and amplifiers.

References

[5.1] R.J. Mears, L. Reekie, S.B. Poole and D.N. Payne, 'Low threshold tunable CW and Q-switched fibre laser operating at 1.55μm', *Electron. Lett.*, 22, 159 (1986)

[5.2] P.L. Scrivener, E.J. Tarbox and P.D. Maton, 'Narrow linewidth tunable operation of Er^{3+}-doped single-mode fibre laser', *Electron. Lett.*, 25, 549 (1989)

[5.3] C.G. Atkins, J.F. Massicott, J.R. Armitage, R. Wyatt, B.J. Ainslie and S.P. Craig-Ryan, 'High-gain, broad spectral bandwidth erbium-doped fibre amplifier pumped near 1.5μm', *Electron. Lett.*, 25, 910 (1989)

[5.4] R.J. Mears, L. Reekie, I.M. Jauncey and D.N. Payne, 'Low-noise erbium-doped fibre amplifier operating at 1.54μm', *Electron. Lett.*, 23, 1026 (1987)

[5.5] E. Desurvire, J,R. Simpson and P.C. Becker, 'High-gain erbium-doped travelling-wave fibre amplifier', *Opt. Lett.*, 12, 888 (1987)

[5.6] T.J. Whitley, 'Laser diode pumped operation of Er^{3+}-doped fibre amplifier', *Electron. Lett.*, 24, 1537 (1988)

[5.7] R.I. Laming, P.R. Morkel, D.N. Payne and L. Reekie, 'Noise in erbium-doped fibre amplifiers', *Proc. ECOC '88*, Brighton, UK (1988)

[5.8] T.J. Whitley and T.G. Hodgkinson, '1.54μm Er^{3+}-doped fibre amplifier optically pumped at 807nm', *Proc. ECOC '88*, Brighton, UK (1988)

[5.9] R.I. Laming, M.C. Farries, P.R. Morkel, L. Reekie and D.N. Payne, 'Efficient pump wavelengths of erbium-doped fibre optical amplifier', *Electron. Lett.*, 25, 12 (1989)

[5.10] M.S O'Sullivan, J. Chrostowski, E. Desurvire and J.R. Simpson, 'High-power narrow-linewidth Er^{3+}-doped fiber laser', *Opt. Lett.*, 14. 438 (1989)

[5.11] W.L. Barnes, P.R. Morkel, L. Reekie and D.N. Payne, 'High-quantum-efficiency Er^{3+} fiber lasers pumped at 980nm', *Opt. Lett.*, 14, 1002 (1989)

[5.12] M. Yamada, M. Shimizu, T. Takeshita, M. Okayasu, M. Horiguchi, S. Uehara and E. Sugita, 'Er^{3+}-doped fiber amplifier pumped by 0.98μm laser diodes', *IEEE Photon. Tech. Lett.*, 1, 422 (1989)

[5.13] R.I. Laming, V. Shah, L. Curtis, R.S. Vodhanel, F.J. Favire, W.L. Barnes, J.D. Minelly, D.P. Bour and E.J. Tarbox, 'Highly efficient 978nm diode pumped erbium-doped fiber amplifier with 24dB gain', *Proc. IOOC '89*, paper 20PDA-4 (1989)

[5.14] K. Iwatsuki, 'Er-doped superfluorescent fiber laser pumped by 1.48μm laser diode', *IEEE Photon. Tech. Lett.*, 2, 237 (1990)

[5.15] R. Wyatt, B.J. Ainslie and S.P. Craig, 'Efficient operation of an array pumped Er^{3+}-doped silica fibre laser at 1.5μm', *Electron. Lett.*, 24, 1362 (1988)

[5.16] C.A. Millar, I.D. Miller, B.J. Ainslie, S.P. Craig and J.R. Armitage, 'Low-threshold CW operation of an erbium-doped fibre laser pumped at 807nm wavelength', *Electron. Lett.*, 23, 865 (1987)

[5.17] Y. Kimura and M. Nakazawa, 'Lasing characteristics of Er^{3+}-doped silica fibres from 1553 up to 1603nm', *J. Appl. Phys.*, 64, 516 (1988)

[5.18] L. Reekie, I.M. Jauncey, S.B. Poole and D.N. Payne, 'Diode-laser-pumped operation of an Er^{3+}-doped single-mode fibre laser', *Electron. Lett.*, 23. 1076 (1987)

[5.19] R. Wyatt, 'High power broadly tunable erbium-doped silica fibre laser', *Electron. Lett.*, 25, 1498 (1989)

[5.20] R.I. Laming, S.B. Poole and E.J. Tarbox, 'Pump excited-state absorption in erbium-doped fibers', *Opt. Lett.*, 13, 1084 (1988)

[5.21] K. Sugiyama and H. Saito, 'GaAsSb-AlGaAsSb double heterojunction lasers', *Jpn. J. Appl. Phys.*, 11, 1057 (1972)

[5.22] S. Uehara, M. Horiguchi, T. Takeshita, M. Okayasu, M. Yamada, M. Shimizu, O. Kogure and K. Oe, '0.98μm InGaAs strained quantum well lasers for erbium-doped fiber optical amplifier', *Proc. IOOC '89*, paper 20PDB-11 (1989)

[5.23] T. Förster, 'Zwischenmolekulare energiewanderung und fluoreszenz', *Ann. Physik*, 2, 55 (1948)

[5.24] D.L. Dexter, 'A theory of sensitized luminescence in solids', *J. Chem. Phys.*, 21, 836 (1953)

[5.25] J.C. Wright, 'Up-conversion and excited state energy transfer in rare-earth doped materials', *Top. Appl. Phys.*, 15, 239 (1976)

[5.26] E. Snitzer and R. Woodcock, 'Yb^{3+}-Er^{3+} glass laser', *Appl. Phys. Lett.*, 6, 45 (1966)

[5.27] V.N. Kalinin, A.A. Mak, D.S. Prilezhaev and V.A. Fromzel, 'lasing properties of Yb^{3+} and Er^{3+} glass laser pumped by a laser', *Sov. Phys. Tech. Phys.*, 19, 835 (1974)

[5.28] A.G. Murzin and V.A. Fromzel, 'Maximum gains of laser-pumped glasses activated with Yb^{3+} and Er^{3+} ions', *Sov. J. Quantum Electron.*, 11, 304 (1981)

[5.29] D.C. Hanna, A. Kazer and D.P. Shepherd, 'Active mode-locking and Q-switching of a 1.54μm Er:glass laser pumped by a 1.064μm Nd:YAG laser', *Opt. Comm.*, 65, 355 (1988)

[5.30] E. Snitzer, H. Po, F. Hakimi, R. Tumminelli and B.C. MacCollum, 'Erbium fiber laser amplifier at 1.55μm with pump at 1.49μm and Yb sensitized Er oscillator', *OFC '88, Tech. Digest Series*, 1, OSA, Washington, DC, USA, paper PD2-1 (1988)

[5.31] M.E. Fermann, D.C. Hanna, D.P. Shepherd, P.J. Suni and J.E. Townsend, 'Efficient operation of an Yb-sensitised Er fibre laser at 1.56μm', *Electron. Lett.*, 24, 1135 (1988)

[5.32] G.T. Maker and A.I. Ferguson, '1.56μm Yb-sensitised Er fibre laser pumped by diode-pumped Nd:YAG and Nd:YLF lasers', *Electron. Lett.*, 24, 1160 (1988)

[5.33] D.C. Hanna, R.M. Percival, I.R. Perry, R.G. Smart and A.C. Tropper, 'Efficient operation of an Yb-sensitised Er fibre laser pumped in 0.8μm region', *Electron. Lett.*, 24, 1068 (1988)

[5.34] W.L. Barnes, S.B. Poole, J.E. townsend, L. Reekie, D.J. Taylor and D.N. Payne, 'Er^{3+}-Yb^{3+} and Er^{3+} doped fiber lasers', *J. Lightwave Tech.*, 7, 1461 (1989)

[5.35] M.A. Chamarro and R. Cases, 'Infrared to visible upconversion of Er^{3+} ions in Yb^{3+} doped fluorohafnate glasses', *J. Luminescence*, 46, 59 (1990)

[5.36] J.E. Townsend, S.B. Poole and D.N. Payne, 'Solution-doping technique for fabrication of rare-earth doped optical fibres', *Electron. Lett.*, 23, 329 (1987)

[5.37] S.B. Poole, 'Fabrication of Al_2O_3 co-doped optical fibres by the solution doping technique', in *Tech. Proc. ECOC*, 433, Brighton, UK (1988)

[5.38] D.C. Hanna, R.G. Smart, P.J. Suni, A.I. Ferguson and M.W. Phillips, 'Measurement of fibre laser losses via relaxation oscillations', *Opt. Comm.*, 68, 128 (1988)

CHAPTER 6

THULIUM-DOPED FIBRE PUMPED IN THE VISIBLE TO NEAR I.R. REGION

6.1 Introduction

The first observation of laser action of Tm^{3+} ions in a glass host came in 1967 when Gandy *et al.* [6.1] reported oscillation at 1.85μm in a flashlamp-pumped silicate glass rod cooled to liquid nitrogen temperatures, although lasing in crystal hosts had been established some years previously [6.2, 6.3, 6.4]. A broad fluorescence in silicate glass, ranging from 1.7μm to 2.2μm, was observed with a full width at half maximum of 200nm. Room temperature operation was subsequently achieved in this same referenced work with a triply-activated glass incorporating Yb^{3+} and Er^{3+} in addition to Tm^{3+}, with laser action at 2.015μm. This work is very interesting with respect to fibre laser operation, since the broad fluorescence band indicates the possibility of a wide tuning range in the 2μm region, a wavelength not covered by existing fibre laser systems to date. From a practical device point of view, the potential laser wavelength in the 2μm region, where several molecules have absorption bands, may have applications in molecular spectroscopy and atmospheric physics. Water vapour, for example, has an absorption band centred at 1.88μm, and carbon dioxide has absorption bands centred at 1.96μm, 2.01μm and 2.06μm. In addition, radiation in the 2μm region has uses in eye safe coherent laser radar, and also in medical applications due to the liquid water absorption at 1.93μm. These features, together with the advantages of incorporation into silica fibre, *e.g.*, the broad absorption bands and long interaction length, make thulium a prime candidate for investigation as a fibre laser activator, particularly as one of the absorption bands is readily accessible by GaAlAs diode laser wavelengths.

This chapter describes the spectroscopy and laser action of a Tm^{3+}-doped silica fibre laser, with the laser performance further developed to demonstrate tunable operation.

6.2 Spectroscopy

A fibre preform was fabricated by the solution doping technique [6.5] with a germano-silica core containing a nominal dopant concentration of 840ppm ($\approx 1.9 \times 10^{19}$ ions/cm^3), with the index difference of 0.0064 between the core and cladding yielding a numerical aperture of 0.14. The LP_{11} mode cut off wavelength was 1.7μm. The host glass composition was 94 mole % SiO_2, 6 mole % GeO_2. Fig.6.1 shows the white light absorption spectrum obtained for this preform. The presence of an absorption band located close to 800nm indicates that GaAlAs diode lasers may be suitable as a pump source, so to simulate these devices a Styryl 9M dye laser was used, operating in the 790-820nm region. The energy level diagram derived from the absorption measurements is shown in Fig.6.2 (the $^1D_2$ level was located by its emission wavelength. See Chapter 7 for details).

There is some divergence of opinion in the literature over the labelling of the $^3F_4$ and $^3H_4$ levels. The notation of Gandy *et al.* [6.1] has been adopted here, where $^3H_4$ lies lower than $^3F_4$, although some authors reverse the labelling of these two levels. Pumping in the 800μm region excites population from the $^3H_6$ ground state to $^3F_4$, from where rapid nonradiative decay populates the metastable level $^3H_4$. Fluorescence then occurs from this level to Stark levels in the ground state multiplet, *i.e.*, the transition is essentially quasi-four-level in nature.

Fluorescence measurements were made when the preform had been pulled down into fibre form with a core diameter of 8.6μm and a cladding diameter of 125μm. Pump light at 797nm was launched into the fibre with a microscope objective, and the fluorescence was measured in both end light and side light. The pump wavelength was set at 797nm because, although the peak absorption is at 783.4nm, the dye laser power was greater at the longer wavelength and the fluorescence signal was maximised for 797nm pumping. End light fluorescence was collimated with a second objective before being passed through a 25cm

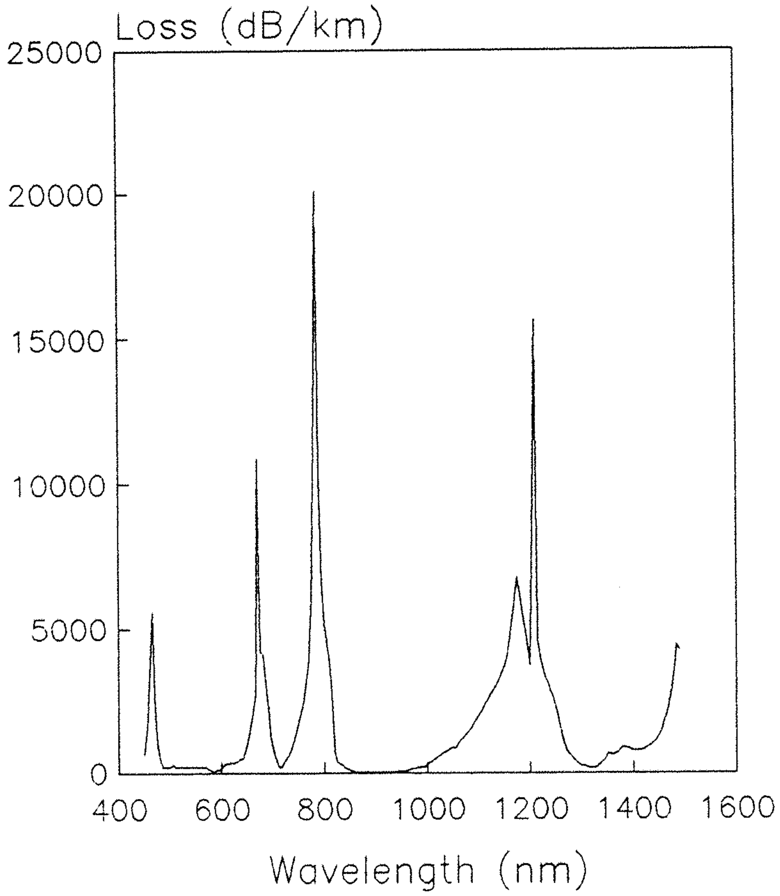

Fig.6.1 Absorption spectrum for fibre preform containing 840ppm Tm^{3+}

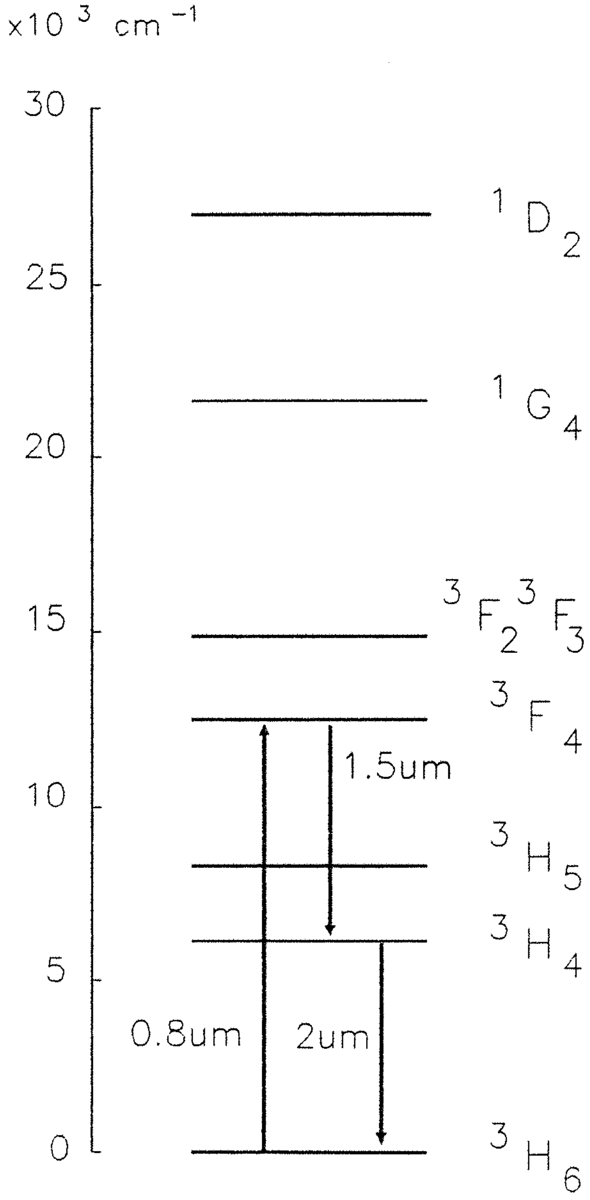

Fig.6.2 Energy levels for Tm^{3+}-doped fibre

monochromator containing a grating blazed for 2μm. Side light was measured with the technique used with ytterbium (see Chapter 4) involving a fibre bundle with one end placed against the thulium fibre and the other at the monochromator input port. In both cases the monochromator wavelength selection mechanism was driven with a stepping motor drive, and the fluorescence was detected with a germanium photo-diode. Pump powers in the region of 100-150mW incident on the launch objective were used, and the fluorescence was analysed over the wavelength range 1.3-2.4μm. Fig.6.3 shows the fluorescence from the side of the fibre where, because of the short optical length involved, the spectrum may be considered to be free from ground state reabsorption effects. These effects are readily apparent when this spectrum is compared with Fig.6.4, which shows the spectrum of fluorescence guided along a 25cm length of fibre. The shift in the peak is due to the emission at shorter wavelengths being reabsorbed by the thermally populated Stark levels in the ground state multiplet, so that transitions to the less populated higher lying Stark levels now dominate the emission. The end light spectrum also shows a weak feature at 1.47μm, due to emission from $^3F_4$ to $^3H_4$, and in fact laser action has also been observed on this transition for the first time in a glass host in fluorozirconate glass co-doped with Tm^{3+} and Tb^{3+} [6.6]. These transitions are indicated by the arrows shown in Fig.6.2.

Although this chapter is concerned mainly with the performance of the thulium-doped fibre when pumped in the 800nm region, the basic spectroscopy was further investigated by pumping the 25cm fibre in the blue at 476nm with an Ar^+ ion laser to probe the $^1G_4$ level. The end light spectrum is shown in Fig.6.5 for wavelengths between 600nm and 1200nm (a grating blazed at 500nm was used for this measurement). There are three emission bands in this region resulting from the Ar^+ ion excitation: red fluorescence centred at 649nm; a double-peaked feature around 800nm, and a weak feature peaking around 1130nm. A spectrum taken under identical conditions, except for an increase in the fibre length to 1.25m, is shown in Fig.6.6. Here the emission band around 800nm has been reduced in intensity, and the central dip is more pronounced. It may be inferred therefore that this fluorescence suffers increasing reabsorption with fibre length, and hence the terminal level is the ground state multiplet: the strong ground state absorption centred around 790nm accounts for the dip in the emission spectrum and produces the double peak effect. This emission must

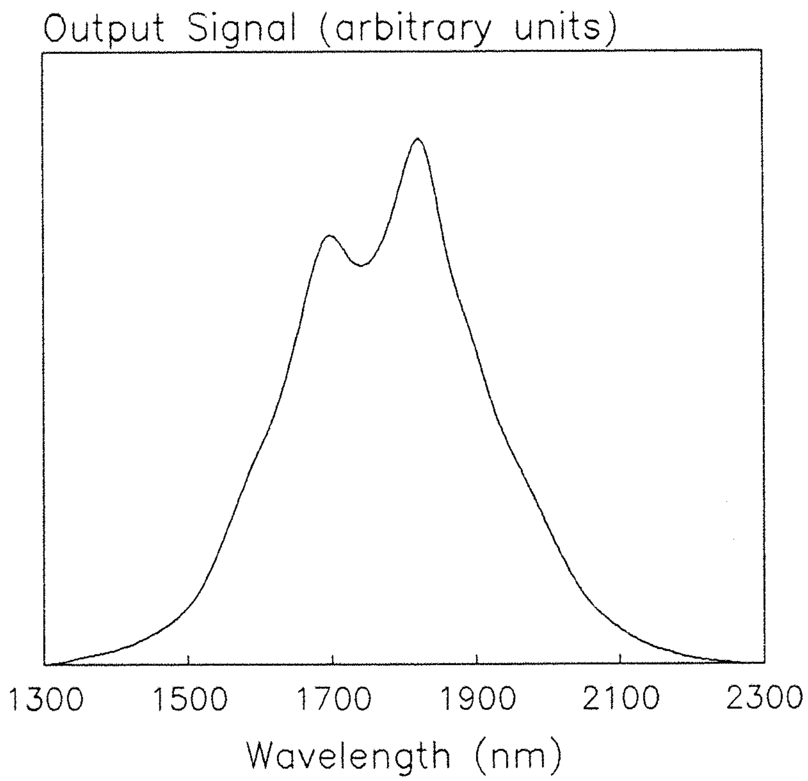

Fig.6.3 Side light fluorescence spectrum for 797nm pump wavelength

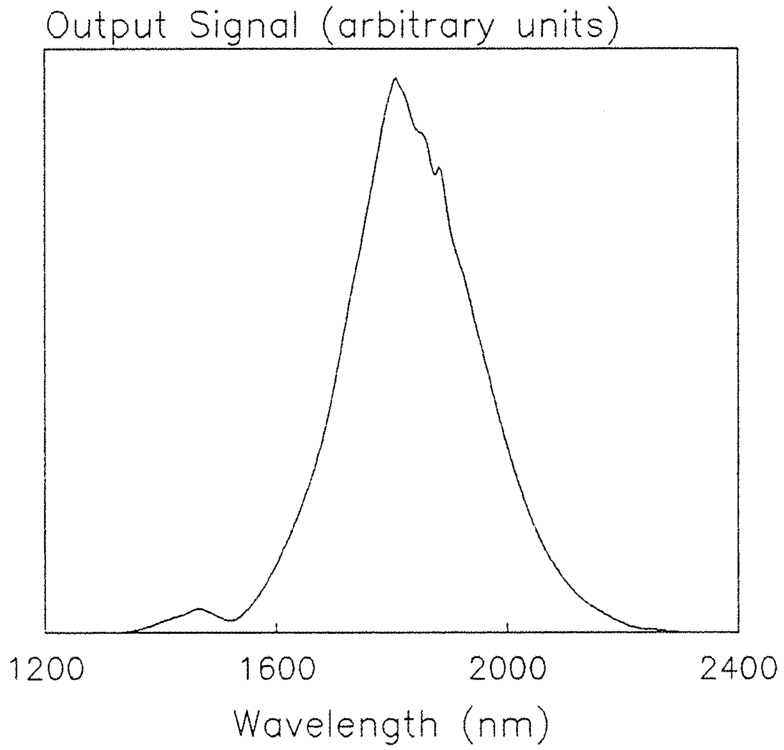

Fig.6.4 End light fluorescence spectrum (25cm fibre) for 797nm pump wavelength

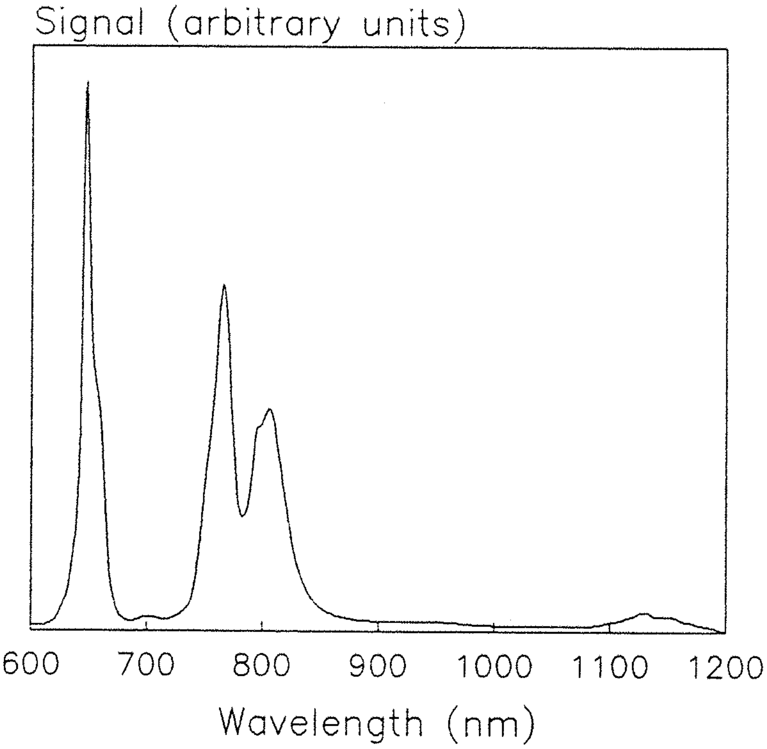

Fig.6.5 End light fluorescence spectrum (25cm fibre) for 476nm pump wavelength

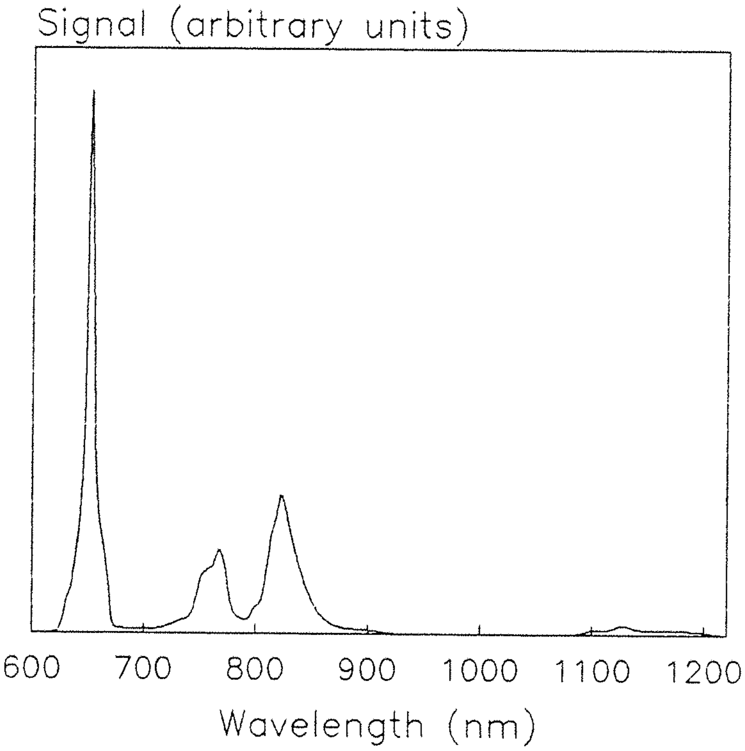

Fig.6.6 End light fluorescenece spectrum (1.25m fibre) for 476nm pump wavelength

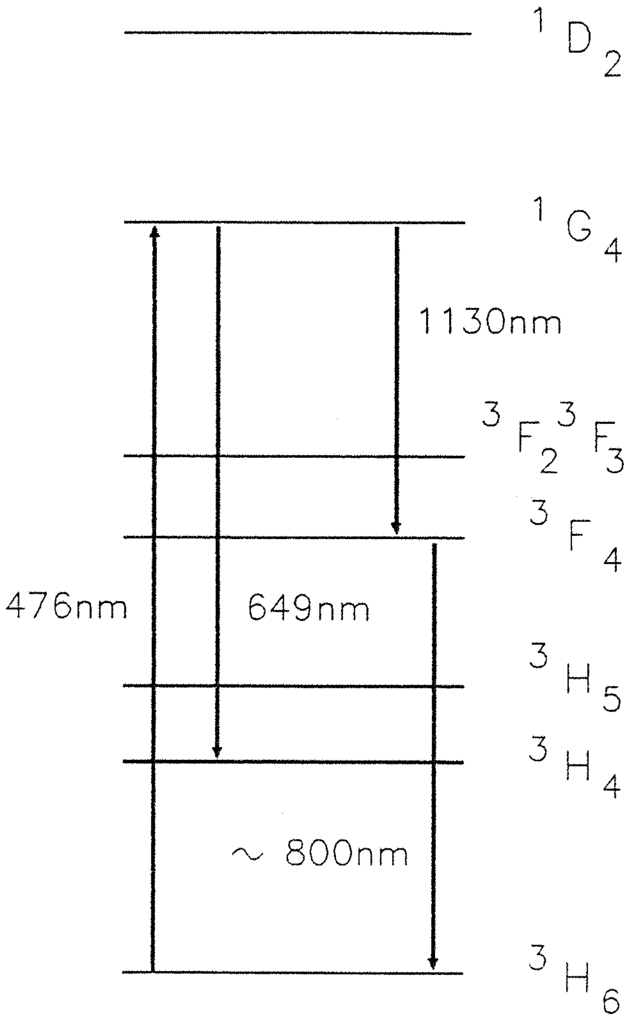

Fig.6.7 Fluorescence transitions following excitation at 476nm

therefore originate from $^3F_4$, terminating on the $^3H_6$ level. The $^3F_4$ level is populated by decay from $^1G_4$, giving fluorescence around 1130nm. The red emission arises from decay from $^1G_4$ to $^3H_4$. These transitions are indicated by the arrows shown in Fig.6.7. However, Ar^+-ion laser pumping is not considered to be an effective means of pumping the thulium system due to the phenomenon of photodarkening, arising from colour centre formation, whereby the transmission of a thulium-doped fibre has been observed to decrease with time when pumped at 475nm [6.7]. The excess loss induced by this photochromic behaviour is therefore likely to preclude the use of Ar^+ ion lasers for pumping Tm^{3+}-doped silica fibres.

The lifetime of the metastable $^3H_4$ level was measured by chopping the Styryl 9M pump beam (set at 803nm) and observing the decay of fluorescence at 1.8μm on an oscilloscope with a digital storage adapter attachment. The technique is very similar to that used for lifetime measurements with ytterbium, except when the measurements were made with thulium the fibre bundle had not yet been obtained, so end light from a 4cm length of fibre was used rather than side light. A monochromator with a grating blazed for 2μm was used to filter out all but the 1.8μm fluorescence, with the signal detected with a fast germanium photo-diode and amplifier. The observed decay in the signal after interruption of the pump beam was single exponential, with a lifetime of about 200μs. Measurements made on the fibre preform gave a similar lifetime. The detector system response was determined as about 50μs, defined as the time taken for the chopped pump signal to fall from 90% to 10% of its initial (uninterrupted) value.

6.3 Laser Performance

To investigate laser action, a Fabry-Perot cavity was set up, with cleaved fibre ends butted against dielectric mirrors at both ends. The fibre was end-pumped by the Styryl 9M dye laser with the light launched into the cavity with a 10X microscope objective. The input mirror was a high reflector (>99.5%) in the range 1.5-2.0μm with transmission >90% at the pump wavelength, and the output coupler had a transmission of 20% at 1.9μm.

The effects of ground state reabsorption were manifested in the conditions under which the laser could operate. Initially a 1.3m fibre was pumped with up to 150mW (incident on the launch objective) at

805nm, but the reabsorption losses prevented oscillation at room temperature. However, by immersing the fibre in a Dewar containing liquid nitrogen the thermal population of the Stark levels in the ground state could be removed, and laser action was then possible. The emission wavelength was 1.876μm, and the incident threshold power was 75mW. An output laser power of about 2.4mW was measured on a thermopile power meter for 125mW incident pump power. By removing increasing lengths of fibre from the Dewar, the wavelength was seen to shift to longer wavelengths (up to 1.9μm) as reabsorption prevented oscillation on the short wavelength components. The threshold also increased until it exceeded the maximum incident power available and laser action was no longer possible with the available pump power.

Clearly, for room temperature operation a shorter fibre was required. With the fibre length reduced to 27cm and pumped at 797nm, room temperature operation was observed, although the lower gain available in the shorter length necessitated a reduction in the output coupling. Emission at 1.96μm was observed, with an output coupler transmission of 3% at this wavelength. The launch efficiency for the pump was determined by monitoring pump transmission through the fibre whilst cutting back the length (as described in Chapter 4 for ytterbium). An incident power of 80mW was used at 797nm and the fibre was cut back from 0.7m to 0.2m. The results indicated a pump absorption coefficient of 8.9m^{-1} (40dB/m) and an overall launch efficiency of 75% of the incident power was launched into the core.

The output characteristic for the 27cm fibre is shown in Fig.6.8, where the slope efficiency with respect to absorbed power is 13% [6.8]. The threshold was 28mW absorbed (corresponding to 40mW incident on the launch optics), although slight adjustment of the fibre butt at the input end (so, strictly, the resonator conditions for which the characteristic applies were altered) was found to reduce this to 21mW absorbed (30mW incident). Since the cut off wavelength for this fibre was 1.7μm, the laser operated in a single transverse mode at 2μm. It should be noted that neither the fibre length nor the output coupler transmission have been optimised for maximum output power, and therefore there is considerable scope for improvement of this fibre laser system, particularly in view of the effect of length on the quasi-four-level laser transition. In fact, improved performance of the thulium-doped fibre laser has been reported in the literature. Hanna *et al.* [6.9] report a 36% slope efficiency from a fibre

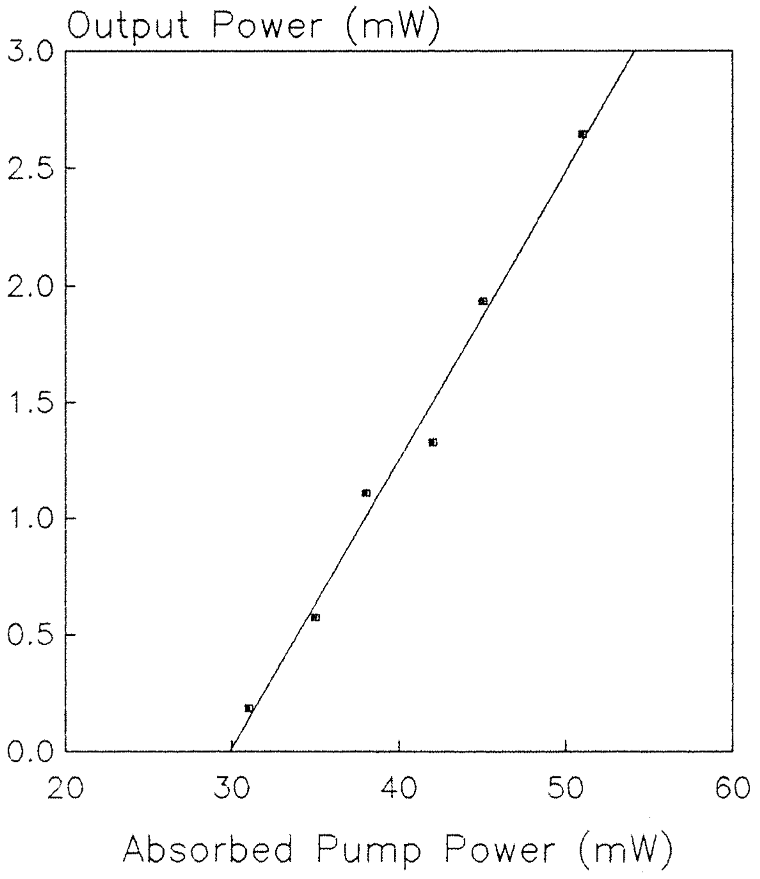

Fig.6.8 Laser characteristic for 27cm fibre pumped at 797nm

containing 3000ppm ($\approx 7 \times 10^{19}$ ions/cm^3) of Tm^{3+}, manufactured by the modified chemical vapour deposition (MCVD) technique. An output power of 44mW was observed at 1.9μm from a 22cm fibre pumped with 167mW (absorbed) from a Styryl 9M dye laser operating at 810nm.

6.4 Tunable Operation

The side light spectrum shown in Fig.6.3 indicates a full width at half maximum of approximately 290nm. This fact, in conjunction with the demonstrated wavelength-selection by progressive removal from liquid nitrogen immersion, suggests that tunable operation should be possible over a substantial range.

The tuning range was investigated using the arrangement shown in Fig.6.9. The cleaved fibre input end of a 1.2m fibre was butted against a dielectric mirror with high reflectivity (>99.5%) over the range 1.7-2.1μm, with the pump light launched with a microscope objective. Wavelength selection was provided by an intracavity three-plate birefringent tuning mechanism taken from a Coherent 599 dye laser. The output from the fibre was collimated through the tuning plates by an intracavity 10X microscope objective which, being a standard objective with no antireflection coating, had a low transmission (approximately 70%) in the 2μm region. This introduced high resonator losses and consequently the output coupling was constrained to be low, at about 1% across the observed tuning range. The fibre laser output was analysed with a 0.25m monochromator (with grating blazed for 2μm), and detected with a germanium photo-diode. The quasi-four-level nature of the laser transition suggests that fibre length will play an important part in determining the available tuning range, due to reabsorption in the ground state multiplet. Hence two fibre lengths were used in the tuning experiments, with the initial 1.2m fibre subsequently cut back to 0.6m.

The tuning curve, representing the photo-diode signal against laser wavelength, is shown in Fig.6.10 for the 1.2m fibre. The fibre laser was tuned in steps of 4nm by small adjustments of the micrometer drive on the tuning mechanism. In practice this was achieved by setting the monochromator wavelength selector on a particular wavelength, and then adjusting the tuning plates to maximise the detector signal. The laser wavelength was continuously tunable from 1866nm to 2014nm, with a maximum output power of the order of 100μW

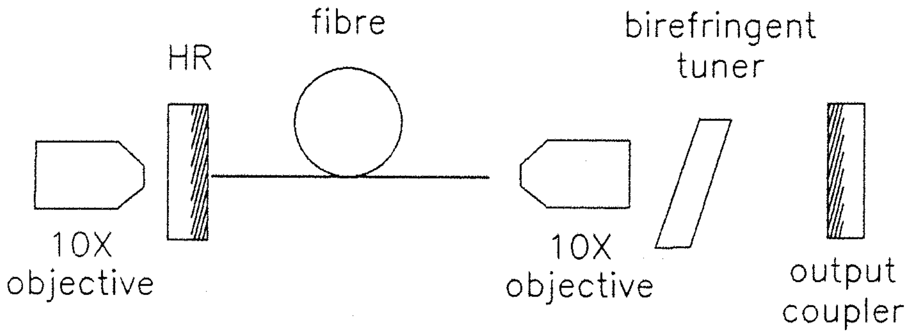

Fig.6.9 Resonator for tunable operation

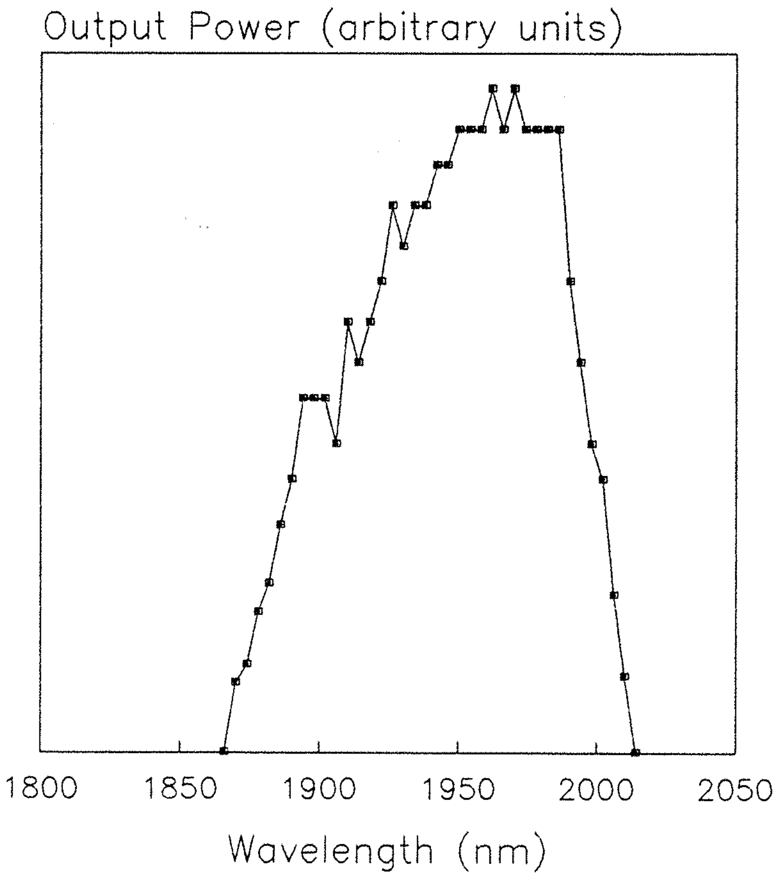

Fig.6.10 Tuning curve for 1.2m fibre pumped at 800nm

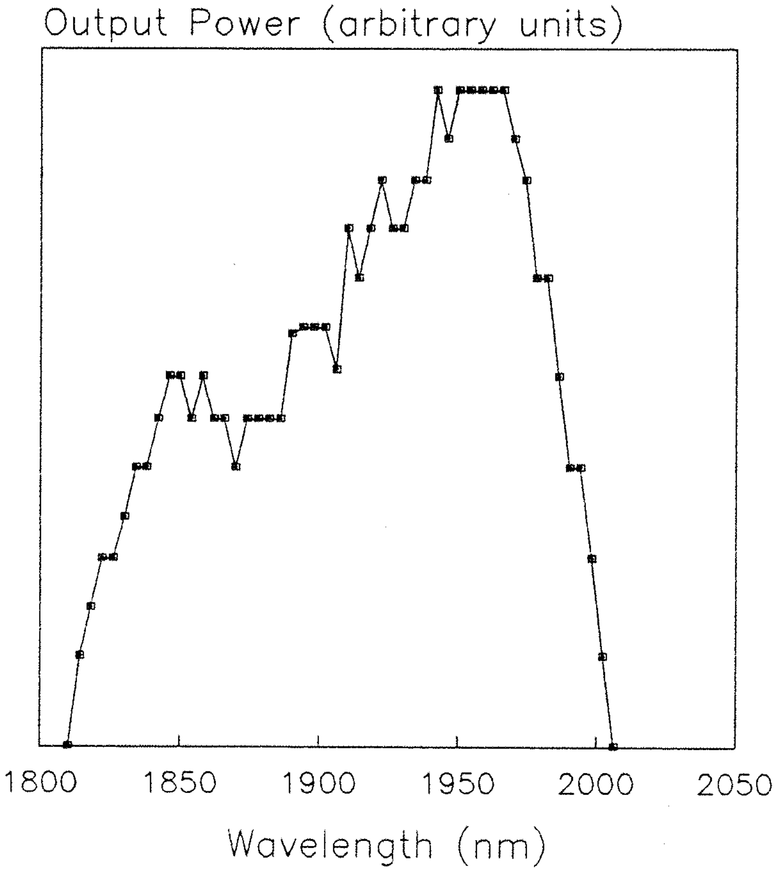

Fig.6.11 Tuning curve for 0.6m fibre pumped at 800nm

for a pump power of 210mW (at 800nm) incident on the launch objective. This extremely low output power was due to the small output coupling needed to overcome the losses introduced by the intracavity objective. The relatively high incident threshold power of 80mW is a further indication of the high resonator loss.

By reducing the fibre length, the reabsorption losses are reduced and consequently allow laser action to take place at shorter wavelengths. This was demonstrated by cutting back the fibre to 0.6m. The corresponding tuning curve is shown in Fig.6.11, where the lower wavelength limit is reduced to 1810nm due to the reduced reabsorption losses. The upper wavelength limit is also reduced (to 2006nm) since there is less pump power absorbed in the shorter fibre and hence less gain at the longer wavelengths. Again, the laser output powers were of the order of 100μW.

It was not necessary to incorporate the fibre loop polarisation controller as used for tuning the quasi-four-level transition in ytterbium (Chapter 4), since no modulation in the extracted power with wavelength was observed. However, power modulations have been reported in a Tm^{3+}-doped silica fibre [6.9] fabricated by the MCVD process, although no polarisation control was applied to counteract this effect, due to the large reabsorption losses introduced in the relatively long length of fibre needed to encompass the discs of the polarisation controller. In this same reference, an extended tuning range for a solution-doped Tm^{3+}-doped fibre (in fact the same fibre used in the work reported in this chapter) was reported, ranging from 1820nm to 2056nm for a 2.2m fibre, and from 1780nm to 1975nm for a 0.6m fibre, although output powers were still restricted to the 100μW level for the reasons discussed above relating to intracavity losses. No power modulations were observed in these tuning curves, and it seems reasonable to assume that the solution-doped fibre had inadvertent polarisation preserving properties.

6.5 Concluding Remarks

Continuous-wave laser action at 2μm has been demonstrated in a Tm^{3+}-doped silica fibre laser. A slope efficiency (with respect to absorbed power) of 13% was measured for a 27cm fibre pumped at 797nm with 3% output coupling. The absorbed power at threshold was about 30mW, and the maximum observed output power at 2μm was about 2.5mW for

50mW absorbed.

The laser transition was continuously tunable over the range 1866–2014nm for a 1.2m fibre pumped at 800nm, and 1810–2006nm for a 0.6m fibre pumped at the same wavelength. In both cases the maximum output power observed was about 100μW for an incident pump power of 210mW.

There is considerable scope for improving the thulium-doped system even further, and in fact both diode-pumped and extended tunable operation have been reported [6.10]. For the tuning demonstration, a Ti:sapphire laser was used to pump a germano-silica fibre (doped with 50ppm) at 788nm. Tuning was achieved with a ruled grating in place of the output coupler, with the lower wavelength limit extending down to 1650nm. A shifted (to longer wavelengths) tuning curve is reported for an alumina-silica fibre (200ppm Tm^{3+}), which tends to suggest that the precise nature of the glass host may be modified to extend or shift the tuning range to suit the particular application of interest.

References

[6.1] H.W. Gandy, R.J. Ginther and J.F. Weller, 'Stimulated emission of Tm^{3+} radiation in silicate glass', *J. Appl. Phys.* 38, 3030 (1967)

[6.2] L.F. Johnson, J.E. Geusic and L.G. Van Uitert, 'Coherent oscillations from Tm^{3+}, Ho^{3+}, Yb^{3+} and Er^{3+} ions in yttrium aluminium garnet', *Appl. Phys. Lett.* 7, 127 (1965)

[6.3] L.F. Johnson, G.D. Boyd and K. Nassan, *Proc. IRE* 50, 86 (1962)

[6.4] M.B. Stoffer and R.H. Hoskins, 'Energy transfer and CW laser action in Tm^{3+}:Er_2O_3', *Appl. Phys. Lett.* 6, 200 (1965)

[6.5] J.E. Townsend, S.B. Poole and D.N. Payne, 'Solution-doping technique for fabrication of rare-earth-doped optical fibres', *Electron. Lett.* 23, 329 (1987)

[6.6] G.H. Rosenblatt, R.J. Ginther, R.C. Stoneman and L. Esterowitz, 'Laser emission at 1.47μm from fluorozirconate glass doped with Tm^{3+} and Tb^{3+}', in *Tunable Solid State Lasers*, vol. 5 of the OSA Proceedings Series, M.L. Shand and H.P. Jenssen, eds., 373 (1989)

[6.7] C.A. Millar, S.R. Mallinson, B.J. Ainslie and S.P. Craig, 'Photochromic behaviour of thulium-doped silica optical fibres', *Electron. Lett.* 24, 590 (1988)

[6.8] D.C. Hanna, I.M. Jauncey, R.M. Percival, I.R. Perry, R.G. Smart, P.J. Suni, J.E. Townsend and A.C. Tropper, 'Continuous-wave oscillation of a monomode thulium-doped fibre laser', *Electron. Lett.* 24, 1222 (1988)

[6.9] D.C. Hanna, R.M. Percival, R.G. Smart and A.C. Tropper, 'Efficient and tunable operation of a Tm-doped fibre laser', *Opt. Comm.* 75, 283 (1990)

[6.10] W.L. Barnes and J.E. Townsend, 'Highly tunable and efficient diode pumped operation of Tm^{3+} doped fibre lasers', *Electron. Lett.* 26, 746 (1990)

CHAPTER 7

Nd:YAG PUMPING OF THULIUM-DOPED FIBRE

7.1 Introduction

The 2μm fibre laser described in the previous chapter, although reasonably efficient, was clearly a low power device operating at the several milliwatts level, and as such its suitability as a directly applicable practical source is probably limited. The low operating power was simply a consequence of the relatively low pump power available from the Styryl 9M source in the 800nm region. An alternative pump source is needed if the fibre laser power is to be increased significantly. A Ti:Sapphire laser, capable of producing about 1W in the Styryl 9M wavelength region (for the same Ar^+ ion pump power), provides a suitable alternative, but unfortunately such a source was not available when these experiments were carried out.

The 0.8μm-pumped $^3H_6$ - $^3F_4$ transition is not the only means of populating the upper laser level $^3H_4$ (see Fig.6.2 for an energy level diagram). The $^3H_6$ - $^3H_5$ pump transition centred at 1.2μm provides an alternative route, although there remains the problem of the requirement of a source in this wavelength region. Fortunately, the broad absorption bands of rare earths in glasses present less of a restriction on the choice of pump wavelengths than a crystalline host, and it was recently pointed out by Hakimi [7.1] that certain Tm^{3+}-doped silica-based fibres exhibit absorption in the wing of this transition at the Nd:YAG wavelength of 1.064μm, some 900cm^{-1} from line centre. The pump scheme is illustrated by the partial energy level diagram shown in Fig.7.1. The pump absorption is extremely weak: the absorption spectrum for the Tm^{3+}-doped fibre used for the experiments

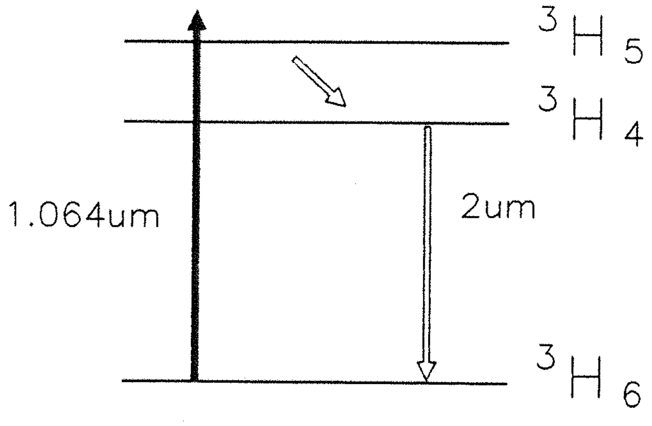

Fig.7.1 Partial energy level diagram for 1.064μm pumping of Tm^{3+}

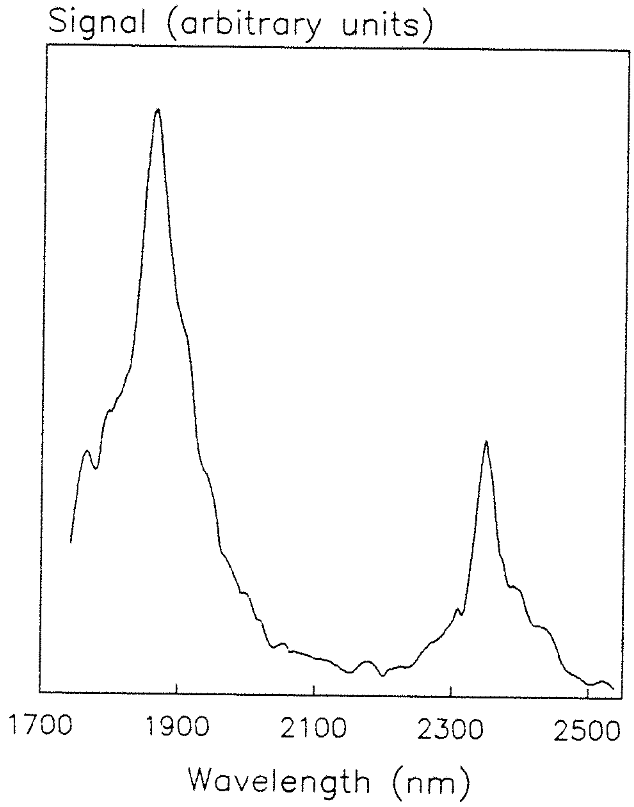

Fig.7.2 Side light fluorescence spectrum

described in Chapter 6 (shown in Fig.6.1) shows that it is only about 2dB/m at 1.064μm in that particular fibre (dopant concentration 840ppm). However, the availability of high power Nd:YAG sources makes this an attractive pump wavelength, since the weak absorption is not an insuperable problem (providing inversion is achieved) where the waveguiding properties of the fibre ensure that a long interaction length can be used to absorb all of the available pump power. In addition, given the convenience and widespread use of Nd:YAG lasers, the Tm^{3+} fibre laser offers a simple and attractive method of wavelength conversion from 1.064μm to the 2μm region.

In this chapter the initial experiments that demonstrated the viability of Nd:YAG pumping of Tm^{3+}-doped fibre, and the developments of the system to include tunable operation and output powers in excess of 1W, are described. A consequence of the 1.064μm pump wavelength is a detrimental (to the 2μm emission) upconversion process involving the production of readily observable blue light via excited state absorption (ESA) from the upper laser level $^3H_4$. This effect is also described, and a comparison is made between several types of Tm^{3+}-doped fibre in an attempt to minimise the ESA in favour of 2μm operation.

7.2 Spectroscopy

Side light and end light fluorescence spectra were recorded for the Tm^{3+}-doped fibre under excitation at 1.064μm from a Spectra-Physics Series 3000 Nd:YAG laser operating with a single transverse mode output beam. The spectroscopic measurements were made not with the 8.6μm core diameter fibre used previously in the Styryl 9M pumped system, but rather with a 17μm core diameter fibre specially made for reasons described below in Section 7.5.

The side light spectrum, obtained by use of the fibre bundle and monochromator method, is shown in Fig.7.2. The pump power was about 7W incident on the launch objective, and the fluorescence signal was detected with a PbS photo-diode and lock-in amplifier combination. The peak of the emission from the $^3H_4$ - $^3H_6$ transition is located at 1.865μm, with a full width at half maximum of about 160nm. Also shown in the figure is a fluorescence peak at 2.345μm arising from the $^3F_4$ - $^3H_5$ transition, since the $^3F_4$ level becomes populated as a result of the ESA process described below in Section 7.5. Laser action has been

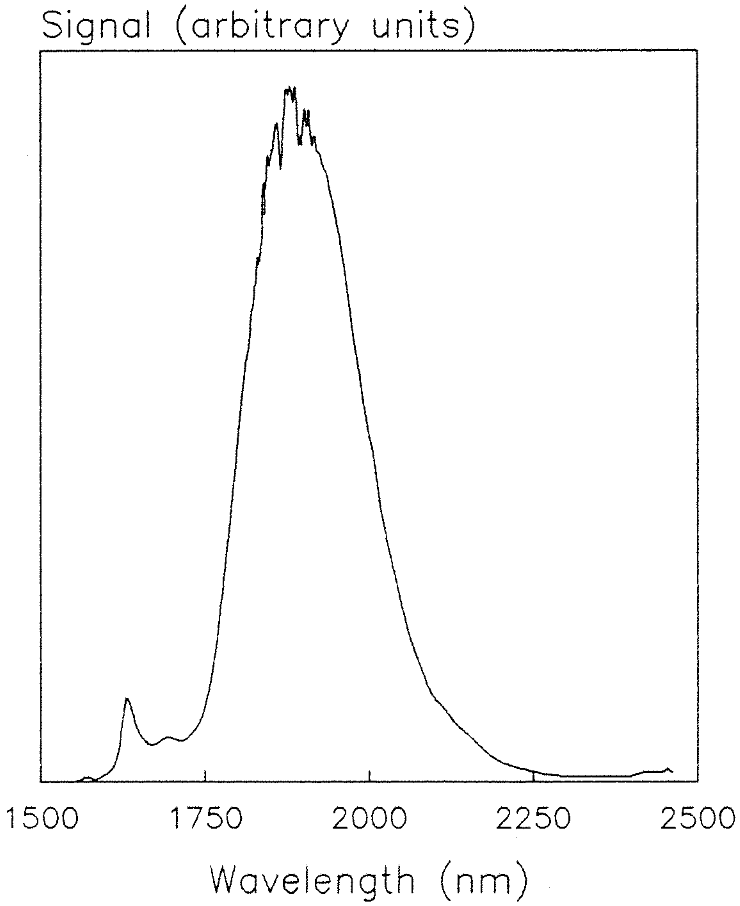

Fig.7.3 End light fluorescence spectrum for 80cm fibre

observed on this transition in a Tm^{3+}-doped flouorozirconate fibre [7.2, 7.3], but is unlikely to be realised in a silica system since the upper level lifetime is so short (≤20μs) compared to the ≈ 1.5ms lifetime of its counterpart in the fluorozirconate host. In addition, the end light spectrum for a 0.8m length of the silica fibre (Fig.7.3), under identical excitation conditions to those used for side light, shows that the emission around 2.3μm is significantly diminished by the losses of the silica host in this wavelength region, further reason to suppose that 2.3μm operation is unlikely. The end light spectrum also shows a slight shift to longer wavelengths for the ≈ 2μm emission due to reabsorption in the ground state Stark levels: the peak of the emission shown in Fig.7.3 is shifted to 1.9μm with a full width at half maximum of about 200nm.

7.3 Preliminary Laser Operation

Initial investigations of YAG-pumped operation were made with the 8.6μm core fibre as used previously with the Styryl 9M pump source. The absorption coefficient at 1.064μm was determined directly by cutting back the fibre (as described in Chapter 4) from 2.0m to 0.1m with a pump power of 40mW incident on the launch objective. This value was chosen after establishing that it was low enough so that any saturation or ESA effects could be reasonably neglected. The check for this was the observation that when the pump power was halved or doubled, the detected output pump power from the fibre showed a corresponding halving or doubling. The exponential decay of unabsorbed pump power with fibre length yielded an absorption coefficient α of $2dBm^{-1}$. In addition, the extrapolated pump power of 17mW at the input end and incident power of 40mW gave an overall launch efficiency of ≈ 45%. Note that during the cut back a high reflector (>99.5%) in the range 1.6-2.1μm was butted at the input end, so that the launch efficiency is applicable for laser operation.

In a simple 2-level system where the pump power is comparable to or greater than the pump saturation power, a non-exponential decay of unabsorbed pump at the output with increasing fibre length is expected. The reduced effective absorption coefficient would yield higher output pump powers than those given by the unsaturated value of α for a given length. For YAG-pumped Tm^{3+} however, the ESA from $^3H_4$ results in an increase in the effective absorption coefficient. The effect is demonstrated in Fig.7.4, where the unabsorbed pump power is shown as a function of fibre length as the fibre was cut back from 4.0m to 0.2m. The incident pump power was 900mW and no mirrors were included in the set-up. The curve calculated using α under small signal conditions (2dBm^{-1} measured for 40mW incident) is also shown for comparison, and demonstrates how the absorption is increased in the presence of ESA.

The increased absorption for high pump powers is further demonstrated in Fig.7.5, which shows the variation of the unabsorbed pump for a fixed length (1m) as the launched power is increased from zero to about 400mW. For pump powers above about 50mW launched, the absorption departs from the 30% level up to nearly 75% of the input power for 380mW launched. This increased absorption is manifested in the strong blue emission, easily observed by the unaided eye for pump powers as low as ≈ 100mW incident on the launch objective.

Laser action was easily achieved with fibre lengths from about 2m to 10m in a Fabry-Perot cavity configuration with the mirrors butted at both ends of the fibre. The input mirror was as described above, being 90% transmissive at the pump wavelength. A variety of output couplers was available, with transmissions in the 2.0-2.4μm region from 1% to about 30%. In determining the optimum length, the quasi-4-level nature of the laser transition due to the thermal population of the lower laser level must be considered. As with the ytterbium fibre, this will impose an optimum length for maximum laser power. This length obviously depends on the amount of pump power input to the fibre, but for a fixed pump level the optimum can be found by monitoring the fibre laser power as the fibre is cut back from the output end (so that the launch is not disturbed and a constant launch efficiency can be assumed). This length dependence was measured using a resonator with 1% output coupling at 2μm. The incident pump power was 1W and the fibre was cut back from 6.0m to 0.5m. The output laser power versus length is shown in Fig.7.6, which shows a pronounced peak for a length of about 1.8m. The sharpness of this response is unexpected, and may in part be due to the sensitivity of the laser performance to the cleave quality of the fibre ends. However, the more gradual fall off in power for lengths greater than about 2m does suggest an approximate optimum may occur in the 0-2m region. In view of this, a series of experiments was performed with a fibre length of 1.8m. Although this is "optimum" for 1W incident, the fibre was in

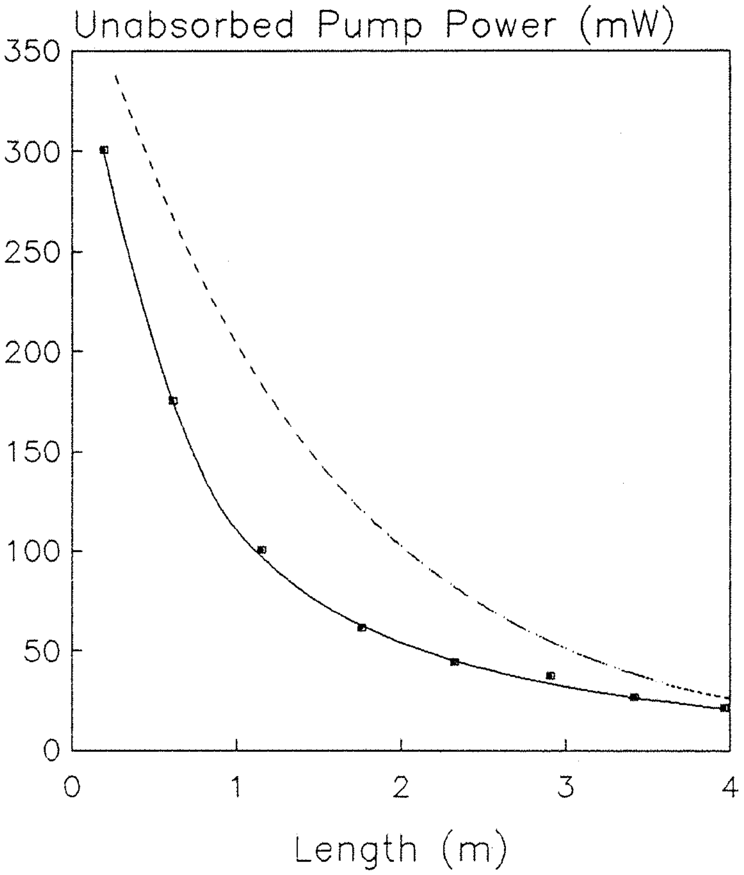

Fig.7.4 Solid line: unabsorbed pump power versus fibre length for 900mW incident. Dotted line: calculated curve for negligible ESA or saturation

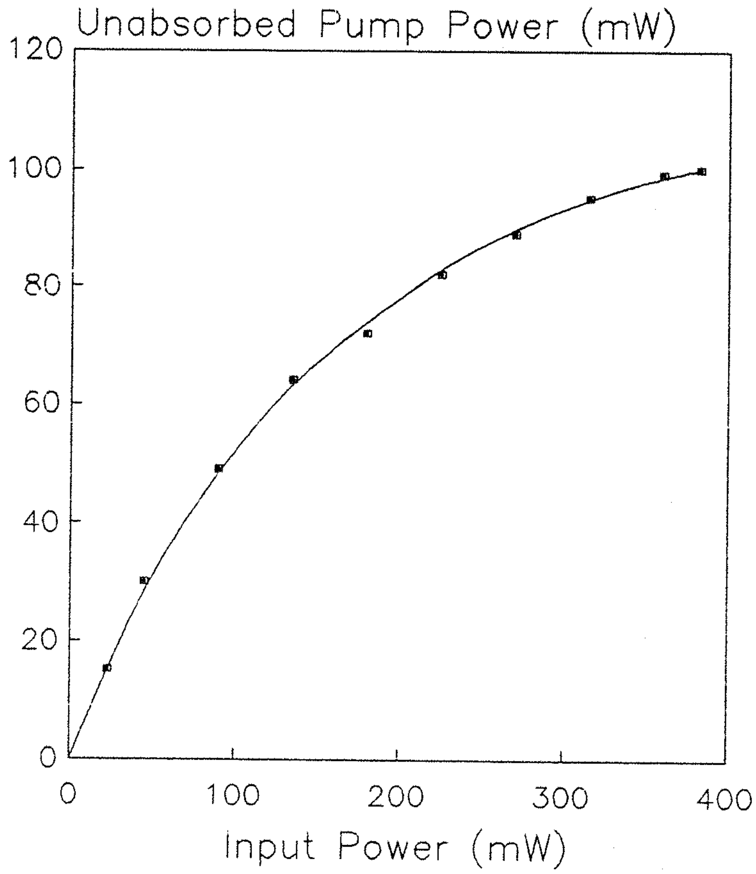

Fig.7.5 Unabsorbed pump power versus input power for 1m fibre

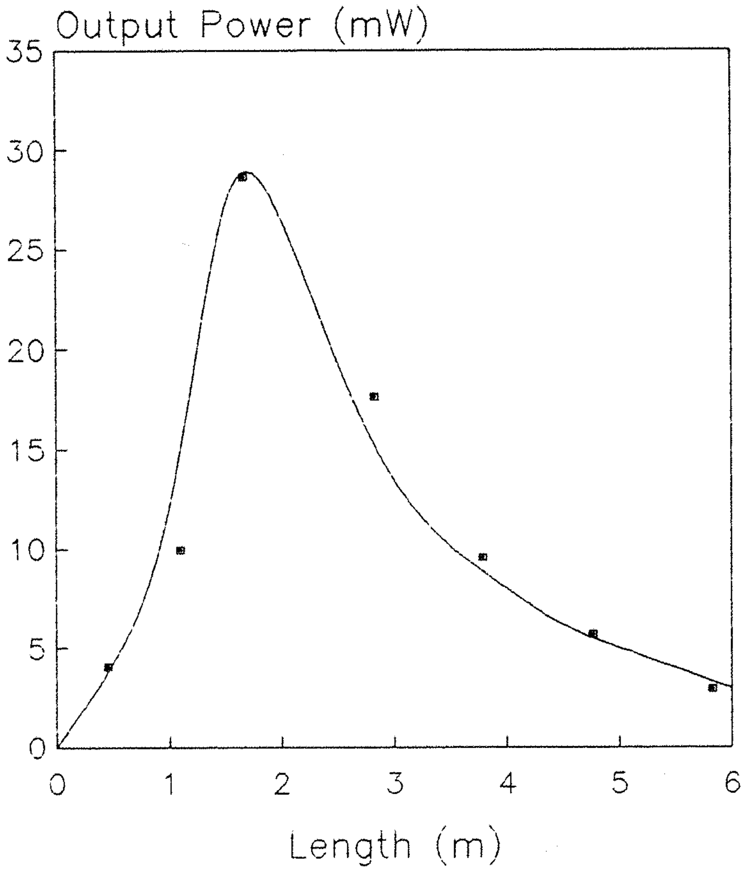

Fig.7.6 Laser power at 2μm versus fibre length for 1W incident power

fact pumped with 3.6W in one instance and up to 2.35W generally.

The YAG laser was capable of emitting up to 10W in the TEM_{00} mode, but the coating on the high reflector at the input end of the fibre was very susceptible to damage. To avoid destroying the mirror, an incident power limit was set at about 3.6W.

Four output couplers were used, with transmissions of 1%, 2.5%, 6% and 34% (all nominal values at 2μm in air). Output powers were measured on a thermopile power meter with a filter to block the pump wavelength so that the fibre laser power could be measured directly. These values were then corrected for the filter transmission (75%) and the transmission of the collimating objective (70% at 2μm, 90% at 1.064μm). The resulting output characteristics are summarised in Table 7.1 below.

Output Coupler Transmission (%)	Slope Efficiency (%)	Absorbed Threshold Power (mW)
1.0	22	70
2.5	24	60
6.0	28	105
34.0	21	635

Table 7.1

The laser wavelength was in all cases 2.0μm with full width at half maximum of ≈ 3.5nm. In the absence of any other suitable mirrors between 6% and 34% transmission for use as output couplers, it was decided to proceed with the 6% coupler, since the corresponding slope efficiency was highest and the threshold modest, at ≈ 105mW absorbed (295mW incident). It was also with this particular mirror that the highest power was observed, 269mW out for 3.6W incident (1.15W absorbed). The laser characteristic obtained using this output coupler is shown in Fig.7.7. The characteristic is linear despite the ESA effects discussed above, due to the fact that once threshold is reached, the population inversion is clamped. This means that an increase in pump power leads to an increase in stimulated emission rather than an increase in the upper laser level population. As a consequence, there is less ESA when the fibre is lasing than when

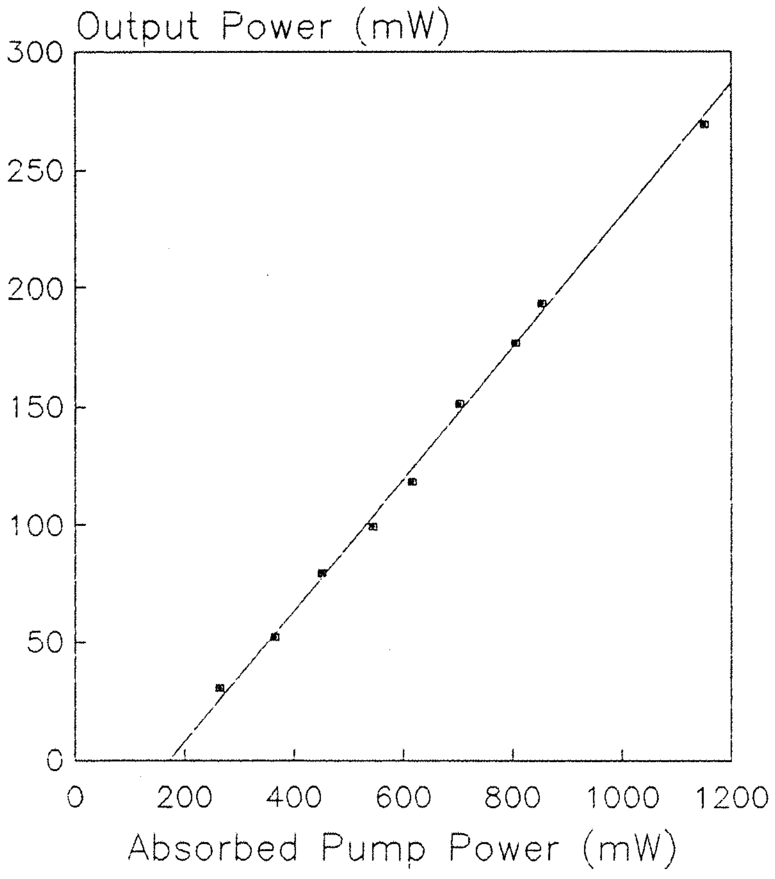

Fig.7.7 Laser characteristic at 2μm for 1.8m fibre (9μm core diameter)

lasing is prevented, for a given pump power above threshold. This effect can be observed experimentally by unbutting one of the cavity mirrors to prevent laser action, when the amount of blue emission is seen to increase noticeably.

As a general comment, it may be said that the YAG-pumped Tm^{3+}-doped fibre laser system shows a greater dependence on the cleave quality and the precision of the mirror butting, with respect to the laser output power, than most other fibre laser systems. The output powers described above were obtained after very careful adjustment of the mirror angles and the butting, and then only when the cleave quality was exceptional (one interference fringe under analysis with an inspection tool). In some instances the difference between a good cleave and a bad one could affect the output power by as much as an order of magnitude. This is believed to be a direct result of the ESA process. In a lossy cavity, such as one with poor quality cleaves, the population of the upper laser level must be relatively high to provide the gain required to overcome these losses. Since the amount of ESA from the upper level is dependent on the upper level population, a lossy cavity is subject to more ESA than a low loss cavity, and hence the laser performance is degraded by the removal of population from the upper level. Direct dielectric coating of the fibre ends to form integral mirrors would alleviate this problem and increase the efficiency of the Tm^{3+}-doped fibre laser system.

7.4 Tunable Operation

Although not expected to be as widely tunable as the Styryl 9M pumped system, the tunability for Nd:YAG pumped operation is a feature that may have important practical applications for simple wavelength conversion from the 1μm to 2μm region.

To investigate the tuning range, the resonator was set up as shown in Fig.6.9, with a set of birefringent tuning plates (taken from a Coherent 599 dye laser) as the wavelength-selective element. A 10X microscope objective was placed intracavity to collimate the output beam through the tuning plates onto the output coupler and to re-launch light into the fibre after reflection at the coupler. The higher threshold imposed by the inclusion of the intracavity objective necessitated the use of a low transmission (1% at 2μm) output coupler. The input mirror was the same high reflector used in the preliminary

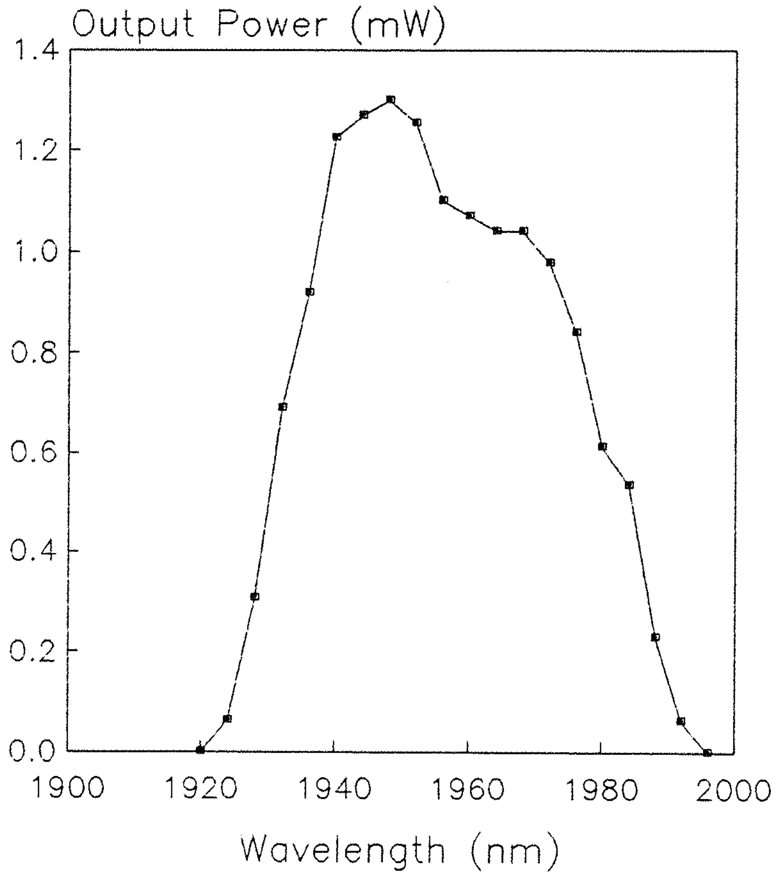

Fig.7.8 Tuning curve for 2m fibre pumped with 3W incident

laser experiments.

A 2m length of fibre was pumped with 3W from the Nd:YAG laser incident on the launch objective. Without the tuning mechanism, the free-running wavelength was 1976nm and the incident threshold power was 1.3W, rising to 2.1W when the tuner was inserted. The wavelength was tuned in steps of 4nm, analysed by a 0.25m grating monochromator and monitored by a germanium photo-diode. The resulting tuning curve is shown in Fig.7.8. Power calibration was performed by measuring the power at the largest detector signal with a thermopile detector and pump filter. Detector readings at all other wavelengths in the tuning range are assumed to scale accordingly. The very low output power (1.3mW maximum for 1350mW launched) is a consequence of both the low output coupling and the high insertion loss of the intracavity objective, as evidenced by the factor of ten increase in incident threshold from 220mW for a butted resonator with 1% output coupling to 2100mW in the case of the tuning resonator. The wavelength-dependent power modulation effects observed with ytterbium were not present here, but the incorporation of a fibre loop polarisation controller might have been beneficial in slightly increasing the output power by offsetting any polarisation-dependent loss at the birefringent plates, as would using higher output coupling at the expense of an increased threshold and possible reduction in the tuning range. The observed tuning range of 76nm from 1920nm to 1996nm (198cm^{-1}) is significantly less than that of the 0.8μm-pumped system, but nevertheless demonstrates an appreciable tuning range in the 2μm region despite the very weak absorption for Nd:YAG pumping.

7.5 High Power Operation

7.5.1 Introduction

In the absence of any signs of output power saturation, the output power of 269mW (the highest observed with this fibre) is believed to be limited by the incident pump power. The pump power limit of 3.6W corresponds to an intensity of 6.2MW/cm^2 at the surface of the input mirror, assuming the pump beam is focused down to a spot size equal to the fibre core. Having decided not to exceed this intensity for fear of causing mirror damage, two possibilities for increasing the fibre laser output power were considered. The first method was to expand the beam at the mirror surface such that a higher pump power could be used without increasing the intensity. In practice this means using an intracavity objective between the input mirror and the fibre so that the pump beam is no longer focused onto the mirror at the butting point. However, experience with tunable operation (see Section 7.4) showed that the losses introduced by intracavity elements drastically increase the threshold and reduce the efficiency. The second technique of increasing the power is to use a fibre with a larger core diameter, so that although the pump beam is still focused on the mirror, the spot may be larger and hence a higher pump power may be used without increasing the intensity.

In the interests of maintaining a low threshold, this second method was adopted. The preform from which the original 8.6μm core diameter fibre was made was drawn into a second fibre having a core diameter of 17μm, *i.e.*, a core area four times that of the original. Hence, with a pump intensity limit of 6.2MW/cm^2, and assuming the pump spot equals the core size, the incident power limit is 14W. This exceeds the maximum power available from the Nd:YAG laser, so mirror damage was not expected to be a problem. With the actual maximum power of about 10W the fibre laser power at 2μm may be scaled from 269mW for 3.6W incident to 750mW for 10W incident. In fact, after careful optimisation of the resonator, an output power nearly twice this figure was finally realised.

7.5.2 Laser Operation

The modified fibre was identical to the original, *i.e.*, dopant concentration 840ppm and numerical aperture 0.15, with the exception that the core diameter was 17μm (measured by white light microscopy) and the cladding diameter was 250μm instead of 125μm since, coming from the same preform as the original, the ratio of core to cladding was maintained. This large outer diameter caused considerable problems when trying to cleave the fibre. The standard cleaving device (a York Technology *FK 11*) was unable to provide enough tension for a satisfactory cleave, and launching pump light and achieving laser action was initially rather difficult. However, a version of the cleaver specially modified by York Technology did allow consistently good cleaves to be obtained.

The attenuation coefficient was checked with the cut back technique, with the input mirror in place so that the overall launch efficiency could be determined (for a 10X objective). The input mirror was >99.5% reflecting in the range 1.6-2.1μm and 90% transmitting at the pump wavelength. With an incident power of 100mW (where ESA and saturation effects were negligible for this fibre) the fibre was cut back from 1.5m to 0.25m. The value of α was found to be 2.0dBm^{-1}, and the overall launch efficiency (ratio of launched power to power incident on the launch objective) was 55%. Taking into account the transmission of the input objective and the mirror gives a coupling efficiency (ratio of launched power to power incident on the fibre end face) of 75%. Pump transmission measurements on a 5cm length of fibre (so short that absorption can be neglected) supported these launch efficiency figures.

A Fabry-Perot resonator was constructed with the fibre butted at both ends. The output coupler was 6% transmitting at 2μm and 80% transmitting at 1.064μm. The output characteristic was determined for several fibre lengths in an attempt to find an optimum. Lengths of 2.8m, 2.0m, 1.6m and 1.4m were pumped with up to 9.6W (the maximum available). Fibre laser output powers were measured on a thermopile detector with the pump light blocked by a filter. The resulting characteristics are summarised in Table 7.2 below, where the output powers have been corrected for the transmission of the collimating objective at the laser wavelength. Slope efficiencies are given with respect to absorbed power.

Length (m)	Slope Efficiency (%)	Absorbed Threshold Power (mW)	Output Power (mW) †
2.8	20	620	520
2.0	23	‡	595
1.6	25	720	560
1.4	37	600	780

† values given for 3W absorbed
‡ not measured

Table 7.2

The highest output power and slope efficiency were observed with the

1.4m length, where an incident power of 9.6W (5W absorbed) yielded 1.24W at 2.01μm, with a threshold of 1.2W incident (600mW absorbed). The laser characteristic is shown in Fig.7.9. The slope efficiency of 37% represents an internal quantum efficiency of 70%. The marked improvement in performance obtained by cutting back from 1.6m to 1.4m is thought to be due more to a high quality cleave and fortuitous mirror alignment than to a strong length dependence effect, although the overall trend is one of improving performance with diminishing fibre length.

The high power point at 1.24W for the 1.4m length was obtained by changing the Nd:YAG lamp current from its normal operating level of 18A to 19A to give the maximum power of 9.6W. This is very likely to alter the pump beam characteristics such that the launch efficiency is no longer the 55% as determined with the 18A current. However, since this new launch efficiency was unknown, 55% was assumed throughout, and it is for this reason that the 1.24W point lies off the straight line fit: it is not believed to be evidence of output power saturation.

A spectrum of the laser emission was taken by analysing the output with a monochromator with a stepping motor drive. The response was monitored on a PbS detector connected to a Y-T chart recorder. Fig.7.10 shows the spectrum for a 1.3m length of fibre pumped at 5 times above threshold. The incident power here was 6W and the fibre laser output was 420mW. The spectrum has two main peaks centred at 1991nm and 2000nm, and both exhibit some degree of modulation. This modulation suggests the presence of an etalon, although the average spacing of 0.8nm would require a 2.5mm gap in air and no features of this dimension existed in the cavity. The effect could be due to a polarisation-related phenomenon, but no polarisation sensitive elements were incorporated. A third possibility is instability in the monochromator drive mechanism.

In a further attempt to optimise the output power with respect to length, a fibre was pumped at a fixed incident power of 9.6W as the length was cut back from 2.0m to 0.7m. Fig.7.11 shows the variation of fibre laser power with length. There was no significant variation of laser wavelength with length, the emission wavelength being 2.0μm in all cases. The highest output power was observed from the 0.7m length. If a launch efficiency of 55% is assumed (despite the fact that the increased lamp current may have changed this value) then the absorbed

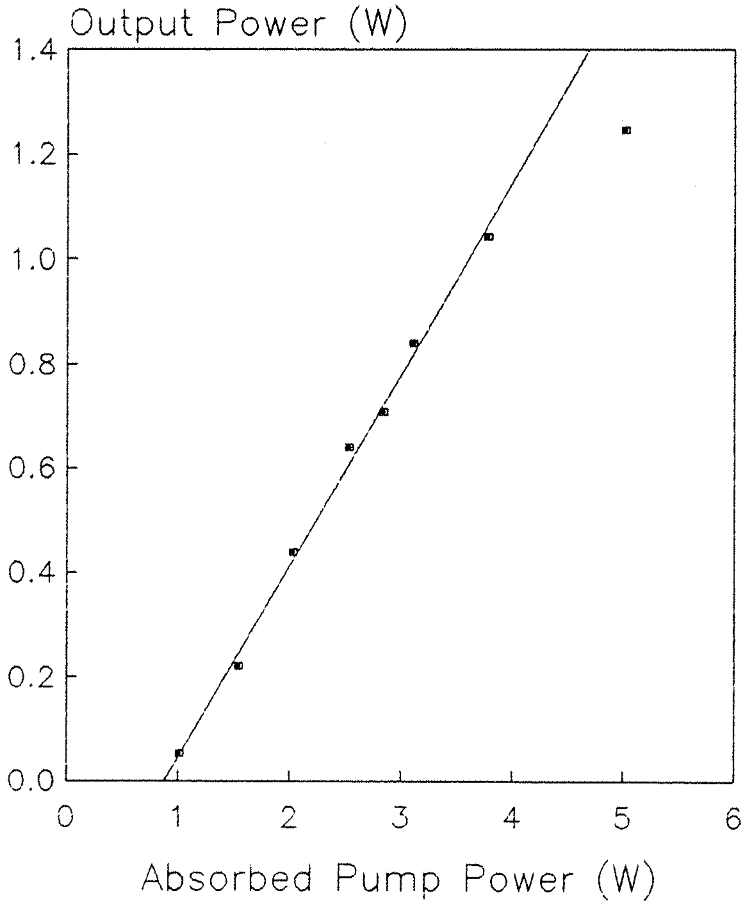

Fig.7.9 Laser characteristic at 2μm for 1.4m fibre (17μm core diameter)

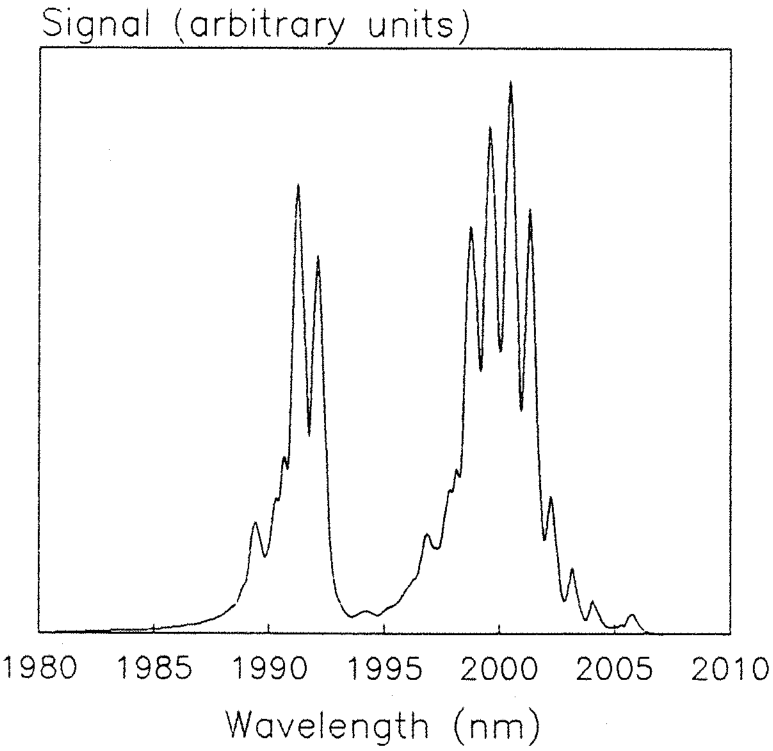

Fig.7.10 Spectrum of laser emission five times above threshold

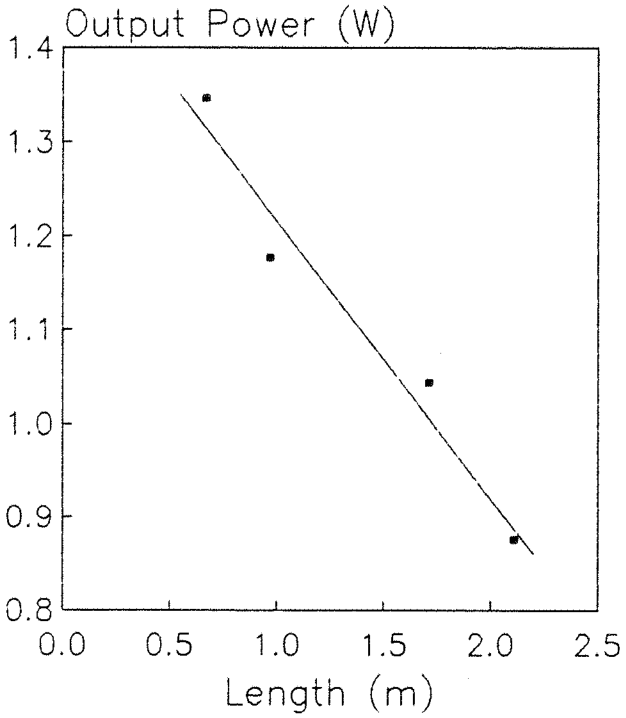

Fig.7.11 Variation of laser power at $2\mu m$ with fibre length for 9.6W incident power

pump power would be 4.4W. The fibre laser power was 1.35W, the highest power observed at any time during this work.

The general trend shown in Fig.7.11 implies that lengths shorter than 0.7m may yield even higher powers, since the fall off in power with increasing length indicates that host absorption and reabsorption in the thermally populated lower laser level is significant for longer lengths. Unfortunately it was not possible to use shorter lengths since, in order to do so, the micropositioning blocks would need to be placed close together in such a way that the fibre would be bent considerably between the two blocks. The large fibre diameter meant that the minimum bend radius was prohibitively large if bending-induced fracture was to be avoided. It is interesting to compare Fig.7.11 with Fig.7.6 for the small core diameter fibre, and speculate that the optimum length for the large core fibre may exhibit a similarly pronounced dependence on fibre length for fibres shorter that 0.7m.

7.5.3 Output Beam Characteristics

The 2μm fibre source has promising applications due to its high power capabilities, but if these are to be realised there remains the requirement that the beam quality be sufficiently good for practical purposes such as launching into a transmission fibre or focusing down to a small spot size.

The beam and mode characteristics (spot size, number of propagating modes) may be predicted from the fibre parameters, *i.e.*, core radius and numerical aperture, assuming a step refractive index profile. However, in practice the index profile of a typical fibre may deviate significantly from an ideal step index. This is demonstrated by Fig.7.12, which shows the refractive index profile for the thulium-doped fibre, where the index difference relative to the cladding glass is plotted against radial distance. The GeO_2 component of the core composition is reduced to GeO in the central region as a consequence of the fabrication process and is subsequently lost, causing a dip to appear in the centre of the index profile. An expanded plot of the core region is shown in Fig.7.13. The refractive index measurements were performed on the fibre preform [7.4], but the index profile is assumed to remain unchanged when the preform is pulled down into a fibre.

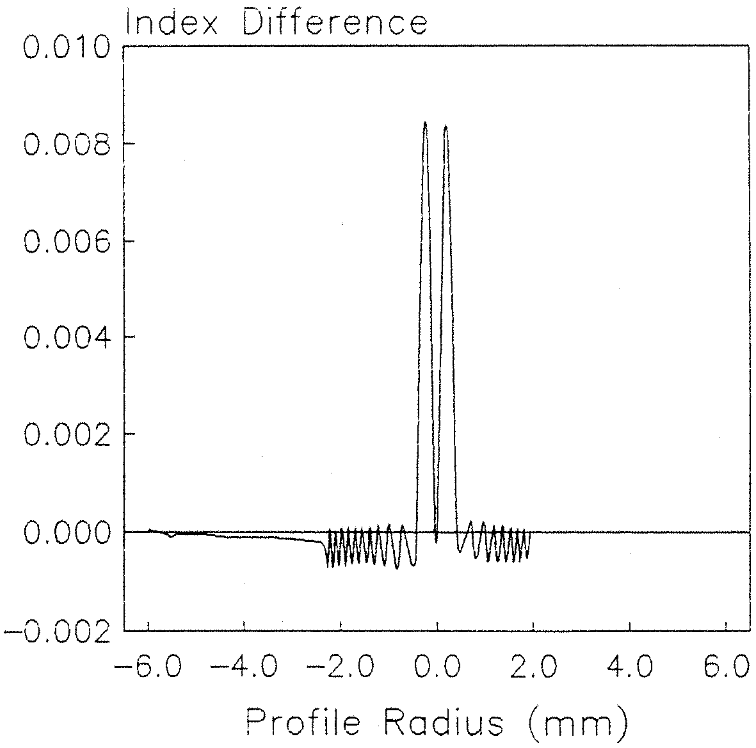

Fig.7.12 Refractive index profile of fibre preform

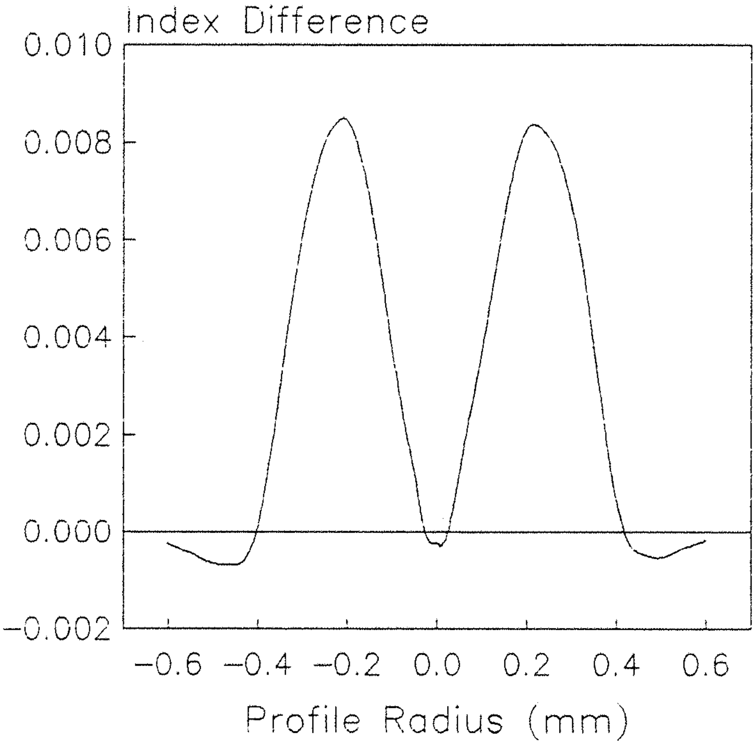

Fig.7.13 As Fig.7.12 with expanded radius scale

Several techniques have been developed [7.5, 7.6, 7.7, 7.8, 7.9, 7.10] to determine the propagation characteristics of fibres with arbitrary refractive index profiles by transforming the profile into an "equivalent step index" (ESI), since analytical solutions for step index profiles are well known [7.11]. If the ESI method predicts an LP_{11} mode cut off, LP_{01} propagation constant, mode field radius and evanescent field close to the parameters of the actual fibre, then even the bending and splice losses can be predicted, and complex methods exist to ensure sufficient accuracy. For the thulium fibre the only parameters of interest are the core radius, determined by the equivalent step width (the "equivalent core radius"), and the numerical aperture, derived from the height of the equivalent step (the "equivalent profile height"), and therefore a much simplified version of the ESI technique may be used [7.5].

The ESI method is used to derive two parameters, the equivalent core radius ρ_e and the equivalent profile height h_e, from an analysis by moments of the refractive index profile of the fibre preform.

The profile moments are defined as

$$\Omega_m = \int_0^1 s(R) R^{m+1}\, dR \qquad (7.1)$$

where
$$s(R) = \frac{n^2(r) - n_{cl}^2}{n_0^2 - n_{cl}^2} \qquad (7.2)$$

and $n(r)$ is the refractive index profile, n_0 is the maximum refractive index, n_{cl} is the cladding refractive index, and r is the radial position across the preform. R is the normalised radius r/ρ, where ρ is the actual core radius, and m gives the order of the moment. Normalised moments are defined as

$$\Omega'_m = \Omega_m/\Omega_0 \qquad (7.3)$$

In the weak guidance approximation, Eq.7.2 becomes

$$s(R) \approx \frac{n(r) - n_{cl}}{n_0 - n_{cl}} \tag{7.4}$$

and $s(R)$ is assumed to be zero for $R > 1$.

The ESI method states that only the even moments are needed to specify any refractive index profile [7.10], and further, that Ω_0 for the actual profile is equal to Ω_0 for the step profile. This is also true for the normalised moment Ω_2'. These equalities give the following:

$$\rho_e = \left(2\Omega_2' \right)^{1/2} \tag{7.5}$$

$$h_e = \Omega_0/\Omega_2' \tag{7.6}$$

where

$$\Omega_0 = \int_0^1 s(R)RdR \tag{7.7}$$

$$\Omega_2' = \frac{\int_0^1 s(R)R^3 dR}{\int_0^1 s(R)RdR} \tag{7.8}$$

Performing the integrations independently on both the right and left hand sides of the profile in Fig.7.13 gives $\rho_e = 7.5\mu$m and $h_e = 0.0064$. The numerical aperture NA for a step index is given by

$$NA = (n_{co}^2 - n_{cl}^2)^{1/2} \tag{7.9}$$

where n_{co} is the core refractive index. In the case of the equivalent step considered here, the core index is raised by a value h_e above the cladding. For the silica-based fibres used in this work, $n_{cl} = 1.4585$. Therefore n_{co} is $n_{cl} + h_e = 1.4649$. Hence the numerical aperture is 0.137 and the normalised frequency $V = (2\pi\rho_e/\lambda) \times (NA)$ then implies that, at the LP_{11} mode cut off where $V = 2.405$ for a step index, the cut off wavelength is 2.7μm. The fibre laser output could therefore be multimode at 2μm. In fact, at 2μm the V-number is 3.23, so only the LP_{11} mode can propagate in addition to the fundamental mode [7.12].

To investigate the actual mode profile, the far field output beam was scanned with a PbS detector in the arrangement shown in Fig.7.14. A 70cm length of fibre was pumped with 7.2W incident on the launch objective from the YAG source, yielding 420mW at 2μm from the fibre laser. The output from the fibre was passed through a filter to remove the pump component before reaching the detector. The detector was fitted with a pinhole aperture (*i.e.*, circular) directly in front of the active area, and was scanned transversely across the beam on a linear translation stage. Note that it is important in such a measurement that the aperture is a circular hole rather than a slit, as the latter would integrate along its length and, for instance, transform a uniform intensity circular profile into something looking very much like a Gaussian.

The beam was scanned at a distance of 60cm from the output coupler. A typical profile is shown in Fig.7.15. This profile was measured after locating the peak signal in a plane perpendicular to the beam propagation direction, but is similar for profiles taken through other regions of the beam, *i.e.*, the profile is symmetrical about a central peak.

A Gaussian curve has been fitted to the data points shown in Fig.7.15, and shows clearly that the fibre laser is operating in its fundamental mode. The beam divergence θ may be found by measuring the spot size $w(z)$ at a known distance z from the waist [7.13]. The expression

$$w(z) = w_0 \left(1 + \lambda z/\pi w_0^2\right)^{1/2} \tag{7.10}$$

where w_0 is the waist spot size and λ is the propagation wavelength, is used to derive the half-angle divergence given by

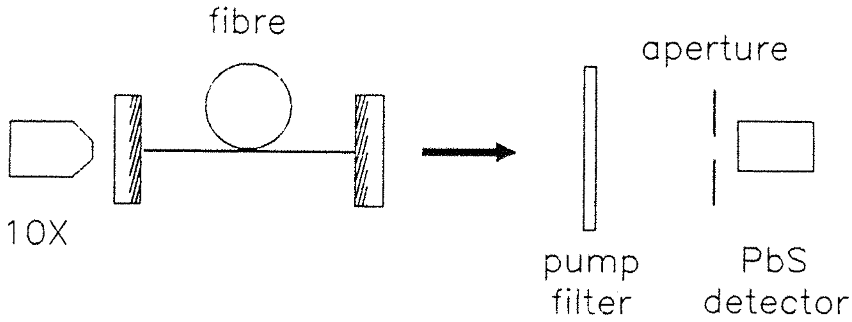

Fig.7.14 Apparatus for scanning the output beam profile

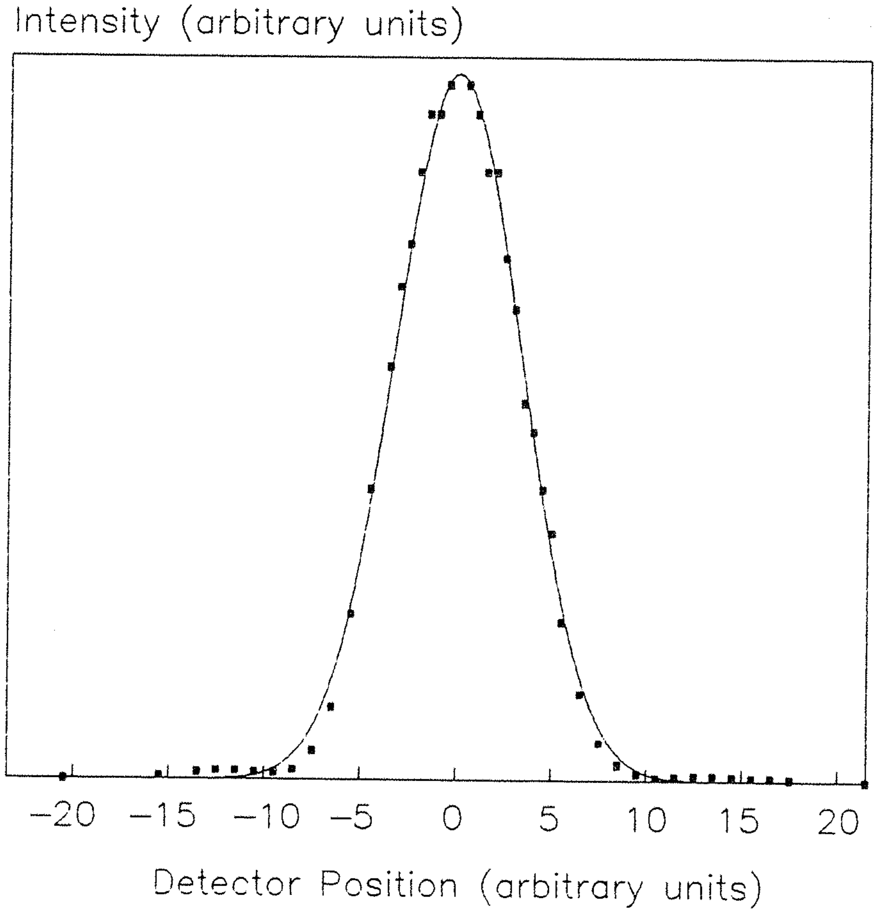

Fig.7.15 Intensity profile of the 2μm fibre laser output beam showing single mode structure

$$\theta = \left. \frac{dw(z)}{dz} \right|_{z \to \infty} \qquad (7.11)$$

as the following

$$\theta = \frac{\lambda}{\pi w_0} \qquad (7.12)$$

Thus by measuring θ directly, the waist spot size w_0 at the fibre output end can be found, providing the distance z is such that $\lambda z/\pi w_0^2 \gg 1$.

Since Fig.7.15 depicts intensity, it is the separation of the $1/e^2$ points on either side of the peak that must be used in conjunction with the distance between the detection position and the output coupler to give the divergence. This measurement yields θ = 103mrad. From Eq.7.12 a waist spot size of 6.2μm is then obtained, assuming a diffraction limited output and taking λ = 2μm. The Gaussian approximation for mode fields [7.14] gives a spot size for the fundamental mode of

$$w_0 = \rho_e \ (\ln \ V)^{-1/2} \qquad (7.13)$$

and so, at 2μm where V = 3.23, the calculated spot size is w_0 = 6.9μm. This is in good agreement with the measured spot size of 6.2μm.

The intensity profile indicates that, although in principle two modes can be supported at 2μm, in practice only the fundamental mode is excited, even when pumped at several times above threshold (in this case up to 6 times the threshold incident power).

The pump profile exhibits a more complicated structure. At 1.064μm the V-number is 6.07, indicating that up to 6 LP modes can propagate [7.12]. A typical profile is shown in Fig.7.16, where the filter has been removed to enable pump light to reach the detector. The full mode structure cannot be seen with a simple linear scan through the beam, but viewing the output on an infrared viewing card

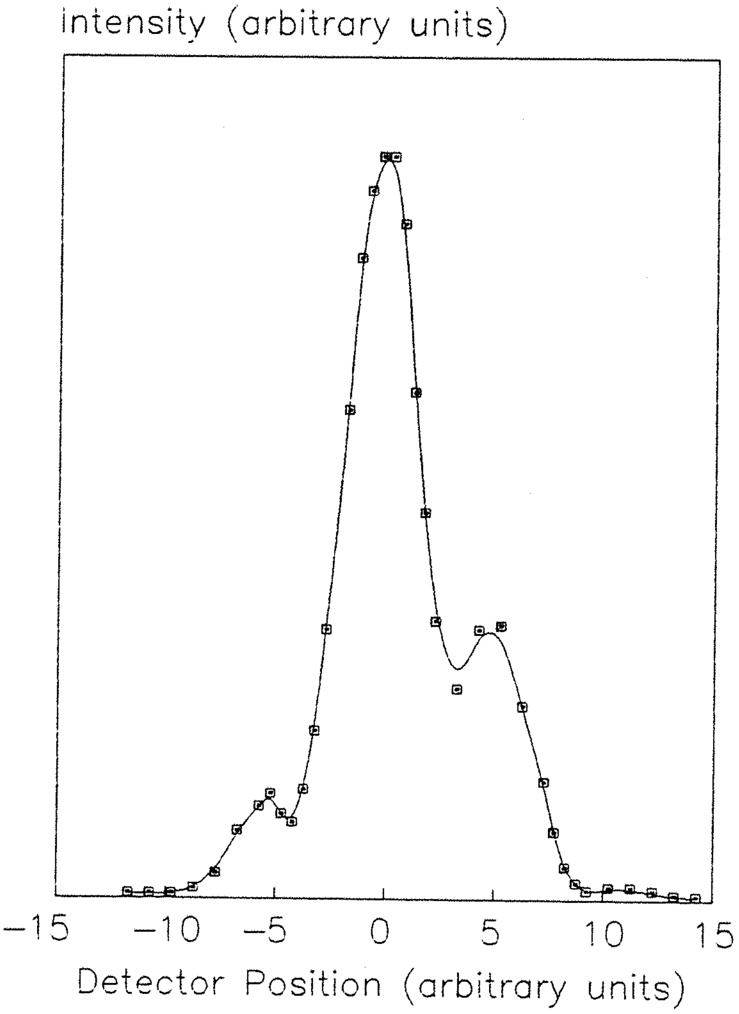

Fig.7.16 Intensity profile of the pump output beam showing multimode structure

confirmed that several modes were propagating.

7.6 Excited State Absorption in Tm^{3+}-Doped Fibre

7.6.1 Introduction

The phenomenon of visible emission from the thulium-doped fibre when pumped at 1.064μm has been described briefly above. In this section the effect is described in more detail, and a rate equation model is developed to describe the effect of the excited state absorption process on the populations of the energy levels, the pump absorption and the small signal gain.

7.6.2 Spectroscopy

A side light fluorescence spectrum (taken with the 8.6μm core diameter fibre) for excitation at 1.064μm is shown in Fig.7.17, where the pump power incident on the launch objective was 6W. The method used to take the spectrum was similar to that described in Section 7.2, with the monochromator here fitted with a grating blazed at 500nm and a photomultiplier tube for signal detection. The predominant feature in the spectrum is a peak in the blue region, centred at 467nm. The blue emission is easily seen with the naked eye for pump powers in the tens of milliwatts region and particularly bright at the multiwatt pump level. There are also much weaker features centred at 368nm, 650nm and 784nm. The blue emission is shown in more detail in Fig.7.18.

The fluorescence lifetimes for these emission wavelengths were measured by interrupting the pump beam with a mechanical chopper and observing the subsequent decay of the side light fluorescence signal on a digital storage oscilloscope, in an experimental arrangement similar to the one shown in Fig.4.5 for the ytterbium lifetime measurements. During the measurements the chopper was situated at the waist of the pump beam to ensure the fastest possible interruption of the beam. However, to determine the system response time the chopper was moved to the fibre output end with the end light signal now monitored by the photomultiplier tube. In this way the continuous wave fluorescence signal from the fibre was chopped, and the decay time was due only to the detection system response. This technique was used because the pump signal was too weak to be observed in side light (the

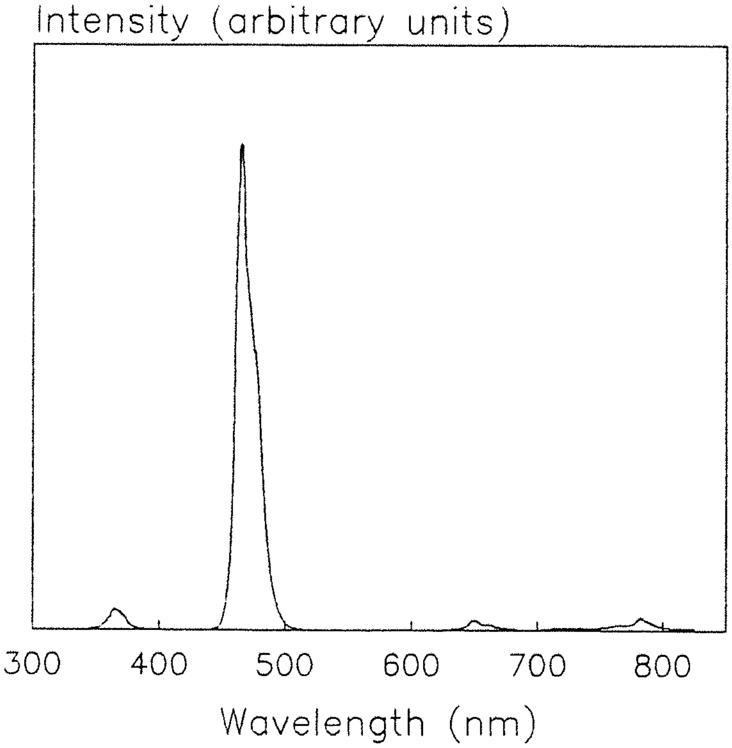

Fig.7.17 Side light upconversion fluorescence spectrum (9μm core diameter fibre)

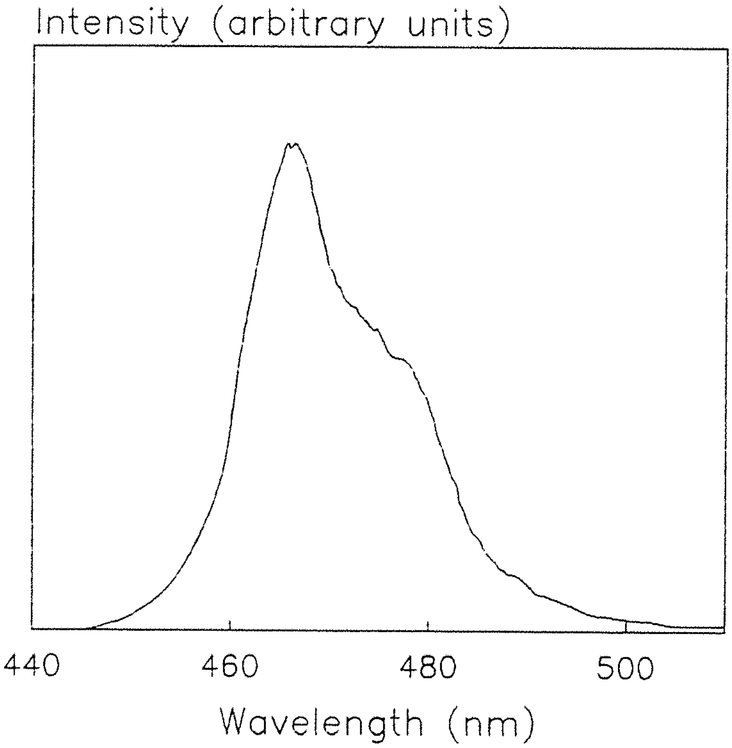

Fig.7.18 As Fig.7.17 with expanded wavelength scale

normal way of measuring system response). The system response, taken as the time for the signal to fall from 90% to 10% of its initial value, was 20μs. Since at the chopping location for this measurement the beam was larger than at the location for lifetime measurements, it may be concluded that in determining the fluorescence lifetimes the system response is ≤ 20μs.

The decay of the blue emission at 467nm was seen to be single exponential with a lifetime of 230μs. The red emission at 650nm also had a measured lifetime of 230μs. The ultraviolet and infrared emissions had much shorter single exponential lifetimes of 20μs, and are therefore likely to be detector-limited (pumping at 797nm with a Styryl 9M dye laser [7.15] gave a lifetime of about 10μs for the infrared decay).

With reference to the energy level diagram of Fig.7.19, the production of the upconverted wavelengths may be described as follows. The blue emission (467nm) arises from decay from the $^1G_4$ level to the Stark levels in the ground state multiplet $^3H_6$, as observed under the direct pumping scheme using 476nm light described in Chapter 6. The red emission (650nm) can also be identified as originating from the $^1G_4$ level since it has the same lifetime. This transition terminates on $^3H_4$, the upper laser level involved in 2μm laser action. Emission at 784nm is thought to be due to decay from $^3F_4$ to $^3H_6$ for the reasons discussed in Chapter 6 involving ground state reabsorption, and emission at 368nm is thought to be due to the $^1D_2$ to $^3H_6$ transition. The high-lying levels are populated by a process of multiphoton sequential absorption of pump and, possibly, fluorescence photons. The process begins with the absorption of a 1.064μm pump photon from the $^3H_6$ ground state into the high energy wing of $^3H_5$, which rapidly decays nonradiatively to $^3H_4$ where population builds up if the fibre is not undergoing laser action at 2μm. Subsequent absorption of a second pump photon from this level into the $^3F_2$ and $^3F_3$ levels is followed by rapid nonradiative decay to $^3F_4$. This level loses population by decay to the ground state giving emission in the infrared around 780nm, and also by absorption by a third pump photon to $^1G_4$, from where the blue and red fluorescence originate. The absorption of the second and third pump photons in this scheme is nearly resonant for both of the relevant transitions, and accounts for the significant amounts of upconverted emission despite the weak absorption of pump light from the ground state. Several mechanisms are

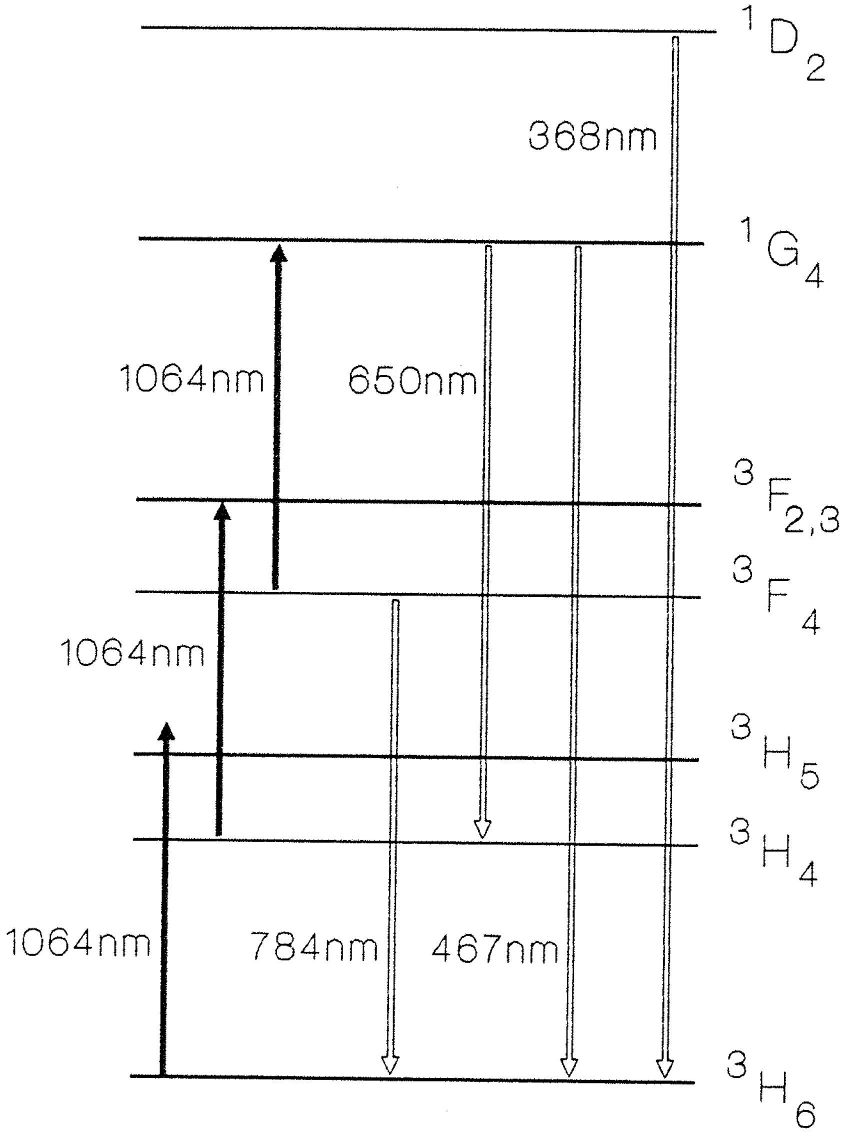

Fig.7.19 Energy levels involved in upconversion in Tm^{3+}-doped fibre

possible for the population of $^1D_2$ [7.16] but the most likely explanation is the absorption of "blue" photons (emitted by radiative relaxation from $^1G_4$ to $^3H_6$) by population in the $^3H_4$ level directly into this $^1D_2$. This is strongly suggested by the increased absorption by the fibre for probe wavelengths of 450-465nm when pumped at 1.064μm compared to when the pump is switched off, after the method of [7.17] and described in [7.16]. Decay from $^1D_2$ to $^3H_4$ is also thought to contribute to the short wavelength side of the blue emission.

The hypothesis that the absorption of three photons is the means by which $^1G_4$ is populated can be validated by measuring the intensity of the blue emission as a function of pump intensity, since the blue intensity will be proportional to the pump intensity raised to the power m, where m is the number of pump photons required to yield one upconverted photon, if phonon-assisted processes and ground state depletion are neglected. A side light monitoring technique (using a fibre bundle to transfer light from the front end of the thulium-doped fibre to the monochromator) was used to measure the blue emission on a photomultiplier tube as the incident pump power was increased from zero to 5W. The 17μm core diameter fibre was used for this measurement. By plotting the logarithm of the blue signal against the logarithm of the incident power, a straight line is obtained with gradient m. This is shown in Fig.7.20, where the gradient over the range of input powers from zero to 1W gives $m = 3$, thus confirming that $^1G_4$ is populated by the absorption of three pump photons. For higher pump powers, ground state depletion becomes significant and the curve begins to saturate such that its gradient falls below $m = 3$.

When laser action occurs from the $^3H_4$ level, the population of this level will differ from its value when lasing does not take place. This has implications for the number of upconverted photons since the reduction in lifetime by stimulated emission means that the population of the excited state is reduced. This was demonstrated by monitoring both the unabsorbed pump power leaving the output end of the fibre, and the side light blue emission, when laser action was allowed and when it was prevented (by unbutting the output coupler). For these measurements a 70cm length of the 17μm core diameter fibre was used. In Fig.7.21 the unabsorbed pump power is plotted against incident pump power for the two cases of lasing and not lasing. This demonstrates that more pump power is absorbed when lasing is prevented, since the $^3H_4$ level is not being clamped by laser action at 2μm. Population can

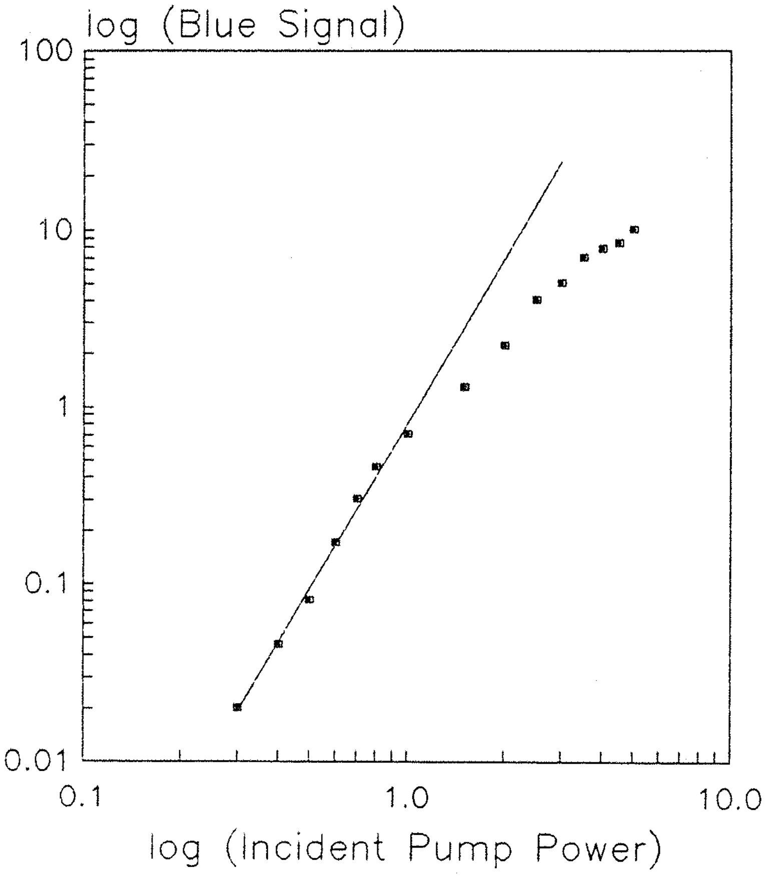

Fig.7.20 Log plot for emission at 467nm versus pump power. Straight line gradient = 3

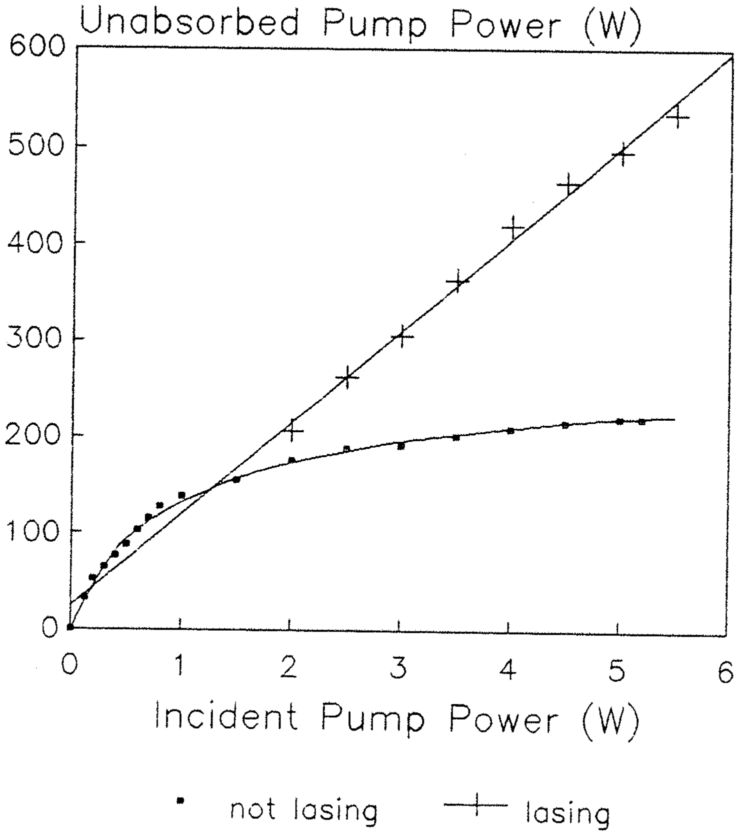

Fig.7.21 Unabsorbed pump power versus incident power for 70cm fibre for lasing (at 2μm) and not lasing cases

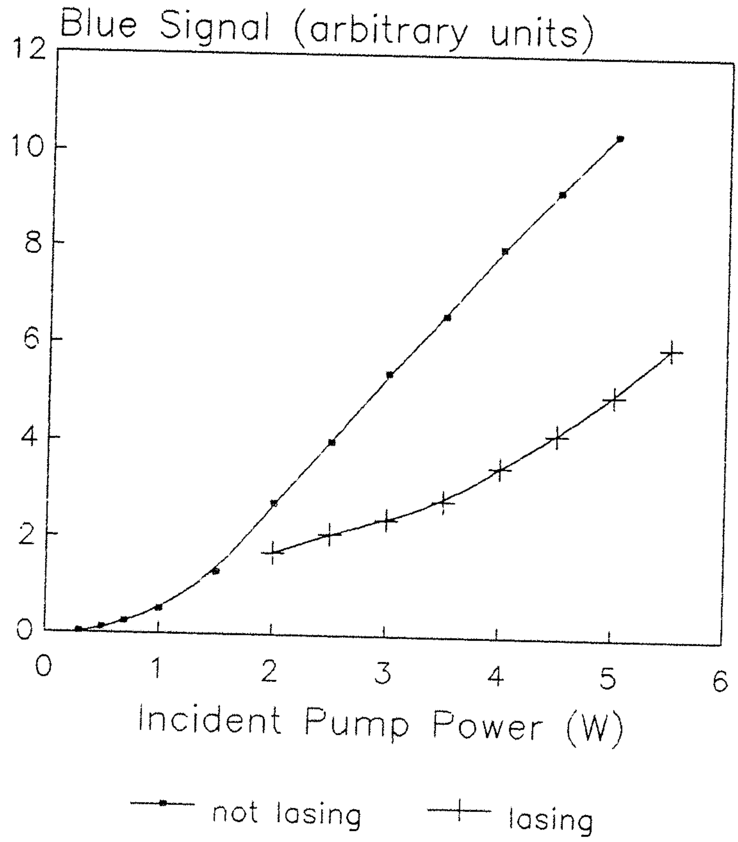

Fig.7.22 Side light fluorescence at 467nm versus pump power for lasing (at 2μm) and not lasing cases

build up in this level and is therefore available for upconversion. The linear (for the range of powers used here) power dependence for the lasing case, as discussed in Section 7.3, indicates that the ESA problem is not as detrimental as might first be thought, since for a given power above threshold the pump absorption during laser action is less than that when oscillation is prevented. Fig.7.22 shows the blue signal at 467nm as monitored on the photomultiplier tube in side light as the pump power is varied for the lasing and non-lasing cases. The non-lasing curve has a cubic dependence on pump power up to 1W as described above. For powers in excess of about 1W, the curve saturates and the power law dependence falls from 3 to about 1.5 (for 5W incident). During laser action, the blue yield is generally much reduced since the amount of upconversion is reduced by the decreased population in $^3H_4$. The point at which the two curves intersect defines threshold. Fig.7.22 indicates that this would occur at about 1.5W incident for the 70cm length of fibre used here, and in fact threshold was measured as 1.2W, in reasonable agreement.

The yield of upconverted fluorescence, for a fixed pump power, has been demonstrated to decrease significantly when laser action occurs at 2μm compared to that observed when laser action is prevented, and the slope efficiency with respect to absorbed power is comparable to that achieved for pump wavelengths that do not lead to excited state absorption. The main problem presented by ESA then, in the 1.064μm pumped scheme, is the imposition of a high threshold, since the removal of upper laser level population by ESA means the pump rate must be high enough to compensate for this loss before inversion can be attained. It is probable that a marked reduction in threshold could be achieved, perhaps by modifications in the host fibre fabrication process to alter the lifetimes and cross sections favourably.

7.7 Modelling of the Thulium-Doped Fibre

7.7.1 Introduction

In this section, a simple rate equation model of the thulium system is used to describe the pump absorption, small signal gain at 2μm, and the populations of the energy levels, in the presence of excited state absorption leading to upconverted emission in the blue. The model

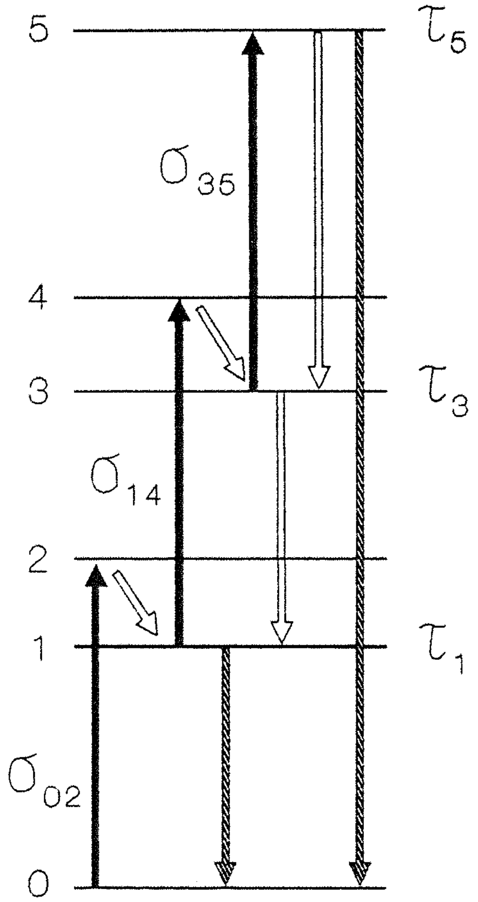

Fig.7.23 Energy levels and notation used in modelling the level populations and laser gain in the Tm^{3+}-doped fibre

considers the ground state and the first five excited states up to $^1G_4$, *i.e.*, any contribution to the blue emission from $^1D_2$, and for that matter the ultraviolet emission, is neglected in order to simplify the analysis. This is justified in view of the short lifetime of $^1D_2$ ($\leq 20\mu s$) and the fact that the ultraviolet emission is very weak compared to the blue. For similar reasons the infrared emission around 780nm arising from the $^3F_4$ – $^3H_6$ transition, and the red emission around 650nm arising from the $^1G_4$ – $^3H_4$ transition, are also neglected.

The remaining transitions that will be considered are shown in Fig.7.23. The energy levels are labelled from 0 to 5, where level 0 represents $^3H_6$, level 1 represents $^3H_4$, level 2 represents $^3H_5$, level 3 represents $^3F_4$, level 4 represents $^3F_{2,3}$ and level 5 represents $^1G_4$. These levels have populations n_i, where i is the level label 0 to 5. The lifetimes of levels 5, 3 and 1 are given by τ_5, τ_3 and τ_1, respectively. Levels 2 and 4 are assumed in this analysis to decay very rapidly such that their lifetimes may be neglected. The absorption cross section for the pump transition (0 to 2) is given by σ_{02}, and the two successive excited state absorption processes (1 to 4 and 3 to 5) have cross sections of σ_{14} and σ_{35}, respectively. The emission cross section for 2μm fluorescence on the 1 to 0 transition is given by σ_{10}.

7.7.2 Rate Equations

The total population n is given by the sum of the individual level populations, such that

$$n = n_0 + n_1 + n_2 + n_3 + n_4 + n_5 \tag{7.14}$$

Since levels 2 and 4 are constrained to be empty this reduces to

$$n = n_0 + n_1 + n_3 + n_5 \tag{7.15}$$

Let the transition rate between levels i and j be W_{ij}. The rate equations for levels 0, 1, 3 and 5 may then be written as

$$W_{10}\, n_1 + W_{50}\, n_5 = W_{02}\, n_0 \tag{7.16}$$

$$W_{02}\, n_0 + W_{31}\, n_3 = (W_{10} + W_{14})\, n_1 \tag{7.17}$$

$$W_{14}\, n_1 + W_{53}\, n_5 = (W_{31} + W_{35})\, n_3 \tag{7.18}$$

$$W_{35}\, n_3 = (W_{53} + W_{50})\, n_5 \tag{7.19}$$

From Eq.7.19, n_5 may be expressed as

$$n_5 = \frac{W_{35}}{W_{53} + W_{50}}\, n_3 \tag{7.20}$$

Substituting for n_5 in Eq.7.18 yields

$$n_3 = \frac{W_{14}}{W_{31} + W_{35} - \dfrac{W_{53} W_{35}}{W_{53} + W_{50}}}\, n_1 \tag{7.21}$$

and substituting for n_3 in Eq.7.17 gives

$$n_1 = \frac{W_{02}}{W_{10} + W_{14} - \dfrac{W_{31} W_{14}}{W_{31} + W_{35} - \dfrac{W_{53} W_{35}}{W_{53} + W_{50}}}}\, n_0 \tag{7.22}$$

Eqs. 7.20, 7.21 and 7.22 may be simplified by noting that the transition rates for decay may be written as

$$W_{10} = \tau_1^{-1} \tag{7.23}$$

$$W_{31} = \tau_3^{-1} \tag{7.24}$$

Level 5, unlike levels 3 and 1, decays to more than one final level in the model and so the total decay rate is given by

$$W_{50} + W_{53} = \tau_5^{-1} \tag{7.25}$$

where the transition 5 → 0 has radiative quantum efficiency η given by

$$\eta = \frac{W_{50}}{W_{50} + W_{53}} \tag{7.26}$$

The transition rate for absorption of the initial photon in the three photon process is given by

$$W_{02} = \frac{\sigma_{02} I}{h\nu} \tag{7.27}$$

where h is Planck's constant, ν is the frequency of the pump light and $I(z)$ is the local pump intensity at distance z along the fibre. By introducing the pump saturation intensity I_s, where $I_s = h\nu/(\sigma\tau_1)$, and the parameter $k(z) = I(z)/I_s$, W_{02} becomes

$$W_{02} = k(z)/\tau_1 \tag{7.28}$$

Similarly, by introducing the parameters

$$\beta_{14} = \sigma_{14}/\sigma_{02} \tag{7.29}$$

$$\beta_{35} = \sigma_{35}/\sigma_{02} \tag{7.30}$$

the transition rates for the two ESA processes may be written as

$$W_{14} = \beta_{14}k(z)/\tau_1 \tag{7.31}$$

$$W_{35} = \beta_{35}k(z)/\tau_1 \tag{7.32}$$

For further simplification in later expressions two further parameters are introduced:

$$\gamma_3 = \tau_3/\tau_1 \tag{7.33}$$

$$\gamma_5 = \tau_5/\tau_1 \tag{7.34}$$

Eqs.7.20, 7.21 and 7.22 may then be written as

$$n_5(z) = \gamma_5\beta_{35}\ k(z)\ n_3(z) \tag{7.35}$$

$$n_3(z) = \frac{\gamma_3\beta_{14}\ k(z)}{1 + \eta\gamma_3\beta_{35}\ k(z)}\ n_1(z) \tag{7.36}$$

$$n_1(z) = \frac{k(z)}{1 + \dfrac{\eta\gamma_3\beta_{14}\beta_{35}k^2(z)}{1 + \eta\gamma_3\beta_{35}k(z)}}\ n_0(z) \tag{7.37}$$

The populations of levels 1,3 and 5 are thus described in terms of the length-independent parameters η, β, γ and the length-dependent parameter $k(z)$. The form of this length dependence of $k(z)$ is considered in the following section.

7.7.3 Pump Absorption

In a simple two-level absorption scheme, the decay of the pump intensity $I(z)$ with distance z along the fibre is expressed as

$$\frac{dI(z)}{dz} = - \sigma_a n' I(z) \tag{7.38}$$

where σ_a is the absorption cross section of the transition and n' is the population difference between the lower and upper level. In the case of the model for the thulium system there are three absorbing transitions acting on the pump light, and the basic equation for pump decay is given by

$$\frac{dI(z)}{dz} = - \left(\sigma_{02} n_0(z) + \sigma_{14} n_1(z) + \sigma_{35} n_3(z)\right) I(z) \tag{7.39}$$

where n_5 has been neglected since it is small with respect to n_3. By utilising the parameters k and β, Eq.7.39 may be rewritten in the following form:

$$- \frac{1}{k} \frac{dk(z)}{dz} = \sigma_{02} n_0(z) \left[1 + \beta_{14} \frac{n_1(z)}{n_0(z)} + \beta_{35} \frac{n_3(z)}{n_0(z)} \right] \tag{7.40}$$

The ratios $n_1(z)/n_0(z)$ and $n_3(z)/n_0(z)$ are found from Eqs.7.36 and 7.37. At this point it is useful to introduce the normalised length

$$w = z/l \tag{7.41}$$

where l is the fibre length, and the parameter

$$f = \sigma_{02} n l \tag{7.42}$$

which for a fixed fibre length is a constant, where $\sigma_{02} n$ is the absorption coefficient α. Eq.7.40 then becomes

$$\frac{dk(w)}{dw} = -fk(w)\,\frac{n_0(w)}{n}\left[1 + \frac{\beta_{14} k(w)}{1 + \dfrac{\eta\gamma_3\beta_{14}\beta_{35}k^2(w)}{1 + \eta\gamma_3\beta_{35}k(w)}}\left[\frac{1 + (1+\eta)\gamma_3\beta_{35}k(w)}{1 + \eta\gamma_3\beta_{35}k(w)}\right]\right] \tag{7.43}$$

The ratio $n_0(w)/n$ is found by substituting for n_1, n_3 and n_5 (by using Eqs.7.35, 7.36 and 7.37) in Eq.7.15 to obtain

$$\frac{n_0(w)}{n} = \left[1 + \frac{k(w)}{1 + \dfrac{\eta\gamma_3\beta_{14}\beta_{35}k^2(w)}{1 + \eta\gamma_3\beta_{35}k(w)}}\left[1 + \frac{\gamma_3\beta_{14}k(w)}{1 + \eta\gamma_3\beta_{35}k(w)}\left(1 + \gamma_5\beta_{35}k(w)\right)\right]\right]^{-1} \tag{7.44}$$

Hence Eqs.7.43 and 7.44 can be used to describe the evolution of the pump intensity with fibre length through the parameter $k(w)$.

7.7.4 Gain on the 2μm Transition

The expression describing the rate of change of laser intensity $I_L(z)$ with distance z along the fibre is

$$\frac{dI_L(z)}{dz} = \sigma_{10} n_i I_L(z) \tag{7.45}$$

where n_i is the population inversion. The upper level population is n_1, and the lower level is a Stark level in the ground state multiplet with a population of an_0, where a is the fraction of the total ground state population residing in the Stark level under conditions of thermal equilibrium. Hence the gain may be expressed by

$$\frac{1}{I_L(z)}\frac{dI_L(z)}{dz} = \sigma_{10}\left(n_1(z) - an_0(z)\right) \tag{7.46}$$

The single pass exponential gain coefficient (the right hand side of Eq.7.46) may then be calculated for various values of the fractional lower level population, a, by substituting for n_1 and n_0 (using Eqs.7.15, 7.35, 7.36 and 7.37) and integrating over the fibre length l.

The population of levels 5, 3 and 1 (Eqs.7.35, 7.36 and 7.37) may now be expressed in terms of the total population n (after appropriate substitutions and use of Eq.7.44), together with the decay of the pump intensity (Eq.7.43) and the laser gain (Eq.7.46). The parameterisation of these expressions was performed to facilitate the use of computer solution methods to calculate the populations, remaining pump intensity (or power in this case, since the fibre area is constant) and gain, for a given fibre length over a range of input pump intensities. Of these, the only directly measurable quantity is the unabsorbed pump power exiting the end of the fibre as a function of incident pump power. This data was obtained by pumping a 74cm length of the 17μm core diameter fibre at 1.064μm and monitoring the output pump power on a power meter while varying the incident power. A cut back determined the launch efficiency to be 40%. Fig.7.24 shows the resulting unabsorbed pump power versus launched pump power curve to which the model will be fitted.

7.7.5 Fitting the Model

Most of the parameters featuring in the model can be estimated on the basis of experimental evidence. The lifetime of level 5 is taken as τ_5 = 230μs, and that of level 3 as τ_3 = 10μs. The level 1 lifetime of τ_1 = 200μs then yields γ_5 = 1.15 and γ_3 = 0.05. The absorption cross

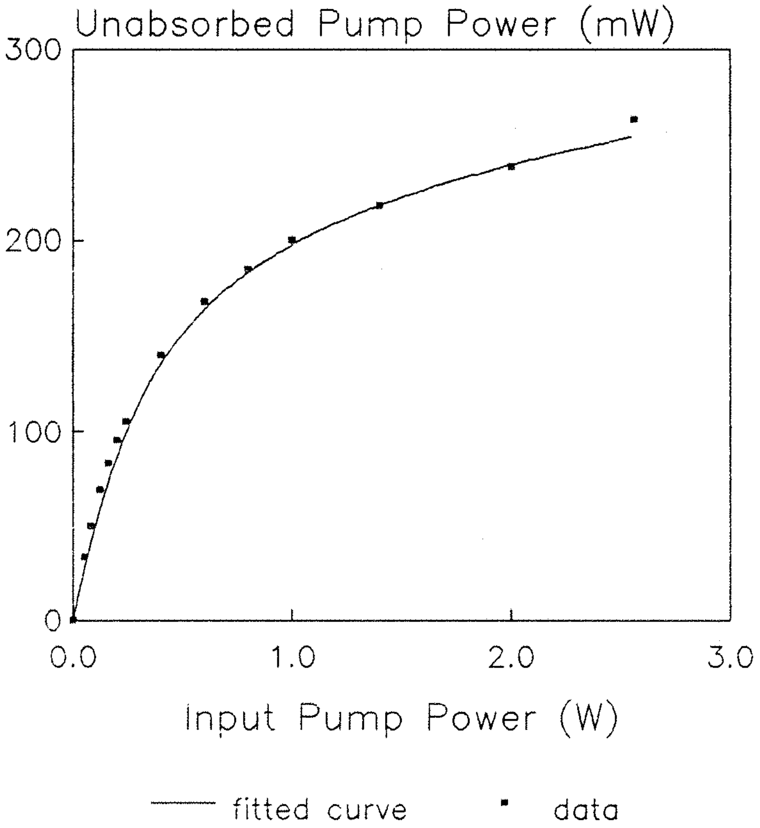

Fig.7.24 Unabsorbed pump power versus input power for 74cm fibre, with curve calculated from the model added

section σ_{02} is found from $\sigma_{02} = \alpha/n$, where the absorption coefficient $\alpha = 0.46\text{m}^{-1}$ and dopant concentration $n \approx 1.86 \times 10^{25}$ ions/m^3 give $\sigma_{02} \approx 2.5 \times 10^{-26}$ m^2. The emission cross section σ_{10} is calculated using the relation [7.19]

$$\sigma_{10} = \frac{\lambda^4 A}{8\pi\, c\, n_{ri}^2\, \Delta\lambda_{eff}} \tag{7.47}$$

where λ is the peak fluorescence wavelength, A^{-1} is the radiative lifetime of the transition, c is the speed of light, n_{ri} is the refractive index of the host and $\Delta\lambda_{eff}$ is the effective width of the fluorescence band, defined as the integrated fluorescence intensity divided by the peak fluorescence intensity. Taking $A^{-1} = 3.4$ms [7.18], $n_{ri} = 1.4585$, $\Delta\lambda_{eff} = 200$nm and $\lambda = 2\mu$m gives $\sigma_{10} \approx 1.4 \times 10^{-24}$ m^2. The radiative quantum efficiency η for level 5 is estimated using the Fuchtbauer–Ladenburg relation introduced in Chapter 4 (Eq.4.1). Measurements on the absorption spectrum (Fig.6.1) for the $^3H_6 \rightarrow {}^1G_4$ transition yield a calculated radiative lifetime of 2.2ms. The measured lifetime of 230μs therefore indicates a quantum efficiency of $\eta \approx 0.1$. Finally, of the "known" parameters, for a fibre length l of 74cm, the length parameter $f = \sigma_{02} n l$ is 0.34.

Two fitting parameters remain, β_{14} and β_{35}, representing the absorption cross sections for the second and third steps in the three photon excitation process of level 5. To proceed, an input pump power P_{in} is set. This defines an initial $k(z)$ value of $k(0) = P_{in}/P_s$. Eq.7.43 is then integrated along the fibre length (using Eq.7.44 to substitute for $n_0(z)/n$) to calculate the total change in the value of k, from which the unabsorbed pump power can be calculated, *i.e.*, the unabsorbed pump power is equal to $[k(0) - k(l)] \times P_{sat}$. This is repeated for several values of the input pump power, *i.e.*, several values of $k(0)$, to produce a curve showing unabsorbed pump power versus input pump power. The cross section parameters are then adjusted until this curve fits the experimental data of Fig.7.24.

Since the absorptions between levels 1 → 4 and levels 3 → 5 are nearly resonant, whereas the ground state absorption terminates in the wings of the level 2 absorption band, the initial assumption that $\beta_{14} \geq 1$ and $\beta_{35} \geq 1$ is made. Fitting the experimental data was achieved by first selecting equal values of β_{14} and β_{35}. Values for these β of 25, 50 and 85 were tried initially, but none were satisfactory, and in fact the problem lies with the relatively high value of β_{35}. Fig.7.25 shows the curves generated for $\beta_{35} = 10$ as β_{14} is varied from 60 to 90. The fit is reasonable for low input powers (<500mW) for $\beta_{14} = 60$, but poor at higher powers. With $\beta_{14} = 90$ the fit is slightly improved for input powers greater than about 1000mW at the expense of the fit at low powers. The fit of the curves is more sensitive to variations in β_{14} for low input powers (≤ 1000mW) and more sensitive to β_{35} for higher powers, as may be expected since the probability of the three photon absorption process has a cubic dependence on input power and is therefore more significant at the higher power levels. The best fit was obtained for $\beta_{14} = 80$ with β_{35} reduced to unity, as shown by the curve fitted to the data in Fig.7.24.

These fitted values of β_{14} and β_{35} are then used to calculate the populations of levels 0, 1, 3 and 5 as a function of input pump power. The ground state population n_0 is found directly from Eq.7.44, and the excited state populations n_1, n_3 and n_5 follow from Eqs.7.37, 7.36 and 7.35, respectively. In Fig.7.26 the populations of the excited levels 1, 3 and 5 are shown as fractions of the total population n against input pump power. These values represent the populations at the end of the 74cm fibre used to obtain the output pump power versus input pump power data. The population of level 1, where laser action at 2μm initiates, is seen to build up rapidly with pump power, whereas the populations of levels 3 and 5 lie substantially below this curve over the range of input powers encountered in this particular experimental set-up. The fraction of the total population residing in level 0 changes by only 10% over the same power range, falling from unity for zero input power to about 0.9 for 2.5W input. The evolution of the populations along the fibre length may be found for a given input power by successive calculations of the populations at the end of differing lengths of fibre. Fig.7.27 shows this dependence for fibre lengths between zero and 1m, for an input power of 1W. For this same input power, the fractional population of level 0 varies little, from 0.85 at the input end to 0.95 at the end of the 1m fibre.

The most significant point arising from these population curves is that n_5 is very small, despite the impression given by the strong blue emission easily visible to the eye that there is a considerable population in this level. The low population is confirmed by the rough

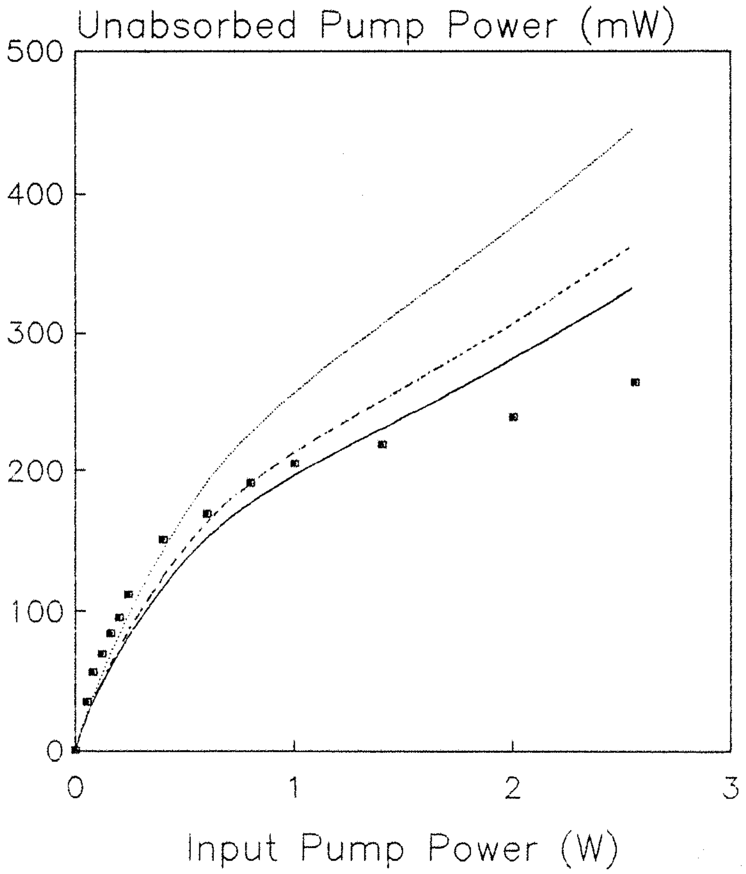

Fig.7.25 Unabsorbed pump power versus input pump power, data points as Fig.7.24.
Curves derived from the model added.
Dotted line: β_{35} = 10, β_{14} = 60
Dashed line: β_{35} = 10, β_{14} = 80
Solid line : β_{35} = 10, β_{14} = 90

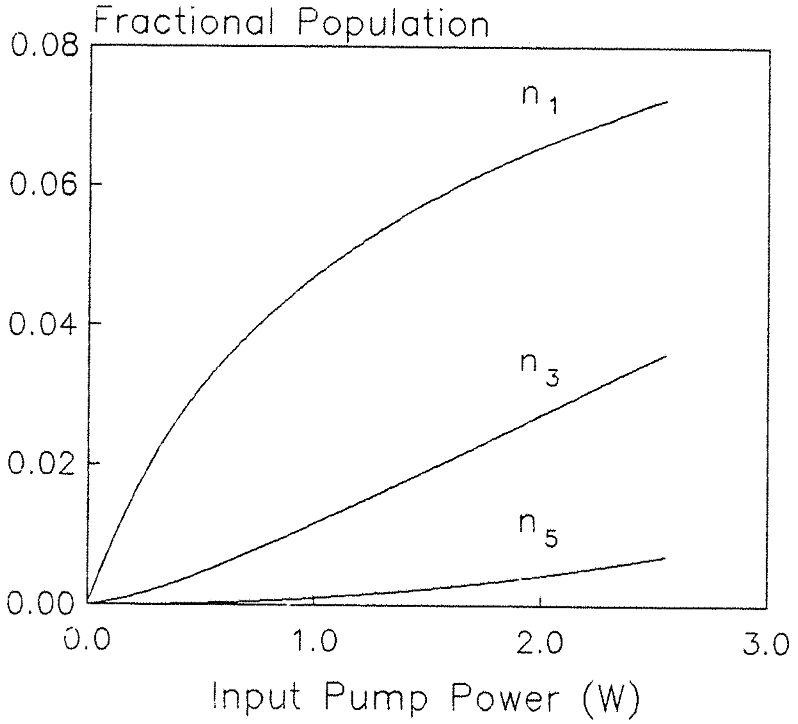

Fig.7.26 Populations of levels 1, 3 and 5 versus input power for 74cm fibre

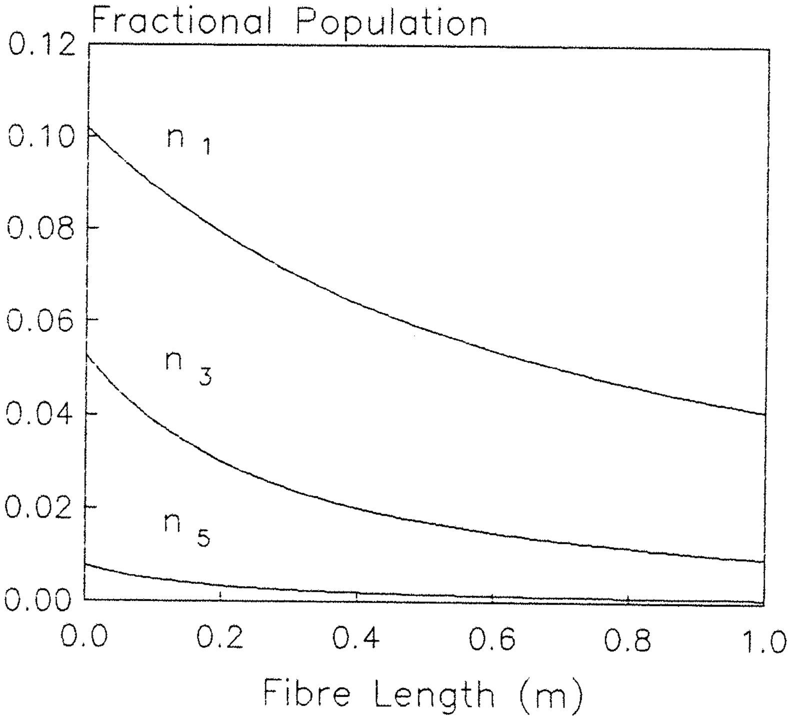

Fig.7.27 Populations of levels 1, 3 and 5 versus fibre length for 1W input power

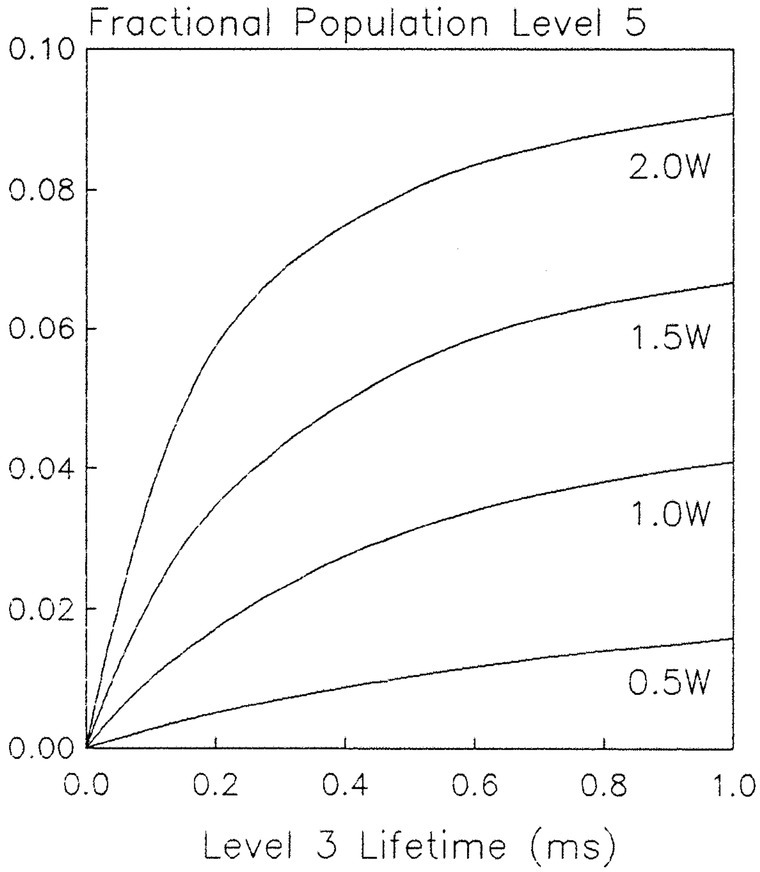

Fig.7.28 Dependence of level 5 population on level 3 lifetime

estimates made by Hanna *et al.* [7.16] who reported that only about 10^{-4} to 10^{-5} of the ground state population was excited to the $^1G_4$ level for a 1W input power to a 9μm core diameter Tm^{3+}-doped fibre. This very low upconversion efficiency is believed to be a direct result of the shortening of the intermediate level lifetimes by nonradiative decay, a feature which removes population from these levels that could otherwise contribute to ESA into the blue emitting level. To demonstrate the detrimental effect that this lifetime shortening has on the yield of upconverted fluorescence, a range of values for the lifetime τ_3 of level 3 ($^3F_4$) was substituted into the model, keeping all other lifetimes fixed at their experimentally observed values. The dependence of the level 5 population ($^1G_4$) on this lifetime is shown in Fig.7.28 for input pump powers of 0.5W. 1.0W, 1.5W and 2.0W. The population is seen to be strongly dependent on τ_3 for lifetimes less than about 200μs, with the response becoming less sensitive for longer lifetimes. The prospects for a significant increase in the population seem poor, since even an increase of τ_3 to 1ms gives only about a factor of two increase in the population over its value with the measured lifetime of around 200μs. An increase in yield could be expected by extending the level 1 ($^3H_4$) lifetime. This was an important factor in the successful demonstration of upconversion laser action at 455nm and 480nm in Tm^{3+}-doped fluorozirconate fibre [7.20], where the lower phonon energies and, therefore, reduced nonradiative decay rates, gave lifetimes for $^3H_4$ and $^3F_4$ of 6.0ms (τ_1) and 1.4ms (τ_3), respectively.

Returning to the original conditions for the silica fibre, the single pass exponential gain coefficient for the $^3H_4 \rightarrow {}^3H_6$ transition may be calculated from Eq.7.46, which is integrated along the fibre length for a range of input powers and values of the lower level population factor, *a*. The dependence of gain on input power for the 74cm fibre is shown in Fig.7.29, where *a* varies from zero to 4% of the total ground state population n_0. At threshold, the single pass gain is just sufficient to offset the total single pass losses. Since the loss mechanism due to ESA and reabsorption is already taken into account by the model, the only remaining loss mechanisms are the fixed mirror transmissions and the fixed coupling and butting losses. A minimum threshold gain coefficient $G_{th}^{min} = \ln\,(R_1R_2)^{-1/2}$ is required to overcome the fixed mirror losses, where R_1 and R_2 are the mirror reflectivities. In the case of the device being modelled here, the

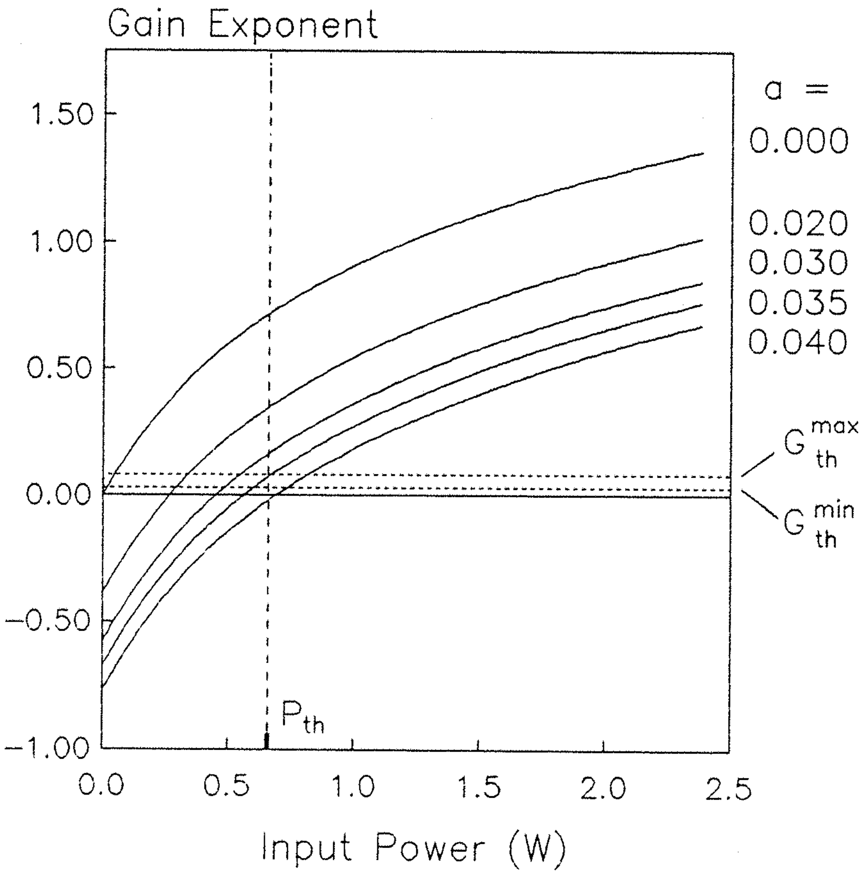

Fig.7.29 Single pass gain exponent for 74cm fibre versus input power for a range of lower laser level population fraction *a*. Measured threshold power and estimated threshold gain are also shown.

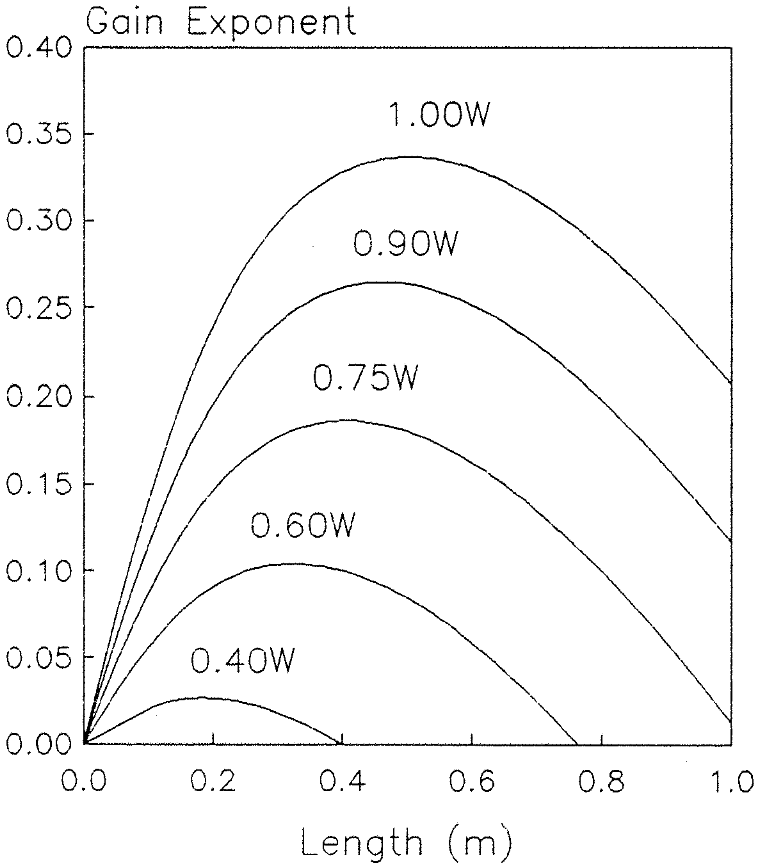

Fig.7.30 Single pass gain exponent versus fibre length for a range of input pump power with lower level population fraction *a* = 0.035

high reflector and 6% output coupler imply $R_1 = 1.00$ and $R_2 = 0.94$, giving $G_{th}^{min} = 0.03$. The unknown coupling and butting losses will increase this required threshold gain exponent. Assuming a worst case loss of 5% at each end, the maximum gain requirement is $G_{th}^{max} \approx 0.08$. From section 7.5.2, the incident threshold power for a fibre of similar length (70cm) was 1.2W, which corresponded to an input power of 660mW. Fig.7.29 indicates that for an input power of 660mW, the required threshold gain exponent of 0.03-0.08 is met for $a \approx 0.035$, *i.e.*, the $a = 0.035$ curve intersects the loss line (region between G_{th}^{max} and G_{th}^{min}) at the measured threshold power. Lower values of a would achieve threshold for a lower input power, and higher values would need a higher input power to overcome the higher lower level reabsorption losses.

The variation of gain with fibre length is shown in Fig.7.30 for input powers ranging from 400mW to 1W, where a has been set at 3.5%. The figure shows that for each pump power there exists an optimum length at which the gain is maximised. The estimated threshold gain exponent requirement of 0.03-0.08 implies that for the particular fibre being modelled, the minimum possible power for which threshold can be achieved is about 400-600mW in a fibre length of 20-30cm (in the most optimistic case where losses are due only to the 6% output coupler, the figure shows that a minimum input power requirement of about 400mW will be sufficient to achieve threshold in a 20cm fibre).

7.8 Characteristics of Fibres with a Modified Core Composition

7.8.1 Introduction

In Section 7.7.5, the role of the intermediate level lifetimes in the upconversion scheme were discussed briefly. The short ($\leq 10\mu s$) lifetime of the $^3F_4$ level is possibly due to clustering of the dopant ions, a situation whereby two or more ions may be close enough for a significant interaction to occur between them. The interaction allows nonradiative energy transfer to take place between an excited ion and a nearby unexcited ion and consequently shortens the radiative lifetime of the excited ion. Clustering occurs during the heating phase of fibre fabrication and it has been estimated [7.21] that approximately 68% of the ions in the 840ppm thulium fibres are clustered. This is beneficial from the point of view of YAG-pumped operation at 2μm since it helps to lessen the population build-up in the intermediate levels, and indicates that a higher doping level (*i.e.*, more clustering) may be even more effective. However, shortening of the upper laser level lifetime would have an adverse effect on the threshold power.

The converse situation, *i.e.*, longer intermediate level lifetimes, was investigated with two additional fibre samples fabricated from preforms in which the refractive index of the core was raised with Al_2O_3 rather than GeO_2. The reason for investigating this change in the host composition is that the incorporation of aluminium improves the solubility of the dopant ions so that they are better dispersed so that any clustering should be reduced. The two fibres both had numerical apertures of 0.15, core diameters of ≈ 6μm and LP_{11} mode cut off wavelengths of 1.1μm, and differed only in their dopant concentrations of 200ppm and 1000ppm.

7.8.2 Spectroscopy

Fluorescence decay lifetimes following excitation at 1.064μm were measured in side light. The transition wavelength was measured with a 0.25m monochromator and the emission was detected with a photomultiplier tube (90%-10% response time 20μs) for fluorescence in the ultraviolet and visible regions, and a Ge photo-diode and amplifier for the infrared (90%-10% response time 50μs). The lifetimes of the emitting levels for the alumina-silica fibres are summarised below in Table 7.3 together with those for the germano-silica fibre for reference. The fluorescence wavelength used for each measurement is also shown. In some cases, notably with the alumina-silica samples, there are two lifetime components, designated in the Table as *f* for the fast component and *s* for the slow component.

The most striking feature of these measurements is that both the $^3F_4$ and $^3H_4$ lifetimes are significantly lengthened in the alumina-silica host. Also apparent is the presence of a fast component in the decays of $^1D_2$ and $^3F_4$. In general, a distribution of decay rates is expected for rare-earths in glass due to the variations in local environment, and if this distribution is large the decays will be highly non-exponential. However, with laser excitation, only subsets of ions are excited and the decays will be more exponential. In the case of $^1D_2$ it is possible that more than one subset is excited, since this level is thought to be populated by the absorption from $^3H_4$ of the 20nm-bandwidth blue emission arising from the $^1G_4$ - $^3H_6$ transition, rather than directly from the laser source. The apparent slow component of the $^3F_4$ decay, however, is not thought to be genuine, but rather an artifact of relaxation from $^1G_4$ to the $^3F_4$ level. This is supported by the close correspondence between the $^3F_4$ slow component and the $^1G_4$ lifetime, but most significantly by results obtained from direct-pumping of $^3F_4$ [7.22] at 785nm which yielded a decay lifetime of 25μs. The difference between the two hosts can therefore be summarised as increased lifetimes for $^1G_4$ and $^3H_4$, both important levels in the upconversion process and likely to have consequences for laser action at 2μm.

Initial Level	Final Level	Emission Wavelength (nm)	Lifetime (μs)					
			Fibre 1		Fibre 2		Fibre 3	
			f	*s*	*f*	*s*	*f*	*s*
$^1D_2$	$^3H_6$	366	40	70	40	70		20
$^1G_4$	$^3H_6$	470		365		355		230
$^1G_4$	$^3H_4$	650		355		350		230
$^3F_4$	$^3H_6$	790	50	270	70	350		10
$^3H_4$	$^3H_6$	1900		500		500		200

Fibre 1: 200ppm Al_2O_3-SiO_2
Fibre 2: 1000ppm Al_2O_3-SiO_2
Fibre 3: 840ppm GeO_2-SiO_2

Table 7.3

The side light technique used for visible fluorescence in the GeO_2-SiO_2 fibre was also employed for the two Al_2O_3-SiO_2 fibres. The pump power incident on the 10X launch objective was 6W at 1.064μm. Figs.7.31 and 7.32 show the spectra from 300nm to 850nm for the 200ppm and 1000ppm fibres, respectively. The blue emission over the 430-520nm range is shown in more detail in Figs.7.33 (200ppm) and 7.34 (1000ppm). Taking into account the sensitivity setting of the signal amplifier and integrating under the spectra, the yield of blue

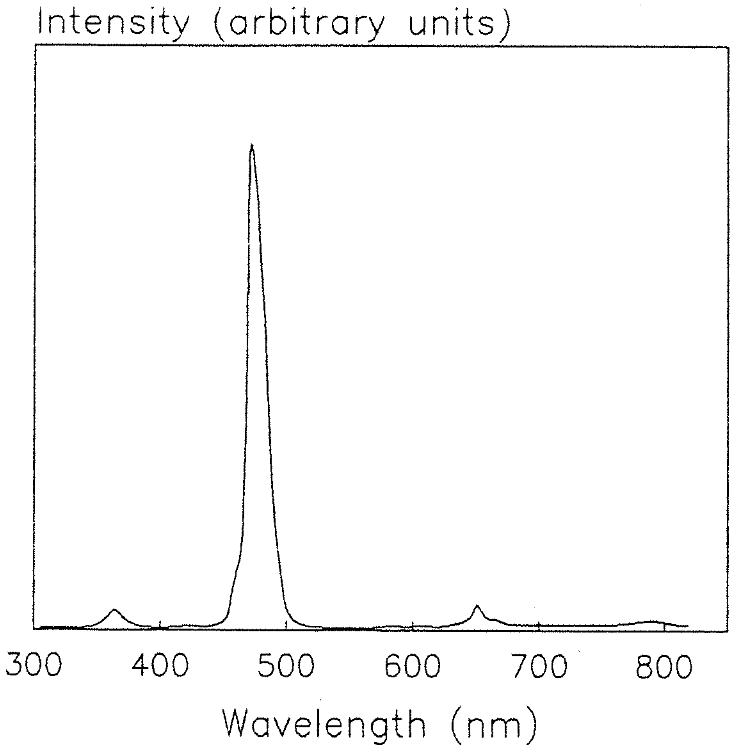

Fig.7.31 Side light upconversion fluorescence spectrum for alumina-silica fibre (200ppm)

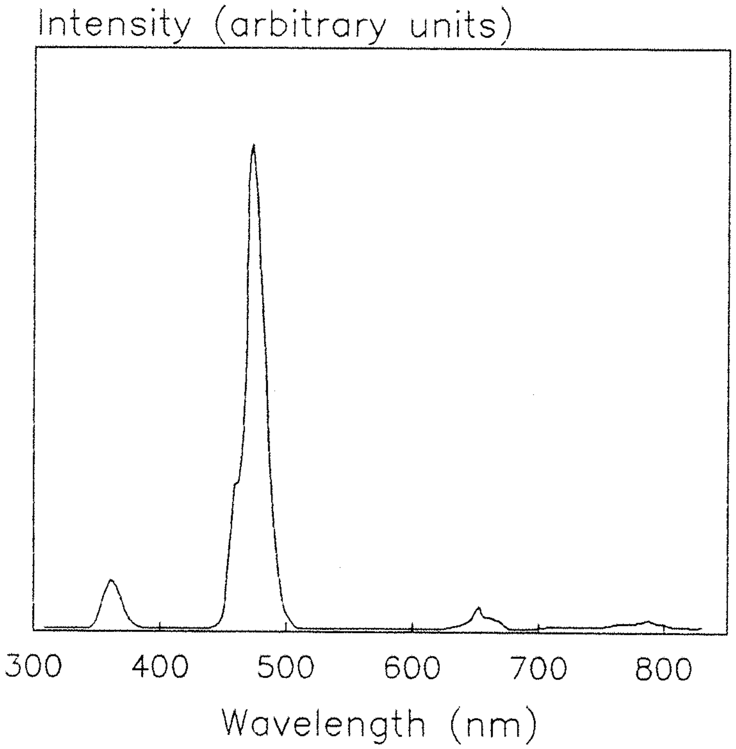

Fig.7.32 Side light upconversion fluorescence spectrum for alumina-silica fibre (1000ppm)

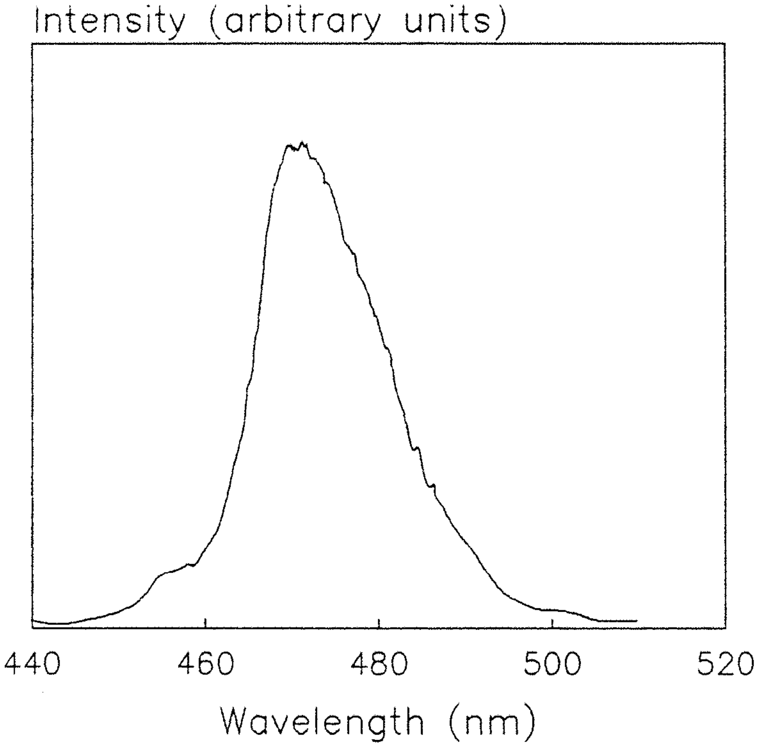

Fig.7.33 As Fig.7.31 with detail of blue emission

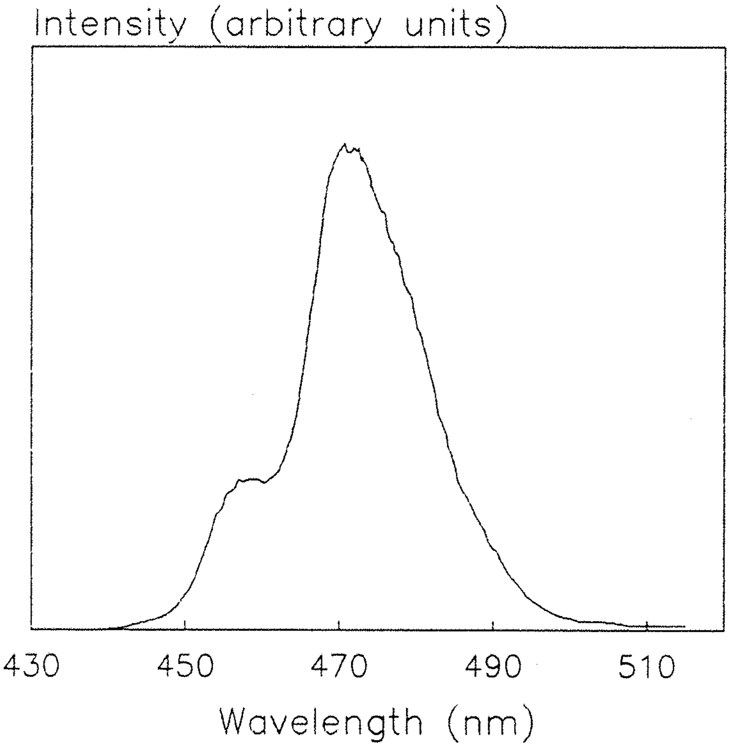

Fig.7.34 As Fig.7.32 with detail of blue emission

fluorescence is approximately 2.5 times larger for the 1000ppm Al_2O_3-SiO_2 fibre than for the comparably-doped 840ppm GeO_2-SiO_2 fibre (Figs.7.17 and 7.18). Correcting roughly for the lower concentration of the 200ppm fibre by multiplying by a factor of 5 gives a similar improvement in the blue yield over the germano-silica fibre. This increase in the upconverted fluorescence is a consequence of the longer lifetimes of the $^1G_4$ and $^3H_4$ levels in the alumina-silica host, where the reduced decay rates permit higher steady-state populations to build up.

7.8.3 Room Temperature Laser Operation

The Al_2O_3-SiO_2 fibres both exhibited laser action at around 2μm when pumped at 1.064μm in Fabry-Perot cavities, although the oscillation was unstable and difficult to maintain. A 1.1m length of the 1000ppm fibre butted against a high reflector (>99.5% at 2μm) at the input end and a 6% transmitting (at 2μm) mirror at the output end had a laser wavelength of 1.92μm. The threshold power was 2.8W incident on the launch microscope objective (10X). For incident powers up to 6W (the maximum available from the Nd:YAG laser at the time), the output laser power was too small to be measurable on a power meter. The laser signal, detected with a PbS photo-diode, was seen to consist of a spike ≤0.2ms in duration coincident with the occlusion of the pump beam by the chopper. This feature was also observed with the 200ppm fibre, which lased at 1.94μm with an incident threshold power of 4.5W for a 4m length of fibre. Again, laser action was very unstable, and re-cleaving the fibre ends did not lead to any improvement. It was impossible to assess the effect of fibre length for either of the fibres due to the instabilities, the negligible output laser power and the difficulty in achieving laser action in the first place. Clearly the alumina-silica fibres are worse performers than their germano-silica counterpart when pumped at 1.064μm, due almost certainly to the increased efficiency of the ESA process, since a higher pump power is then required to overcome the ESA losses and achieve threshold. To compensate for the higher gain requirement it should be possible to empty the lower laser (Stark) level by cooling with liquid nitrogen, thus reducing reabsorption losses on the laser transition and consequently reducing the gain requirement. Such experiments are described in the following section.

7.8.4 Liquid Nitrogen Cooled Laser Operation

The effect of cooling was investigated using the 200ppm fibre, since reabsorption losses in regions of the fibre exposed to room temperature would be less of a problem than with the 1000ppm sample simply because of the lower doping level. Fig.7.35 shows the end light fluorescence signal at 2μm as a function of pump power for a 6.6m fibre at room temperature and when cooled in a Dewar containing liquid nitrogen. The measurement was performed by analysing the 2μm end light signal with a monochromator and PbS photo-diode, using a chopped pump beam and locked-in phase-sensitive detector to amplify and recover the signal. The 2μm yield is substantially greater for the cooled fibre because of the reduction in ground state reabsorption. The pump absorption is correspondingly higher for the cooled fibre, as shown in Fig.7.36 where output pump power is plotted against input power for the cooled and uncooled fibre. Liquid nitrogen cooling was therefore expected to improve the laser performance of the Al_2O_3-SiO_2 fibre.

A Fabry-Perot cavity was set up with a high reflector (>99.5% at 2μm and 90% transmitting at the pump wavelength) at the input and a mirror transmitting 6% at 2μm as the output coupler. Fibre lengths between 1.0m and 10.0m were used, with all but ≈ 10cm at each end of the fibre immersed in a Dewar containing liquid nitrogen. The fibre was pumped with up to 6W but, as with the room temperature operation, the output power (of the order of μW) was too low to be reliably measured on a power meter. The establishment of laser action was, however, much easier to achieve and more readily maintained than in the room temperature case. With this improved stability, it was possible to make some assessment of the variation of performance with fibre length. Spectra of the laser emission were recorded by analysing the end light emission with a monochromator and PbS photo-diode, and the area under the spectra for various fibre lengths was taken as a measure of the output power. Fig.7.37 shows this output power versus fibre length. With so few data points it is difficult to assess whether the form of the curve is due to the three-level nature of the transition (imposed by the cooling) or to variations in the cleave quality of the fibre ends but, as with Fig.7.6 for the 840ppm germano-silica fibre, the output power shows a pronounced peak with length (in this case at about 5.5m) suggesting that the Tm^{3+}-doped fibre system is particularly sensitive to fibre length.

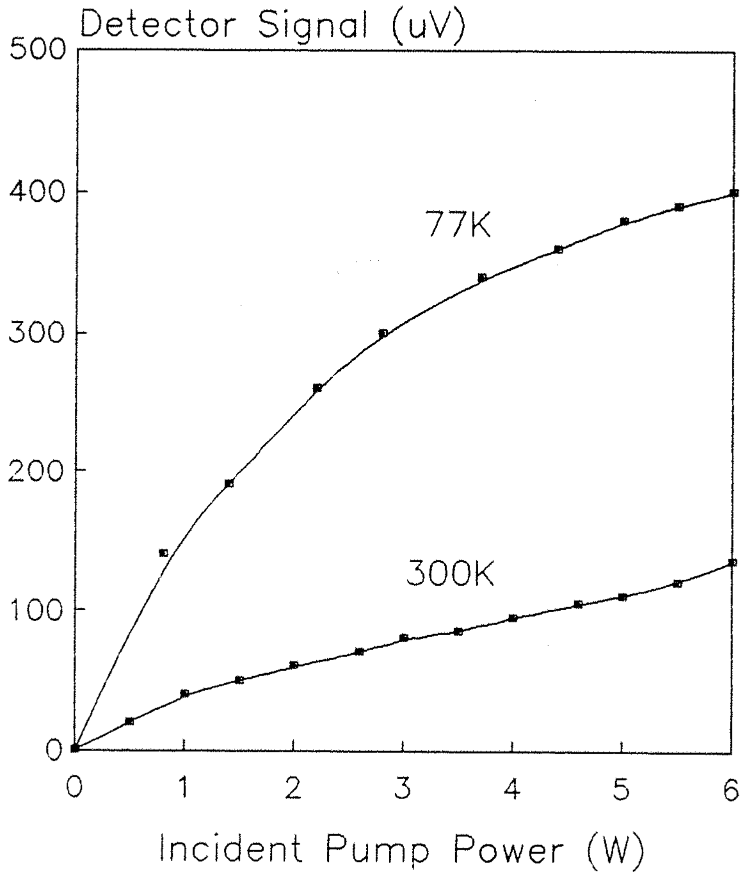

Fig.7.35 End light 2μm fluorescence at 77K and 300K versus pump power

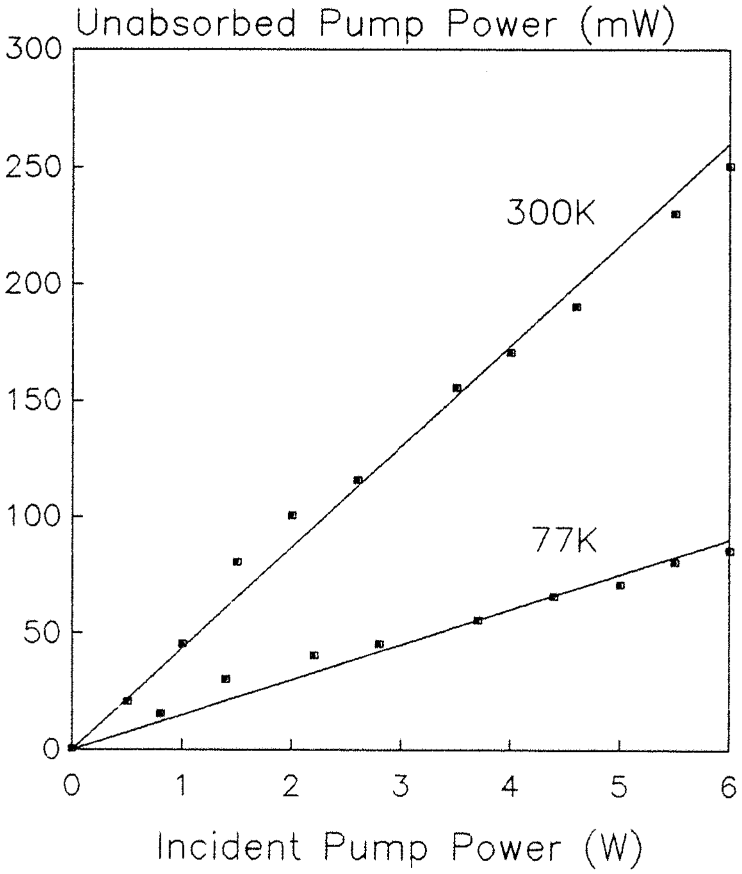

Fig.7.36 Unabsorbed pump power versus pump power at 77K and 300K

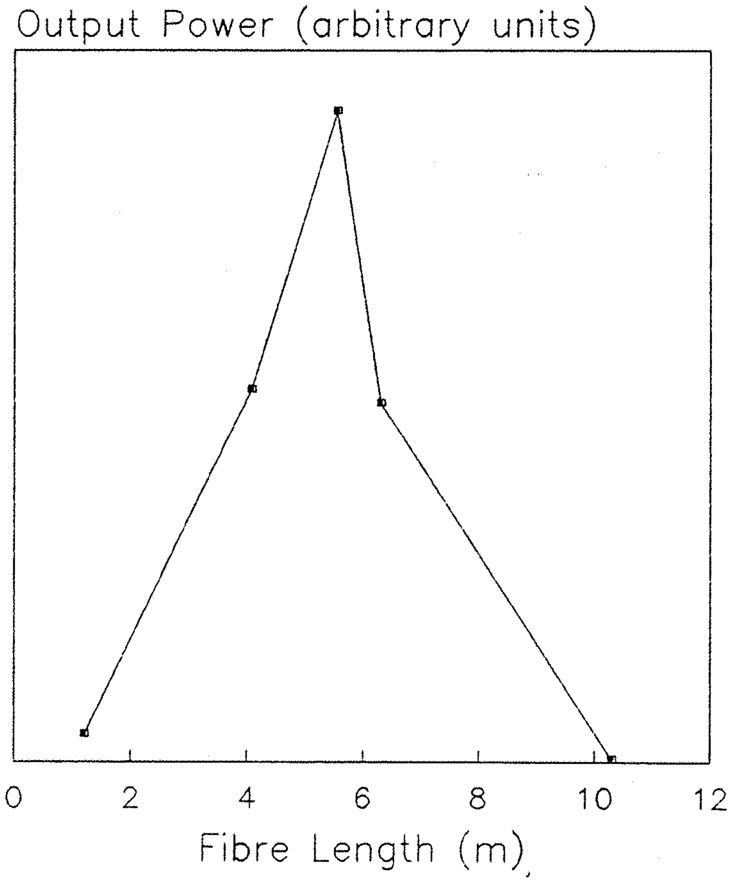

Fig.7.37 Laser power at 1.85μm versus fibre length at 77K

The laser spectrum was generally a continuous emission ranging from about 1.82μm to 1.88μm with a full width at half maximum of typically 40nm, although this emission appeared to comprise four main lines at (approximately) 1.84μm, 1.85μm, 1.86μm and 1.87μm (by slightly unbutting the output end, the spectrum was narrowed to 3.7nm centred at 1.85μm due to the etalon formed between the fibre end face and the mirror). The output wavelength is shifted from its room temperature value of ≈ 1.94μm for a 4m fibre, compared to ≈ 1.85μm for a similar length at 77K, since the emptying of the ground state multiplet Stark levels allows laser action to take place to the lower-lying levels without suffering reabsorption.

The laser action again took the form of a spike coincident with the time at which the pump was blocked by the chopper, as observed for room temperature operation in section 7.8.3. The spike was most apparent when the input or output end of the fibre was slightly unbutted. Fig.7.38 shows the oscilloscope trace taken from a fast InAs photo-diode (with filters to block the pump signal) located at the end of a liquid nitrogen cooled 10m length of fibre with both ends slightly unbutted, and pumped with 6W incident on the launch objective. The spike is ≈ 0.15ms in duration at its full width at half maximum. An expanded trace is shown in Fig.7.39, where the presence of relaxation oscillations confirms that the spike is indeed due to laser action. Fig.7.40 shows superimposed traces for the laser spike and the pump signal (obtained by removing the pump filters). The laser spike is initiated above the fluorescence signal immediately the pump signal begins to fall from its steady level. Other traces were similar irrespective of chopping rate, *i.e.*, the laser spike was always coincident with the pump switch-off.

The spike at the beginning of the pump trace is indicative of the temporal evolution of the absorption experienced by the pump light as ESA begins to take effect. Initially, as the pump is switched on, the only absorbing transition is $^3H_6$ - $^3H_5$, but when $^3H_4$ and subsequently $^3F_4$ become populated they present an additional source of pump absorption due to ESA, and so the pump transmission is decreased.

With the output end butted, the build-up time for threshold is reduced and oscillation begins virtually as soon as the pump beam is incident, although a spike still occurs when the beam is chopped, as shown in Fig.7.41. As the input end is gradually butted, the pre-spike laser signal increases in magnitude until it is comparable to the

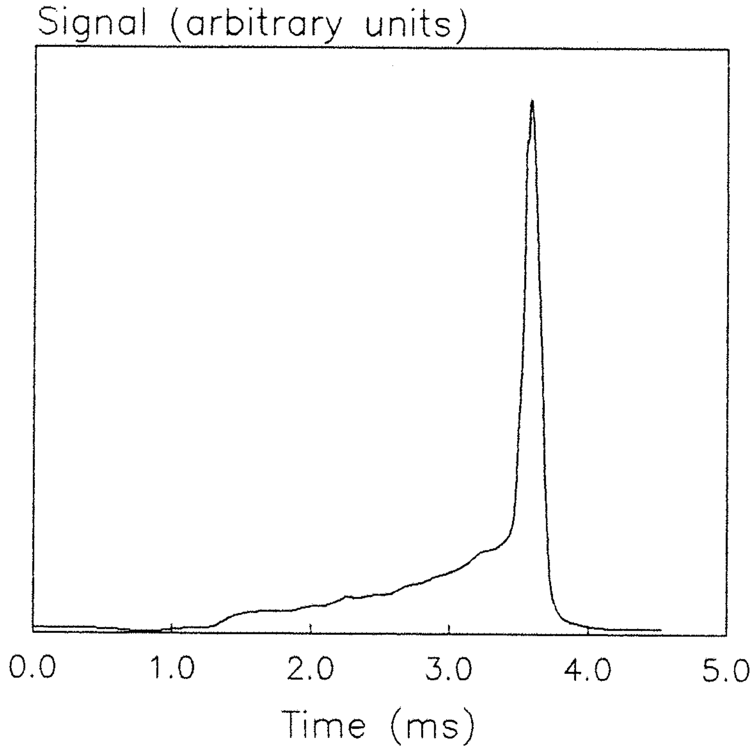

Fig.7.38 Laser oscillation (spike) with both ends of the fibre slightly unbutted

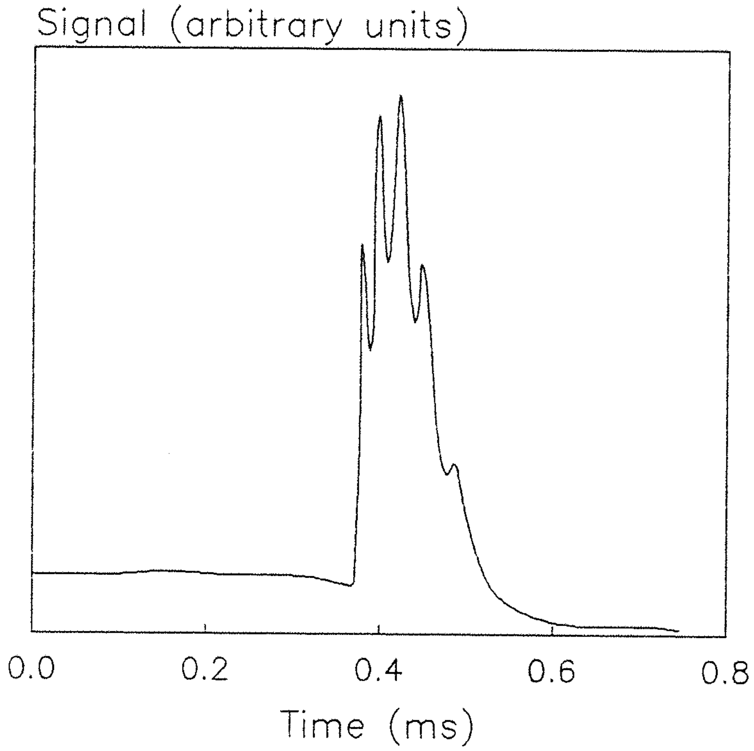

Fig.7.39 As Fig.7.38 with expanded time scale

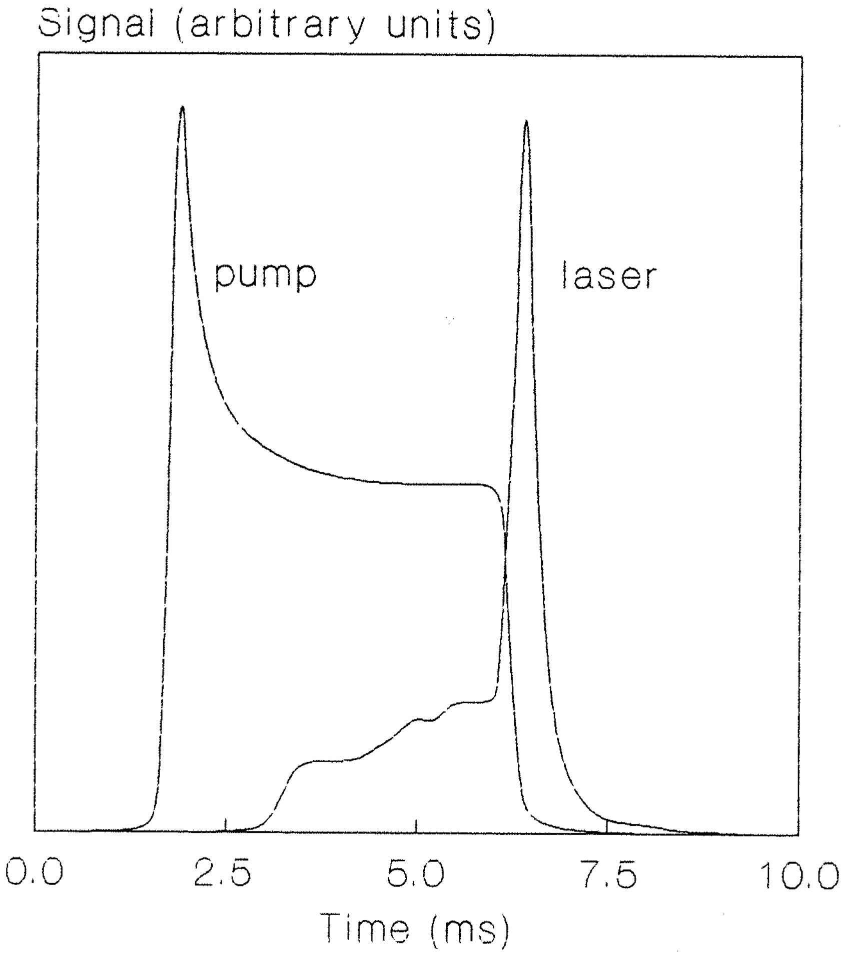

Fig.7.40 Transmitted pump signal with laser signal superimposed

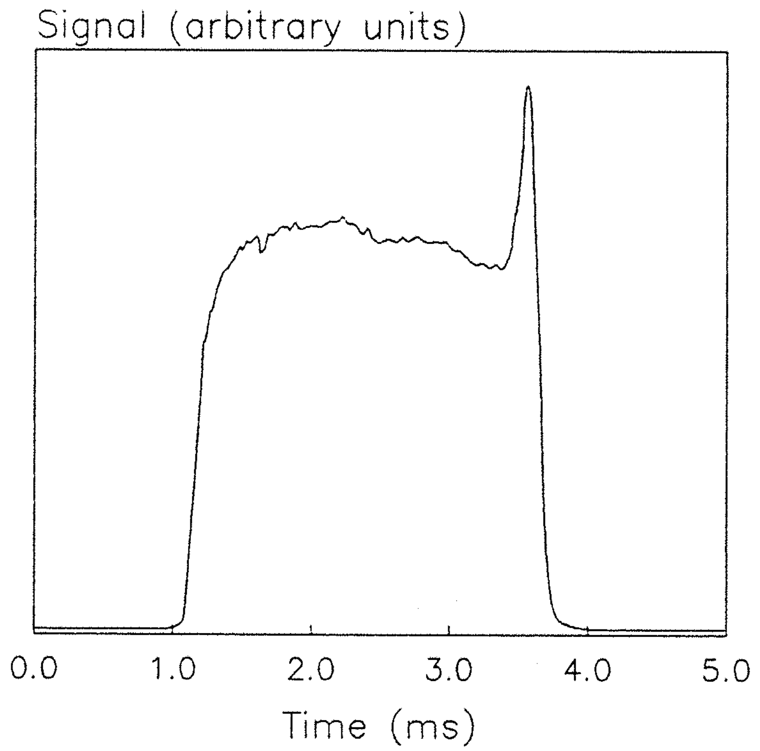

Fig.7.41 Laser oscillation with fibre output end butted, input end unbutted slightly

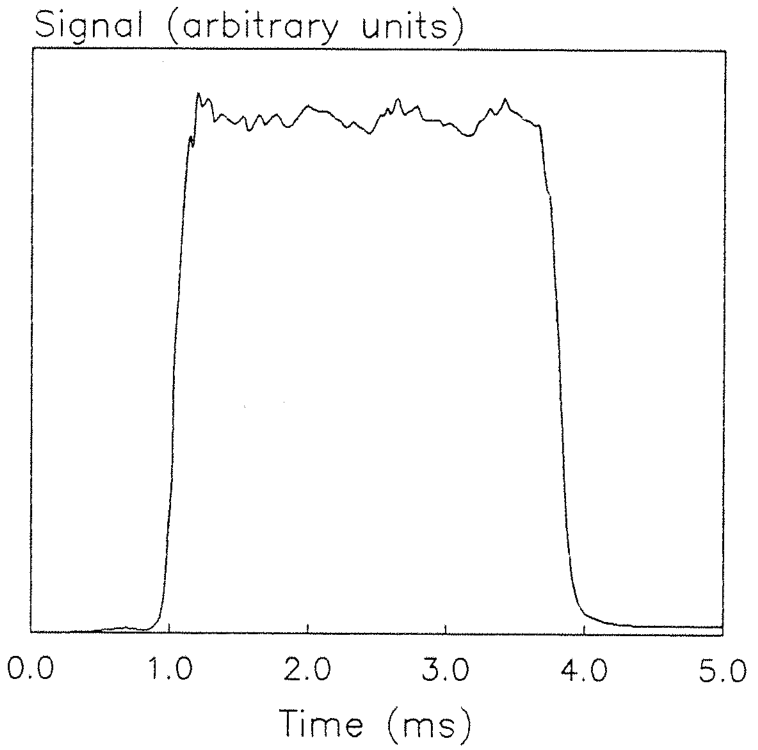

Fig.7.42 Laser oscillation with both ends of the fibre butted

spike, such that the laser signal becomes "smooth" throughout the pumping cycle, as shown in Fig.7.42. The spiking behaviour at the end of the pumping cycle was observed for various chopping rates, indicating that it is not dependent on the length of time for which the fibre is pumped. The spike is attributed to the circulatory nature of the excitation processes taking place in the fibre and arises as a result of excited state absorption removing population from the upper laser level. Under conditions of high cavity losses, such as one or both of the fibre ends being unbutted, the population inversion requirement on the $^3H_4$ - $^3H_6$ transition may be too great for laser action to occur. Population is then removed from $^3H_4$ mainly by ESA, eventually populating $^1G_4$ and relaxing back both directly to the ground state and also to $^3H_4$ (with fluorescence at ≈ 650nm), where the ESA cycle begins again. When the pump source is blocked, the removal by ESA of population from this level ceases, and the rapid build-up of population in the upper laser level due to the $^1G_4$ - $^3H_4$ relaxation overcomes the threshold inversion requirement to give laser action for as long as this inversion is maintained. Since the fibre is now unpumped, the inversion is maintained only briefly and hence the laser output is in the form of a spike. As the losses are reduced, by butting one end for instance, the threshold inversion requirement is also reduced and eventually reaches the point where, despite the ESA loss, laser action occurs during the pump cycle. Even so, when the pump is blocked the rapid population build-up in $^3H_4$ still gives a spiked output at the end of the cycle. The thulium-doped fibre is in effect self-Q-switching, where the switching loss mechanism is ESA, storing energy in the form of population circulating around the energy levels until it is "switched off" to decrease the loss and allow oscillation through a rapid population build-up in the upper laser level. This phenomenon was not observed with the germano-silica fibre, where ESA is a less effective loss mechanism.

7.9 Concluding Remarks

Continuous-wave laser action at ≈ 2µm has been demonstrated in Tm^{3+}-doped silica based fibres when pumped by a Nd:YAG source at 1.064µm, despite the very weak absorption at the pump wavelength (about 2 dB/m). A 1.8m length of fibre containing a nominal dopant ion concentration of 840ppm and with a core diameter of 8.6µm yielded

270mW of laser output for 1.2W absorbed. The LP_{11} mode cut off wavelength of 1.7μm ensured that the laser output was single transverse mode. The slope efficiency with respect to absorbed power was 28% for 6% total output coupling, representing an internal pump quantum efficiency above threshold of 0.53 (*i.e.*, 53% of the absorbed pump photons are converted into laser photons), and the threshold power was 105mW absorbed (295mW incident on the launch optics). In addition, tunable laser emission has been demonstrated over the range 1920nm to 1996nm, with a launched power threshold of about 1W.

The free-running fibre laser output power was increased further by using a second fibre from the same preform pulled down to a core diameter of 17μm, so that higher pump powers could be used without increasing the pump intensity at the high reflector on the input end of the fibre. A 0.7m length of the larger core fibre yielded 1.35W at 2μm for an absorbed pump power of 4.4W. The slope efficiency with respect to absorbed power was 37% for 6% total output coupling (measured with a 1.4m fibre), representing an internal pump quantum efficiency above threshold of 0.70. The threshold power with this length was 600mW absorbed (1.2W incident). Measurements of the output beam profile confirmed that, although this fibre can in principle support two transverse modes at 2μm, the output was in fact clearly single transverse mode.

For the range of pump powers (up to ≈ 10W) used in the experiments described in this chapter, no evidence of fibre laser output power saturation was found. It should therefore be possible to achieve even higher output powers than the 1.35W described above simply by increasing the pump power. Nd:YAG laser powers well in excess of those used here are available, and 2μm fibre laser outputs at the multiwatt level may be anticipated. The limiting factor in the laser output is likely to be thermally induced damage, particularly at the mirror surface at the input end, although a launch system involving a microscope objective (or other suitable lens) placed intracavity between the mirror and the fibre may circumvent this problem if the higher threshold requirement can be met by the pump source. The power handling capabilities may then be limited by nonlinear effects such as stimulated Brillouin scattering and stimulated Raman scattering, since heat deposition problems within the fibre itself can be alleviated by reducing the doping level so that the pump power is absorbed over a greater length. The reduced power absorbed per unit length may then be small enough to render thermally-induced stresses negligible. In some applications, however, a short highly doped fibre may be desirable, and the thermal effects may then become problematical. It has been estimated [7.23] that the maximum heat dissipation, where the maximum stress induced by differential expansion across the fibre radius reaches the tensile strength of the host material, is in the region of 1W/cm to 10W/cm. Taking the experimental values of 4.4W absorbed in a 0.7m fibre gives an average absorbed power per unit length of about 60mW/cm, *i.e.*, 1 to 2 orders of magnitude below the value at which thermally-induced stresses become important. Higher output power may also be possible through a modification in the fibre design to facilitate a cladding-pumped arrangement [7.24], where pump light (possibly from a multimode source) is launched not just into the fibre core, but into the surrounding cladding material as well, so that high pump powers (but at a lower intensity over the larger area) may be used without risk of input mirror damage. A second, outer, cladding layer (of lower refractive index than the first) provides guidance for the pump light, which is progressively absorbed into the doped fibre core as it propagates through the inner cladding [7.25, 7.26].

Some preliminary investigations into cladding pumped operation of Tm^{3+}-doped fibres were made using two fibres pulled from the 1000ppm Al_2O_3-SiO_2 preform (there was insufficient 840ppm GeO_2-SiO_2 preform remaining for any further fibres to be pulled from this). These new fibres had core/cladding diameters of 3.8μm/125μm and 2.8μm/90μm, respectively. However, initial results from these fibres were disappointing, with pump transmissions typically only a few percent through about 30cm of fibre. The poor results are believed to be caused by pump attenuation at the interface between the inner and outer cladding materials: silicone rubber was used as the outer cladding material, and has proved to be far from ideal in this application.

Although laser performance at 2μm has been the main area of interest in the Tm^{3+}-doped fibre, the striking blue fluorescence leads inevitably to speculation into the possibility of visible laser emission in a silica host, particularly as this has now been achieved for Tm^{3+}-doped fluorozirconate fibres [7.20]. Several attempts to achieve visible laser emission were made, using mirrors highly reflecting at ≈ 470nm butted at both ends of the fibre. The two alumina-silica (200ppm and 1000ppm) fibres were tried, as was the germano-silica (840ppm) fibre. Fibre lengths up to 6m were used, and although in general the etalon effects common during the butting procedure were observed (periodic variations in the output fluorescence signal as the fibre end approaches the mirror), the fibres did not reach threshold for pump powers up to 6W incident on the launch objective (the maximum available at the time). Liquid nitrogen cooling was also tried, with the intention of emptying the thermal population in the ground state Stark levels, but this still did not allow laser action to take place in the blue. The low population of $^1G_4$ suggested by experiment and modelling imply that thulium-doped silica fibres will require considerable modifications in the host design to increase the excited state absorption before visible laser emission can be realised.

Modifications in host design may also prove beneficial to the laser performance at 2μm, particularly if the energy level structure can be tailored to increase the ground state absorption at 1.064μm and reduce the ESA. Since this is essentially the opposite situation to that desired for visible laser emission, the particular fibre applications will therefore dictate the specific fibre host design, a subject of important on-going research.

References

[7.1] Farhad Hakimi, then at the Polaroid Corporation, private communication

[7.2] L. Esterowitz, R. Allen and I. Aggarwal, 'Pulsed laser emission at 2.3μm in a thulium-doped fluorozirconate fibre', *Electron. Lett.*, 24, 1104 (1988)

[7.3] R. Allen, L. Esterowitz and I. Aggarwal, 'Diode pumped thulium doped fiber laser at 2.29μm', Paper TUJ23, in Technical Digest, Conference on Lasers and Electro-Optics (1989)

[7.4] J.E. Townsend, Optical Fibre Group, Department of Electronics and Computer Science, University of Southampton.

[7.5] F. Martinez and C.D. Hussey, '(E)ESI determination from mode-field diameter and refractive index profile measurements on single-mode fibres', *IEE Proc. J*, 135, 202 (1988)

[7.6] P.J. Samson, 'Usage-based comparisons of ESI techniques', *J. Lightwave Tech.*, LT-3, 165 (1985)

[7.7] F. Martinez and C.D. Hussey, 'Enhanced ESI for the prediction of waveguide dispersion in single-mode optical fibres', *Electron. Lett.*, 24, 1019 (1984)

[7.8] C. Millar, 'Direct method for determining equivalent step index profiles for monomode fibres', *Electron. Lett.*, 17, 458 (1981)

[7.9] C. Pask and F. Ruhl, 'New method for equivalent step index fibre determination ', *Electron. Lett.*, 19, 643 (1983)

[7.10] C.D. Hussey and C. Pask, 'Theory of profile moments description of single-mode fibres', *IEE Proc. H*, 129, 123 (1982)

[7.11] A. Yariv, 'Optical Electronics', ch.3, 3rd ed., Holt-Saunders (1985)

[7.12] D. Gloge, 'Weakly guiding fibres', *Appl. Opt.*, 10, 2252 (1971)

[7.13] O. Svelto, 'Principles of Lasers', ch.4, 3rd ed., Plenum (1989)

[7.14] A.W. Snyder and J.D. Love, 'Optical Waveguide Theory', ch.15, Chapman and Hall (1983)

[7.15] D.C. Hanna, I.M. Jauncey, R.M. Percival, I.R. Perry, R.G. Smart, P.J. Suni, J.E. Townsend and A.C. Tropper, 'Continuous-wave oscillation of a monomode thulium-doped fibre laser', *Electron. Lett.*, 24, 1222 (1988)

[7.16] D.C. Hanna, R.M. Percival, I.R. Perry, R.G. Smart, J.E. Townsend and A.C. Tropper, 'Frequency upconversion in Tm- and Yb:Tm-doped silica fibers', *Opt. Comm.*, 78, 187 (1990)

[7.17] P.R. Morkel, M.C. Farries and S.B. Poole, 'Spectral variation of excited state absorption in neodymium doped fibre lasers', *Opt. Comm.*, 67, 349 (1988)

[7.18] D.C. Hanna, R.M. Percival, R.G. Smart and A.C. Tropper, 'Efficient and tunable operation of a Tm-doped fibre laser', *Opt. Comm.*, 75, 283 (1990)

[7.19] R.R. Jacobs and M.J. Weber, 'Dependence of the $^4F_{3/2} \rightarrow {}^4I_{11/2}$ induced-emission cross section for Nd^{3+} on glass composition', *IEEE J. Quantum Electron.*, QE-12, 102 (1976)

[7.20] J.Y. Allain, M. Monerie and H. Poignant, 'Blue upconversion fluorozirconate fibre laser', *Electron. Lett.*, 26, 166 (1990)

[7.21] J.E. Townsend, Optical Fibre Group, Department of Electronics and Computer Science, University of Southampton, private communication

[7.22] W.S. Brocklesby and J.R. Lincoln, Laser Group, Department of Physics, University of Southampton, private communication

[7.23] D.C. Hanna, M.J. McCarthy and P.J. Suni, 'Thermal considerations in longitudinally pumped fibre and miniature bulk lasers', SPIE Proceedings, Fiber Laser Sources and Amplifiers, 1171, 160 (1989)

[7.24] H. Po, E. Snitzer, R. Tumminelli, L. Zenteno, F. Hakimi, N.M. Cho and T. Haw, 'Double clad high brightness Nd fiber laser pumped by GaAlAs phased array', OFC '89, Houston, USA, postdeadline paper PD7-1

[7.25] D. Marcuse, 'launching light into fiber cores from sources located in the cladding', *J. Lightwave Tech.*, 6, 1273 (1988)

[7.26] R. A. Lieberman, L.L. Blyler and L.G. Cohen, 'A distributed fiber optic sensor based on cladding fluorescence', *J. Lightwave Tech.*, 8, 212 (1990)

CHAPTER 8

CONCLUSIONS

8.1 Introduction

Three different species of rare-earth dopant ions have been investigated as laser activators in silica-based optical fibres, and the performance characteristics, spectroscopy and other relevant features have been described. In the following sections, the main experimental results are summarised, and some suggestions are made for further work.

8.2 Ytterbium-Doped Fibre

Ytterbium-doped fibre proved to be a far more interesting system than might have been expected initially. Its deceptively simple energy level scheme, comprising just two multiplets, yielded not only laser action on three- and quasi-four-level transitions, but also significant amounts of superfluorescence power and the phenomenon of cooperative luminescence in the visible region.

The results of the experiments may be summarised as follows. Continuous-wave single mode laser oscillation was observed at 974nm (three-level transition) and around 1040nm (quasi-four-level transition) for pump wavelengths in the region of 0.8-0.9μm. A maximum of 9mW was observed at 974nm for 27mW absorbed at 900nm in a 50cm fibre doped with about 600ppm Yb^{3+}. A 4m length yielded up to 28mW at 1050nm for 72mW absorbed at 850nm. The oscillation wavelength was selectable mainly by appropriate choice of fibre length, since reabsorption of the three-level emission precluded the use of a long fibre for laser action at 974nm, whereas the quasi-four-level emission was less sensitive to the fibre length due to reduced reabsorption losses. The optimum length for three-level emission was that length for which the unabsorbed pump power leaving the output end of the fibre was equal to the pump saturation power: a longer fibre would provide an absorbing region at the signal wavelength, whereas a shorter fibre would not maximise the available gain. The lack of excited state absorption (ESA) in the Yb^{3+} system is credited as the reason for the high slope efficiencies measured for both laser transitions. With respect to absorbed power, the highest observed slope efficiencies were 63% at 974nm and 78% at 1036nm, in a 20cm and 1.1m fibre, respectively, pumped at 900nm in both instances. The absorbed threshold powers were measured as about 10mW for pumping both transitions at 900nm, and about 30mW for the quasi-four-level transition pumped at 850nm, indicating that GaAlAs diode laser pumped operation should be a possibility. The four-level transition was tunable from 1000nm to 1162nm using prisms as intracavity dispersive elements, although the resonator was not optimised with respect to output coupling and the output powers were negligibly small. Severe modulation of the output laser signal with laser wavelength was found to be due to the birefringent nature of the fibre in conjunction with polarisation-sensitive cavity losses. The incorporation of a fibre loop polarisation controller was effective in significantly reducing this problem.

The laser transitions have been modelled with a simple rate equation analysis which takes no account of the pump or signal mode profiles. This was justified due to the good overlap of the two profiles since they both propagated single mode in the fibre. A reasonable agreement between experiment and theory was found, and the model has applications in predicting the minimum threshold power for a given value of resonator loss by calculating the three- and four-level gain as a function of fibre length and input pump power.

The high gain available from the Yb^{3+}-doped fibre allowed efficient superfluorescent operation, with up to 12mW emitted at 974nm for 32mW absorbed at 900nm in a 50cm fibre, and 27mW emitted at 1040nm for 67mW absorbed at 850nm in a 5m fibre. Slope efficiencies were 47% and 62%, respectively, with respect to absorbed power. The superfluorescence was found to have a linewidth of about 3nm at 974nm and about 20-25nm at 1040nm, with some evidence of line narrowing for the higher pump powers.

The generation of Q-switched laser pulses on both transitions was also possible, with ≈ 25ns pulses at 974nm and ≈ 100ns pulses at 1036nm. Peak output powers were in excess of 1W in both cases. Improvements of the loss modulation will be necessary to prevent prelasing, a feature that makes a precise determination of the pulse energy difficult. The low diffraction efficiency of the modulator meant that lasing could not be held off in some situations. A modulator providing a higher loss in its "closed" state would solve the problem, and multiwatt peak powers may then be anticipated as a result.

The use of a high power pump source such as a Ti:Sapphire laser rather than the Styryl 9M dye laser used as a pump in these experiments would prove beneficial in increasing the laser power available in both free-running and tunable modes of operation, but unfortunately represents a distinct departure from the trend towards diode pumping convenience. However, the continuing developments in diode laser technology by no means rule out significant progress in diode pumped operation of the Yb^{3+} fibre laser.

From a spectroscopic point of view, further investigations into the visible emission in the green may give a greater insight into the cooperative luminescence phenomenon. The factors that may influence the visible fluorescence yield, such as dopant ion concentration, need to be identified. This was not performed during the course of the experiments described above, since an integrating sphere, necessary for accurate measurements of the emitted radiation, was not available at the time.

8.3 Ytterbium-Erbium-Doped Fibre

A brief investigation was made into the characteristics of Er^{3+}-doped fibres sensitised with an Yb^{3+} co-dopant, the intention being to pump the Er^{3+} ions via energy transfer from excited Yb^{3+} ions at wavelengths which are inefficient or impractical for pumping singly-doped Er^{3+} fibres.

A Styryl 9M dye laser was used to simulate GaAlAs diode wavelengths in the 800-845nm region. The presence of pump excited state absorption (ESA) in Er^{3+} in this wavelength region was manifested as an increase in the threshold power and a decrease in the slope efficiency at around 800nm and 840nm. The upconversion fluorescence due to the ESA was also found to be maximised at these wavelengths. The most favourable pump wavelength in the 0.8μm region was identified as 820-830nm, where the threshold power was 5mW absorbed and the slope efficiency was nearly 9% with respect to absorbed power for a 70cm fibre. Continuous-wave single mode laser action was observed at 1.564μm, with a maximum measured output power of 3mW for 40mW absorbed in a 70cm fibre pumped at 825nm. Tunable operation over a continuous range from 1.521μm to 1.562μm was demonstrated with an intracavity prism to provide wavelength dispersion. The typical threshold powers for cw laser action are readily obtainable from GaAlAs diode lasers, and Yb^{3+} co-doping appeared to offer an effective means of diode pumping Er^{3+}-doped fibres at wavelengths in the long wavelength tail of the 807nm absorption peak where Er^{3+} absorption is falling off, with the additional feature of avoiding, or at least reducing, the effects of pump induced ESA. However, 980nm has since been identified as perhaps the optimum pump wavelength for Er^{3+} since ESA is avoided completely, and direct diode pumping with 980nm diodes will probably become commonplace if such pump sources (still very much in the development stage) prove to be reliable. If not, then Yb^{3+} may yet find a role since the 974nm emission wavelength of Yb^{3+}-doped fibre lasers would be suitable as a pump source.

8.4 Thulium-Doped Fibre

Thulium-doped fibre was investigated as a means of producing a laser source in the 2μm region, where sources are required for medical applications, in coherent laser radar, and for uses in molecular spectroscopy. Once again a Styryl 9M dye laser was used to simulate GaAlAs diode laser wavelengths, and continuous-wave single mode laser oscillation was demonstrated with a threshold power of 20-30mW absorbed in a $\approx$ 30cm fibre pumped at 797nm. The slope efficiency was 13% with respect to absorbed power, and the maximum output power at 2μm was 2.5mW for 50mW absorbed. Continuously tunable laser operation was observed over the range 1866nm to 2014nm for a 1.2m fibre and 1810nm to 2006nm for a 0.6m fibre, using a set of birefringent tuning plates for wavelength selection. No optimisation of output coupling was performed for either the cw or tunable operation, and hence some improvement in the performance may be expected.

The fibre was also found to possess sufficient absorption at the 1.064μm to permit laser operation using a Nd:YAG pump source. It was then possible to significantly increase the fibre laser output power at 2μm simply by using high input power from a Nd:YAG laser. A 28% slope efficiency was measured with respect to absorbed power for a 1.8m fibre identical to the one employed in the experiments with the Styryl 9M pump source. The threshold power was about 100mW absorbed. A maximum fibre laser power of 270mW was observed at 2μm for 1.2W absorbed. The laser wavelength was tunable from 1920nm to 1996nm, although with a large penalty in the form of an increased threshold (≈ 1W launched) due to losses introduced by the intracavity elements necessary for tuning.

A modification in the fibre design allowed even greater output power to be achieved. A new fibre was fabricated with a core area four times greater than that of the original fibre, so that a higher pump power could be used without increasing the intensity beyond the damage threshold of the input mirror. A 0.7m fibre yielded 1.35W for 4.4W absorbed at 1.064μm. The slope efficiency (for a 1.4m fibre) was 37% with respect to absorbed power, and the threshold power was 600mW absorbed. The overall conversion efficiency from Nd:YAG laser output power to fibre laser output power is about 15%, and thus this arrangement represents a simple and reasonably efficient method of converting the output of a Nd:YAG laser into emission at 2μm. An investigation of the fibre laser output profile demonstrated it to be single transverse mode although this larger fibre could in principle support two modes at 2μm. Higher output powers are anticipated by modifying the fibre design further so that the pump power is propagated in the cladding region and gradually absorbed by the core along the fibre length. In this way a large fibre diameter (inclusive of the cladding) should permit very high pump powers to be used without reaching the damage intensity threshold at the input end, and if all this power can be subsequently absorbed by the core, then multiwatt cw operation can be anticipated.

In addition to the laser performance of Nd:YAG pumped Tm^{3+}-doped fibre, the blue fluorescence due to upconversion of the pump radiation has also been studied. Laser action in the blue was not achieved due to the unfavourably short lifetimes of intermediate levels in the upconversion process. A change in the core composition, which was initiated to increase these lifetimes, was unsuccessful in realising visible laser emission. This is attributed to the high nonradiative decay rates of ions in a silica host, compared to fluorozirconate hosts where longer radiative lifetimes have allowed sufficient population to build up in the blue emitting level for laser action to take place. The gain on the 2μm transition has been modelled to predict the minimum threshold in the presence of upconversion, as a function of fibre length and input pump power, with the thermal population in the terminal (Stark) laser level acting as a loss mechanism for the 2μm emission. The amount of population residing in the level responsible for visible emission is shown to be almost negligibly small, although an increase in the intermediate level lifetimes is postulated to increase this population. Further work on the silica host components will be necessary before laser action in the visible will be possible in Tm^{3+}-doped silica fibre.

8.5 Final Summary

The investigations into rare-earth-doped fibres described in this thesis provide further evidence that laser devices of this type exhibit a wide range of interesting features which may find practical applications in a variety of situations. Continuous-wave single mode laser oscillation has been demonstrated in three distinct wavelength regions: 1μm, 1.5μm, and 2μm. In addition, phenomena such as amplified spontaneous emission, cooperative luminescence and excited state absorption have been observed. Diode laser pumping has been shown to be viable, since the thresholds for laser action in the ytterbium-, ytterbium-erbium- and thulium-doped fibres are attainable with currently available GaAlAs diode lasers. The >1W continuous-wave operation of the thulium system under Nd:YAG excitation has shown that fibre lasers need not necessarily be low power devices, and may compete with established laser sources in a variety of applications.

APPENDIX

PUBLISHED PAPERS

The following published papers were included in the bound thesis. These have not been digitised due to copyright restrictions, but their doi are provided.

Hanna, D. C., Percival, R. M., Perry, I. R., Smart, R. G., Suni, P. J., Townsend, J. E., & Tropper, A. C. (1988). Continuous-wave oscillation of a monomode ytterbium-doped fibre laser. Electronics Letters, 24(17), 1111. Available at: http://dx.doi.org/10.1049/el:19880755

Hanna, D. C., Percival, R. M., Perry, I. R., Smart, R. G., Suni, P. J., & Tropper, A. C. (1989). Continuous-Wave Tunable and Superflourescent Operation of a Monomode Ytterbium-Doped Fiber Laser. Advanced Solid State Lasers. Available at: http://dx.doi.org/10.1364/assl.1989.jj1

Hanna, D. C., Perry, I. R., Smart, R. G., Suni, P. J., Townsend, J. E., & Tropper, A. C. (1989). Efficient superfluorescent emission at 974 nm and 1040 nm from an Yb-doped fiber. Optics Communications, 72(3-4), 230–234. Available at: http://dx.doi.org/10.1016/0030-4018(89)90401-x

Hanna, D. C., Percival, R. M., Perry, I. R., Smart, R. G., Suni, P. J., & Tropper, A. C. (1990). An Ytterbium-doped Monomode Fibre Laser: Broadly Tunable Operation from 1·010 µm to 1·162 µm and Three-level Operation at 974 Nm. Journal of Modern Optics, 37(4), 517–525. Available at: http://dx.doi.org/10.1080/09500349014550601

Hanna, D. C., Percival, R. M., Perry, I. R., Smart, R. G., & Tropper, A. C. (1988). Efficient operation of an Yb-sensitised Er fibre laser pumped in 0.8 µm region. Electronics Letters, 24(17), 1068. Available at: http://dx.doi.org/10.1049/el:19880724

Hanna, D. C., McCarthy, M. J., Perry, I. R., & Suni, P. J. (1989). Efficient high-power continuous-wave operation of monomode Tm-doped fibre laser at 2µm pumped by Nd:YAG laser at 1.064µm. Electronics Letters, 25(20), 1365. Available at: http://dx.doi.org/10.1049/el:19890912

Hanna, D. C., Jauncey, I. M., Percival, R. M., Perry, I. R., Smart, R. G., Suni, P. J., Townsend, J. E., Tropper, A. C. (1988). Continuous-wave oscillation of a monomode thulium-doped fibre laser. Electronics Letters, 24(19), 1222. Available at: http://dx.doi.org/10.1049/el:19880831

Hanna, D. C., Percival, R. M., Perry, I. R., Smart, R. G., Suni, P. J., & Tropper, A. C. (1989). Continuous-Wave Oscillation of a Monomode Thulium-Doped Silica Fiber Laser. Advanced Solid State Lasers. Available at: http://dx.doi.org/10.1364/assl.1989.jj3

Hanna, D. C., Perry, I. R., Lincoln, J. R., & Townsend, J. E. (1990). A 1-Watt thulium-doped cw fibre laser operating at 2 µm. Optics Communications, 80(1), 52–56.
Available at: http://dx.doi.org/10.1016/0030-4018(90)90505-n